A precise measurement of the Z boson cross-section and a test of the Standard Model using the LHCb detector

Author: Ronan Wallace
Student number: 11277271

The thesis is submitted to University College Dublin in fulfilment of the requirements for the degree of Doctor of Philosophy.

School of Physics

Head of School: Prof. Padraig Dunne
Supervisor: Prof. Ronan McNulty
Doctoral Studies Panel: Prof. Tara Shears
Dr. John Quinn

August 2015

Contents

Abstract

Measurements of production cross-sections for Z bosons that decay to muons are presented in this thesis. The data used to perform the measurements were recorded by the LHCb detector during pp collisions at centre-of-mass energies of 7 and 8 TeV, corresponding to integrated luminosities of approximately 1.0 and 2.0 fb^{-1}. The cross-sections are measured for muons in the pseudorapidity range $2.0 < \eta < 4.5$ with transverse momenta $p_T > 20$ GeV/c. The dimuon mass is restricted to $60 < M_{\mu^+\mu^-} < 120$ GeV/c^2. Total cross-sections are determined with a precision of approximately 2%. Cross-sections are also measured as functions of kinematic variables relating to the Z boson.

Ratios of production cross-sections of electroweak bosons are presented using measurements of W boson production. A precise test of the Standard Model is provided by the measurement of the ratio

$$\frac{\sigma_{W^+\to\mu^+\nu_\mu} + \sigma_{W^-\to\mu^-\bar{\nu}_\mu}}{\sigma_{Z\to\mu^+\mu^-}}$$

where the uncertainty due to luminosity, and other correlated uncertainties, cancels. This cancellation allows the cross-section ratios to be measured with an overall precision below 1%.

Measurements of electroweak boson cross-section ratios as functions of muon η are presented for the first time. Measurements of cross-section ratios and ratios-of-ratios of cross-sections at different centre-of-mass energies are also presented for the first time. Cross-section ratios at different centre-of-mass energies are determined with a precision of approximately 1.6%. Ratios-of-ratios of cross-sections are measured with an overall precision below 1%.

All measurements are consistent with the predictions of the SM. It is expected that the data presented here will help place significant constraints on the form of proton PDFs.

Declaration of Authorship

I hereby certify that the submitted work is my own work, was completed while registered as a candidate for the degree stated on the Title Page, and I have not obtained a degree elsewhere on the basis of the research presented in this submitted work.

The W boson cross-sections were measured by Simone Bifani. The FEWZ predictions were provided by Katharina Müller.

"The ability to understand a question from all sides meant one was totally unfit for action. Fanatical enthusiasm was the mark of a real man."

Thucydides

Acknowledgements

I would first like to acknowledge my supervisor, Prof. Ronan McNulty. The opportunity to play a small role at the great project that is CERN and the LHC is not something I take lightly, and it is thanks to his vision that students at Irish universities get a seat at that table. I would also like to thank him for the countless suggestions that have gone into improving the quality of this document.

Thank you to the Irish and European people who made these studies possible. This thesis was produced as part of the output of the DGPP, funded under the Programme for Research in Third Level Institutions (PRTLI) Cycle 5 and co-funded by the European Regional Development Fund. Perhaps I can repay the debt by putting my skills to good use over the coming years.

I would also like to thank my colleagues, home and abroad, who have helped me along the way. In particular I would like to thank Simone Bifani. Charged with bringing me up to speed in the world of High Energy Physics, I daresay he has done a decent job. Many thanks to you my friend, your time has been very much appreciated. This last year in particular has been a blast. Phil and Steve, tag-team extraordinaire, thanks for continuing to be available to answer my nagging questions. Wenchao, memories of your quiet diligence have helped me plug away when the prize was still months away.

I am also very grateful to Katharina Müller who has provided me with plenty of opportunities over the years, from speaking at conferences to experiencing life as a visiting researcher at UZH in Zürich. Thanks to Jonny Anderson for the fruitful collaboration at that time and the others at UZH that gave me such a warm welcome.

All the people that have encouraged my passion for physics deserve a special mention. Dad, I remember the Chemistry set yourself and Mam bought me, and the little notebook you gave to record results. On the first page you drew the internationally recognisable symbol of the atom, electrons orbiting the nucleus. I think I still remember that feeling of *wow, this is so incredibly important, but it seems so complicated, I want to understand.* There is a word for that I am sure. My science teachers at St. Peter's College, Jim Doyle, Judith Thomas, Seán Rossiter. Thanks for pretending not to be frustrated with all the questions.

To my family, Brendan, Mary, Conor and Gareth. Thank you for all your support. I hope you all know that I love you all very much. I probably don't say it often enough, and I know it probably sounds corny reading it in an academic thesis, but it seems

bizarrely appropriate right now as I write, given the amount of energy, blood, sweat and tears that have gone into these pages.

Simona, I am so incredibly lucky to have met you on my path. You are the only one to have experienced first hand the madness of the last year. Thanks so much for helping me through it all. From staring at plots to considering the most appropriate quotation to be inserted at the beginning of a thesis, you have contributed to this more than you know. I love you so much! Long may our adventure continue!

Ireland's EU Structural Funds
Programmes 2007 - 2013

Co-funded by the Irish Government
and the European Union

European Regional
Development Fund
Investing in your future

An Roinn Post, Fiontar agus Nuálaíochta
Department of Jobs, Enterprise and Innovation

HEA | HIGHER EDUCATION AUTHORITY
AN tÚDARÁS um ARD-OIDEACHAS

Abbreviations

ALICE	**A** **L**arge **I**on **C**ollider **E**xperiment
ATLAS	**A** **T**oroidal **L**HC **A**pparatus
BFKL	**B**alitsky-**F**adin-**K**uraev-**L**ipatov
BSM	**B**eyond **S**tandard **M**odel
CDF	The **C**ollider **D**etector at **F**ermilab
CKM	**C**abibbo **K**obayashi **M**askawa
CMS	**C**ompact **M**uon **S**olenoid
DGLAP	**D**okshitzer-**G**ribov-**L**ipatov-**A**ltarelli-**P**arisi
ECAL	**E**lectromagnetic **C**alorimeter
FSR	**F**inal **S**tate **R**adiation
GEC	**G**lobal **E**vent **C**ut
HCAL	**H**adronic **C**alorimeter
HPD	**H**ybrid **P**ixel **D**etector
IP	**I**nteraction **P**oint
IP	**I**mpact **P**arameter
IT	**I**nner **T**racker
LHC	**L**arge **H**adron **C**ollider
LHCb	**L**arge **H**adron **C**ollider **b**eauty experiment
LINAC	**LIN**ear **AC**celerator
LL	**L**eading **L**ogarithm
LO	**L**eading **O**rder
MC	**M**onte **C**arlo
MD	**M**agnet **D**own
MU	**M**agnet **U**p
NLL	**N**ext-to-**L**eading **L**ogarithm

NLO	**N**ext-to-**L**eading **O**rder
NNLL	**N**ext-to-**N**ext-to-**L**eading **L**ogarithm
NNLO	**N**ext-to-**N**ext-to-**L**eading **O**rder
OT	**O**uter **T**racker
PDF	**P**arton **D**istribution **F**unction
PMT	**P**hoto **M**ultiplier **T**ube
PS	**P**roton **S**ynchrotron
PSB	**P**roton **S**ynchrotron **B**ooster
PV	**P**rimary interaction **V**ertex
QCD	**Q**uantum **C**hromo**D**ynamics
QED	**Q**uantum **E**lectro**D**ynamics
RICH	**R**ing **I**maging **CH**erenkov detector
RMS	Square-**R**oot of the **M**ean-**S**quared
SM	**S**tandard **M**odel
SPS	**S**uper **P**roton **S**ynchrotron
SPD	**S**cintillating **P**ad **D**etector
SSB	**S**pontaneous **S**ymmetry **B**reaking
SVD	**S**ingular **V**alue **D**ecomposition
TCK	**T**rigger **C**onfiguration **K**ey
TT	**T**racker **T**uricensis
VELO	**VE**rtex **LO**cator

Chapter 1

Introduction

Particle physics is the field of enquiry that concerns itself with the fundamental particles of nature and their interactions. There are four such interactions, in one-to-one correspondence with the four fundamental forces of nature: gravity, electromagnetism, the weak nuclear force and the strong nuclear force. Each force acts on fundamental particles that are charged with respect to that force. It is not understood why these forces exist, rather, it is accepted that they do, and classifying their effect on fundamental particles is a worthwhile pursuit.

Theories and measurements go hand-in-hand in understanding these forces. As with all branches of science, observations, measurements, and human thirst for patterns and predictability, inspire the design of theoretical models to describe nature. Sophisticated models describe the observed data, but also go one step further to provide predictions of new phenomena, motivating new experiments. Measurements then validate or invalidate these predictions, and the cycle continues.

The theoretical framework that best describes the interactions of fundamental particles is called quantum field theory. This framework incorporates the quantum theory developed in the early 20^{th} century, and interprets particles as manifestations of fields that pervade all of space. In the laboratory, particle interactions are best studied using energetic beams of stable particles that are brought into collision with other stable particles. The latter can be at rest (fixed-target), or constitute a second energetic beam. Given the initial particle species and their energy, quantum field theories may be used to predict rates of specific interactions in the laboratory. These rates are referred to as cross-sections.

The primary objective of this thesis is the measurement of the Z boson cross-section using the data collected by the LHCb detector from proton-proton collisions during

LHC Run-I [1] [2]. The Z boson is the fundamental particle that is responsible for the mediation of electrically neutral weak interactions. Similar to the photon, it is an electrically neutral particle. Two more important properties of the Z boson are its mass, which is 91.2 GeV/c^2, and its half-life, which is $\mathcal{O}(10^{-23})$ s [3]. The mass of the Z boson is quite large with respect to the masses of the particles to which it decays.

In the analysis presented here, the Z boson is reconstructed through its decay to muons and anti-muons. This particular decay channel accounts for $(3.366 \pm 0.007)\%$ of all Z boson decays [3]. Muons have masses of 105.7 MeV/c^2 and half-lives of about 2.2 x 10^{-6} s [3]. The relatively long half-life is significant because it allows the muon to be observed by a detector. Mass-energy conservation dictates that the mass difference between the Z boson and the two muons be translated into momentum for the muons. The presence of a Z boson is thus inferred from the existence of two oppositely charged, high momentum muons.

After its discovery in 1983, precision measurements of the Z boson's properties were performed at the Large Electron Positron collider (LEP), which operated between 1989-2000 [4]. In terms of precision, many of the LEP measurements remain unrivalled, however, measurements of production in a hadronic environment at the LHC are important for a number of reasons. First, they help to unravel the sub-structure of the proton, to assign the proportion of quarks and gluons therein. The unique geometry of the LHCb detector is an advantage in this regard. Second, isolated, high momentum leptons from decays of the Z boson typically have a high trigger efficiency; studies requiring a Z boson in the event benefit from this. Third, the relatively clean signature allows a number of calibration studies to be performed, the results of which may be used in a variety of different analyses. These include the estimation of lepton reconstruction efficiencies and the evaluation of corrections to jet energy and lepton momentum.

The W boson is the fundamental particle that is responsible for the mediation of electrically charged weak interactions. It has one unit of electric charge, has a mass of 80.4 GeV/c^2, has a lifetime similar to the Z boson, and decays to muons and neutrinos $(10.57 \pm 0.15)\%$ of the time [3]. Another objective of this thesis is the measurement of ratios of W boson to Z boson cross-sections. The ratio of the cross-sections is a much more precisely determined observable than either of the cross-sections themselves, as many of the common experimental systematic uncertainties cancel. It is thus more sensitive to phenomena that are not accounted for by existing predictions, as well as differences between these predictions.

The nominal energy in the centre-of-mass frame of the colliding protons (centre-of-mass energy) was set at two distinct values during LHC Run-I. As a consequence, the Run-I

data set is naturally divided into two sub-sets of data, corresponding to two different centre-of-mass energies. The measurements mentioned above are performed on both of these data sets separately. The final objective of this thesis is to measure ratios of quantities that have been determined at different centre-of-mass energies. These measurements are sensitive to new phenomena when certain criteria relating to the evolution of cross-sections with centre-of-mass energy are met.

The remainder of this thesis is organised as follows: Chapter 2 introduces the established theoretical framework used to predict observable quantities at particle colliders; Chapter 3 describes the apparatus used to collect the data, the Large Hadron Collider and the LHCb experiment; Chapter 4 describes the measurement of Z boson cross-sections on two separate data samples; Chapter 5 describes how these may be combined with W boson cross-section measurements to form new observables that are both experimentally and theoretically well-determined; and Chapter 6 is devoted to conclusions. Finally, Appendices A - G give additional information on various aspects of the analysis.

Chapter 2

Theory

The main focus of this thesis is the measurement of electroweak boson cross-sections and their ratios, detailed in Chapters 4 and 5. These measurements test the current understanding of the sub-atomic world, which is best described by the theoretical framework known as the Standard Model (SM) of particle physics. This chapter is a review of this theory. The first part describes relativistic quantum field theory. The second part introduces the particles of the SM and their properties, as well as the construction of the SM lagrangian. The third is a discussion of hadron structure. The fourth part deals with the various computational tools for calculating these cross-sections, as well as event generation.

2.1 Quantum field theory

The mathematical language that describes fundamental particles and their interactions is called quantum field theory. One of the main advantages of this theory is its ability to describe changes in the total number of particles of a system. This is an essential feature of any theory hoping to describe proton collisions at the Large Hadron Collider (LHC). A snapshot of the result of one such collision is shown in Figure 2.1, where the black lines represent the new particles created in the collision. Indeed, flexibility in the number of particles goes beyond just the empirical evidence. The very notion of a single, point-like, particle existing in isolation is dispelled by the principles of quantum mechanics. These dictate that at distance scales less than one Compton wavelength $\lambda = \frac{\hbar}{2mc}$, pairs of particles are being readily produced, for short periods of time, from the energy intrinsic to the vacuum [5]. As one looks ever more closely, a single particle must actually be thought of as a swarm of particles.

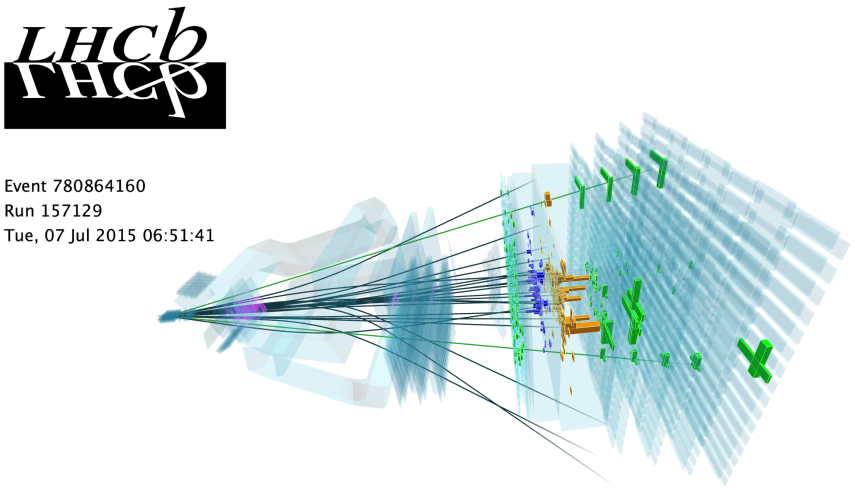

Figure 2.1: Display of a proton-proton collision event containing a Z boson that decays to muons at the LHC. The muons are represented by green lines. Particles from the rest of the event are represented by black lines. Energy deposits left in the detector are represented by blue, green and orange blocks.

The following sections describe field theory, how field theory is quantised, and finally, how interactions are handled (perturbation theory). In the midst of these, the interpretation of a particle as an excitation of a field is explained.

2.1.1 Field theory

In the abstract mathematical sense, a quantity that has a value at every point of space-time is called a field.

$$\phi(x) \equiv \phi(\vec{x}, t) \tag{2.1}$$

There are different types of fields, scalar fields, vector fields and tensor fields. An example of a scalar field is a temperature field - every point in space-time has a temperature associated with it. An example of a vector field is a wind velocity field. The wind velocity field is similar to the temperature field in that the wind has a strength, but it differs in that it also has a direction. The concept of the field is needed in order to make the laws of physics local and to explain the communication of forces over large distances. Without such a concept, forces are felt instantaneously without any medium for transmission, contrary to intuition. Einstein called this “spooky action at a distance”.

The dynamics of a field (or set of fields) is governed by a function called the lagrangian

$$L(t) = \int d^3x \ \mathcal{L}\left(\phi, \partial_\mu \phi\right), \tag{2.2}$$

which depends on the field(s) and its derivative(s). Associated to every lagrangian is a dimensionless functional called the action $S = \int dt \ L(t)$. The equations of motion of the field

$$\partial_\mu \left(\frac{\partial \mathcal{L}}{\partial \left(\partial_\mu \phi\right)} \right) - \frac{\partial \mathcal{L}}{\partial \phi} = 0 \tag{2.3}$$

may be determined from the principle of least action [6].

A useful class of lagrangians are those for free field theories. These lagrangians are quadratic in the fields, and consequently, the equations of motions are linear. One example is the free Klein-Gordon equation for scalar fields.

$$\partial_\mu \partial^\mu \phi + m^2 \phi = 0 \tag{2.4}$$

This equation of motion arises from the application of Equation 2.3 to the Klein Gordon lagrangian

$$\mathcal{L}_{KG} = \frac{1}{2} \partial_\mu \phi \partial^\mu \phi - \frac{1}{2} m^2 \phi^2. \tag{2.5}$$

The solution to the Klein-Gordon equation is a linear combination of plane waves in momentum space, given by the Fourier expansion of the field ϕ

$$\phi\left(\vec{x}, t\right) = \int \frac{d^3p}{\left(2\pi\right)^3} \ e^{i\vec{p}\cdot\vec{x}} \ \phi\left(\vec{p}, t\right), \tag{2.6}$$

where the Fourier coefficients satisfy a harmonic oscillator equation. Every point in space oscillates like a harmonic oscillator with frequency $\omega_{\vec{p}}^2 = \vec{p}^2 + m^2$ [5].

Another important quantity in field theory is the conjugate momentum of the field, π, defined as

$$\pi = \frac{\partial \mathcal{L}}{\partial \dot{\phi}} \tag{2.7}$$

not to be confused with the 3-momentum $\vec{p}$ above.

Free field theories do not describe interactions between fields, by definition, but they are of great importance if interaction terms, that eventually get added to the lagrangian, are weakly coupled. In these cases the solutions to the equations of motions can be built on top of the free field solutions with the formalism of perturbation theory.

2.1.2 Canonical quantisation

The transition from field theory to quantum field theory is done by imposing commutation (or anti-commutation) relations on the field and its conjugate momentum, in analogy with quantum mechanics [7]. This is called canonical quantisation. A quantum field is an operator valued function of space and time that satisfies the commutation relations [5].

Consider the Klein-Gordon lagrangian for a scalar field as described in Section 2.1.1. If Equation 2.6 is expanded as an infinite sum of creation and annihilation operators ($a^\dagger$ and a), one may compute the energy spectrum of the theory [6, 7]. The creation operator acts on the vacuum state and creates an excited state of energy $\omega = \sqrt{p^2 + m^2}$. If one takes this excited state and acts with the momentum operator, the eigenvalue is the 3-momentum $\vec{p}$. Acting on the excited state with the angular momentum operator and setting $\vec{p} = 0$ gives the intrinsic angular momentum of the state, which in this case is 0. These ingredients allow the excited state of the field to be interpreted as a particle, since it has the correct energy, momentum and spin [5].

Particles with integer spin are called bosons as they obey Bose-Einsteins statistics. The Klein-Gordon field introduced above gives rise to bosons as the states have integer spin. Particles with half-integer spin obey Fermi-Dirac statistics and are called fermions. The spin of a field is determined by the type of commutation relations imposed in the quantisation step. The imposition of commutation relations dictates that the resulting particles are bosons, whereas the imposition of anti-commutation relations dictates that the resulting particles are fermions. The fact that spin-statistics [8] is a consequence of quantisation, as opposed to something that is enforced by hand, is another reason for using quantum field theories to describe nature.

The spin-0 lagrangian was given in Equation 2.5. The spin-1 and spin-1/2 lagrangians are given below as they describe the particles that are the subject of this thesis. The Proca lagrangian describes spin-1 particles

$$\mathcal{L}_{Proca} = -\frac{1}{4} \left(\partial^\mu V^\nu - \partial^\nu V^\mu \right) \left(\partial_\mu V_\nu - \partial_\nu V_\mu \right), \tag{2.8}$$

given here for a massless field V. The Dirac lagrangian describes spin-1/2 particles

$$\mathcal{L}_{Dirac} = i\bar{\Psi}\gamma^\mu \partial_\mu \Psi - m\bar{\Psi}\Psi. \tag{2.9}$$

Here Ψ is a four component vector called a Dirac spinor, and $\bar{\Psi}$ is called the Dirac adjoint with

$$\bar{\Psi} = \Psi^{\dagger}\gamma^{0}, \tag{2.10}$$

while the γ^{μ} are 4 x 4 matrices.

2.1.3 Interactions

In this section, interactions are added to the free scalar field theory described by Equation 2.5. Before doing so, an important quantity, which will aid the understanding of interacting theories, is introduced. This quantity is called the Feynman propagator [7]. In the free Klein-Gordon theory it is given by

$$\begin{aligned} \langle 0|\, T\phi(x)\phi(y)\, |0\rangle &= \int \frac{d^4x}{(2\pi)^4}\, \frac{ie^{ip\cdot(x-y)}}{p^2+m^2-i\epsilon} \\ &\equiv D_F(x-y). \end{aligned} \tag{2.11}$$

It is interpreted as the quantum mechanical amplitude for the quantum field $\phi(y)$ to excite the ground state of the free theory $|0\rangle$, for the excited state to propagate from y to x, and for the excited state to be annihilated at x. The symbol T is the time ordering symbol, which ensures that in the sequence of fields immediately following it, fields that occur at later times are placed to the left. The factor $i\epsilon$ is included in the integral to denote the fact that the singularity that would otherwise arise in the integration along the real x^0 axis is avoided.

The interacting Klein-Gordon theory is obtained by adding an interaction term

$$\mathcal{L}_{\text{int}} = \frac{\lambda}{4!}\phi^4 \tag{2.12}$$

to the free lagrangian in Equation 2.5. This quantum field theory does not form part of the SM but is useful for illustrative purposes. For the perturbative techniques to apply, the dimensionless number λ should be small, with $\lambda << 1$. Since the ground state of the interacting theory is different to the ground state of the free theory, it is denoted by $|\Omega>$ and the Feynman propagator in the interacting field theory is

$$\langle\Omega|\, T\phi(x)\phi(y)\, |\Omega\rangle = \frac{\langle 0|\, T\Big\{\phi(x)\phi(y)\, \exp(-i\int dt\ \mathcal{L}_{\text{int}})\Big\}\, |0\rangle}{\langle 0|\, T\Big\{\exp(-i\int dt\ \mathcal{L}_{\text{int}})\Big\}\, |0\rangle}. \tag{2.13}$$

If the coupling constant λ is small, the interaction term can be considered a small perturbation of the free theory, and the exponential can be expanded in powers of $-i\int dt\ \mathcal{L}_{\text{int}}$.

The computation of the Feynman propagator in the interacting field theory becomes an exercise of evaluating time ordered products of fields. Using Wick's theorem [7], the first non-trivial term in the expansion of the numerator in Equation 2.13 is

$$\langle 0|\, T\phi(y)\phi(x)\ (-i)\int d^4z\ \frac{\lambda}{4!}\phi^4\ |0\rangle = 3\cdot\Big(\frac{-i\lambda}{4!}\Big)D_F(x-y)\int d^4z\ D_F(z-z)D_F(z-z) + 12\cdot\Big(\frac{-i\lambda}{4!}\Big)\int d^4z\ D_F(x-z)D_F(y-z)D_F(z-z) \tag{2.14}$$

Drawing each Feynman propagator as a line, and each point as a dot, the first term can be depicted graphically as the product of Figures 2.2(a) and 2.2(b), while the second term may be represented by Figure 2.2(c). The value of the diagram can be recovered

(a) (b) (c)

Figure 2.2: Diagrams representing the corrections to the free Feynman propagator in ϕ^4 theory.

by assigning D_F to each line, $(-i\lambda)\int d^4z$ to each vertex and unity to each external line. These assignments are called the Feynman rules in position space for ϕ^4 theory.

There is thus a diagrammatic interpretation of Equation 2.13. The total amplitude can be written down by applying the Feynman rules to all possible diagrams with external points x and y. The example above is for the calculation of the Feynman propagator in the interacting Klein-Gordon theory, but any amplitude in the theory may be calculated in this way. Furthermore, rules may be derived for any lagrangian. The following sections will involve writing down lagrangians for theories relevant to the interactions of particles in nature. Amplitudes of scattering processes are calculated with exactly the same techniques as discussed in this section.

2.2 The Standard Model

The Standard Model (SM) is a relativistic quantum field theory that describes the interactions between particles due to three of the four fundamental forces of nature: the strong interaction, the weak interaction and the electromagnetic interaction.[1] Particles

[1]The fourth fundamental force, gravity, is not incorporated into the SM.

called quarks and leptons constitute the matter content of theory, and forces between these are communicated, or mediated, via other particles called gauge bosons. The fundamental particles of the SM are displayed in Figure 2.3. There are six quarks of dif-

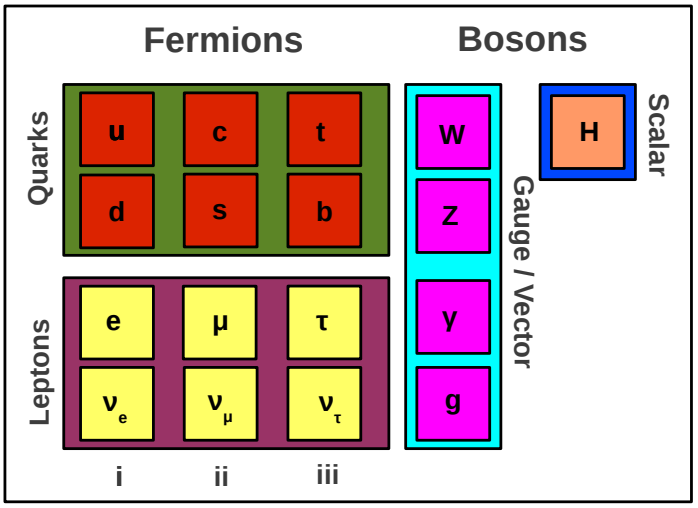

Figure 2.3: Particle content of the SM. The abbreviations are explained in the text.

ferent flavour, the up-, down-, charm-, strange-, top- and bottom-quark, or u, d, c, s, t, b for short. The quarks have fractional electric charge $+\frac{2}{3}$ for u, c, t and $-\frac{1}{3}$ for d, s, b. Another quantum number, unique to quarks and gluons, is colour. Quarks can be coloured either red (r), green (g), or blue (b) (or anti-red ($\bar{r}$), anti-green ($\bar{g}$), anti-blue ($\bar{b}$)). There are six leptons, three of which have one unit of electric charge. The charged leptons are the electron, the muon and the tau-lepton (e, μ, τ). The neutral leptons are called the electron-, the muon- and the tau-neutrino (ν_e, ν_μ, ν_τ). The quarks and leptons are fermions since they obey Fermi-Dirac statistics; their intrinsic angular momentum (spin) is half-integer. It is also convenient to think of the quarks and leptons as members of one of three families called the first (i), second (ii) and third (iii) generations of matter. Lepton masses increase from the first to the third generation.

The electromagnetic force is mediated by the electrically neutral photon (γ). This force is felt by all particles with electric charge. The weak force is mediated by the charged W and neutral Z. It is the only force that governs neutrino interactions. Gluons (g) are carriers of the strong force, which acts on particles with colour charge, i.e. quarks. Gluons carry two colour indices, allowing quarks to change colour. For example, a blue quark (q^b) may change into a red quark (q^r) if it emits a blue/anti-red gluon ($g^{b\bar{r}}$): $q^b \rightarrow g^{b\bar{r}} q^r$. Photons, gluons, W and Z particles all have one unit of intrinsic angular

momentum. They thus obey Bose-Einstein statistics and are referred to collectively as bosons.

The masses of all particles in the SM are generated by a mechanism called spontaneous symmetry breaking (SSB). The symmetry breaking leads to the appearance of four scalar particles (spin-0 and thus bosons). One of these is called the Higgs boson (H), which gives rise to the masses of electroweak bosons and fermions. Further details on SSB and the Higgs boson are given in Section 2.2.5.

To make predictions for how these particles interact, it is necessary to construct the SM lagrangian. The general strategy is to start with a lagrangian describing a free system and then add the necessary interaction terms, while at the same time adhering to what is called the gauge principle.

2.2.1 The gauge principle

Consider the lagrangian describing free Dirac fermions

$$\mathcal{L}_0 = i\bar{\Psi}(x)\gamma^\mu\partial_\mu\Psi(x) - m\bar{\Psi}(x)\Psi(x). \tag{2.15}$$

The fermion field may be transformed by a multiplicative phase, defined as the exponential of $i \equiv \sqrt{-1}$ times some factor. If this factor is independent of the space-time point, the value of the field at every space-time point is multiplied by the same factor. This is called a global phase transformation.

The lagrangian above is invariant under global phase transformations of the form

$$\Psi(x) \rightarrow \Psi'(x) \equiv e^{iQ\theta}\Psi(x), \tag{2.16}$$

where the argument of the exponential is factored into Q and θ by convention. If the transformation is made local, corresponding to the replacement of θ with $\theta(x)$ (meaning that the value of the field is changed by different amounts at different points), the lagrangian is no longer invariant. If a new spin-1 field $A_\mu(x)$ is introduced, and it is defined such that it transforms as

$$A_\mu(x) \rightarrow A'_\mu(x) \equiv A_\mu(x) - \frac{1}{e}\partial_\mu\theta(x), \tag{2.17}$$

then the lagrangian

$$\mathcal{L} = \mathcal{L}_0 - eQA_\mu(x)\bar{\Psi}(x)\gamma^\mu\Psi(x) \tag{2.18}$$

is invariant under local phase transformations. The new term is an interaction term, involving the fermion and A_μ fields. The lagrangian must include an additional Proca lagrangian for the spin-1 A_μ field (see Equation 2.8). Defining

$$D_\mu \Psi(x) \equiv (\partial_\mu - ieQA_\mu(x))\Psi(x), \tag{2.19}$$

and the electromagnetic field strength tensor as

$$F_{\mu\nu} = \partial_\mu A_\nu - \partial_\nu A_\mu, \tag{2.20}$$

the full lagrangian of the quantum theory of electrodynamics (QED) is

$$\mathcal{L}_{QED} = \bar{\Psi}\gamma^\mu \left(i\not{D} - m\right)\Psi - \frac{1}{4}(F_{\mu\nu})^2. \tag{2.21}$$

This lagrangian provides a theory that describes the electromagnetic interactions between electrically charged fermions, mediated by photons. A mass term for the photon field A_μ is not added since such a term is not gauge invariant.

In Section 2.1.3, a term, quartic in scalar fields, was added to the Klein-Gordon lagrangian to describe interactions between fields. It was seen that the amplitude for a particle to propagate between two points was represented by Feynman diagrams, and that corrections to the free field amplitude involved four-legged vertices. For QED, the interactions are represented by three-legged vertices. The relevant term in the lagrangian is the $A\bar{\Psi}\Psi$ term, which is cubic in fields. Two fields correspond to fermions, and one to the photon. Corrections to propagators, indeed any amplitude in QED, involve diagrams that have vertices like the one shown in Figure 2.4. Feynman diagrams appear several

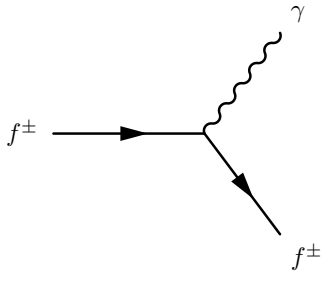

Figure 2.4: The vertex representing the interaction term of the QED lagrangian between charged fermions ($f^\pm$) and photons (γ).

more times in this thesis. In some cases it is to represent interaction vertices, in others it is to represent the quantum amplitudes of various processes.

QED predicts an array of quantities that agree with experimental measurements to an astonishing degree [7]. The lagrangian that describes QED can be constructed from a lagrangian describing free fermions by requiring that this lagrangian is invariant under local phase transformations. It is important to stress that local invariance has no motivation other than that it leads to the correct lagrangian, and predicts the existence of the photon. Since the imposition of invariance under local phase transformations successfully constructs the lagrangian of QED, it is also taken as the basis for constructing other lagrangians of the SM. This is known as the gauge principle.

2.2.2 Lie groups

The transformation given by Equation 2.16 is also known as a $U(1)$ transformation. $U(1)$ is a group, in the mathematical sense, and the exponential factor that multiplies the field is an element of the representation of that group [9]. The $U(1)$ group is a member of a family of groups, $SU(N)$ or Lie groups, consisting of N x N matrices. U denotes the fact that the matrices are unitary and S denotes the fact that the matrices have determinant 1.[2] Lie groups are infinitesimally generated, which means that every element of the group can be obtained by continuously transforming the identity element by infinitesimal amounts. The $SU(N)$ group elements are generated by N generators, and for $N > 1$, there are $N^2 - 1$ independent generators.

The particles in the SM transform under the combination of three symmetry groups. The combination can be represented by the group product, written as $SU(3)_C \otimes SU(2)_L \otimes U(1)_Y$. The subscripts specify the types of fields that the symmetry transformations apply to. Coloured fields (C) transform under $SU(3)$ transformations, left-handed fields (L) transform under $SU(2)$, and fields with another quantum number called hypercharge (Y) transform under $U(1)$ transformations. These concepts are defined and developed in the following sections, where it will be shown that each symmetry group can be loosely associated with a force: $SU(3)_C$ with the strong interaction, $SU(2)_L$ with the weak interaction, and $U(1)_Y$ with the electromagnetic interaction. It isn't a strict correspondence. The weak and electromagnetic forces are unified and, for example, the $U(1)$ transformation of fermion fields in QED is embedded in the $SU(2)_L \otimes U(1)_Y$ portion of the SM group structure.

The $U(1)$ transformation in the previous section corresponds to multiplication of fields by a number. In the following sections, fields are subject to $SU(2)$ and $SU(3)$ transformations, which correspond to matrix multiplication of fields. It will also be shown that

[2] When $N = 1$, the S is redundant and is dropped. Hence, $U(1) \equiv SU(1)$.

invoking the gauge principle, and insisting that the lagrangians are invariant under local versions of these transformations, requires the addition of three new fields for $SU(2)$ and eight new fields for $SU(3)$. The number of additional fields that are required for the lagrangian to remain invariant under local phase transformations is equal to the number of independent generators of the underlying Lie group.

2.2.3 Quantum chromodynamics

There is a considerable amount of evidence to suggest that quarks interact via the strong force and have an additional quantum number called colour charge [10]. This idea of colour arose due to the discovery of particles called baryons (B) that seemed to be composed of three quarks with the same flavour, electric charge and spin quantum numbers ($B \equiv qqq$). Three fermions in the same state is disallowed due to Pauli exclusion, but the concept of colour solves the problem. The solution in this example is to assign different colours to the quarks such that they are coloured red, green and blue ($B \equiv q_r q_g q_b$) and are thus in unique quantum states. The study of the interactions between coloured particles is called quantum chromodynamics (QCD).

Since the quarks are coloured they are described by a triplet of fermionic fields

$$\Psi = \begin{pmatrix} \Psi^r \\ \Psi^g \\ \Psi^b \end{pmatrix}, \tag{2.22}$$

where r, g, b labels the quark colour. A free Dirac lagrangian

$$\mathcal{L}_0 = \bar{\Psi}(x)\left(\gamma^\mu \partial_\mu - m\right)\Psi(x) \tag{2.23}$$

is invariant under global $SU(3)$ transformations

$$\Psi^\alpha(x) \rightarrow \left(\Psi^\alpha\right)'(x) \equiv \left[e^{i\frac{\lambda^a}{2}\theta_a}\right]^\alpha{}_\beta \Psi^\beta(x), \tag{2.24}$$

which rotate the colour fields into one another. The λ^a $(a = 1, ..., 8)$ matrices are the generators of $SU(3)$ and the Greek indices α, β label the colour. Invoking the gauge principle, one introduces eight gauge bosons G_a^μ (gluons) and, as before with QED, the additional interaction terms can be absorbed into a covariant derivative

$$D^\mu \Psi = \left[\partial^\mu + i g_s \frac{\lambda^a}{2} G_a^\mu(x)\right]\Psi. \tag{2.25}$$

The strength of the QCD interaction, g_s, has been separated out and plays a similar role to λ (Equation 2.12) in interacting Klein-Gordon theory. To have gauge invariant kinetic terms for the gluons, one must define the gluon equivalent of $F_{\mu\nu}$ (Equation 2.20)

$$G_a^{\mu\nu} = \partial^\mu G_a^\nu - \partial^\nu G_a^\mu + g_s f^{abc} G_b^\mu G_c^\nu. \tag{2.26}$$

The third term does not appear in $F_{\mu\nu}$. This additional term arises due to the non-abelian nature of the $SU(3)$ symmetry group and gives rise to cubic and quartic interactions between the gluon fields in addition to the interactions between the fermion and gluon fields. These interactions are represented by the vertices in Figure 2.5. The f^{abc}

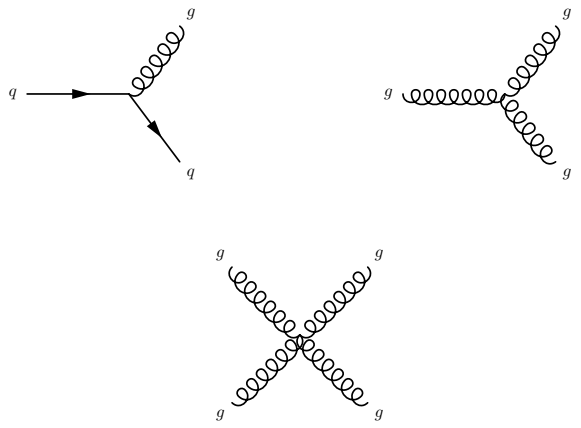

Figure 2.5: The vertices representing the interaction terms of the QCD lagrangian between quarks (q) and gluons (g).

are $SU(3)$ structure constants [7]. With these definitions, the lagrangian for QCD can be written succinctly as

$$\mathcal{L}_{QCD} = \bar{\Psi}(i\not{D} - m)\Psi - \frac{1}{4}(G_a^{\mu\nu})^2. \tag{2.27}$$

Note the similarity with the QED lagrangian in Equation 2.21.

The presence of cubic and quartic interactions between the gluon fields makes the phenomenology of QCD very different to that of QED, particularly in how the strength of the electromagnetic and strong forces vary with energy. In QED the strength increases with energy, making the charge of an electron seem small at large distances (or low energy) and large at small distances (or high energy). In general, the smaller charge of a fermion at lower energies is due to the screening effect of charged fermion pairs arising from fluctuations in the vacuum.

The QED coupling constant α is related to the coefficient of the interaction term in Equation 2.19 such that $\alpha = \frac{(eQ)^2}{4\pi}$. The dependence of α with energy Q is given by the beta-function.

$$\beta(\alpha) \equiv \frac{\partial\alpha}{\partial(\ln Q^2)} = \frac{2\alpha^2}{3\pi} \tag{2.28}$$

At the scale relevant to this analysis $\alpha(M_Z) \approx 1/127$, whereas at low energies, there is the familiar value $\alpha \approx 1/137$.

Screening also occurs in QCD, however, the gluon interactions in the vacuum create an anti-screening effect which make colour charge larger at higher energies. The corresponding beta-function for QCD is

$$\beta(\alpha_s) \equiv \frac{\partial\alpha_s}{\partial(\ln Q^2)} = -\Big(11 - \frac{2n_f}{3}\Big)\frac{\alpha_s^2}{2\pi}, \tag{2.29}$$

where α_s is related to the strong coupling in the QCD lagrangian (see Equations 2.25 and 2.27) in the same way as the QED case with $\alpha_s = \frac{g_s^2}{4\pi}$. Since the QCD beta-function is negative ($n_f = 6$), the coupling gets large at low energies. This gives rise to the phenomena of asymptotic freedom, where quarks are essentially free at high energies, and confinement, where quarks and gluons bind together to such a great extent that no isolated colour charge has yet been observed. At the scale relevant to this analysis, the value of the strong coupling constant is $\alpha_s(M_Z) = 0.118$.

2.2.4 Electroweak unification

The third fundamental force that is described by the SM is that of the weak interactions, so-called because its strength is about a million times less than that of the strong force. A number of experimental observations motivate the choice of underlying symmetry group and place restrictions on terms appearing in any lagrangian.

- The weak force is transmitted by two charged ($W^{\pm}$) and one neutral (Z) force carrier.
- β-decay processes like hadronic $n \to pe^-\bar{\nu}_e$ and leptonic $\mu^- \to e^-\nu_e\bar{\nu}_\mu$ couple to the weak force with the same strength [11].
- Due to the angular distributions of decay products observed in experiment, the charged weak current couples to left-handed fermions and right-handed anti-fermions.[3]

[3]The handedness of a particle refers to the relationship between the momentum and spin vectors of that particle. If these vectors are parallel, the particle is right-handed. If they are anti-parallel, the particle is left-handed.

This implies a breaking of the discrete symmetries of parity $\mathcal{P}$ (reflections in a mirror) and charge conjugation $\mathcal{C}$ (replacement of particle with anti-particle).

- The neutral weak current couples to left- and right-handed charged fermions, with different interaction strengths. This current differs from the photon in that it also couples to neutrinos.
- The vast majority of neutrinos are left-handed. Right-handed neutrinos must exist to account for neutrino oscillations and masses, but these are not included in the SM.

These requirements motivate the choice of an $SU(2)$ symmetry group to account for the similar behaviour, with respect to the charged weak force, of up- and down-type left-handed fermions.[4] The corresponding fields are arranged in doublets

$$\begin{pmatrix} u \\ d \end{pmatrix}_L \qquad \begin{pmatrix} c \\ s \end{pmatrix}_L \qquad \begin{pmatrix} t \\ b \end{pmatrix}_L$$
$$\begin{pmatrix} \nu_e \\ e^- \end{pmatrix}_L \qquad \begin{pmatrix} \nu_\mu \\ \mu^- \end{pmatrix}_L \qquad \begin{pmatrix} \nu_\tau \\ \tau^- \end{pmatrix}_L \tag{2.30}$$

to highlight the fact that these fields transform into one another under $SU(2)$ transformations. The couplings of right-handed fermions to the neutral force carrier can be accounted for by an additional $U(1)$ symmetry. This allows the

$$e_R,\ \mu_R,\ \tau_R,\ u_R,\ d_R,\ c_R,\ s_R,\ t_R,\ b_R \tag{2.31}$$

fields to be added to the theory. Letting f denote fermion fields, and ν neutrino fields, the free, and massless, fermion lagrangian is then

$$\mathcal{L}_0 = \sum_f \bar{\Psi}_L(x)\gamma^\mu\partial_\mu\Psi_L(x) + \sum_{f\neq\nu} \bar{\Psi}_R(x)\gamma^\mu\partial_\mu\Psi_R(x) \tag{2.32}$$
$$= \mathcal{L}_0^L + \mathcal{L}_0^R \tag{2.33}$$

where the left- and right-handed spinor components have been projected out using the γ^5 operator. Defining the projection operators as

$$P_L = \frac{1-\gamma^5}{2}, \qquad P_R = \frac{1+\gamma^5}{2}, \tag{2.34}$$

[4] The fermions $u, c, t, \nu_e, \nu_\mu, \nu_\tau$ are up-type while d, s, b, e, μ, τ are down-type.

	ν_e	e_L	e_R	u_L	d_L	u_R	d_R
t_3	1/2	-1/2	0	1/2	-1/2	0	0
Y	-1	-1	-2	1/3	1/3	4/3	-2/3
Q	0	-1	-1	2/3	-1/3	2/3	-1/3

Table 2.1: Values of third component of weak isospin (t_3), electric charge (Q) and hypercharge (Y) for up- and down-type quarks a leptons.

the left- and right-handed fermion fields are

$$\Psi_L = P_L\Psi, \qquad \Psi_R = P_R\Psi. \tag{2.35}$$

The imposition of $SU(2)$ local gauge invariance on the left-handed part of the lagrangian requires the introduction of three additional vector fields W_i^μ $(i = 1, 2, 3)$. The left-handed lagrangian becomes

$$\mathcal{L}^L = \sum_f \bar{\Psi}_L(x)\gamma^\mu \left(\partial^\mu - ig\frac{\vec{\tau}}{2}\cdot\vec{W}(x)\right)\Psi_L(x) - \frac{1}{4}F_i^{\mu\nu}F_{i\mu\nu} \tag{2.36}$$

where $\vec{\tau}$ encodes the generators of the $SU(2)$ group and the weak interaction strength g has been factored out, similar to what was done for QCD. The weak field strength tensor is

$$F_i^{\mu\nu} = \partial^\mu W_i^\nu(x) - \partial^\nu W_i^\mu(x) + g\epsilon_{ijk}W_j^\mu(x)W_k^\nu(x). \tag{2.37}$$

which, as in the QCD case of Equation 2.26, has one more term than the electromagnetic field strength tensor.

The $W_{1,2}(x)$ vector fields combine to give the observed $W^\pm$ bosons. The $W_3(x)$ field cannot be interpreted as the Z boson because it only couples to left-handed fields. The solution is to invoke a new $U(1)$ symmetry, giving rise to a new vector field B^μ, whose conserved charge is called hypercharge (Y). This new charge is defined in terms of other charges as the difference between the electric charge Q and the charge associated with transformations of the $W_3(x)$ field, t_3, which is called the third component of weak isospin [12, 13].

$$\frac{Y}{2} = Q - t_3 \tag{2.38}$$

The hyper-, electric, and third component of weak isospin charges for left- and right-handed fermion fields are given in Table 2.1.

The left- and right-handed lagrangians are amended to include the interactions between the field B^μ and the spinor fields. Kinetic terms for the new field are added to give the

unified electroweak lagrangian

$$\mathcal{L}_{EW} = \sum_f \bar{\Psi}_L(x)\gamma^\mu\Big(\partial^\mu - ig\frac{\vec{\tau}}{2}\cdot\vec{W}(x) - ig' y_{\Phi_L} B^\mu(x)\Big)\Psi_L(x) - \frac{1}{4}F_i^{\mu\nu}F_{i\mu\nu}$$
$$+ \sum_{f\neq\nu} \bar{\Psi}_R(x)\gamma^\mu\Big(\partial^\mu - ig' y_{\Phi_R} B^\mu(x)\Big)\Psi_R(x) - \frac{1}{4}H^{\mu\nu}H_{\mu\nu}, \tag{2.39}$$

where

$$H^{\mu\nu} = \partial^\mu B^\nu - \partial^\nu B^\mu. \tag{2.40}$$

The strength of the interaction with the B^μ field is g'. By considering admixtures of the B and W_3 fields, one obtains the physical photon and Z boson. The admixture is parameterised by the weak mixing angle θ_W.

$$\begin{aligned} B^\mu &= \cos\,\theta_W\ A^\mu - \sin\,\theta_W\ Z^\mu \\ W_3^\mu &= \sin\,\theta_W\ A^\mu + \cos\,\theta_W\ Z^\mu \end{aligned} \tag{2.41}$$

With the requirement that

$$g\,\sin\,\theta_W = g'\,\cos\,\theta_W = e \tag{2.42}$$

the field A^μ couples vectorially to left- and right-handed fields and is interpreted as the photon. The Z^μ has vector and axial-vector couplings to fermions g_v and g_a

$$g_v = \frac{t_3}{2} - eQ\,\sin^2\,\theta_W, \qquad\qquad g_a = \frac{t_3}{2}, \tag{2.43}$$

where t_3 is the third component of weak isospin given in Table 2.1.

In summary, the $SU(2)_L \otimes U(1)_Y$ symmetry requires four fields, W_1, W_2, W_3, and B. Some of the properties of the observed the $W^\pm$, Z and photon are obtained by superpositions of these fields. The most important property of the observed $W^\pm$ and Z bosons, their large mass, has not been accounted for yet. This is the subject of the next section.

2.2.5 Spontaneous symmetry breaking and mass

Suppose a system has an infinite family of degenerate ground states due to some symmetry. If one of these states is chosen to be the unique ground state, then the original symmetry is broken. This is called spontaneous symmetry breaking (SSB). To see the effect of the symmetry breaking in action, consider a lagrangian involving a complex

scalar field.

$$\mathcal{L} = \partial_\mu \phi^\dagger \partial^\mu \phi - V(\phi), \qquad V(\phi) = \mu^2 \phi^\dagger \phi + h\left(\phi^\dagger \phi\right)^2 \tag{2.44}$$

The lagrangian is invariant under the global phase transformation

$$\phi(x) \to \phi'(x) \equiv e^{i\lambda}\phi(x). \tag{2.45}$$

In other words, the lagrangian is invariant under the action of a $U(1)$ symmetry group, generated by λ. Finite minima of the potential are ensured by the requirement $h > 0$. If $\mu^2 > 0$ there is a unique minimum, but if $\mu^2 < 0$ there is an infinite set of ground states

$$\phi_0 = \frac{\nu}{\sqrt{2}} e^{i\lambda}, \qquad \nu = \sqrt{\frac{\mu^2}{2h}}, \tag{2.46}$$

and if a particular ground state is chosen, at $\lambda = 0$ say, the symmetry is broken. If the ground state is excited to

$$\phi(x) = \frac{1}{\sqrt{2}}(\nu + \phi_1 + i\phi_2) \tag{2.47}$$

then the potential becomes

$$V(\phi) = V(\phi_0) - \mu^2\phi_1^2 + h\nu\phi_1\left(\phi_1^2 + \phi_2^2\right) + \frac{h}{4}\left(\phi_1^2 + \phi_2^2\right)^2. \tag{2.48}$$

It is clear from this equation that ϕ_1 has a mass term but ϕ_2 does not. The excitations described by ϕ_2 are in directions around the degenerate minimum energy state, and there is no mass term penalty for such excitations. The massless excitation is called a Nambu-Goldstone boson, and there are as many of these as there are generators of the broken symmetry group [14]. There is only one of these in the case considered above.

In the SM, these ideas are extended to the symmetry group governing electroweak interactions $SU(2)_L \otimes U(1)_Y$. This is done such that the weak part is broken and the electromagnetic part remains unbroken, a choice motivated by the experimental fact that W and Z bosons are massive while the photon is massless. A new field arises, the Higgs boson, as well as three Goldstone bosons (two charged, one neutral). The example above considered global symmetries. In the case of the SM, the symmetry is a local one and the Goldstone bosons can be removed from the lagrangian by a suitable choice of gauge. Their degrees of freedom remain, but are now interpreted as longitudinal polarisation states of the $W^\pm$ and Z bosons. Longitudinal polarisation states are characteristic of all massive particles. To see this explicitly consider a complex scalar

doublet[5]

$$\Phi = \frac{1}{\sqrt{2}} \begin{pmatrix} \phi_1 - i\phi_2 \\ \phi_3 - i\phi_4 \end{pmatrix}. \tag{2.49}$$

Using a similar lagrangian and potential to before, the ground state is

$$\Phi_0 = \frac{1}{\sqrt{2}} \begin{pmatrix} 0 \\ \nu \end{pmatrix}. \tag{2.50}$$

If the ground state is excited to

$$\Phi = \frac{1}{\sqrt{2}} \begin{pmatrix} -i\omega_1 - \omega_2 \\ \nu + H - i\omega_3 \end{pmatrix}. \tag{2.51}$$

the scalar potential becomes

$$V(\Phi) = h\nu H^2 + h\nu H\left(H^2 + \vec{\omega}^2\right) + \frac{h}{4}\left(H^2 + \vec{\omega}^2\right)^2, \tag{2.52}$$

where it is clear that the H field has a mass term but the ω_i fields do not. To see the conferral of mass to the electroweak bosons, write down the scalar lagrangian with the necessary covariant derivative and evaluate it at the ground state.

$$\begin{aligned} \mathcal{L}_S|_{\Phi=\Phi_0} &= \left| \left(\partial^\mu - ig\frac{\vec{\tau}}{2} \cdot \vec{W}^\mu - i\frac{1}{2}g'B^\mu \right) \Phi_0 \right|^2 - V(\Phi_0) \\ &= \frac{e^2}{4\,\sin^2\theta_W}\nu^2\; W_\mu^+ W^{-\mu} + \frac{e^2}{8\,\sin^2\theta_W\,\cos^2\theta_W}\nu^2\; Z_\mu Z^\mu - V(\Phi_0) \end{aligned} \tag{2.53}$$

The W and Z boson masses are

$$M_W = \frac{e}{2\,\sin\theta_W}\nu \qquad\qquad M_Z = \frac{e}{2\,\sin\theta_W\,\cos\theta_W}\nu, \tag{2.54}$$

and as desired, there is no mass term for the A_μ field.

The mass terms for a Dirac field have the form

$$\begin{aligned} m\bar{\Phi}\Phi &= m(\bar{\Phi}_R\Phi_R + \bar{\Phi}_R\Phi_L + \bar{\Phi}_L\Phi_R + \bar{\Phi}_L\Phi_L) \\ &= m(\bar{\Phi}P_LP_R\Phi + \bar{\Phi}P_LP_L\Phi + \bar{\Phi}P_RP_R\Phi + \bar{\Phi}P_RP_L\Phi) \\ &= m(\bar{\Phi}_R\Phi_L + \bar{\Phi}_L\Phi_R) \end{aligned} \tag{2.55}$$

where use has been made of the projection operators $P_{L,R}$ of Equation 2.34. Equation 2.55 is invariant under $U(1)$ gauge transformations but not $SU(2)$ transformations.

[5]To keep $U(1)_{QED}$ unbroken, the hypercharge of this scalar must be 1.

In other words, fermion mass terms are forbidden in the SM because they break gauge invariance. To include fermions mass terms in a gauge invariant way, interactions between the fermions and scalar field H are added with the following lagrangian

$$\mathcal{L}_Y = -\Big(1 + \frac{H}{\nu}\Big) \sum_f m_f \bar{\Phi}_f \Phi_f. \tag{2.56}$$

The strength of the couplings between the fermions and Higgs scalar, and hence the fermion masses, are not predicted by the theory and must be determined from experiment.

2.3 Scattering and factorisation

The scattering of high energy leptons on nuclear targets has been a very successful method of determining hadron structure. Not being affected by the strong nuclear force, leptons can penetrate deep into the hadron to interact with the quarks. In experiments during the 1960s, the rate of large angle electron scattering from a hydrogen target was measured [15]. The rate was expected to be small, since previous proton-proton collision experiments resulted in the production of hadrons colinear to the beam axes, supporting the hypothesis that the constituents of the proton disfavoured partaking in hard collisions [7]. The rate was found to be large, suggesting that elastic collisons were taking place between the electron and proton. However, for the vast majority of these large-angle scattering events, the proton broke up.

The parton model was introduced to account for these results [16]. The model claims that the proton consists of quarks and other uncharged particles that keep the proton intact. The quarks carry the electric charge necessary for the scattering to occur. The other uncharged particles (gluons) are responsible for binding the proton together as well as the production of hadrons, which occurs through the exchange of momentum with the struck quark.

The electron-proton scattering process is represented by the Feynman diagram in Figure 2.6(a). The initial proton and electron have momenta P and k, the exchanged photon has momentum $q = k - k'$, and the final state electron momentum is k'. Deep inelastic scattering occurs when $-q^2 \equiv Q^2 >> m_P^2$ (deep), where the proton is being probed at energies much larger than its mass, and $(P+q)^2 \equiv W^2 >> m_P^2$ (inelastic), where the struck proton obtains energies that are also much larger than its mass, causing it to break up.

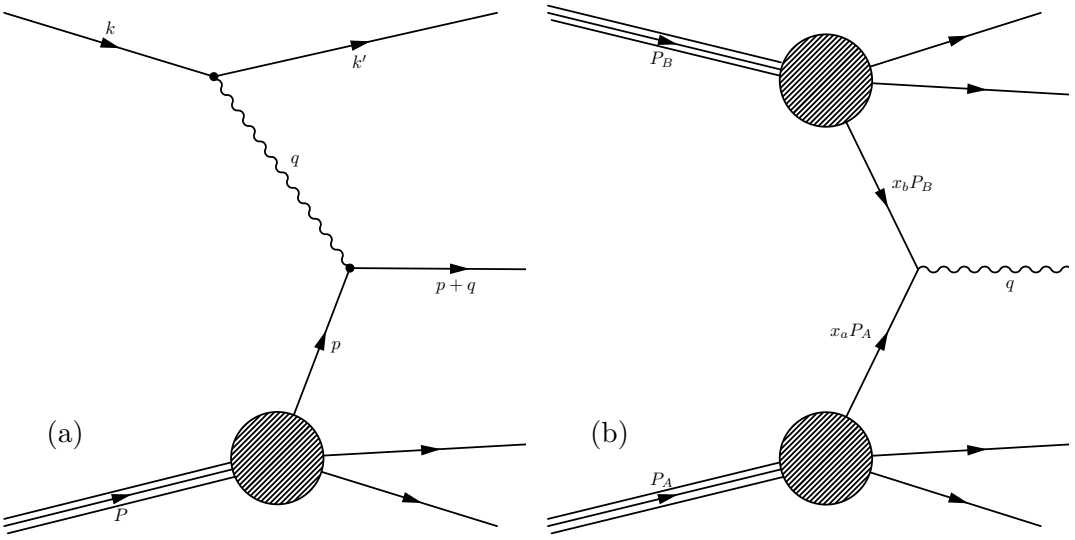

Figure 2.6: Feynman diagrams representing (a) *ep* and (b) *pp* deep inelastic scattering.

Consider the centre-of-mass frame, where the proton constituents are travelling toward the electron at relativistic velocities, colinear to the proton velocity. Any transverse momentum that the constituents may have is suppressed by α_s. The constituent momentum p is thus a fraction x of the proton's longitudinal momentum P such that $p = xP$. The probability that a proton contains a parton with this momentum cannot be computed from perturbation theory since it depends on processes that take place in an energy regime where perturbative expansions don't converge; it must be determined from experiment instead. This probability is also called a parton density function (PDF). For a particular parton species q, the PDF is a function of x and Q^2, $f_q = f_q(x, Q^2)$, in agreement with data [17–21]. The original parton model considered the PDFs as functions of x only, to reflect the data at the time [22]. This phenomenon is known as Bjorken scaling, which is a good approximation at low Q^2. The QCD-improved parton model takes into account a dependence on Q^2 and more will be said about this in Section 2.3.2. To determine the total electron-proton scattering cross-section, one must multiply the electron-quark scattering amplitude by the PDF, integrate over all possible momentum fractions and sum over all parton species.

The extension of these ideas to proton-proton scattering is straightforward. In this case, one parton from each proton participates in the interaction, which is represented in

Figure 2.6(b). The cross-section is given by

$$\sigma_{pp\to V} = \sum_{q_a,q_b} \int dx_a dx_b \underbrace{f_{q_a/A}\left(x_a, Q^2\right) f_{q_b/B}\left(x_b, Q^2\right)}_{PDFs} \hat{\sigma}_{q_a q_b}(x_a, x_b, Q^2). \tag{2.57}$$

The formula expresses the proton-proton (pp) cross-section as the sum of contributions from individual partonic cross-sections ($\hat{\sigma}$), which are weighted according to the particular partons involved (q_a from hadron A, q_b from hadron B) and their momentum fractions with respect to the total proton momenta (x_a, x_b). The information for how to assign these weights is encoded in the parton distribution functions (PDFs). The PDFs are not predicted by the SM itself but must be determined from fits to data obtained in previous experiments. Equation 2.57 is a consequence of one of the factorisation theorems of QCD [23], where factorisation refers to the separation of perturbative ($\hat{\sigma}$) and non-perturbative phenomena (PDFs).

Consider the proton-proton collision represented by Figure 2.6(b). In the centre-of-mass frame the protons have 4-momenta

$$P_A = (E, 0, 0, E)\,, \qquad\qquad P_B = (E, 0, 0, -E)\,, \tag{2.58}$$

and the centre-of-mass energy squared is $s = 4E^2$. The 4-momentum of the intermediate particle is

$$\begin{aligned} q &= x_a P_A + x_b P_B \\ &= \left(\left(x_a + x_b\right) E, 0, 0, \left(x_a - x_b\right) E\right) \end{aligned} \tag{2.59}$$

which implies that the invariant mass of the intermediate particle is

$$Q^2 \equiv M^2 = x_a x_b s. \tag{2.60}$$

Defining a variable y using the zeroth component of q

$$q^0 = M \cosh\, y, \tag{2.61}$$

one has

$$\begin{aligned} \cosh\, y &= \frac{x_a + x_b}{2\sqrt{x_a x_b}} \\ &= \frac{1}{2}\Big(\sqrt{\frac{x_a}{x_b}} + \sqrt{\frac{x_b}{x_a}}\Big). \end{aligned} \tag{2.62}$$

This gives

$$x_a = \frac{M}{\sqrt{s}} e^{y}, \qquad x_b = \frac{M}{\sqrt{s}} e^{-y}. \tag{2.63}$$

In this thesis, Z boson production is measured at different centre-of-mass energies, $\sqrt{s}$, and rapidities, y. Equation 2.63 demonstrates the link between the proton momentum fractions of the partons and the rapidity, and thus, these measurements can be used to constrain PDFs as functions of x and Q^2.

2.3.1 Parton distribution functions

In general, a PDF takes the form

$$f\left(x, Q^2\right) = \mathrm{F}\left(x, Q^2\right) x^{m\left(Q^2\right)} \left(1 - x\right)^{n\left(Q^2\right)}. \tag{2.64}$$

The function F is a polynomial in x, whose coefficients and powers are given by parameters that depend on Q^2. The probability of finding a parton with momentum fractions of 0 or 1 vanishes. This is reflected in the factors $x^{m\left(Q^2\right)}$ and $(1-x)^{n\left(Q^2\right)}$, which control the low- and high-x behaviour, respectively. The values of the parameters at various Q^2 must be constrained empirically using data. The energy reach of the experiment, and indeed the particular process under study, determines the values of Q^2 that the hadron structure is probed at. Since the momentum fractions are related to the rapidity of the particle produced in the Drell-Yan process (see Equation 2.63), different experiments can also probe different regions of the PDF phase-space due to differing geometric acceptances. Figure 2.7 shows how various experiments cover this phase-space, where the coverage is due to the geometry of each experiment and the energy scale of the processes studied. The green domain represents fixed target data, which probe PDFs in the low-Q^2 and quite a broad range of x. Experiments at the Tevatron have a higher Q^2 but do not encompass as broad a range of x. The LHC experiments are represented by the orange and blue domains. These cover a broad range of both x and Q^2. The regions accessible to the Large Hadron Collider beauty (LHCb) detector are indicated by the orange domains. A Z boson produced in LHCb with an invariant mass of 91 GeV/c^2 corresponds to momentum fractions $x_{a,b}$ of $\sim 10^{-4}$ and $\sim 10^{-1}$, and $Q^2 \sim 10^4$ GeV/c^2.

The proton is a bound state, consisting of three quarks (two u-quarks, one d-quark) held together with gluons. The three quarks are called valence quarks. Quark anti-quark pairs may also arise due to fluctuations of the QCD vacuum. Such quarks are called sea-quarks. The sea is the source of all anti-quarks and s-quarks in the proton. It is also an additional source of u- and d-quarks. The PDFs for each proton constituent

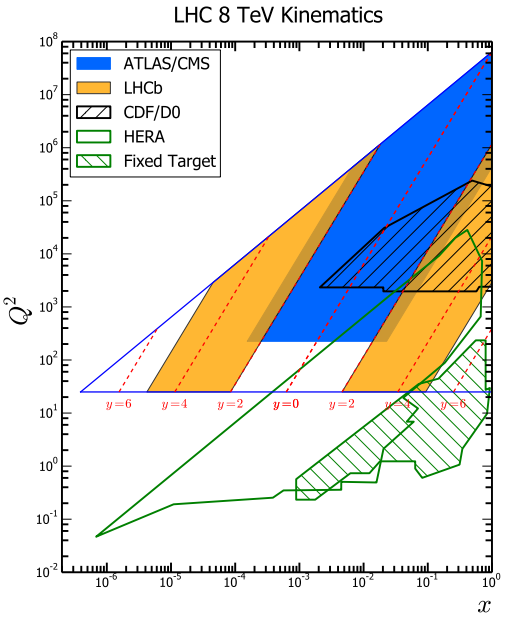

Figure 2.7: The coverage of the $x - Q^2$ phase-space probed by various experiments [24]. The dashed red lines are lines of constant rapidity.

may be represented by

$$u, \bar{u},\ d, \bar{d},\ s, \bar{s},\ g.$$

Heavy quarks (c, b, t) are given special treatment.[6]

PDFs are extracted by fitting Equation 2.57 to data. The cross-sections are usually measured as functions of rapidity, where the correspondence between the rapidity and the value of the PDF at a particular Q^2 is given by Equation 2.63. The best choice of parameters $(p_1, ..., p_n$ say, which specify F, m and n in Equation 2.64) is obtained by minimising a χ^2:

$$\chi^2(p_1, ..., p_n) = \sum_{i,j}^{N} \Big(\sigma_i^{data} - \sigma_i^{NNLO}(p_1, ..., p_n)\Big) C_{ij}^{-1} \Big(\sigma_j^{data} - \sigma_j^{NNLO}(p_1, ..., p_n)\Big). \quad (2.65)$$

Suppose there are N cross-section measurements, denoted by σ_i^{data} (i=1,...,N), with covariance matrix C_{ij}. The predictions at NNLO in perturbative QCD (see Section 2.4.2), given by Equation 2.57, are represented by σ_i^{NNLO}. The minimisation amounts to choosing parameters $p_1, ..., p_n$ to best describe the data and, in this way, the PDFs are extracted.

[6] Various schemes account for the heavy quark PDFs. These are the Fixed-Flavour-Number-Scheme, the Zero-Mass-Variable-Flavour-Number-Scheme and the General-Mass-Variable-Flavour-Number-Scheme. More details can be found in Ref [25].

The PDFs listed above are not independent. It is more convenient to extract the following linearly independent combinations of PDFs:

$$u_v = u - \bar{u},\ d_v = d - \bar{d},\ S = 2(\bar{u} + \bar{d} + \bar{s}),$$

$$s + \bar{s},\ s - \bar{s},\ \Delta = \bar{u} - \bar{d},\ g,$$

where the subscript v denotes a valence quark distribution. Further constraints on the PDFs come in the form of number sum rules. It is required that there are two up valence quarks in the proton at the lowest energy scale Q_0^2

$$\int_0^1 dx\ u_v(x, Q_0^2) = 2 \tag{2.66}$$

and there is one down valence quark

$$\int_0^1 dx\ d_v(x, Q_0^2) = 1. \tag{2.67}$$

The fraction of the proton momentum that a particular parton is expected to have is $\int dx\ x\ f(x)$. It follows that the fractional momenta of all species adds up to unity

$$\int_0^1 dx\ x[u_v(x, Q_0^2) + d_v(x, Q_0^2) + S(x, Q_0^2) + g(x, Q_0^2)] = 1. \tag{2.68}$$

In Figure 2.8, $x\ f(x)$ is plotted for different combinations of parton species, at the lowest energy scale $Q_0^2 = 1$ GeV^2.

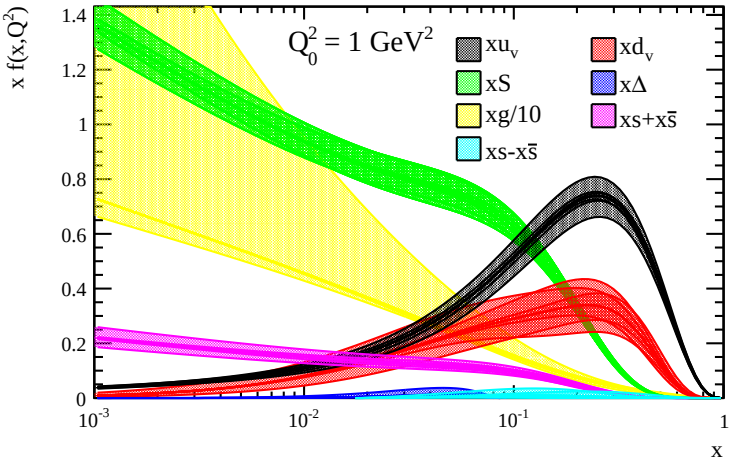

Figure 2.8: NNLO MSTW08 PDFs at input scale $Q_0^2 = 1$ GeV^2. Parameters and uncertainties are taken from Ref [25].

2.3.2 PDF evolution

Initial, low energy, scattering experiments [15] demonstrated that the parton distribution functions were dependent on the fractional momentum x and independent of the Q^2 of the process, a phenomenon known as Bjorken scaling. However, at higher proton momenta, partons are more likely to radiate gluons as their energy is greater. Similarly, at higher gluon momenta, the rate at which quark anti-quark pairs are created increases. These effects lead to Q^2-dependent scattering, and deviations from pure scaling behaviour, known as scaling violations. The reshuffling of partons in the proton is governed by the Dokshitzer-Gribov-Lipatov-Altarelli-Parisi or DGLAP equations [26–29]. These are given below in Equations 2.69 and 2.70.

$$\frac{dq_i(x,Q^2)}{d(\ln\,Q^2)} = \frac{\alpha_s(Q^2)}{2\pi}\int_x^1 \frac{dw}{w}\left[q_i(w,Q^2)\mathcal{P}_{qq}\left(\frac{x}{w}\right) + g(w,Q^2)\mathcal{P}_{qg}\left(\frac{x}{w}\right)\right] + \mathcal{O}(\alpha_s^2(Q^2)) \tag{2.69}$$

$$\frac{dg(x,Q^2)}{d(\ln\,Q^2)} = \frac{\alpha_s(Q^2)}{2\pi}\int_x^1 \frac{dw}{w}\left[q_i(w,Q^2)\mathcal{P}_{gq}\left(\frac{x}{w}\right) + g(w,Q^2)\mathcal{P}_{gg}\left(\frac{x}{w}\right)\right] + \mathcal{O}(\alpha_s^2(Q^2)) \tag{2.70}$$

These equations lead to two important observations. The first is that the PDFs increase as $\ln\,Q^2$, which is quite a slow growth. It is not surprising that these scaling violations were not detected until many measurements were made over a range of Q^2. The second is that the quark and gluon PDFs are coupled. For example, the rate of change of the quark PDF with $\ln\,Q^2$ depends on the quark PDF and its probability to radiate a gluon $\mathcal{P}_{qq}$, but it also depends on the gluon PDF and the probability for it to radiate a quark $\mathcal{P}_{qg}$. This means that as quark PDFs decrease, gluon PDFs increase, and vice versa.

The right-hand-side of the DGLAP equations indicate that partons at high-x tend to radiate and drop to lower values of x, forming new partons at low-x. The left-hand-side tells us that this happens more often at higher values of Q^2. In this way, the PDFs decrease at high-x, increase much more rapidly at low-x, and as Q^2 increases, the proton has more and more constituents sharing its momentum. With the help of these equations, parameters that are extracted from fits to data at a certain Q^2 (as in Equation 2.65) can be evolved to any other value, facilitating the prediction of the cross-section for some other process at this new scale.

Parton distributions depend on the longitudinal momentum fraction x as well as the hard scale of the process Q^2. The probability to find partons with smaller and smaller x grows, particularly for gluons, and is characterised by a $\ln \frac{1}{x}$ dependence. This can be seen in Figure 2.8 at $Q^2 = 1$ GeV^2. It is an open question as to whether the probability becomes infinite at the smallest x values, or whether gluon recombination occurs, a hypothetical phenomenon called saturation. The evolution of parton distributions with x is given by the Balitsky-Fadin-Kuraev-Lipatov, or BFKL, equation [30–32].

2.3.3 Different PDF fits

It is clear from the preceding discussion that the explicit form for PDFs depends on the particular parameterisation chosen, the flavour decomposition of the proton, and the data used in the extraction. Several phenomenologists have produced PDFs that differ due to choices made in their construction. The PDF sets used in this analysis to compare cross-section measurements with predictions are listed in Table 2.2, where the data that is considered in each PDF set is also indicated. The data can be broadly separated into two types, depending on whether it was collected at fixed-target or collider experiments. The data can be further classified as deep inelastic lepton-hadron (or lepton-nucleon) scattering as in Figure 2.6(a), Drell-Yan as in Figure 2.6(b), or inclusive jet production. The PDF sets from the MSTW [25], MMHT [33], CT [34, 35], and NNPDF [36, 37] groups include data from all of the data-types listed above.

The NNPDF23Coll set is an example of a PDF set extracted from a reduced set of data, in this case collider data only. This can be used, for example, to study the impact that certain data sets have on the PDF parameters. The HERAPDF set [21] only includes collider data from HERA. This data is used by all other PDF fitting groups. The ABM [38] and JR [39] sets use a combination of fixed-target and HERA data, although the JR set does not use νN scattering data. Finally, the ATLAS collaboration has extracted a PDF set called epWZ [40] using ATLAS and HERA data. Further differences between the PDF sets can be found in the references, also given in Table 2.2.

The MMHT PDF set is an update of the MSTW PDF set. Similarly, the NNPDF30 and CT14 sets are updates of the NNPDF23 and CT10 sets.

	Fixed-target			Collider			
	$\ell^{\pm}had$	pp/pd DY	νN	HERA CC/NC/jets	TEVATRON DY/jets	LHC DY/jets	LHC $t\bar{t}/Wc$
MSTW08 [25]	✔	✔	✔	✔	✔		
MMHT14 [33]	✔	✔	✔	✔	✔	✔	✔
CT10 [34]	✔	✔	✔	✔	✔		
CT14 [35]	✔	✔	✔	✔	✔	✔	
NNPDF23 [36]	✔	✔	✔	✔	✔	✔	
NNPDF23Coll [36]				✔	✔	✔	
NNPDF30 [37]	✔	✔	✔	✔	✔	✔	✔
HERAPDF1.5 [21]				✔			
ABM12 [38]	✔	✔	✔	✔		✔	
JR09 [39]	✔	✔		✔			
epWZ [40]				✔		✔	

Table 2.2: This analysis considers different PDF sets. These are listed above, as well as the data considered for each fit. The fixed target data includes results from the BCDMS, NMC, SLAC, NuSea, NuTeV, Chorus and CCFR experiments. The collider data includes data from H1, Zeus, D0, CDF, CMS, ATLAS and LHCb. Some abbreviations in the table are listed: proton-proton (pp), proton-deuteron (pd), Drell-Yan (DY), charged-current (CC), neutral-current (NC), neutrino-nucleon (νN).

2.4 Calculating cross-sections

2.4.1 Monte Carlo integration

Consider two initial-state particles, A and B, with momenta p_A and p_B, that scatter to produce n final-state particles with momenta $p_1,\ p_2\ ...\ p_n$. The quantum mechanical initial- and final-states can be represented by $|p_A\ p_B\rangle$ and $|p_1\ p_2\ ...\ p_n\rangle$. The quantum mechanical amplitude for the process is represented by the overlap of these two states at equal times [7]

$$\langle p_1\ p_2\ ...\ p_n|\, S\, |p_A\ p_B\rangle\,, \tag{2.71}$$

where the matrix, S, evolves the initial state from the infinite past to the infinite future. The S-matrix can be written as a sum of an interacting piece and a non-interacting piece. The former can be expressed in terms of another matrix, T. The latter is just the identity.

$$S = 1 + iT \tag{2.72}$$

It is now possible to define the matrix element $\mathcal{M}$

$$\langle p_1\ p_2\ ...\ p_n|\, iT\, |p_A\ p_B\rangle = (2\pi)^4\ \delta^4(p_A + p_B - \sum_n p_n)\ i\mathcal{M}(p_A, p_B \to p_1,\ p_2 ...\ p_n). \tag{2.73}$$

It was mentioned in Section 2.1.3 that the Feynman rules and Feynman diagrams are convenient tools for calculating amplitudes. To be precise, the procedure calculates matrix elements.

To calculate the cross-section for some process (see, for example, Equation 2.57) one must integrate a matrix element over the relevant phase-space of final-state momenta.

These integrals have the form

$$I = \int_V d^n x f(x) \tag{2.74}$$

where f is a function of the momenta of the final state particles and V is the volume of the multi-dimensional space. If N random points x_i (i=1,...,N) in the volume V are chosen, the central limit theorem of statistics gives

$$I \simeq < f > = \frac{V}{N} \sum_{i=1}^{N} f(x_i). \tag{2.75}$$

This equation indicates that the cross-section may be computed by evaluating the matrix element at several points in phase-space. The estimated error on the integral is given by

$$E = V \sqrt{\frac{< f^2 > - < f >^2}{N-1}}. \tag{2.76}$$

Thus, the error on the integral decreases as the inverse of the square-root of the number of points sampled.

The Monte Carlo (MC) method involves randomly selecting points in the phase-space, evaluating the matrix element f at these points, and averaging the results to obtain the integral I. The error E is made small by increasing the number of randomly chosen points. In later chapters this uncertainty will be referred to as the uncertainty due to numerical integration. The fact that the points correspond to final-state momenta make the MC method ideal for generating events that can be passed through detector simulation.

2.4.2 Fixed-order perturbation theory

The matrix elements mentioned in the previous section are calculated with the aid of perturbation theory, which gives a series of contributing terms that become less and less significant at higher powers of an expansion parameter, or coupling constant. Typically one decides on the desired theoretical precision and truncates the perturbation series at a fixed order. This idea is represented schematically in Equation 2.77.

$$\sigma = \sigma_0 + \left(\frac{\alpha_s}{2\pi}\right)\sigma_1 + \left(\frac{\alpha_s}{2\pi}\right)^2 \sigma_2 + \left(\frac{\alpha_s}{2\pi}\right)^3 \sigma_3 + ... \tag{2.77}$$

The first term, σ_0 is called the leading-order (LO) contribution to the cross-section. The second term is the next-to-leading-order (NLO) contribution, represented by $\alpha_s \sigma_1$, where this has a factor of α_s due to the additional strong interaction vertex in the Feynman diagram. The LO process is shown in Figure 2.9(a), while Figures 2.9(b)-

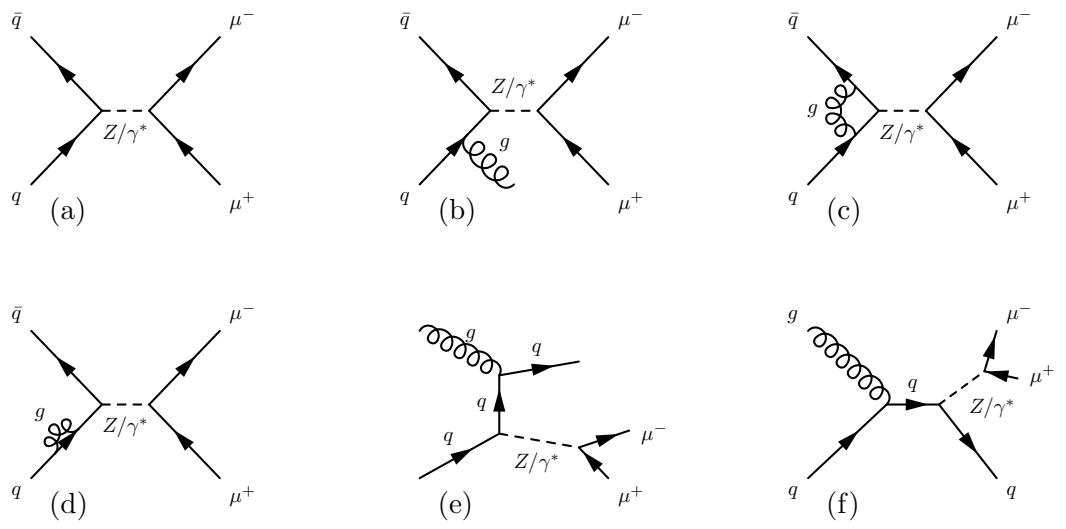

Figure 2.9: Feynman diagrams representing Z production at LO (a) and NLO (b-f) in the strong coupling constant α_s for $q\bar{q}$ initiated production.

(f) represent NLO processes. In particular, Figure 2.9(b) corresponds to radiation of gluons from initial state-quarks and Figures 2.9(c)-(d) represent corrections to the $q\bar{q}Z$ interaction vertex and the quark propagators. The final two diagrams represent qg initiated production of Z bosons. Since the value of $\alpha_s(M_Z)$ is about 0.12, this NLO correction is expected to be about 10% of the leading-order term. The next-to-next-to-leading-order (NNLO) term includes the real emission of two gluons as well as two loop corrections (propagator and vertex corrections with quark loops). The calculations become more complex at higher and higher orders. Measurements in this analysis are compared to NNLO predictions of the Drell-Yan process using the FEWZ [41] (version 3.1) and DYNNLO [42] (version 1.4) generators.

2.4.3 Analytic resummation

For fixed-order perturbation theory to give an accurate estimate of the cross-section, the higher order terms must be small, where small is ensured by $\alpha_s(M_Z) << 1$. It turns out that this is not a sufficient condition to ensure that all higher order terms are small as there are regions of phase-space in which the matrix element (and hence the σ_i) are large, negating the smallness of α_s. In particular, a singularity in the matrix element for electroweak boson production at low transverse momentum is caused by colinear and soft emission of initial-state gluons. The cross-sections obtain additional factors of the form $L = \ln(Q^2/Q_0^2)$, where Q_0^2 is small and L is thus large. The total cross-section in

Equation 2.77 can be rewritten as

$$\sigma = \sigma_0 + \left(\frac{\alpha_s}{2\pi}\right)(\sigma_{12}L^2 + \sigma_{11}L + \sigma_{10}) + \left(\frac{\alpha_s}{2\pi}\right)^2(\sigma_{24}L^4 + \sigma_{23}L^3 + \sigma_{22}L^2 + \sigma_{21}L + \sigma_{20}) + \\ + \left(\frac{\alpha_s}{2\pi}\right)^3(\sigma_{36}L^6 + \sigma_{35}L^5 + \sigma_{34}L^4 + \sigma_{33}L^3 + \sigma_{32}L^2 + \sigma_{31}L + \sigma_{30}) + ... \quad (2.78)$$

where the contributions with large logarithms have been separated from those that are well behaved. At $\mathcal{O}(\alpha_s)$ there is one potentially soft and/or one potentially colinear gluon, so the order of the power series is 2. At $\mathcal{O}(\alpha_s^2)$ there are potentially four large logarithms per diagram, so the order is 4. The problem for the perturbation expansion is that $\alpha_s L \sim 1$, or worse.

To describe electroweak boson transverse momentum spectra, it is necessary to account for these large logarithms that appear at all orders of α_s in the perturbation series. The contributions

$$\sum_{k=1}\left(\frac{\alpha_s}{2\pi}\right)^k \sigma_{k,2k} L^{2k} \quad (2.79)$$

are known as the leading-logarithms (LL) since they give the largest contribution to the cross-section at each order of α_s. The terms

$$\sum_{k=1}\left(\frac{\alpha_s}{2\pi}\right)^k \sigma_{k,2k-1} L^{2k-1} \quad (2.80)$$

have one less power of L and are referred to as next-to-leading-logarithms (NLL). The definition of next-to-next-to-leading-logarithms (NNLL) is as one might expect. One mathematical procedure for resumming these logarithms is known as the Collins-Soper-Sterman resummation formalism [43], which involves a transformation into a conjugate space (impact parameter space) where these sums exponentiate. The resummed logarithms may be combined with the well behaved parts of the fixed-order cross-sections using so-called matching procedures. This allows predictions at arbitrary order in α_s, that also take into account logarithmic enhancements at higher orders of α_s. In Figure 2.10 the resummed cross-section, differential in Z boson transverse momentum, is compared to the fixed-order result. The resummed distribution is much more representative of measured distributions at low p_T. Of course, this is not to say that the resummation is correct and fixed order perturbation theory is incorrect. It is that they both have their own domains of applicability. For the Z boson transverse distribution, resummation describes the low p_T domain and fixed order perturbation theory describes the high p_T domain. Measurements in this analysis are compared to NLO+NNLL predictions of the Drell-Yan process using the RESBOS [44–46] generator.

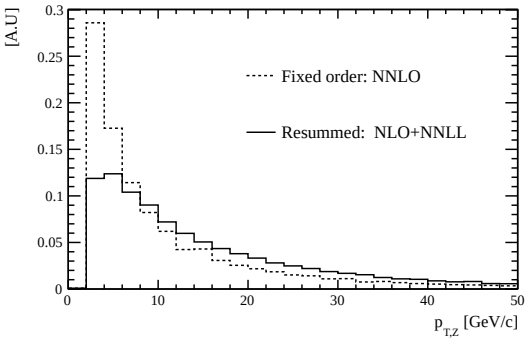

Figure 2.10: Predicted Z boson transverse momentum distribution. The dashed line indicates the fixed-order result of DYNNLO, while the solid line indicates the resummed result of RESBOS.

2.4.4 Parton showers

Fixed-order perturbation theory with, when necessary, logarithmic resummation are excellent tools for computing cross-sections. However, they cannot describe the many particles that are produced in hadron collisions. In this section, an algorithm that describes the radiative cascade of partons, and their subsequent hadronisation, is discussed. The algorithm is known as the parton shower.

Highly energetic electrons are known to radiate photons. In a similar way, the partonic content of the proton (quarks and gluons) radiate gluons. In a parton shower, initial- and final-state partons are evolved from high energy down to Λ_{QCD} ($\sim$ 200 MeV) through a sequence of gluon splittings. Around scales close to Λ_{QCD}, non-perturbative effects start to take over and partons hadronise to form the colour neutral particles that we observe in nature. The parton shower thus has the ability to describe the large particle multiplicities seen at hadron colliders. Since there is no limit to the number of branchings that can take place, the shower approximates gluon radiation from partons to all orders in α_s. The shower thus resums large logarithms due to soft and colinear gluon emission. Typically one uses a LO matrix element, so the formal accuracy of the predicted cross-sections is LO+NLL.

For this analysis, the PYTHIA8 [47] and HERWIG++ [48] parton shower MC programmes have been used to generate detector-simulated events, assess systematic uncertainties, and evaluate final-state radiation corrections. A major difference between the two programmes is how the shower is ordered. With HERWIG++, the shower is ordered by

having the large-angle emissions come first. In PYTHIA8, emissions are ordered in transverse momentum. There are also differences in the hadronisation models, with PYTHIA8 using the string model [49] and HERWIG++ using the cluster model [50].

An important parameter in parton showers is the intrinsic/primordial k_T/p_T, referred to here as the intrinsic k_T. This parameter accounts for the fact that the momenta of the partons may not be colinear with the proton momentum. Fermi motion of partons has a magnitude on the order of an inverse proton radius (Λ_{QCD}) and may cause this. Unresolved initial state radiation may give the partons a small kick in transverse momentum. In addition there may be certain aspects to the parton shower algorithm that do not take into account the interactions between the partons. These effects are considered together. The intrinsic k_T is assumed to be Gaussian distributed and the parameter that is set for the shower is the square-root of the mean-squared (RMS) of this distribution, i.e. $\sqrt{< k_T >^2}$. The value is extracted from fits to Drell-Yan data, as the width of the peak in the transverse momentum distribution is quite sensitive to the choice. The parameter is typically set to about 2 GeV/c, but it is important to extract the value in complementary scenarios such as different masses of Drell-Yan production, different centre-of-mass energies and different rapidity ranges. The latter two are most relevant to this analysis.

2.4.5 NLO matching

In general, fixed-order calculations do a good job of describing features of events whose final-states involve relatively few partons that are well-separated and have large transverse momenta. On the other hand, the parton shower is able to describe many parton final-states, where these partons are almost colinear or have small transverse momenta with respect to one another. One way of combining the best features of both approaches is called NLO matching, where a fixed-order NLO matrix element is matched to a parton shower. There are two main approaches to correcting the parton shower and they are called the POWHEG [51, 52] and MC@NLO [53, 54] approaches. The formal accuracy of these predictions is NLO+NLL. Measurements in this thesis are compared to POWHEG and MC@NLO with PYTHIA [55], HERWIG [56, 57], HERWIG++ [48] and HERWIRI [58–60] parton showers.

2.4.6 Theoretical uncertainties

Four different types of theoretical uncertainty are relevant to the predictions of cross-sections and cross-section ratios in this thesis. These uncertainties are due to the choice

of scale, the strong coupling constant (α_s), the PDFs, and numerical integration.

Scale

One type of divergence that arises in quantum field theories is due to unspecified momenta in amplitudes represented by diagrams with loops, as in Figures 2.9(c) and 2.9(d). These divergences are handled with a technique called renormalisation, which essentially absorbs the divergences into the bare parameters of the theory (mass and coupling constant), yielding the physical parameters. Renormalisation depends on a set of conditions called renormalisation conditions [7]. These conditions depend on an arbitrary mass scale, which is called the renormalisation scale μ_R, and are required to give precise definitions to the physical parameters. The perturbatively calculated cross-sections given by Equation 2.77 depend on μ_R.

As mentioned in Section 2.3, the cross-section for hadronic production of vector bosons (and virtual photons) factorises into a perturbative part and a non-perturbative part. The factorisation depends on an additional energy scale, μ_F, called the factorisation scale. In Equation 2.57, μ_F has been set to the mass of the intermediate boson, denoted by Q.

The factorisation and renormalisation scales are not physical. If it were possible to include all terms of the perturbative expansion in Equation 2.77, the cross-section would not depend on these. In practice, calculations are performed at a fixed order, and the result depends on the choice of scale.

Usually, cross-sections are calculated with the factorisation (μ_F) and renormalisation (μ_R) scales set to M_Z. The scale dependence is evaluated using the 7-point method [61]. With this method, the cross-section is re-evaluated with six additional combinations of scales; $(\mu_F/2, \mu_R)$, $(\mu_F, \mu_R/2)$, $(\mu_F/2, \mu_R/2)$, $(2\mu_F, \mu_R)$, $(\mu_F, 2\mu_R)$, and $(2\mu_F, 2\mu_R)$. The envelope defined by these observables about the nominal choice, (μ_F, μ_R), sets the scale uncertainty.

Coupling constant, α_s

The strong coupling constant α_s depends on the renormalisation scale (see Section 2.2.3).

$$\alpha_s \equiv \alpha_s(\mu_R) \tag{2.81}$$

It is usually quoted at $\mu_R = M_Z$. This is a convenient choice of scale, for which perturbative calculations are reliable. Each PDF fitting group extracts a value of $\alpha_s(M_Z)$, as it is treated as a free parameter in the PDF fit. Special PDF sets are provided, where the value of $\alpha_s(M_Z)$ is varied by its 68.3% confidence level uncertainty. These are used to compute the uncertainties on cross-sections due to α_s.

PDF

Uncertainties on PDFs are due to the uncertainties obtained on the parameters $(p_1, ..., p_n)$ extracted from the global fit to data (see Equation 2.65). These parameters are correlated with one another, so the evaluation of an uncertainty for any observable that depends on PDFs needs to take the covariance matrix into account.

Numerical integration

The numerical integration uncertainties are evaluated as in Equation 2.76. Since it is possible to make these uncertainties arbitrarily small, these uncertainties are often negligible compared to those of PDF, scale and α_s.

Chapter 3

LHC machine and LHCb experiment

The data used to make the measurements in this thesis were collected by the Large Hadron Collider beauty experiment (LHCb), a fundamental particle detector housed on the Large Hadron Collider (LHC) ring [1] [2]. This chapter describes both the LHC and LHCb, with particular focus on their aspects relevant in performing the measurements.

3.1 LHC

The LHC is the most powerful and energetic particle accelerator in the world. It is located on the Franco-Swiss border, 100 m below the ground. The LHC is a colliding beam facility; particle beams are accelerated to velocities close to the speed of light in a circular ring, whose circumference is 27 km, before being brought into collision at various interaction points on the ring. These interaction points (IP) are indicated in Figure 3.1(a). The LHCb experiment is located at IP8. Other large experiments are located at IP1, IP2 and IP5, including the ATLAS, ALICE and CMS experiments.

When the LHC was commissioned, one of the main goals was to look for experimental confirmation of a mechanism to explain electroweak boson masses, as well as fermion masses (see Section 2.2.5). One such mechanism involves the existence of a hitherto unknown, massive, scalar particle, the so-called Higgs boson. Collision experiments involving hadrons can be used to produce Higgs bosons via gluon fusion, vector boson ($W^{\pm}$, Z) fusion, Higgs radiation (Higgsstrahlung), and associated production with $t\bar{t}$.

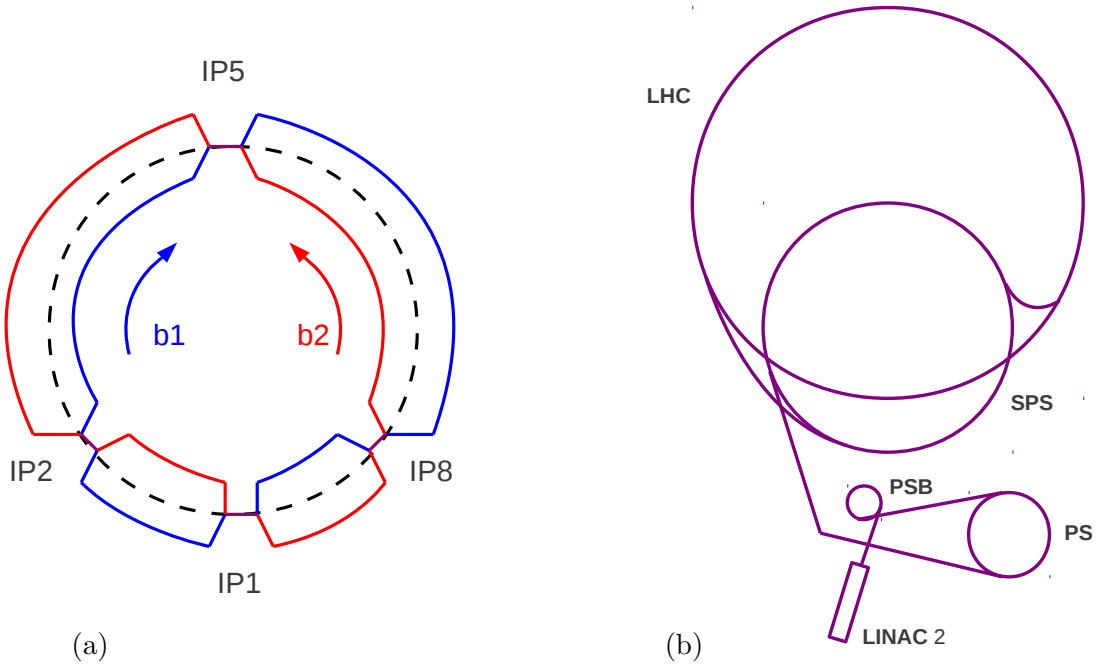

Figure 3.1: (a) Schematic of the LHC ring (dotted) and relative location of detector caverns, labelled here as IP1, IP2, IP5 and IP8. The LHCb detector is located at IP8. The orientations of LHC beam one (b1, blue, clockwise) and LHC beam two (b2, red, anti-clockwise) are also indicated. The figure is not to scale - the separation of the beams is on the order of cm while the radius of the LHC ring is on the order of km. (b) Proton injection chain from LINAC 2 through to LHC, via the Proton Synchrotron Booster (PSB), the Proton Synchrotron (PS) and the Super Proton Synchrotron (SPS).

The discovery of the Higgs boson was announced during the first LHC run period (Run-I). The achievement of this primary objective has ensured that the LHC project will be forever considered a success. The LHC continues to test the SM to its limits, and indeed look for evidence of new physics beyond the SM (BSM).

3.1.1 Proton acceleration

Protons are prepared for use in the LHC by stripping electrons from H_2 molecules. They are then accelerated in straight lines through a linear accelerator (LINAC 2) by means of an electric field. The sections of LINAC 2, through which the protons pass, alternate between regions of zero and non-zero electric field. As the protons pass through, the

electric field flips polarity to allow the protons to continue travelling in one direction, instead of being trapped in a potential well.

LINAC 2 brings the proton energies up to 50 MeV. They then enter the Proton Synchrotron Booster (PSB), which consists of four synchrotron rings that accelerate the protons to 1.4 GeV. From here they pass into the Proton Synchrotron (PS) where they are accelerated to 25 GeV. Then they pass to the Super Proton Synchrotron (SPS) where they reach 450 GeV. At this energy the protons are injected into the LHC ring. The various accelerating stages are depicted schematically in Figure 3.1(b).

During Run-I, protons were accelerated up to energies of 4 TeV in the LHC. In June 2015 they were accelerated to 6.5 TeV, heralding the beginning of Run-II. Proton beams at these high energies are contained within the LHC ring with the aid of dipole (bending) and quadrupole (focusing) magnets, where the required magnetic field strengths are about 8 T. The large electric currents that produce these magnetic fields flow in NbTi superconductors, which are cooled to about 2 K using super fluid He.

3.1.2 Filling scheme

The beams described above are not continuous streams of protons, but rather spatially separated packets of $\mathcal{O}(10^{11})$ protons. The configuration of these bunches is chosen in order to give as much data as possible to the experiments, and to maximise the time before the beam intensity (see Section 3.1.4) degrades. In addition, it is necessary to dump the beam of protons on a regular basis. Large gaps in the bunch train allow this to be done safely. Roughly 30–40 interactions occur at the ATLAS and CMS interaction points (IP1 and IP5) per bunch crossing, whereas about 2 occur at LHCb's interaction point, IP8.

The LHC rings are filled with bunches at locations defined by the radio-frequency system. These locations are called buckets, and a sequence of ten buckets is called a slot. There are 3600 slots in each beam and, given the relativistic speeds at which the protons travel, each slot is separated by 25 ns. In each slot, one bucket is filled while the other nine are nominally empty. Only some of the slots are filled. For example, during Run-I, much of the data was taken with 1262 filled slots. Protons that occupy nominally empty buckets in a slot give rise to what is called satellite charge. In a similar way, protons that leak into nominally empty slots give rise to what is called ghost charge.

Data are recorded for four different types of bunch crossing [62]. The first type is bunch-bunch (bb), where a filled bucket in beam one collides with a filled bucket in beam two at the interaction point. The majority of recorded data are of this type. The second type

is bunch-empty (be), where a filled bucket in beam one collides with an empty bucket in beam two. The third type is empty-bunch (eb), where the roles of beam one and beam two are interchanged. Finally, there is the empty-empty (ee) configuration, where the buckets are both empty. These last three types are used for calibration studies.

3.1.3 Beam energy and centre-of-mass energy

An important quantity in colliding beam experiments is the centre-of-mass energy, $\sqrt{s}$, which is the total energy available in the centre-of-mass frame of the colliding beams. The Higgs boson cross-section increases with $\sqrt{s}$, so the LHC is designed to maximise this quantity. It also gives an upper limit to the mass of any particle produced during the collisions, so it is a very important parameter in the context of searches for new particles.

The centre-of-mass energy for proton-proton collisions at the LHC is just twice the beam energy. During RUN-I, data was taken at nominal centre-of-mass energies of $\sqrt{s} = 7$ TeV and $\sqrt{s} = 8$ TeV. Currently, RUN-II data is being collected at $\sqrt{s} = 13$ TeV. In the context of the analysis presented in this thesis, the centre-of-mass energy is important because cross-section predictions are specified at particular centre-of-mass energies. If the actual centre-of-mass energy is different to the nominal centre-of-mass energy, comparisons between measurements and predictions would be difficult to interpret. To measure the actual centre-of-mass energy, the proton beam energies must be measured.

At the LHC, the beam energy is determined in two ways, both of which rely on calculating the momentum P. The first is to integrate the magnetic field, B, over the beam path as expressed in Equation 3.1

$$P = \frac{Ze}{2\pi} \oint dx \; B(x), \tag{3.1}$$

where Z is the atomic number of the hadron and e is the proton charge. This is done using the magnetic calibration curves of the dipole magnets (magnetic transfer functions). This leads to an uncertainty on the beam energy of about one part per mille, although there is some discussion over whether or not all sources of uncertainty have been taken into account in this estimation [63].

The second method is to use the different frequencies of rotation of protons and lead ions [64], with the momentum given by Equation 3.2

$$P \approx m_p c \sqrt{\frac{f_p}{2(f_p - f_i)} \left(\left(\frac{m_i}{Z m_p} \right)^2 - 1 \right)}, \tag{3.2}$$

where f_p and f_i are the revolutions frequencies of the protons and lead ions, and m_p and m_i are their masses. A measurement of the beam energy was determined with this method at 4 TeV and 450 GeV during the p-Pb run in January and February of 2013. The precision on the beam energy at 4 TeV was determined to be 0.65%. No measurement was performed at 3.5 TeV, however, the energy at injection to the LHC ring of 450 GeV may be extrapolated to higher energies using the magnetic transfer functions. The extrapolated beam energy is consistent with 3.5 TeV with a precision of 0.1%, but as mentioned above, it is not known if all sources of uncertainty have been taken into account. Since there is good reason to believe that there are no additional uncertainties related to beam energy at 3.5 TeV compared to those at 4 TeV, the same relative uncertainty of 0.65% is taken [64]. As a consequence, the beam energy uncertainty is fully correlated between different centre-of-mass energies.

3.1.4 Luminosity

The factor of proportionality between the event rate ($\frac{\mathrm{dN}}{dt}$) of a specific process and the related cross-section (σ) is called the instantaneous luminosity, L; it is a flux, a measure of the number of particles crossing an area in unit time [65].

$$\frac{\mathrm{dN}}{dt} = L\sigma \tag{3.3}$$

The instantaneous luminosity of two colliding bunches is given by Equation 3.4.

$$L = N_1 N_2 f \sqrt{(\mathbf{v}_1 - \mathbf{v}_2)^2 - \frac{\mathbf{v}_1 \times \mathbf{v}_2}{\mathrm{c}^2}} \int d^3x \; dt \; \rho_1(\vec{x}, t) \; \rho_2(\vec{x}, t) \tag{3.4}$$

The prefactors N_1, N_2 and f are the bunch populations of beams one and two and the revolution frequency. The factor involving the velocities of the bunches $\mathbf{v}_{1,2}$ is the Mϕller factor, which approximates to $2c$ for highly relativistic beams and small crossing angles [66]. The integral over the bunch densities ρ_1 and ρ_2 is known as the beam overlap integral. In order to measure the instantaneous luminosity, it is necessary to determine the total charge in the LHC ring (and hence the populations of the bunches) and the beam overlap integral.

The beam overlap integral is measured using two methods, van der Meer scans [67] and beam-gas imaging [68], the latter being unique to LHCb. In the case of the van der Meer scan, the overlap integral is inferred by moving the beams across one another and examining the variation of some interaction rate that is proportional to the luminosity. With beam-gas imaging, the interaction region at LHCb is injected with an inert gas, for example Ne. The overlap integral is then determined using the spatial distribution

of beam-gas interaction vertices [62]. The beam-gas method complements the van der Meer scan for a number of reasons.

- The effect of complicated beam-beam interactions is not a concern.
- There is no need to make assumptions about the beam profile (see Ref [62]).
- The sources of uncertainty for each method are independent and uncorrelated. Thus, the relative uncertainty on the combination is much reduced with respect to the individual determinations.
- Beam-gas imaging may be used to determine the total ghost charge in the ring.

It is important to emphasise that the luminosity is fully determined only during dedicated calibration runs. However, rates of certain observables (number of tracks, number of vertices, etc) that are proportional to the luminosity are recorded during these calibration runs and during normal data-taking. The factors of proportionality that are determined during the calibration runs can then be used to determine the luminosity during normal data-taking.

When L is integrated over a data-taking period, one obtains the integrated luminosity $\mathcal{L}$,

$$\mathcal{L} = \int dt\ L. \tag{3.5}$$

The integrated luminosity is a measure of the size of the data set. It determines the number of events, N, that one expects to observe due to a process with cross-section σ.

$$N = \mathcal{L}\sigma \tag{3.6}$$

To maximise the statistical significance of any measurement, and to maximise the sensitivity of searches for new (rare) phenomena, it is desirable to obtain as large an integrated luminosity as possible.

3.2 LHCb

The LHCb detector is a single-arm spectrometer primarily designed for reconstructing B-mesons that decay in the forward region. Since B-mesons are relatively long-lived, their experimental signature is a decay vertex that is significantly displaced from the primary interaction vertex. Reconstruction of these secondary decay vertices is best achieved in a low occupancy environment. This is achieved by offsetting the colliding beams so that there is a low number ($\sim$1.8 in Run-I) of interactions per bunch crossing.

Figure 3.2 is a side-view of the LHCb detector; the beam pipe (grey) passes through the middle of the detector, and most of the detector instrumentation/material (coloured) is located after the magnet. As with most high energy physics experiments, the detector is designed to identify, and measure the energies and momenta of, final-state particles. This is facilitated by the layered structure. The particle tracking system consists of the Vertex Locator (VELO), Tracker Turicensis (TT), magnet and T-stations (T1, T2, T3). The calorimeter system consists of the Scintillating Pad Detector (SPD), Pre-Shower detector (PS), the Electromagnetic Calorimeter (ECAL) and the Hadronic Calorimeter (HCAL). The particle identification system consists of the Ring Imaging Cherenkov detectors (RICH) and the muon system (M1-M5). These components are explained in more detail in the following sections and in Ref. [1].

3.2.1 Co-ordinate system

Co-ordinates in LHCb are defined with respect to Cartesian axes in a right-handed frame, as in Figure 3.3. The z-axis is in the direction of the clockwise rotating beam, as viewed from above, and points from IP8 to IP1 (see Figure 3.1). The positive direction of the x-axis points toward the centre of the LHC ring. The y-axis completes the right handed system, and points vertically upwards.

3.2.2 Vertex Locator

The Vertex Locator (VELO) consists of 42 silicon modules surrounding the interaction point, as shown in Figure 3.4. Each module consists of an R-type sensor and a Phi-type sensor as shown in Figure 3.5(a). The R-type sensor provides information on the radial distance of a charged particle's trajectory, while the Phi-type sensor provides azimuthal information. A picture of a VELO module is given in Figure 3.5(b). The resolution on the primary interaction vertex (PV) and impact parameters (IP) of tracks with respect to this vertex are maximised by having the modules as close as possible

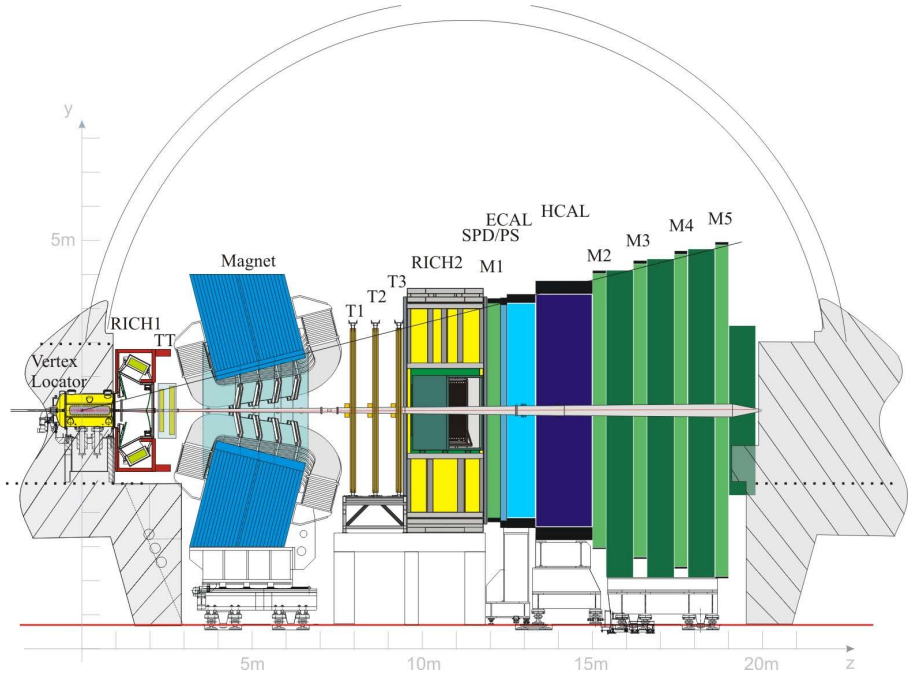

Figure 3.2: Side-view of LHCb detector in the direction of the positive x-axis. RICH1, RICH2 = Ring Imaging Cherenkov detectors 1 and 2. TT= Tracker Turicensis. T1, T2, T3 = Tracking stations 1, 2 and 3. SPD/PS = Scintillating Pad Detector / Preshower. ECAL = Electromagnetic Calorimeter. HCAL = Hadronic Calorimeter. M1, M2, M3, M4, M5 = Muon stations 1, 2, 3, 4, and 5.

to the beam pipe.[1] During beam injection, the VELO modules are retracted to avoid radiation damage. Once the beams are stable, the modules close around the beam to a distance of ∼8 mm, allowing an IP resolution of $(15{+}29/p_T)$ μm. Further details on the VELO can be found in Ref. [69].

3.2.3 Tracker Turicensis

The Tracker Turicensis (TT) is located between the magnet and RICH1. The detector consists of four p^+ on n-type silicon layers, which are shown in Figure 3.6. The layers are grouped in pairs (TTa and TTb) that are separated by ∼30 cm. The silicon strips in the first and last layers are vertically oriented whereas the second and fourth layers are rotated by ±5° with respect to the vertical. Orienting the strips vertically improves the spatial resolution of hits in the x-direction and thus the momentum resolution in this direction. The slight rotations with respect to the vertical of the second and third layers allows hits in the y-direction to be measured as well, albeit at lower resolution. Further details on the TT can be found in Ref. [71].

[1] The IP is defined as the distance of closest approach of the line defining the track and the interaction vertex.

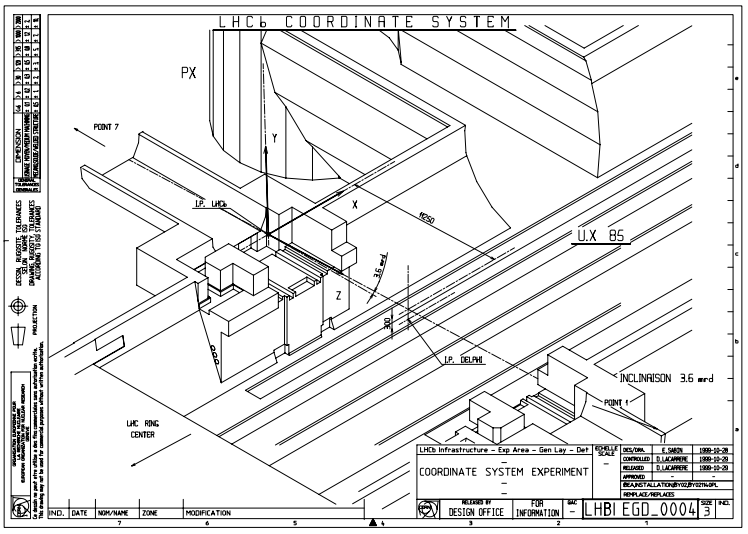

Figure 3.3: Drawing of LHCb co-ordinate system. The z-axis is in the direction of the clockwise rotating proton beam, b1 (see Figure 3.1). The x-axis points toward the centre of the LHC ring and the y-axis points vertically upwards.

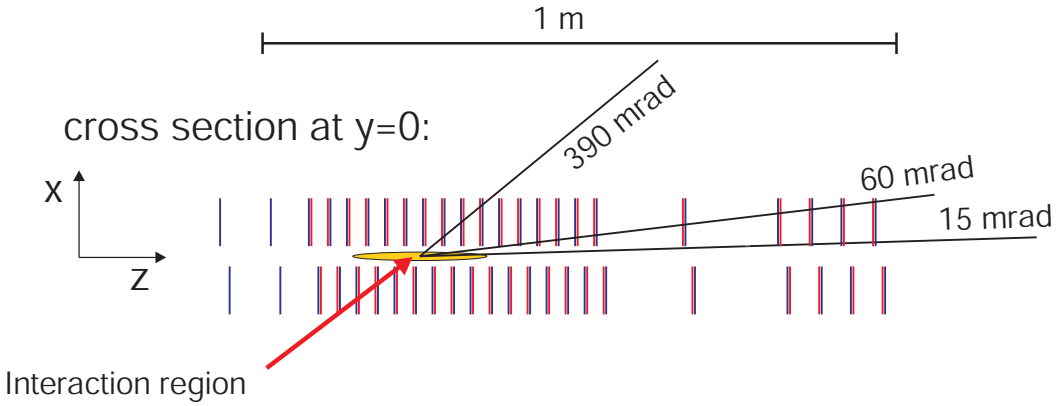

Figure 3.4: VELO module positions.

The purpose of the TT is to help with a fast reconstruction of track momentum in the trigger. It also plays a role in reducing the rate of randomly associated hits (ghosts). TT hits are not used in the search for long tracks, the primary tracks of this analysis (see Section 3.2.6). In this thesis, this fact is used in the measurement of the muon tracking efficiency.

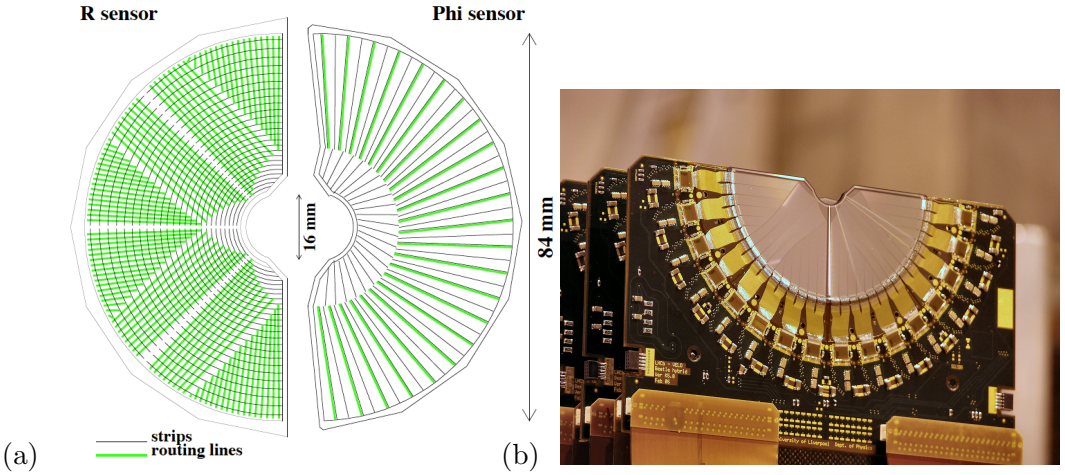

Figure 3.5: (a) R- and Phi-type sensors. (b) VELO module.

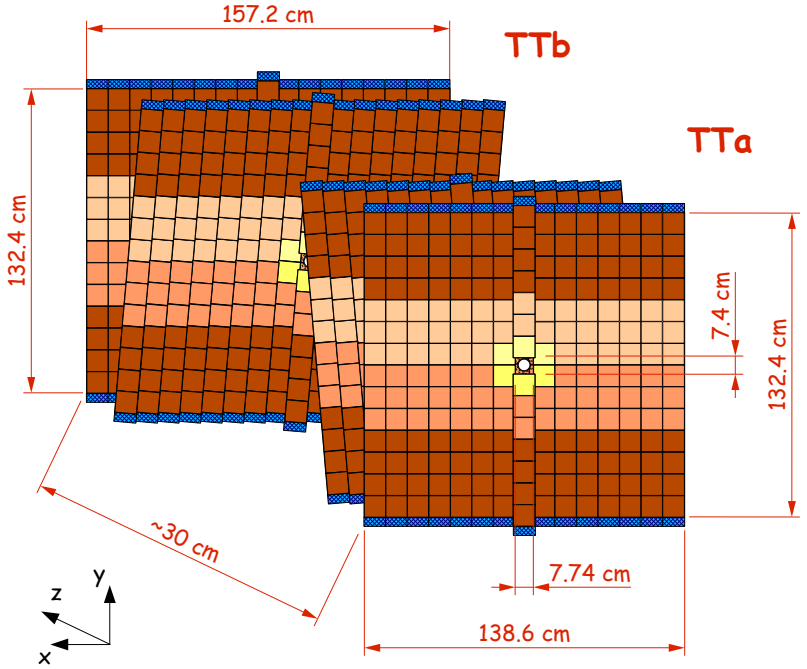

Figure 3.6: The TT sub-detector [70].

3.2.4 Spectrometer dipole magnet

A spectrometer dipole magnet is positioned between the VELO and the tracking stations. Its primary function is to bend charged particles in order to obtain estimates of their momentum. The main component of the magnetic field is oriented along the y-axis and thus positively and negatively charged particles are separated in the x-z plane.

In order to achieve the required momentum resolution for charged particles, the magnetic field integral $\int B \cdot dl$ must be measured with sub per mille precision and the position where the B-field is strongest must be determined with a precision of a few millimetres [1]. These are measured using an array of Hall-probes that can be moved along the z-axis. The strength of the field as a function of z co-ordinate is indicated in Figure 3.7.

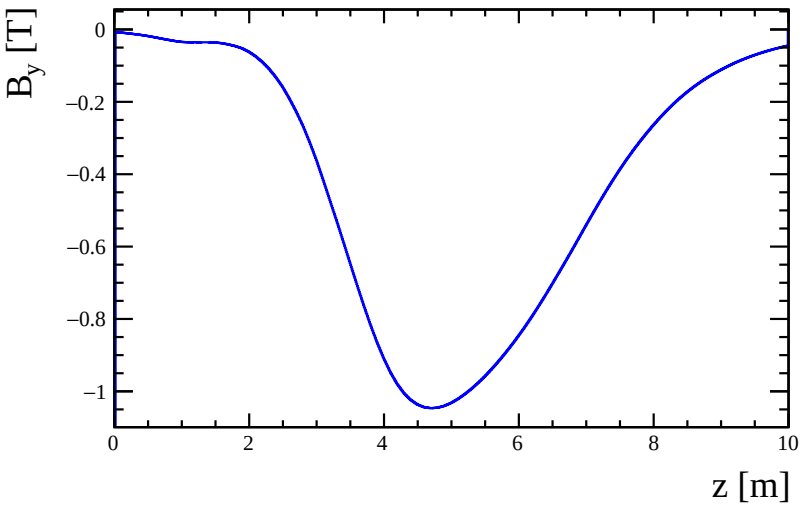

Figure 3.7: The strength of the magnetic field in the y-direction as a function of z co-ordinate.

The polarity of the magnet may be reversed. In this thesis, the two configurations are referred to as Magnet Up (MU) and Magnet Down (MD). The polarity is flipped periodically in order to have MD and MU sub-samples that are approximately equal in size. The relative proportion of MD data to MU data in this thesis (see Chapter 4) is 2:1 for data collected at $\sqrt{s} = 7$ TeV and 1:1 for data collected at $\sqrt{s} = 8$ TeV. Further details on the LHCb spectrometer dipole magnet can be found in Ref. [72].

3.2.5 T-stations

Between the magnet and RICH2 there are three tracking stations called T1, T2 and T3 (T-stations) located about 9 m from the interaction point. The T-stations are composed of an outer tracker (OT) and an inner tracker (IT), as shown in Figure 3.8.

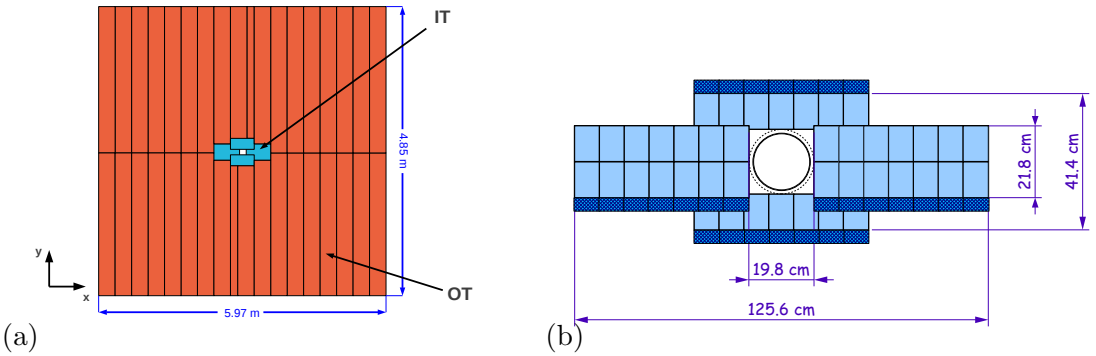

Figure 3.8: (a) Schematic of a T-station showing the inner tracker (IT) and outer tracker (OT). (b) Dimensions of the IT.

Inner tracker

The component of the T-station closest to the beam pipe, where particle the flux is highest, is called the IT. It is a silicon strip detector similar to the TT. There are four inner tracker boxes and each box consists of four layers of silicon strips. The inner two layers are aligned at $\pm 5°$, in a similar way to those of the TT. Further details on the IT can be found in Ref. [71].

Outer tracker

The rest of the T-station is called the OT. The OT is a straw tube drift-time detector. Each OT module consists of four layers, and the inner two layers are aligned at $\pm 5°$, similar to the TT and IT. Further details on the OT can be found in Ref. [73].

3.2.6 Track and vertex reconstruction

The tracking system is used to reconstruct the trajectories and momenta of charged particles. It is also used to determine the position of interaction and decay vertices from tracks that lead back to a common point. Several types of track are defined, depending on the sub-detector hits used to reconstruct the track. These tracks are listed below and sketched in Figure 3.9.

VELO tracks are reconstructed from hits in at least three VELO modules.

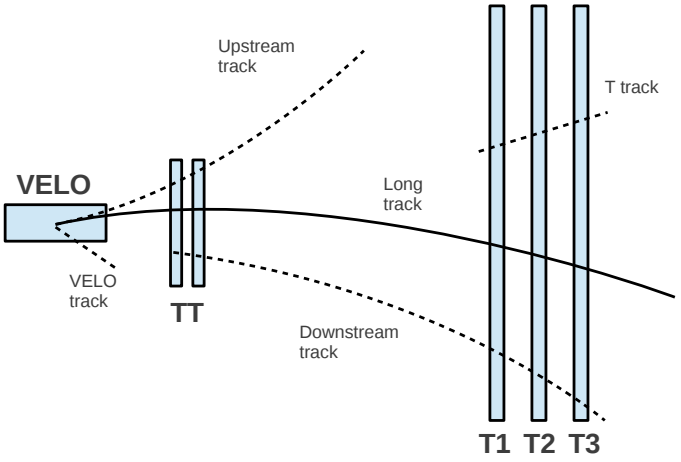

Figure 3.9: LHCb track types.

Upstream tracks are reconstructed from hits in the VELO and the TT sub-detector. They do not reach the T-stations.

Downstream tracks are reconstructed from hits in the TT and T-stations. They are used to reconstruct long-lived particles that decay outside of the VELO, such as K_s mesons and Λ baryons.

T-tracks only have hits in the T-stations.

Long tracks are found using hits from the VELO and T-stations. Once the long track has been found, TT hits are added to improve the momentum estimate. Long tracks have the most precise momentum estimate. The tracks used in this analysis are long tracks.

MuonTT tracks are reconstructed using hits in the TT and muon stations (see Section 3.2.9). In this thesis, these tracks are used to determine the muon tracking efficiency.

A number of fitting algorithms are used to fit a track to the hits in the various tracking stations. These are based on the Kalman filter method [74]. In regions of negligible

magnetic field, for example in the VELO, straight line tracks are fitted to the hits. Parabolic trajectories are fitted to match hits in regions where the magnetic field is more influential, for example the T-stations (c.f Figs 3.2 and 3.7). In this thesis, the quality of the fit to the detector hits is used to select good tracks for the analysis, both in the trigger (see Section 3.2.10) and in the selection of Z boson candidates offline (see Section 4.1).

Two types of vertex are relevant to the analyses presented in Chapters 4 and 5, the PV and the Z boson decay vertex. The PV is the location of the hard proton-proton interaction. A minimum of four tracks are required to form a PV. For more details on the reconstruction of PVs at LHCb, consult Ref. [75]. The midpoint along the vector defining the distance of closest approach (see Figure 3.10) between the muon tracks is used to seed the Z boson decay vertex position. A fit based on a χ^2 minimisation procedure, involving the muon momenta and their covariance matrices, is performed to extract an improved Z boson vertex position, as well as the corresponding Z boson momenta and mass. In Chapters 4 and 5, the kinematic variables of the Z boson refer to those after this fitting procedure, whereas the kinematic variables of the muon refer to those before this fitting procedure. The quality of the vertex fit is quantified by the χ^2/ndf, which is the χ^2 divided by the number of degrees of freedom. In this analysis, the χ^2/ndf of the vertex fit is used to enrich Z boson candidate samples in heavy flavour background (see Section 4.3.1). It is also used by the dimuon trigger to decide which events are saved for offline analysis (see Section 3.2.10).

3.2.7 Particle Identification (RICH)

A number of sub-detectors are used for the purpose of particle identification. These include the Ring Imaging Cherenkov detectors (RICH1 and RICH2), the calorimeters, and the muon system.

The purpose of the RICH detectors is to identify particles over a wide range of momenta. This is done by measuring particle velocities that, when combined with independent measurements of particle momenta, translate into measurements of particle masses. The particles are then identified by association with the known masses [3].

The velocity of the particle is measured in the RICH detectors using the Cherenkov effect. When relativistic particles enter a medium at speeds that exceed the speed of light in that medium, photons are emitted at an angle θ_C (the Cherenkov angle) with respect to the direction of the particle. The radiation arises from the excitation of the medium under the action of the field of the particle moving in it. For this reason the

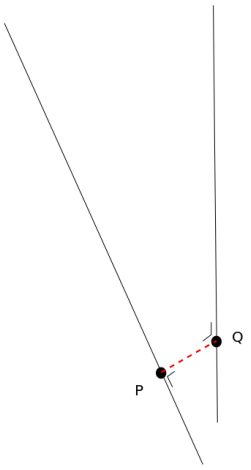

Figure 3.10: The initial position of the Z boson decay vertex is located along the line of closest approach of the muon momentum vectors.

medium is referred to as the radiator. The radiation is distinct to bremsstrahlung, which is the type of radiation emitted by a charged particle as it moves in the field of a nearby nucleus. The Cherenkov angle is related to the particle velocity $v = \beta c$ and the refractive index of the radiator n by

$$\cos\theta_C = \frac{1}{\beta n}. \tag{3.7}$$

Therefore, if the refractive index is known and if θ_C is measured, the particle velocity can be measured.

RICH1 is located ∼1.5 m from the interaction point, upstream of the magnet, between the VELO and the TT, and is sketched in Figure 3.11(a). It is designed to measure the velocities of low momentum (a few GeV/c) and medium momentum ($<$ 60 GeV/c) particles. RICH2 is located after the T-stations, before the calorimeters and muon system. A sketch of RICH2 is given in Figure 3.11(b). It is designed to measure the velocities of particles over a range of momenta, from 15–150 GeV/c. The Cherenkov photons are reflected, first from a spherical mirror and then from a planar mirror, before they reach an array of Hybrid Pixel photon Detectors (HPD). A photograph of a HPD is shown in Figure 3.12(a). The Cherenkov light form rings from which θ_C may be determined. This angle is given as a function of momentum for different particles and

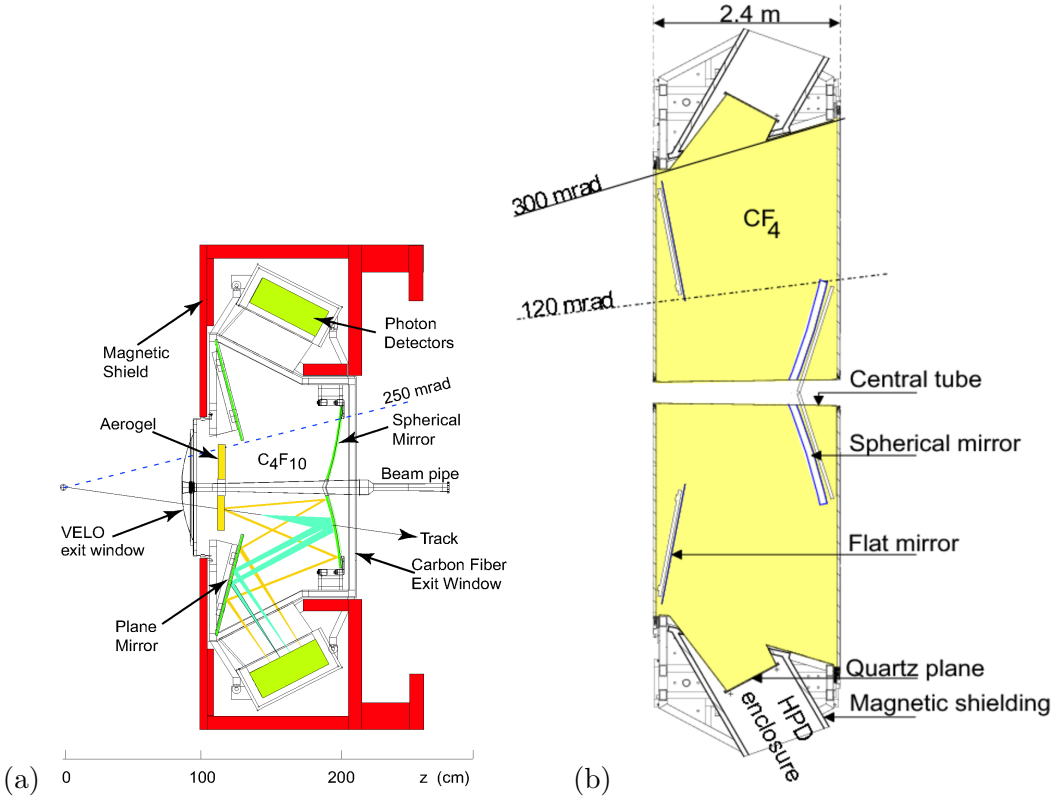

Figure 3.11: (a) Schematic of RICH1 and (b) schematic of RICH2, taken from Ref [1].

radiators in Figure 3.12(b). Further details on the RICH detectors can be found in Ref. [76].

3.2.8 Calorimetry

The calorimeter system consists of four sub-detectors, the Scintillating Pad Detector (SPD), the Pre-Shower (PS), the Electromagnetic Calorimeter (ECAL) and the Hadronic Calorimeter (HCAL). The purpose of this system is the identification of hadrons, electrons, photons, and the measurement of their energies and positions.

Electrons and positrons moving through dense materials emit photon radiation via bremsstrahlung. If the emitted photon is energetic enough, it may decay into an electron-positron pair, which in turn may radiate due to bremsstrahlung. This cascade effect is called an electromagnetic shower. Electromagnetic calorimeters induce these showers with layers of dense material, such as Pb. The thickness of these materials is usually expressed in interaction lengths, denoted by X_0, defined as the distance over which the particle is reduced to 1/e of its original energy.

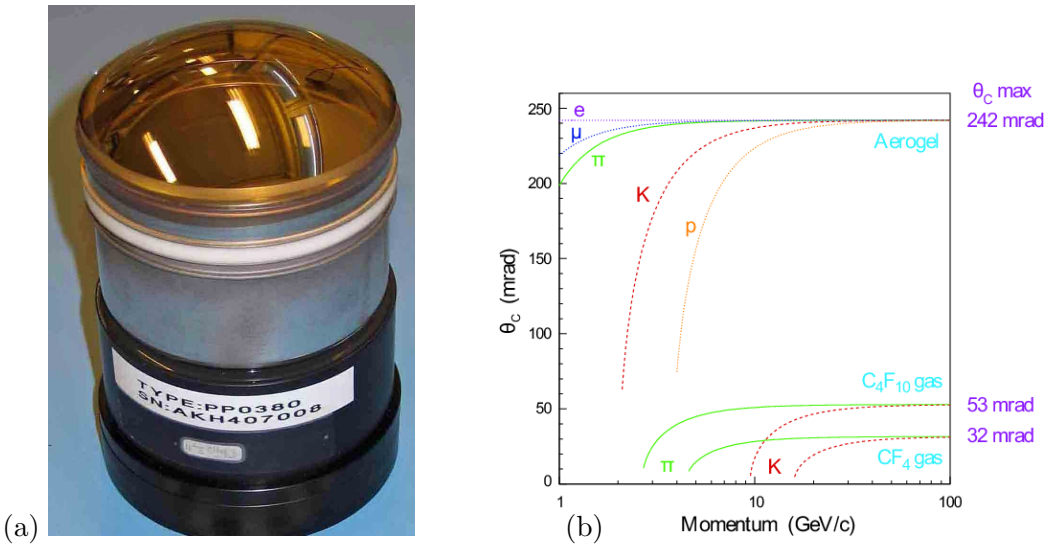

Figure 3.12: (a) Photograph of Hybrid Pixel Detector (HPD), and (b) Cherenkov angle as a function of momentum for different radiators, taken from Ref [1].

The energy loss due to bremsstrahlung is inversely proportional to the mass of the accelerating particle, and is thus relatively large for the lightest particles, i.e. electrons. For heavier particles like muons and hadrons, energy loss due to bremsstrahlung is small compared to energy loss due to interactions with the nuclei in the material. The effect of these interactions with nuclei is to produce secondary hadrons with lower energies, which in turn interact with other nuclei and so on, producing a hadronic shower. Hadronic calorimeters induce these showers with layers of dense material. The thickness of these materials is usually expressed in hadronic interaction lengths λ_I, defined as the mean distance that a hadron travels before interacting.

For both electromagnetic and hadronic calorimeters, the dense layers that induce the showers are interwoven with scintillating material. These absorb the energy of ionising particles and re-emit it as light, which gets collected in a photo multiplier tube (PMT). The energy of the collected radiation is roughly proportional to the original energy of the particle. It is thus important to calibrate the response of the calorimeter material with a test-beam facility. Particular aspects of calorimetry at LHCb are given in the next few sections. Further details can be found in Ref. [77].

SPD/PS

Starting at the interaction point and moving in the direction of increasing z, the first two planes of scintillating material in the calorimeter system are the SPD and PS. These planes are separated by a 15mm ($2.5X_0$) Pb sheet [1]. The granularity of both the SPD

and PS (and ECAL) is indicated in Figure 3.13(a). Each cell in this figure represents an SPD module consisting of scintillator material and a PMT.

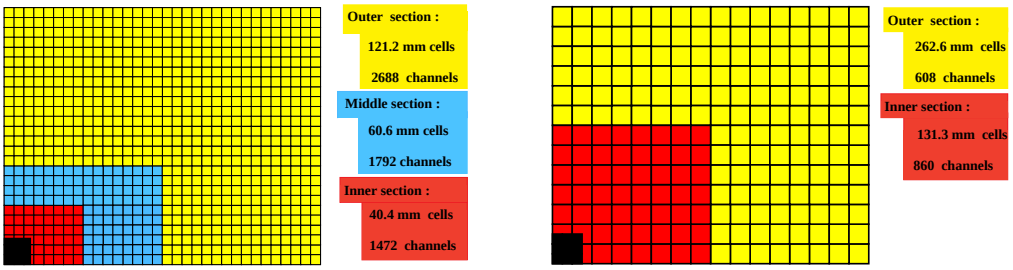

(a) (b)

Figure 3.13: (a) Lateral segmentation of the PS, SPD and ECAL. (b) Lateral segmentation of the HCAL. In both cases one quarter of the detector front face is shown [77].

Since the first layer of the calorimeter system (SPD) is a scintillating material, and since there is no absorber material preceding it to induce pair-production from neutrals, the energy absorbed by the scintillators in the SPD can be attributed to charged particles produced in the primary collision. The benefits of this are two-fold. First, the combination of information in the SPD and PS can be used to distinguish between charged and neutral particles (see Figure 3.14). Second, the SPD may be used as a charged

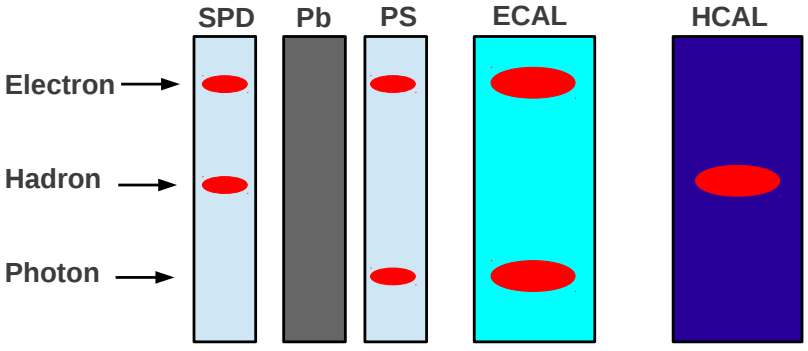

Figure 3.14: Signal (red ellipse) deposited in the scintillating material of the calorimeter (blue) by an electron, photon and hadron. Adapted from Ref. [78].

particle multiplicity counter. In the LHCb trigger, upper limits on the SPD multiplicity are imposed in order to reject high multiplicity events that would take large amounts

of time to process online[2]. These thresholds need to be accounted for in cross-section measurements, especially those of Z boson production, where events often involve hard jets and large charged-particle multiplicities. The necessary correction is explained in more detail in Section 4.4.3.

ECAL

The segmentation of the ECAL is similar to that of the SPD and PS as in Figure 3.13(a). Each module consists of 66 alternating layers of lead (2mm) and scintillator material (4mm), corresponding to $25X_0$. In this thesis, ECAL energy information is used to reduce backgrounds in W boson candidate samples. See Section 5.1 for more details.

HCAL

The segmentation of the HCAL is shown in Figure 3.13(b). Hadronic showers are induced with iron layers and the energy is measured using scintillator material and PMTs. In the HCAL modules, the iron and scintillator layers are parallel to the z-axis. The total thickness of the HCAL corresponds to $5.6\lambda_I$. In this thesis, HCAL energy information is used to reduce backgrounds in W boson candidate samples. See Section 5.1 for more details.

3.2.9 Muon system

The outermost layers of the LHCb detector are dedicated to muon identification. The system consists of five muon stations labelled M1-M5. M1 is located before the PS and M2-M5 are after the calorimeters. These latter four are interleaved with thick layers of iron, labelled as muon filters in Figure 3.15(a). Multi-wire proportional chambers (MWPC) are used in all stations except for the inner regions of M1 where the large particle flux would age such technology at an unacceptable rate. Instead, triple-GEM tubes are used in this region [1]. Each muon station is divided into four regions R1-R4 with increasing distance from the beam axis. These regions have roughly equal occupancy and, as a consequence, the spatial resolution does not need to be so precise in the outer regions. Further details on the LHCb muon system can be found in Ref. [80].

[2]In the context of this thesis, online refers to real-time analysis as the data is being taken, while offline refers to analysis of data after it has been stored.

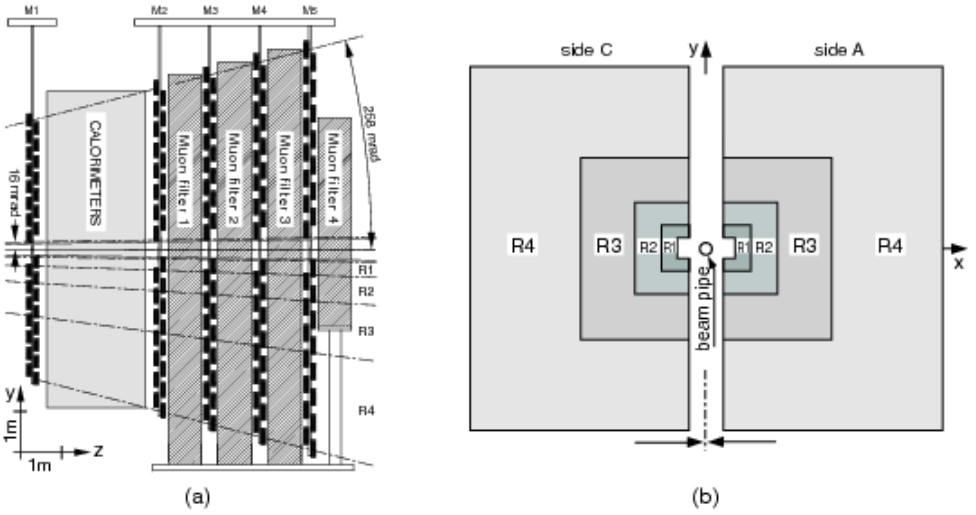

Figure 3.15: (a) Components of the LHCb muon system and (b) subdivision of muon stations in to regions R1-R4. Taken from Ref. [79].

The measurements in this analysis rely on the trigger decision from the muon system as well as muon identification. Tracks are labelled as muons if they satisfy the $isMuon$ condition. This condition is summarised in Table 3.1.

Momentum range (GeV)	Muon Detector Hits
$1 < p < 6$	M2&M3
$6 < p < 10$	M2&M3&(M4 || M5)
$p > 10$	M2&M3&M4&M5

Table 3.1: The $isMuon$ criteria. Hits from different combinations of muon system sub-detectors (M2-M5) are required in order to identify the track as a muon, where these combinations depend on the momentum p of the track.

3.2.10 Trigger

During Run-I, the frequency of proton bunch crossings at LHCb was about 10 MHz [81]. Only a subset of these events were recorded due to finite read-out times and data storage limitations. It is the trigger system that selects the most interesting events to obtain a more manageable rate. This trigger consists of two stages, Level-0 (L0) and the High Level Trigger (HLT), and uses information from the sub-detectors described above in order to make its decision. Further details on the LHCb trigger system and performance can be found in Refs. [81] and [82].

L0

The L0 trigger is implemented in custom electronics on the actual detector. During data-taking in 2011 it reduced the rate from 11 MHz to about 870 kHz [82]. The L0 trigger uses information from the calorimeter, muon system or VELO.

Only muon system triggers are relevant for measurements described in this thesis. One such trigger is used to select signal candidates and requires events that have less than 600 hits in the SPD, and at least one muon with $p_T > 3.7$ GeV/c. This trigger is called L0Muon. A second is used to determine the efficiency of the SPD hit threshold in L0Muon (see Sections 3.2.8 and 4.4.3). It requires events with less than 900 SPD hits that have a dimuon (two muons, combined) with $p_T^{\mu^1} \cdot p_T^{\mu^2} > 10.5$ GeV/c. This trigger is called L0DiMuon.

HLT

The HLT trigger is implemented on farm of PCs adjacent to the detector. The HLT is divided into two stages called HLT1 and HLT2. During data-taking in 2011, HLT1 processed the L0 rate and used a partial event reconstruction to reduce the rate to 43 kHz. HLT2 then performed a more complete event reconstruction, reducing the rate to 3 kHz.

Three triggers are relevant for this analysis at the HLT1 level. The first accepts events that satisfied L0Muon and have a muon with $p_T > 4.8$ GeV/c, with momentum $p > 8$ GeV/c and good track-fit quality ($\chi^2/ndf < 4$). Hlt1SingleMuonHighPT is the name of this trigger. The second accepts events that satisfied L0Muon, or L0DiMuon, and contain two muons with $p_T > 0.5$ GeV/c, each having momentum $p > 6$ GeV/c, good track-fit quality ($\chi^2/ndf < 4$) and a dimuon invariant mass $M_{\mu^+\mu^-} > 2.7$ GeV/c^2. This trigger is called Hlt1DiMuonHighMass. The third trigger is a random trigger that was rate limited at either 11 or 97 Hz throughout the data-taking periods. This trigger is called Hlt1MBNoBias.

Two triggers are relevant for this analysis at the HLT2 level. The first accepts events containing a muon with $p_T > 10$ GeV/c that satisfied any trigger at HLT1. This trigger is called Hlt2SingleMuonHighPT. The second trigger accepts events that satisfied any trigger at HLT1 containing a dimuon with a vertex $\chi^2/ndf < 25$ and an invariant mass $M_{\mu^+\mu^-} > 40$ GeV/c^2. This trigger is called Hlt2DiMuonZ.

Trigger combinations

In the analysis described in this thesis, a signal event must have at least one muon that satisfies each of L0Muon, Hlt1SingleMuonHighPT and Hlt2SingleMuonHighPT, as in Section 4.1. Events that satisfy each of L0DiMuon, Hlt1DiMuonHighMass and Hlt2DiMuonZ are used to evaluate efficiencies in Section 4.4.3. Additional background studies are performed using events that satisfy Hlt1MBNoBias (see Section 4.3.2).

3.3 Variables of interest

There is sufficient data from Run-I to measure Z boson cross-sections as functions of a number of different variables. This section is devoted to the definition of these variables.

Rapidity

Consider the Lorentz transformations between frames S and S', which are in relative motion along the x-axis such that the x- and x'-axis are colinear. Then

$$\begin{pmatrix} x' \\ ct' \end{pmatrix} = \frac{1}{\sqrt{1-\frac{v^2}{c^2}}} \begin{pmatrix} 1 & -v/c \\ -v/c & 1 \end{pmatrix} \begin{pmatrix} x \\ ct \end{pmatrix} \tag{3.8}$$

and with the redefinition $\tanh\varphi \equiv v/c$,

$$\begin{pmatrix} x' \\ ct' \end{pmatrix} = \begin{pmatrix} \cosh\varphi & -\sinh\varphi \\ -\sinh\varphi & \cosh\varphi \end{pmatrix} \begin{pmatrix} x \\ ct \end{pmatrix}. \tag{3.9}$$

The variable φ is the rapidity of the Lorentz boost. In high energy physics, the rapidity, y, corresponds to the particular φ that parameterises the Lorentz boost along the z-axis that takes an observer from the lab frame to a frame in which the particle moves perpendicular to the beam. The Lorentz boost along the z-axis of a 4-vector is described by the matrix equation

$$\begin{pmatrix} E' \\ p'_x \\ p'_y \\ p'_z \end{pmatrix} = \begin{pmatrix} \cosh\varphi & 0 & 0 & -\sinh\varphi \\ 0 & 1 & 0 & 0 \\ 0 & 0 & 1 & 0 \\ -\sinh\varphi & 0 & 0 & \cosh\varphi \end{pmatrix} \begin{pmatrix} E \\ p_x \\ p_y \\ p_z \end{pmatrix}. \tag{3.10}$$

Requiring that $p'_z = 0$ gives

$$y \equiv \varphi|_{p'_z=0} = \tanh \frac{p_z}{E} = \frac{1}{2}\ln\left(\frac{E+p_z}{E-p_z}\right). \tag{3.11}$$

The measurement of the rapidity distribution of Z bosons is particularly interesting for PDF fitting because of the relation between the rapidity and the fractional momenta of the partons, $x_\pm = \frac{M}{\sqrt{s}}e^{\pm y}$ (see Section 2.3).

Pseudorapidity

Related to the rapidity is the pseudorapidity η, which is obtained from the formula for y given by Equation 3.11. In the limit where $m << p$, the energy can be approximated by the momentum and

$$y|_{m<<p} \approx \frac{1}{2}\ln\left(\frac{p+p_z}{p-p_z}\right) \equiv \eta. \tag{3.12}$$

Transverse momentum

The transverse momentum, p_T, is the momentum that a particle has perpendicular to the beam axis, as measured in the lab-frame. As explained in Section 3.2.1, the beam axis is the z-axis of a Cartesian co-ordinate frame. The transverse momentum is defined as

$$p_T = \sqrt{p_x^2 + p_y^2}. \tag{3.13}$$

Measurements of the Z boson p_T distribution probe both perturbative and non-perturbative QCD, and may be used to place constraints on the gluon PDF [83].

ϕ^*

The ϕ^* variable is defined as

$$\phi^* = \frac{\tan\left(\phi_{acop}/2\right)}{\cosh\left(\Delta\eta/2\right)}, \tag{3.14}$$

with $\phi_{acop} = \pi - |\Delta\phi|$, where $\Delta\phi$ is the azimuthal difference of the two muons and $\Delta\eta$ denotes the difference in pseudorapidities of the muons. The ϕ^* variable is constructed to probe the same physics as the Z boson p_T distribution. Experimentally, ϕ^* can be determined with greater precision than p_T because it depends on measurements of muon angles as opposed to muon momenta [84].

Chapter 4

Measurement of the Z boson cross-section

The LHC operated with colliding proton beams between 2010-2013 at centre-of-mass energies of $\sqrt{s} = 7$ TeV and $\sqrt{s} = 8$ TeV. Collisions at $\sqrt{s} = 13$ TeV commenced in 2015. The measurements in this thesis are performed with 1 fb^{-1} of data recorded at $\sqrt{s} = 7$ TeV during 2011, and 2 fb^{-1} of data recorded at $\sqrt{s} = 8$ TeV during 2012. These data sets are referred to as Sample-I and Sample-II.

4.1 Candidate selection

The Z boson candidates are selected by requiring a pair of well-reconstructed tracks of opposite charge, identified as muons, with a combined invariant mass, $M_{\mu^+\mu^-}$, in the range $60 < M_{\mu^+\mu^-} < 120$ GeV/c^2. Each muon track must have a transverse momentum $p_T > 20$ GeV/c and lie in the pseudorapidity range $2 < \eta < 4.5$. The relative uncertainty on the momentum measurement is required to be less than 10% and the probability χ^2 of the track fit must be larger than 0.1%. These two criteria are known as the track quality criteria. Track quality variables, in both data and simulated samples, are compared in Figure 4.1. Both tracks are required to be identified as muons as per the $isMuon$ criteria, which are detailed in Table 3.1. At least one of the muons is required to trigger the event at all stages of the trigger: L0Muon, Hlt1MuonHighPT and Hlt2SingleMuonHighPT (see Section 3.2.10). In total, 58,466 (136,702) Z boson candidates are selected in Sample-I (Sample-II). Figure 4.2 shows the invariant mass distribution of selected events.

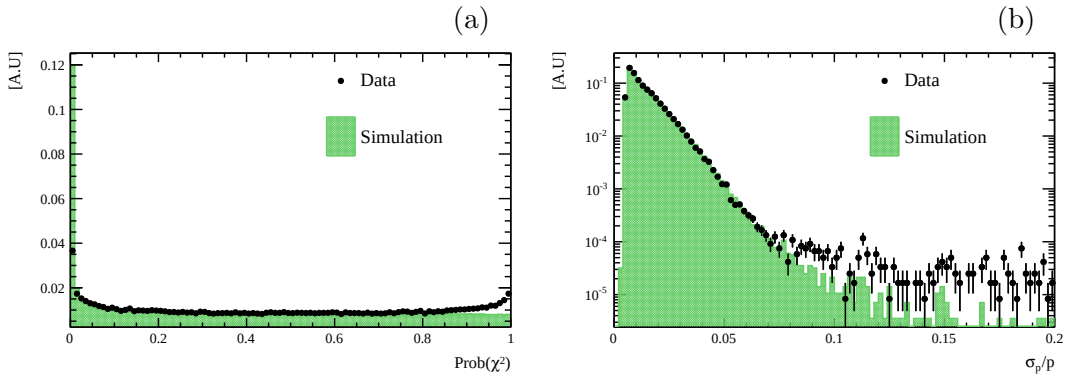

Figure 4.1: The figures show track quality of muons in Z boson candidate SAMPLE-I, where the track quality criteria have been relaxed. Muon-track probability χ^2 is displayed in (a) and the relative uncertainty on muon momenta is displayed in (b).

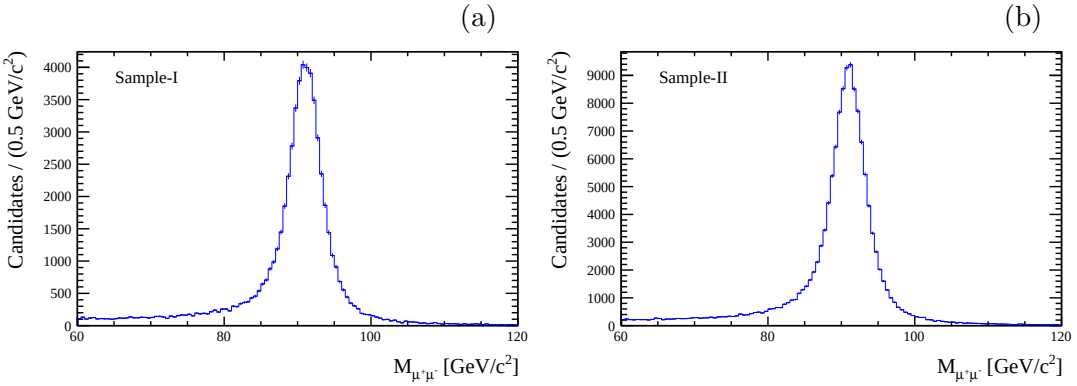

Figure 4.2: Invariant mass of dimuon candidates in (a) SAMPLE-I and (b) SAMPLE-II. SAMPLE-I corresponds to 1 fb^{-1} of data recorded at $\sqrt{s} = 7$ TeV, while SAMPLE-II corresponds to 2 fb^{-1} at $\sqrt{s} = 8$ TeV.

4.2 Beam crossing angles

The p_T distributions of Z boson candidates are shown in Figure 4.3, separately for each magnet polarity of Sample-I and Sample-II. There is some indication that the underlying p_T distributions are different for magnet down and magnet up in Sample-I, whereas a difference is not evident in Sample-II.

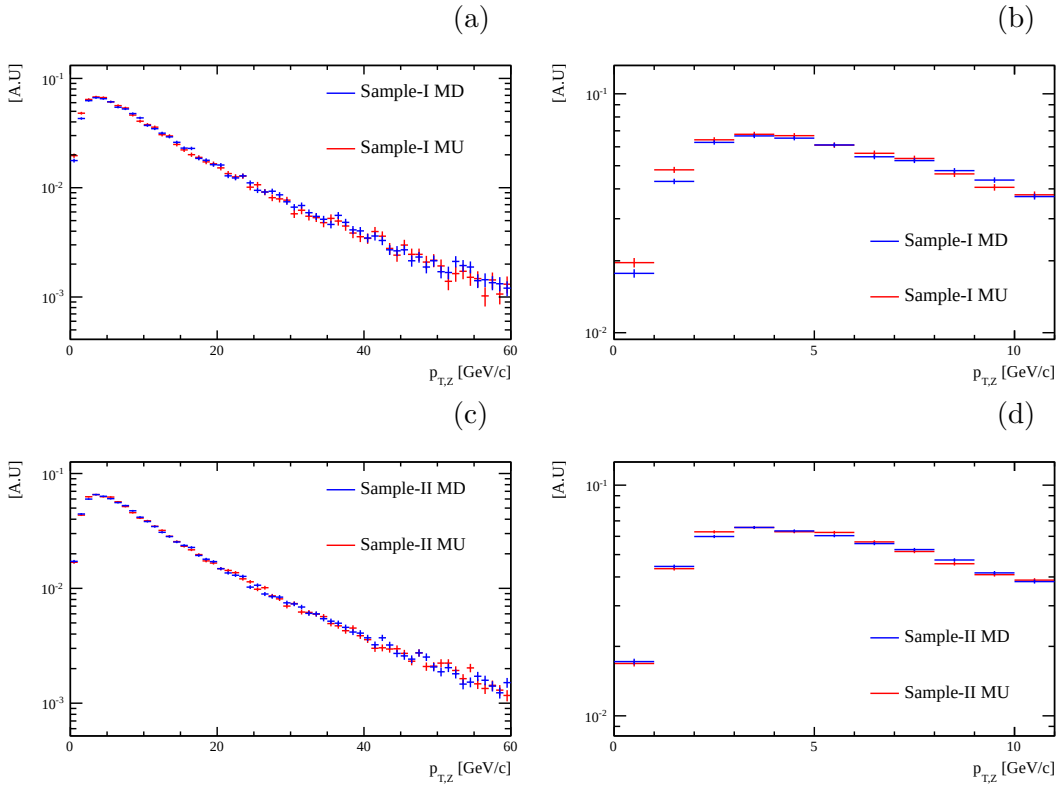

Figure 4.3: Distribution of candidates in Z boson p_T for Sample-I in (a) and (b) and Sample-II in (c) and (d). The same data are plotted in (a) and (b), but the p_T range differs. Similar for (c) and (d). The distributions in magnet polarity sub-samples are similar in Sample-II, but differ in the low p_T region in Sample-I.

One difference between data taking conditions for Sample-I and Sample-II was the effective crossing angle of the proton beams. The effective crossing angle is a combination of the internal and external crossing angles. The external angle (Figure 4.4(a)) is generated by magnetic correctors to prevent multiple bunch crossings within the LHCb beam pipe. The internal angle is generated by three magnets, acting in consort with the LHCb spectrometer dipole magnet, as shown in Figure 4.4(b). These three ensure that the beam orbits do not get warped over successive cycles, which would be the case if the spectrometer dipole magnet acted alone. Further details on the internal and external crossing angles can be found in Refs. [85] and [86].

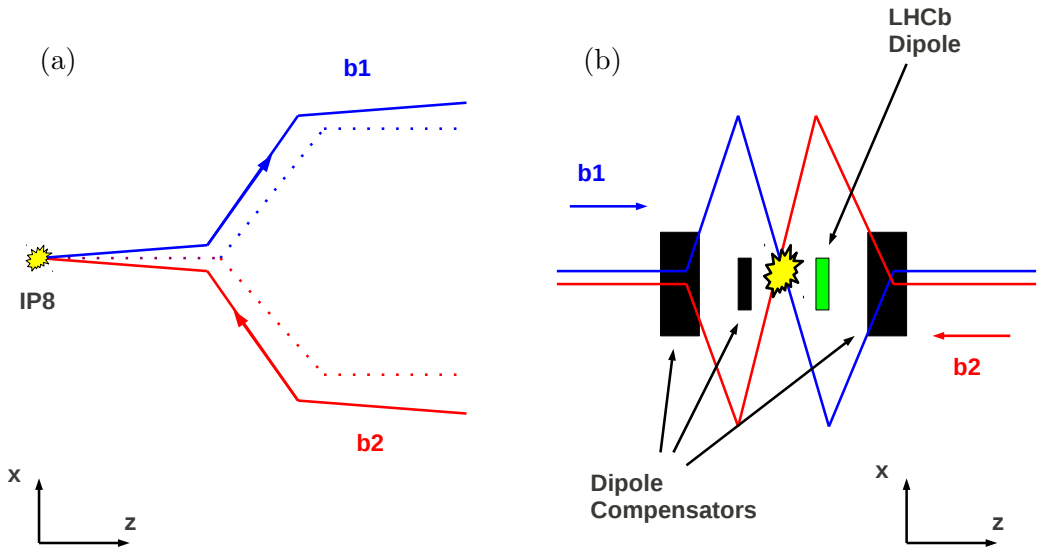

Figure 4.4: The crossing angle of the beams is a combination of (a) external and (b) internal angles. Panel (b) is a close-up view of the interaction point displayed in panel (a). The solid lines show the path of the beams near interaction point 8 (IP8). The dotted lines show the path in the case of zero external angle. Beam one (b1) is blue and travels into the LHCb acceptance, while beam two (b2) is red and travels away from the LHCb acceptance.

For Sample-I, the beams crossed in the horizontal plane, the plane of the LHC ring. The effective crossing angle depended on the magnet polarity due to the different external angles required to avoid parasitic interactions [85]. For Sample-II, the beams crossed in a plane that was tilted with respect to the horizontal. This allowed the absolute value of the effective crossing angle to be the same for both polarities [87].

A study was performed to quantify the effect of beam crossing geometry by generating Z bosons using simulation configured with the relevant beam crossing angles. The configuration of the beams are as in Table 4.1 and Figure 4.5. The resulting Z boson p_T distributions are compared in Figure 4.6.

	Sample-I		Sample-II	
	MD	MU	MD	MU
Crossing plane	Horizontal	Horizontal	Tilted	Tilted
Effective half crossing angle (μRad)	-520	+20	-236	+236

Table 4.1: Beam crossing conditions.

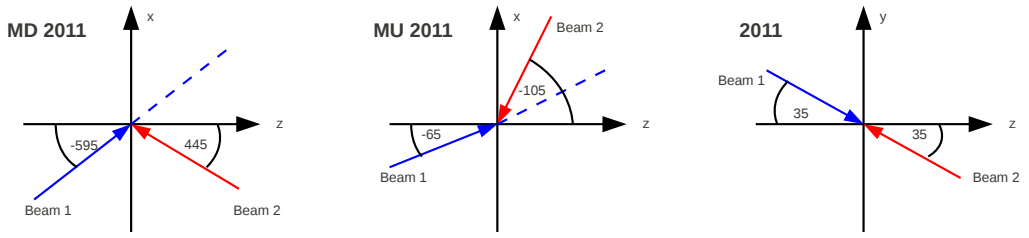

(a) (b) (c)

Figure 4.5: Angles in μRad between the beams and the LHCb z-axis during SAMPLE-I data-taking. The angles are consistent with the half crossing angles of Table 4.1. The crossing angle is defined as the angle between the extension of beam 1 (blue dotted) and beam 2 (red arrow).

In SAMPLE-I, the p_T distributions in MD and MU samples differ at low values. An interpretation of this result is that the larger crossing angle (when the magnet polarity is down) is giving the Z boson a small p_T boost, reducing the number of events in the first bin. Since the goal is to compare measurements with theoretical predictions, where the longitudinal boost vector of the Z boson and the beam axis are colinear, a correction must be applied for this crossing angle effect. The correction used here is to redefine the z-axis as the direction of beam one (b1) and measure p_T with respect to this new axis, z', which is shown in Figure 4.7. This choice is motivated by the fact that b1 must carry the high momentum parton required to produce a Z boson inside the acceptance of LHCb.[1]

The p_T distribution in this new reference frame is shown in Figure 4.8. Comparing Figure 4.6(b) and Figure 4.8(b), the distributions are now consistent irrespective of the polarity. When the same procedure is applied to the data there is a similar improvement, although the rotation of frame does not account for the full difference.

Two final comments must be made. First, the cross-sections are measured in a fiducial volume with requirements on the muon momenta, pseudorapidities and Z mass. Thus the muon momenta and pseudorapidities must be calculated in the primed coordinate frames. These primed quantities are then subjected to the selection cuts of

[1] To give some feeling for the values, and assuming a Z boson is produced inside the LHCb acceptance, a typical quark/anti-quark from beam 1 will have about 25% of its proton's momentum whereas the anti-quark/quark from beam 2 will have 0.05% of its proton's momentum.

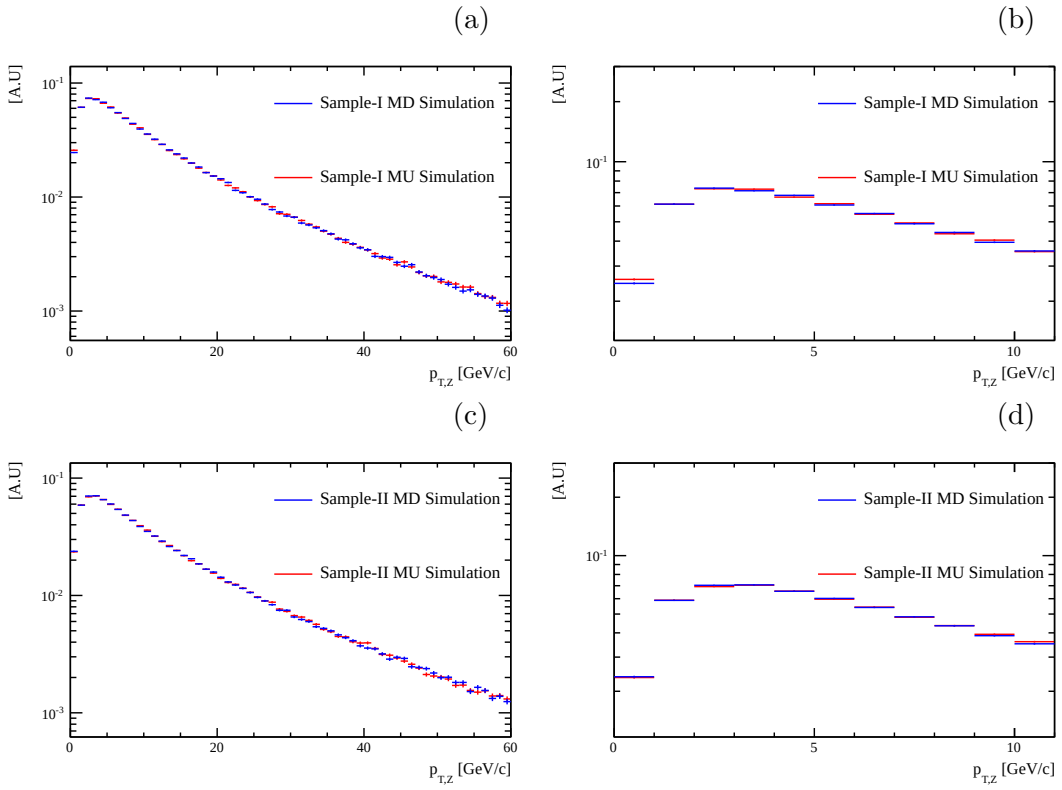

Figure 4.6: Simulated distribution of candidates in Z boson p_T (x-axis) for beam crossing conditions similar to SAMPLE-I in (a) and (b) and SAMPLE-II in (c) and (d). Distributions are normalised to the number of events in each sample. As in data, a discrepancy in the low p_T region for SAMPLE-I conditions is observed (see panel (b)).

Section 4.1. Second, muon reconstruction efficiencies have been calculated in the unprimed co-ordinate frame as a function of pseudorapidity (see Section 4.4.2). These efficiencies are not re-calculated in the primed co-ordinate frames; instead, the unprimed pseudorapidities of each muon are used to correct for muon inefficiencies. This poses a problem for muons that are inside the fiducial volume in the primed frame but not inside the fiducial volume of the unprimed frame (there is no efficiency for them). Since the changes in pseudorapidity are small, and since this is only a problem for a handful of events, these strays are treated as if they came from the neighbouring bin on the edge of the unprimed fiducial volume.

The effect of different beam crossing angles has a negligible impact on the cross-section results. It is therefore not considered in the total systematic uncertainty.

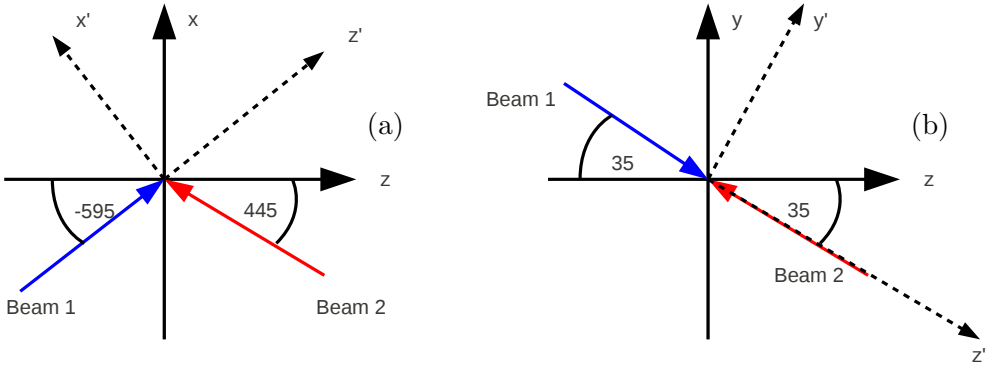

Figure 4.7: Rotated co-ordinate frame (dotted axes, primed labels) in which corrected p_T is measured. The z'-axis follows the direction of beam 1. The values shown are for the MD configuration in the (a) x-z plane and (b) y-z plane. Similar rotations are made for MU.

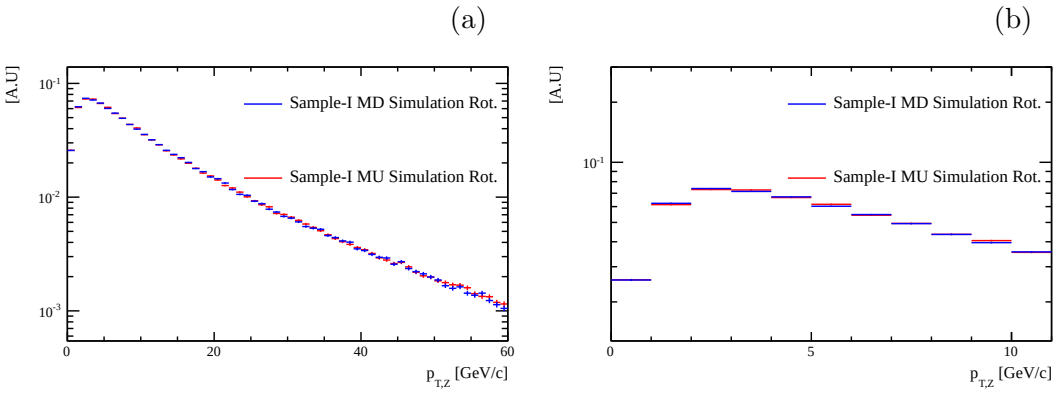

Figure 4.8: Simulated distribution of candidates in Z boson p_T for beam crossing conditions similar to SAMPLE-I in (a) and (b). In this case the reference frame has been rotated and p_T is measured with respect to the direction of b1.

4.3 Purity

The background contribution to the $Z \rightarrow \mu^+\mu^-$ candidate samples is very low. Five different sources are investigated. These include decays of heavy flavour hadrons, hadron misidentification, $Z \rightarrow \tau^+\tau^-$, $t\bar{t}$ and W^+W^-. These are described in Sections 4.3.1, 4.3.2, 4.3.3, 4.3.4 and 4.3.5, respectively. The same procedures are applied to the analyses of SAMPLE-I and SAMPLE-II. For the sake of clarity, only numbers pertaining to the analysis of SAMPLE-I are mentioned in the discussion. The summary in Section 4.3.6 brings both sets of background estimates together.

4.3.1 Heavy flavour

The production of $b\bar{b}$ and $c\bar{c}$ can contribute to the background if the resulting heavy flavour hadrons decay semi-leptonically. This contribution is estimated from data using two independent heavy flavour enriched samples, labelled HF-VTX and HF-ISO below. Both samples are based on the sample described in Section 4.1. In addition to these requirements, the dimuon invariant mass requirement is relaxed to $M_{\mu^+\mu^-} > 40$ GeV/c^2 and special cuts are applied to increase the proportion of heavy flavour decays in the sample.

Muons from signal result in tracks inside the detector whose orientations suggest a common origin vertex. Muon tracks arising from decays of b- and c-hadrons will have a large vertex χ^2/ndf (see Section 3.2.6). These ideas are represented graphically in Figure 4.9. The first sample (HF-VTX) requires a low probability for the two selected

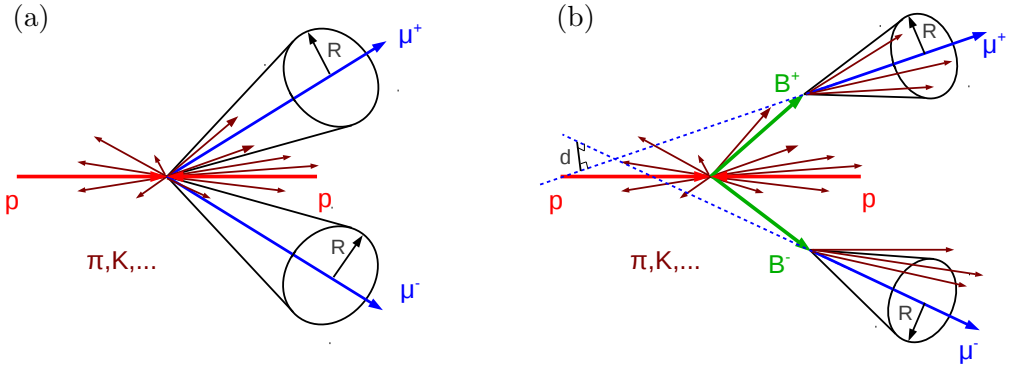

Figure 4.9: Schematic representation of muons arising from (a) $Z \rightarrow \mu^+\mu^-$ decays and (b) decays of B-hadrons. Due to finite resolution on muon momenta, even muon tracks from signal do not lead back to the exact same point. However, this impact parameter (thin black line d in (b)) is much greater for heavy flavour decays. Decays of B-hadrons also have higher momentum tracks within the $\eta - \phi$ cone about the muon.

muons to come from the same vertex (dimuon vertex fit $\chi^2/ndf > 100$), thus enriching the sample in heavy flavour backgrounds.

The second sample (HF-ISO) is composed of events that contain two muons that are poorly isolated, which are characteristic of QCD processes like $b\bar{b}$ and $c\bar{c}$ production. To quantify the degree of isolation of the muon, the variable $p_T^{\mu-\text{cone}}$ is defined. It is the sum of the transverse momenta of tracks inside a cone around the muon, where the cone is defined using the radius parameter $R = \sqrt{\Delta\eta^2 + \Delta\phi^2} = 0.5$. Here, $\Delta\eta$ and $\Delta\phi$ give the separation between the muon track and neighbouring tracks in η and azimuthal angle ϕ. If a track (excluding the muon track) is inside the cone it contributes to the cone momentum. A variable, z, is then constructed. It is defined as

$$z = \frac{p_T^{\mu}}{p_T^{\mu} + p_T^{\mu-cone}}, \tag{4.1}$$

where p_T^{μ} is the transverse momentum of the muon whose isolation is being quantified. Well-isolated muons have z values close to 1 while poorly isolated muons have values closer to 0. Requiring that both of the final state muons have $z < 0.7$ defines the second heavy flavour sample, HF-ISO.

The efficiency of the vertex fit χ^2 requirement on heavy flavour events is determined from data. To do this, one assumes that the HF-ISO sample is 100% heavy flavour. The effect of the vertex χ^2 cut is then checked on this sample and is found to have an efficiency of 34%. In a similar fashion, the efficiency of the muon isolation cut can be determined by assuming the HF-VTX sample is 100% heavy flavour and applying the isolation criteria. The efficiency is determined to be 29%.

The resulting dimuon invariant mass distributions of the two heavy flavour enriched samples are shown in Figure 4.10. Since the heavy flavour background falls off rapidly with dimuon invariant mass, an exponential is fitted to each distribution to determine the background contribution. The portion of the distribution between 60–120 GeV/c^2, denoted by the red hatching, constitutes background to the signal. Integrating the exponential function in the signal regions gives 65.5 events for the HF-VTX sample and 47.9 events for the HF-ISO sample. Applying the efficiencies of the cuts on the heavy flavour samples gives estimated backgrounds of 195 ± 7 and 165 ± 7 for the HF-VTX and HF-ISO samples, respectively. The uncertainty quoted here is due to the uncertainties on the fit parameters.

In order to apply the efficiencies of the cuts on heavy flavour events as above, the isolation of the final state muons and the vertex fit χ^2 of the dimuon candidate must be

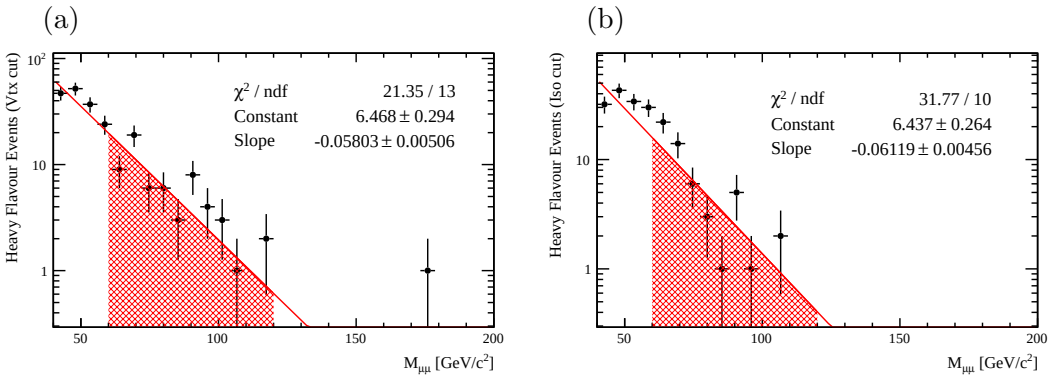

Figure 4.10: Mass distributions of heavy flavour samples (a) with vertex $\chi^2/ndf > 100$ and (b) $z < 0.7$ for both muons. The shaded area under the curve represents the heavy flavour background in this analysis. The muons are required to have transverse momentum greater than 20 GeV/c.

largely uncorrelated for heavy flavour events. This assumption has been verified using simulated $b\bar{b}$ and $c\bar{c}$ events, where the correlation coefficient is determined to be 0.4.

The best estimate for the heavy flavour background and its systematic uncertainty are evaluated using a number of cross-checks, which are now described. There are relatively few candidates in the HF-ISO and HF-VTX samples. The first cross-check aims at increasing the size of the heavy flavour samples. This is done by reducing the muon p_T threshold (all thresholds between 10 and 20 GeV/c^2 in 1 GeV/c^2 steps) to allow more statistics for the mass fit. Most of the additional candidates have invariant masses below 60 GeV/c^2. Figure 4.11 shows the mass distributions of the HF-VTX and HF-ISO samples, where the p_T threshold is at 14 GeV/c^2. The quality of the fit is improved,

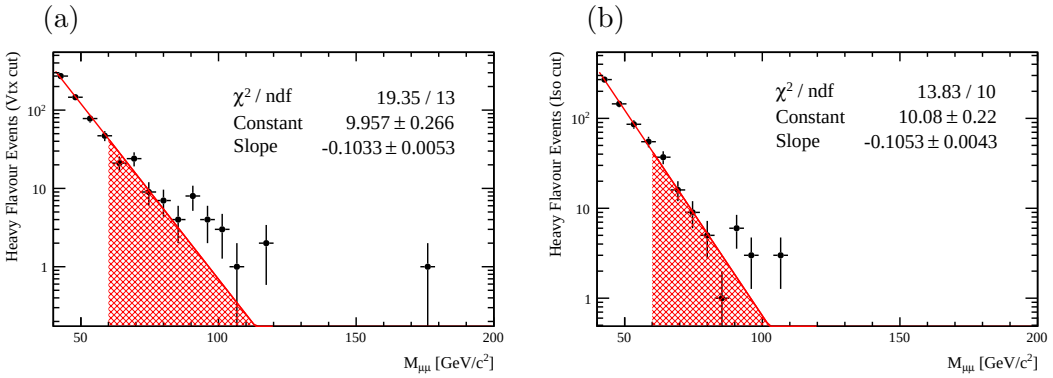

Figure 4.11: Mass distributions of heavy flavour samples (a) with vertex $\chi^2/ndf > 100$ and (b) $z < 0.7$ for both muons. The shaded area under the curve represents the heavy flavour background in this analysis. The muons are required to have transverse momentum greater than 14 GeV/c.

especially in the low mass region. The procedure of evaluating integrals and dividing

by efficiencies is repeated with different muon transverse momentum thresholds. Different background estimates are obtained, which are given in Tables A.3 and A.4 of Appendix A.

The second cross-check assesses the impact of fitting the exponential in different mass ranges. Instead of fitting the full mass range, where the result can be affected by residual signal in the samples, fitting in a restricted range between 40–60 GeV/c^2 is also investigated. The background contamination in this specific mass range is expected to be larger than in the sample considered as a whole. Results of this procedure are detailed in Tables A.5 and A.6 and of Appendix A.

Considering the estimates from the different cross-checks, and their spread, a heavy flavour background of 227 ± 32 events is assigned. More detail on how this number is arrived at is given in Section 4.5, where systematic uncertainties are discussed.

4.3.2 Hadron misidentification

Pions or kaons may be misidentified as muons if they decay in flight before they reach the muon stations or if they have sufficient energy to traverse the calorimeters and be detected in the muon stations. Two cases are distinguished, that where there is one good muon and one misidentified hadron, and that where there are two misidentified hadrons. In both cases di-track samples are formed and weighted by a momentum dependent probability ($\mathcal{P}_{\text{misid}}$) for the tracks to be misidentified as muons. A cross-check of the method is performed using same-sign muon-pair events.

$\mathcal{P}_{\text{misid}}$ is measured using tracks selected from randomly triggered events (see Section 3.2.10). The vast majority of tracks in these events are not muons, so the fraction of these tracks identified as muons is considered an upper limit on $\mathcal{P}_{\text{misid}}$. Shown in Figure 4.12 is the fraction of tracks satisfying the $isMuon$ criteria (see Table 3.1) as a function of logarithm of momentum. Only tracks above 12 GeV/c are considered to avoid steps in the data when crossing the momentum thresholds at 6 and 10 GeV/c. The distribution has been fitted with the following function

$$\mathcal{P}_{misid}(p) = \left(1 - e^{-\frac{p_0}{p}}\right) + (p_1 + p_2 \cdot p) \tag{4.2}$$

The exponential describes decays in flight while the linear component describes punch-through. A discussion on this expected form can be found in Ref. [88].

The first hadron misidentification background to the signal is a high p_T muon accompanied by a misidentified hadron. To quantify this, a muon-hadron sample passing the

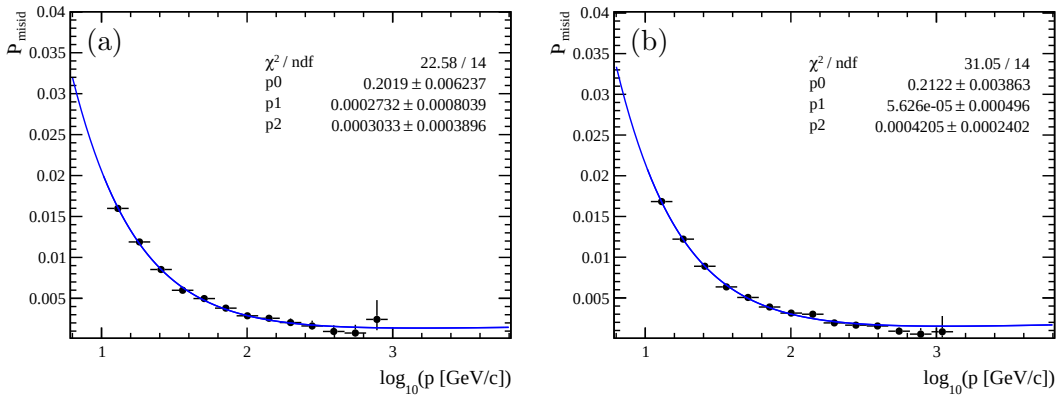

Figure 4.12: The probability for a hadron to be misidentified as a muon in (a) SAMPLE-I and (b) SAMPLE-II.

analysis cuts is made, where it is required that the event would have been triggered in the absence of the hadron. The mass distribution of the muon-hadron candidate is shown in Figure 4.13. This sample contains a small contribution from signal events due to the inefficiency of the muon trigger and identification. An exponential function is used to model the background while a Gaussian models the signal contamination. Note that each candidate has been scaled by the probability for the hadron to be misidentified. The integral under the fitted exponential gives 2.3 ± 0.2 events.

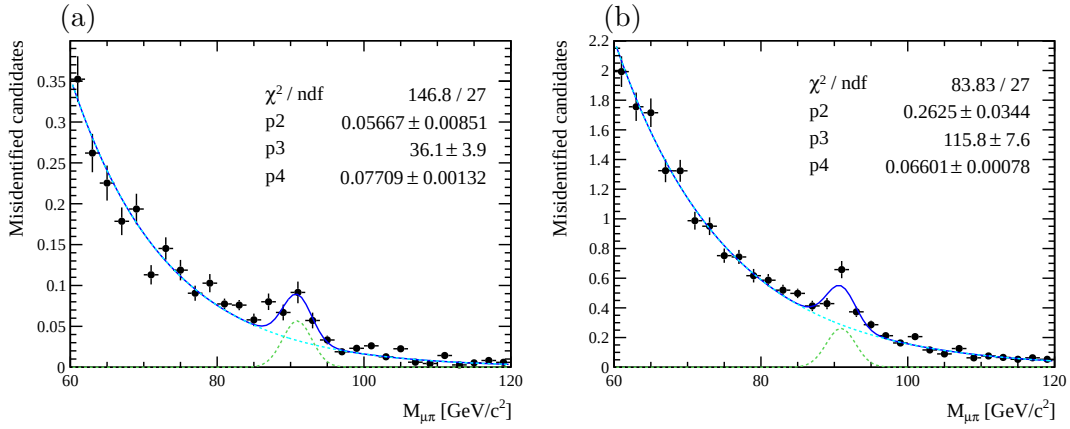

Figure 4.13: Distribution of masses for muon-track combinations in (a) SAMPLE-I and (b) SAMPLE-II. Each candidate has been scaled by the probability of hadron misidentification, as given by Equation 4.2, with parameters as in Figure 4.12.

The second hadron misidentification background process is where both muon candidates are misidentified hadrons. To evaluate this, di-hadron candidates are formed by combining pions and kaons from randomly triggered events and imposing the analysis cuts.

Both legs of the combination have been scaled by $\mathcal{P}_{\text{misid}}$, as specified by Equation 4.2, with parameters from Figure 4.12.

The rate at which unbiased (by the trigger) data is taken is limited throughout the data taking period, so the integrated luminosity of this data does not correspond to the integrated luminosity of the sample used to select Z candidates. The randomly triggered sample thus needs to be normalised to the Z candidate sample.

The rate limit depends on the configuration of the trigger (TCK) and was either 11 or 97 Hz. One can safely assume that this allotted bandwidth is always saturated (i.e. the LHCb event rate is never less than 11 or 97 Hz) so the rate limitation amounts to an effective prescale. At relativistic speeds, proton bunches rotate around the LHC at a frequency f of 11245 Hz. The number of colliding bunches (CB) depends on the run, so the bunch-bunch (bb) collision rate is $f \cdot \text{CB(run)}$. Not all of the randomly triggered rate corresponds to bb crossings, but also be, eb and ee crossings (see Section 3.1.2). The Z candidate sample is uniquely bb crossing-type, so an additional scaling by the bb fraction of the randomly triggered data (typically 70%) is required. Formula 4.3 gives the effective prescale, where the dependency on trigger configuration and run is made explicit.

$$p_{\text{eff}}\,(\text{TCK,run}) = \frac{\text{R}\,(\text{TCK}) \cdot \frac{N_{\text{bb}}}{N_{\text{bb}}+N_{\text{be}}+N_{\text{eb}}+N_{\text{ee}}}}{f \cdot \text{CB}\,(\text{run})} \tag{4.3}$$

Shown in Figure 4.14 is this effective prescale for candidates in the di-hadron sample.

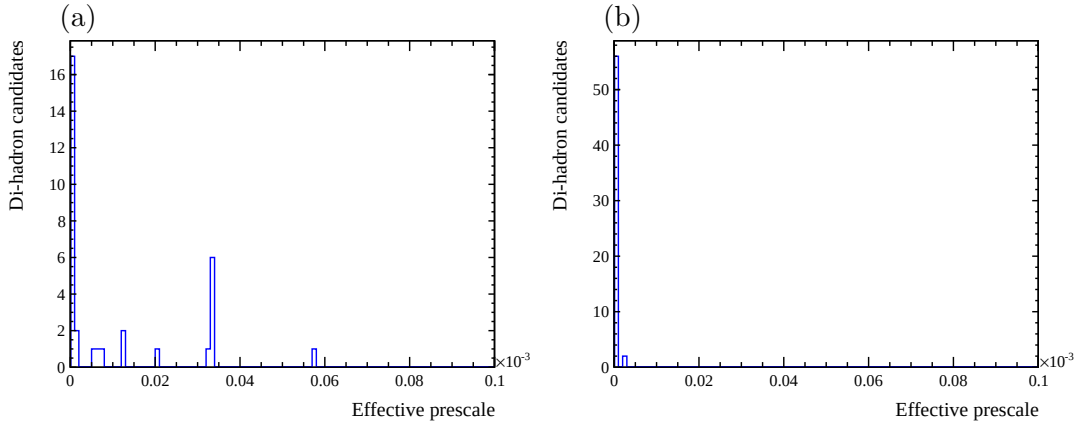

Figure 4.14: The plot shows the effective prescale calculated using Equation 4.3 for events in the di-hadron sample. Plot (a) is for Sample-I and plot (b) is for Sample-II.

Once the candidates in the di-hadron sample have been weighted by misidentification probabilities, and once the luminosity of the sample is corrected with p_{eff} to match that of the Z candidate sample, the contribution from this background is estimated to be

114 ± 31. The uncertainty is driven by the uncertainty on the parameters of $\mathcal{P}_{\text{misid}}$ and the statistics in the di-hadron sample. The mass distribution of these background events is shown in Figure 4.15 as black points.

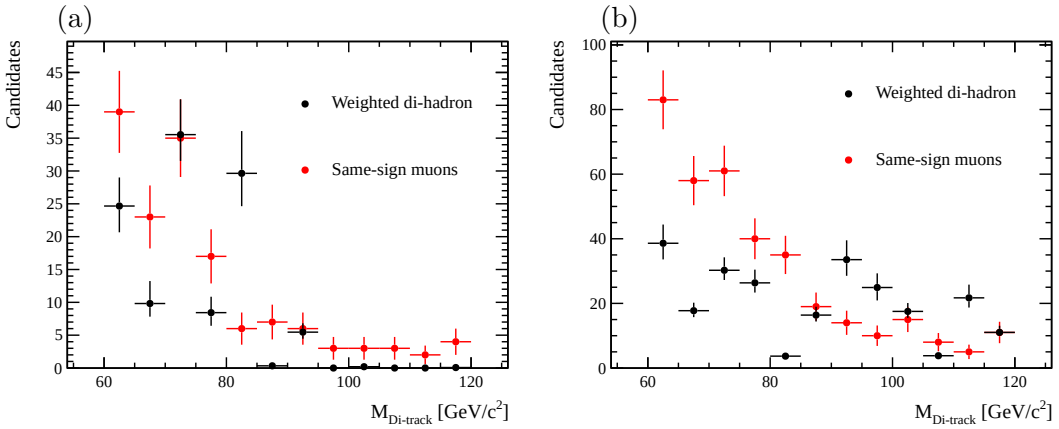

Figure 4.15: Masses of charged track combinations in (a) SAMPLE-I and (b) SAMPLE-II. In the case of the black points, the tracks are hadrons from randomly triggered data that have been weighted by a hadron misidentification probability and an effective prescale to normalise the sample to the Z candidate sample. The red points indicate the masses of dimuon candidates with muons of the same electric charge.

Muon misidentification is due to hadrons that have either decayed-in-flight or have punched through the calorimeters. The probabilities for these to happen depend on momentum, so it should not matter whether the two muons have the same charge or opposite charge. Thus, an alternative evaluation of the misidentification background can be found from pairs of same-sign muons. This has been checked explicitly on randomly triggered data, where there are 1313 events that have two high-p_T tracks. In 680 of these events, the tracks have the same sign, while in 633 of these events, the tracks have opposite sign. Using the same-sign dimuon sample, 148 events with both muons having the same charge are found by the Z selection. The red points in Figure 4.15 show the masses of these same-sign dimuons. This background estimate also includes a possible contribution from W (or Z if one of the muons is outside of the acceptance) production together with a misidentified muon.

In conclusion, the contribution to the background due to hadron misidentification is estimated to be $(114 \pm 31) + (2.3 \pm 0.2) = 116 \pm 31$ events, the sum of μ-hadron and hadron-hadron backgrounds. The uncertainty here is the statistical uncertainty due to the number of di-hadron events and the uncertainty on the parameters in $\mathcal{P}_{\text{misid}}$. The number of events in the same-sign sample (148) is used to set an additional systematic uncertainty, which is discussed in Section 4.5.

4.3.3 $Z \to \tau^+\tau^-$

Remaining backgrounds are determined using a combination of simulation and previous measurements. The LHCb simulation generates events with decay products inside the detector volume, subject to additional kinematic constraints. The restrictions on the decay products are known as the generator cuts, and their efficiency is known as the generator cut efficiency, ε_{cut}. To obtain background estimates, one imposes the $Z \to \mu^+\mu^-$ selection on the simulated sample, divides the number of these events by ε_{cut} to obtain the number of events that would have been produced without the cuts, and then uses the total cross-section (or 4π cross-section) to calculate an effective luminosity, $\mathcal{L}_{eff}$. The ratio of $\mathcal{L}_{eff}$ and the luminosity of the sample used to measure the Z boson cross-section is used to scale the number of events in the simulated sample passing the $Z \to \mu^+\mu^-$ selection to give the background estimate.

Decays from $Z \to \tau^+\tau^-$ can be background to the signal if both taus decay leptonically to muons and neutrinos. The tau background is estimated from PYTHIA simulation that has been normalised to a weighted average of ATLAS and CMS cross-sections [89, 90]. First, the number of $Z \to \tau^+\tau^-$ decays in the sample is divided by ε_{cut}. Then, using the measured cross-section to evaluate $\mathcal{L}_{eff}$, the events passing the $Z \to \mu^+\mu^-$ selection criteria are normalised to 1 fb^{-1}. The relevant numbers are given in column four of Table 4.2. The estimate is $59 \pm 4 \pm 4$ events for SAMPLE-I. The first uncertainty here is due to the statistics in the simulation sample and the second is due to the uncertainty on the measured cross-section.

4.3.4 $t\bar{t}$

Decays of top quark pairs may contribute if both top quarks decay semi-leptonically. At NLO the 4π $t\bar{t}$ cross-section is about 160 pb [91] and at $\sqrt{s} = 7$ TeV this can be thought of as a mix of the gg and qq production mechanisms in the ratio 4:1. Using PYTHIA8 simulation as well as the measured cross-sections [92, 93] in Table 4.2, a contribution of $4.5 \pm 0.1 \pm 0.2$ events is expected.

4.3.5 W^+W^-

Production of W pairs contributes to the sample if both W bosons decay to a muon and a neutrino. At NLO the 4π W^+W^- cross-section is about 45 pb [94], which is slightly smaller than the measured values of about 53 pb [95, 96]. This contribution has been estimated with the use of PYTHIA8 simulation and measured cross-sections, as above.

	$t\bar{t}(gg)$	$t\bar{t}(qq)$	$Z \to \tau^+\tau^-$	W^+W^-
	SAMPLE-I			
Events	2008493	1609793	1045497	104499
ϵ_{cut}	0.049	0.068	0.36	0.29x0.1057x0.1057
σ_{ATLAS} [pb]	140.8 ± 13.6	35.2 ± 3.4	970 ± 97	54.4 ± 5.9
σ_{CMS} [pb]	129.6 ± 5.6	32.4 ± 1.4	1000 ± 102	52.4 ± 5.1
σ_{GPDs} [pb]	131.2 ± 4.8	32.8 ± 1.2	984 ± 70	53.3 ± 3.9
$\mathcal{L}_{eff.}$ [fb^{-1}]	312.4	721.8	2.951	605.1
$Z \to \mu^+\mu^-$ selection	679	1689	174	1191
Background estimate	2.2	2.3	59	2
	SAMPLE-II			
Events	1017496	1007498	4046990	1037552
ϵ_{cut}	0.049	0.067	0.37	0.30x0.1057x0.1057
σ_{ATLAS} [pb]	195.5 ± 39.1	34.5 ± 6.9	1136 ± 22.7	70 ± 7
σ_{CMS} [pb]	195.5 ± 39.1	34.5 ± 6.9	1136 ± 22.7	70 ± 7
σ_{GPDs} [pb]	195.5 ± 39.1	34.5 ± 6.9	1136 ± 22.7	70 ± 7
$\mathcal{L}_{eff.}$ [fb^{-1}]	106.2	435.9	9.65	49.4
$Z \to \mu^+\mu^-$ selection	448	1170	709	9152
Background estimate	8.4	5.4	147	3.7

Table 4.2: Summary of background estimation using simulation and measured cross-sections. The branching fractions of W boson decays to muons are included with the generator cut efficiency for the W^+W^- simulation.

Background	Estimation	SAMPLE-I	SAMPLE-II
Heavy flavour ($b\bar{b}$,$c\bar{c}$)	Data-driven	227 ± 32	490 ± 72
Hadron misidentification	Data-driven	116 ± 45	262 ± 110
$Z \to \tau^+\tau^-$	PYTHIA8+σ_{GPDs}	59 ± 6	147 ± 7
$t\bar{t}$	PYTHIA8+σ_{GPDs}	4.5 ± 0.2	14 ± 2
W^+W^-	PYTHIA8+σ_{GPDs}	2.0 ± 0.2	3.7 ± 0.4
Total		409 ± 56	916 ± 132
Purity		0.993 ± 0.002	0.993 ± 0.002

Table 4.3: Background composition of the candidate samples.

Since the W boson is forced to decay to muons in this sample, a correction is required to account for the branching fraction, which is 10.57% [3]. This is included with ϵ_{cut} in Table 4.2. The background amounts to $2.0 \pm 0.2 \pm 0.1$ events.

4.3.6 Total

The background composition of the candidate sample is summarised in Table 4.3. The total background contribution in the Z sample in the range 60–120 GeV/c^2 amounts to 409 ± 56 events. The purity is defined as the ratio of signal to candidate events and is

given by $\rho = 0.993 \pm 0.002$. For this analysis the purity is assumed not to vary with y, p_T and ϕ^* of the Z boson, nor the η of the muons. The assignment of an appropriate systematic uncertainty due to this assumption is discussed in Section 4.5.5.

4.4 Cross-section

4.4.1 Cross-section definition

Cross-sections are quoted in the kinematic range defined by the measurement and are corrected for quantum electrodynamic (QED) final-state radiation (FSR) in order to provide a consistent comparison with NLO and NNLO QCD predictions. No corrections are applied for initial-state radiation, electroweak effects, nor their interplay with QED effects. The cross-sections are measured as functions of rapidity (y), transverse momentum (p_T) and ϕ^* of the Z boson, which have been defined in Section 3.3.

The cross-section in a given bin i of η^μ, y, p_T and ϕ^* of the Z boson, with both final-state muons inside the fiducial region, is measured as

$$\sigma_{Z\to\mu^+\mu^-}(i) = \frac{\rho}{\mathcal{L}} \frac{f_{\mathrm{FSR}}(i)}{\varepsilon_{\mathrm{GEC}}(i)} \sum_j U_{ij} \left(\sum_k \frac{1}{\varepsilon(\eta_k^{\mu^+}, \eta_k^{\mu^-})} \right)_j . \tag{4.4}$$

The indices i and j run over the bins of the variable under study. The index k runs over the candidates contributing to bin j. The total muon reconstruction efficiency for an event is given by $\varepsilon(\eta_k^{\mu^+}, \eta_k^{\mu^-})$, which is dependent on the pseudorapidity of the two muons, and is described in Section 4.4.2. The matrix U corrects the data for bin migrations due to detector resolution effects. It is determined using an unfolding procedure, which is described in Section 4.4.6. The efficiency of the requirement on the number of SPD hits in the hardware trigger is denoted by $\varepsilon_{\mathrm{GEC}}$. The correction factors for QED final-state radiation are denoted by $f_{\mathrm{FSR}}(i)$ and are determined for each bin, as described in Section 4.4.5. The integrated luminosity is denoted by $\mathcal{L}$. Though not entering the expression for the cross-section, an uncertainty due to the beam energy is assigned to all cross-sections. More detail on these individual components is given below. Once the binned cross-sections are determined, they are summed to give the total cross-section

$$\sigma_{Z\to\mu^+\mu^-} = \sum_i \sigma_{Z\to\mu^+\mu^-}(i). \tag{4.5}$$

Tag	Probe		
	Trigger	ID	Tracking
Long track	Long track	Long track	MuonTT track
$isMuon$	$isMuon$	-	-
TOS	-	-	-
$\mathrm{P}(\chi^2) > 0.1\%$	$\mathrm{P}(\chi^2) > 0.1\%$	$\mathrm{P}(\chi^2) > 0.1\%$	-
$\sigma_\mathrm{P}/\mathrm{P} < 0.1$	$\sigma_\mathrm{P}/\mathrm{P} < 0.1$	$\sigma_\mathrm{P}/\mathrm{P} < 0.1$	-
$p_T > 20$ GeV/c	$p_T > 20$ GeV/c	$p_T > 20$ GeV/c	$p_T > 20$ GeV/c
$2 < \eta < 4.5$	$2 < \eta < 4.5$	$2 < \eta < 4.5$	$2 < \eta < 4.5$

Table 4.4: Summary of requirements on tag and probe tracks defining samples for muon reconstruction efficiency studies.

The most precise estimate of the total cross-section is obtained by summing the differential cross-sections determined as a function of rapidity, where uncertainties due to data unfolding are negligible.

4.4.2 Muon reconstruction efficiencies

In this analysis, the presence of a Z boson is inferred from the existence of two high-p_T muons in the final-state. When such a muon enters the LHCb acceptance, there is a possibility that the detector fails to associate the combination of hits in the various sub-detectors with the presence of a high momentum muon. Firstly, the tracking software has some inefficiency. Secondly, even when a track has been reconstructed, it may not be identified as a muon due to inefficiencies in the particle identification. Thirdly, the trigger system that has about 1 μs to partially reconstruct and identify a muon, is also less than 100% efficient. In order to make comparisons with theoretical predictions, the data must be corrected for these inefficiencies. The corrections can be determined using simulation, which has the advantages of quasi-infinite statistics and no background. However, simulation may not model crucial effects like detector occupancy, which typically reduce efficiencies. For this reason, the muon reconstruction efficiencies are determined using the data itself, by implementing the tag-and-probe method on the Z resonance. The tag-and-probe samples used here have $\mathcal{O}(10^4)$ events, so uncertainties are at the per mille level.

The tag-and-probe method requires a pure sample of Z bosons. The final-state decay products are labelled, one as the tag, the other as the probe. The requirements on the tags and probes of this analysis are summarised in Table 4.4. The tag must be identified as a muon and be consistent with triggering the event, while the probe is defined so that it is unbiased by the requirement for which the efficiency is being measured. By checking

if the probe satisfies a tracking, identification or trigger requirement, the efficiency of the probe may be determined. It is the number of events in the sample where the probe satisfies this requirement, divided by the total number of events in the sample. In this analysis, the efficiency is studied as a function of several variables, which describe both the muon kinematics and the detector occupancy of the event.

Trigger efficiency

The candidate samples of Section 4.1 are examples of tag-and-probe samples that may be used to measure the trigger efficiency. The efficiency is given by the fraction of events that have two muons that fire the trigger. The efficiencies as functions of probe muons and anti-muons are shown in Figure 4.16 for the sub-samples of the data where the magnet polarity is down. The efficiencies vary between 71.6% and 82.0% with uncertainties

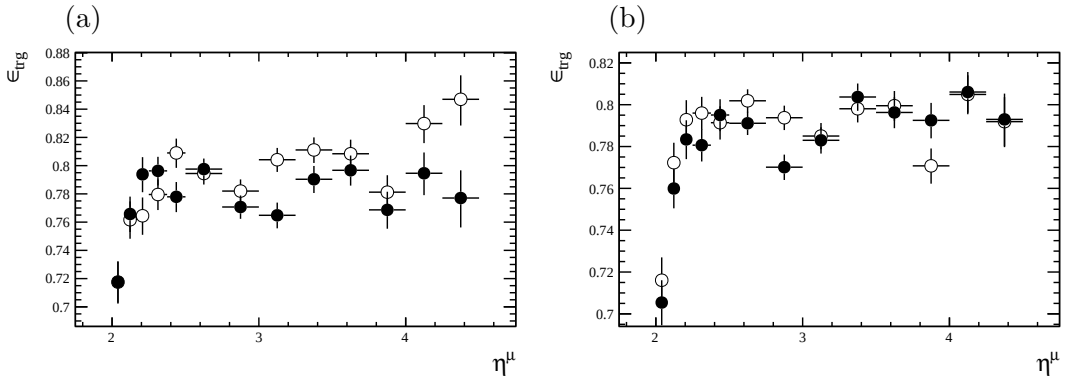

Figure 4.16: Muon trigger efficiencies as functions of η in (a) SAMPLE-I and (b) SAMPLE-II with the LHCb magnet in the down configuration. Filled markers represent muons and open markers represent anti-muons.

between 0.5% and 1.2%. These values are given in Table 4.5. The uncertainties ($\delta\epsilon_{trg}$) are statistical in nature, and therefore uncorrelated between bins. Since the purity of the sample is so high, no additional uncertainty is considered. Only one muon candidate is required for the event to pass the trigger requirements so the overall trigger efficiency is about 95%.

Identification efficiency

To determine the muon identification efficiency, tag-and-probe samples are constructed with fully reconstructed tag tracks that are identified as muons, and probes that are long tracks. The invariant mass of the tag-and-probe combination is required to be between

η	ϵ_{trg}	$\delta\epsilon_{trg}$
2.000-2.080	0.716	0.008
2.080-2.165	0.760	0.007
2.165-2.250	0.781	0.007
2.250-2.375	0.783	0.006
2.375-2.500	0.788	0.006
2.500-2.750	0.794	0.004
2.750-3.000	0.779	0.004
3.000-3.250	0.777	0.005
3.250-3.500	0.801	0.005
3.500-3.750	0.795	0.006
3.750-4.000	0.773	0.007
4.000-4.250	0.820	0.007
4.250-4.500	0.812	0.010

Table 4.5: Single muon trigger efficiencies and their total uncertainties as a function of pseudorapidity. These numbers correspond to SAMPLE-I. The corresponding efficiencies for SAMPLE-II can be found in Appendix B.

60–120 GeV/c^2. To reduce background, an additional cut is placed on the azimuthal separation of the muons $|\Delta\phi|$, which must be greater than 2.7 radians. The efficiencies as functions of probe muons and anti-muons are shown in Figure 4.17 for the sub-samples of the data where the magnet polarity is up. The efficiencies vary between 91.3% and

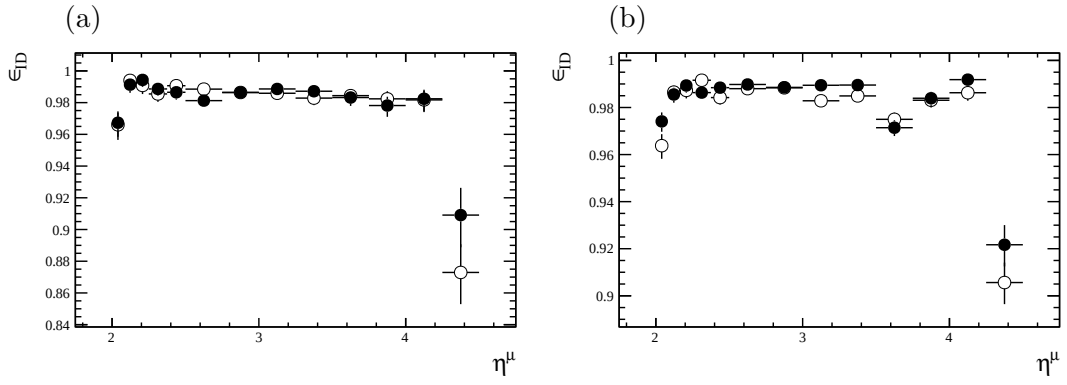

Figure 4.17: Muon identification efficiencies as functions of η in (a) SAMPLE-I and (b) SAMPLE-II with the LHCb magnet in the up configuration. Filled markers represent muons and open markers represent anti-muons.

99.2% with uncertainties between 0.1% and 0.9%. These values are given in Table 4.6. The first component of the total uncertainty ($\delta\epsilon_{ID}^{TP}$) is statistical in nature, and therefore uncorrelated between bins. A second uncertainty ($\delta\epsilon_{ID}^{sys.}$) of 0.1% accounts for additional backgrounds in the tag-and-probe sample. This uncertainty is correlated across muon η bins.

η	ϵ_{ID}	$\delta\epsilon_{ID}^{TP}$	$\delta\epsilon_{ID}^{sys.}$	$\delta\epsilon_{ID}$
2.000-2.080	0.966	0.004	0.001	0.004
2.080-2.165	0.989	0.002	0.001	0.002
2.165-2.250	0.992	0.002	0.001	0.002
2.250-2.375	0.988	0.002	0.001	0.002
2.375-2.500	0.986	0.002	0.001	0.002
2.500-2.750	0.986	0.001	0.001	0.001
2.750-3.000	0.987	0.001	0.001	0.001
3.000-3.250	0.987	0.002	0.001	0.002
3.250-3.500	0.987	0.002	0.001	0.002
3.500-3.750	0.986	0.002	0.001	0.002
3.750-4.000	0.983	0.003	0.001	0.003
4.000-4.250	0.981	0.003	0.001	0.003
4.250-4.500	0.913	0.008	0.001	0.008

Table 4.6: Single muon identification efficiencies and their total uncertainties as a function of pseudorapidity. The corresponding efficiencies for SAMPLE-II can be found in Appendix B.

Tracking efficiency

To determine the muon tracking efficiency, a fully reconstructed muon is used as the tag and a MuonTT track is used as the probe. MuonTT tracks are reconstructed using hits in the Muon and TT sub-detectors. These can be used as probes because the efficiency to reconstruct a long track is not expected to depend on hits in these particular sub-detectors [74]. The probe requirements are summarised in Table 4.4. A tighter mass window of 70–110 GeV/c^2 is imposed to reduce background in the sample. The efficiency is determined by examining all long tracks of the event (excluding the tag). The probe is deemed efficient if one of these long tracks satisfies the following criteria.

- At least 40% of the Muon hits are common between the long track and MuonTT track.
- At least 60% of the TT hits are common between the long track and MuonTT track, if the long track has TT hits.
- The tag and long track 4-vectors combine to give an invariant mass greater than 40 GeV/c^2.

The lower limit of 40 GeV/c^2 on the invariant mass of the tag and long tracks is required to prevent the MuonTT track being matched to soft long tracks from the underlying event.

Two corrections are made to the tracking efficiency as determined using the tag-and-probe method, ϵ_{trk}^{TP}. These are described here, and in more detail in Ref. [97]. The first correction accounts for the bias of the MuonTT track method to determine the efficiency, C^{bias}. This is determined using simulation by comparing efficiencies to reconstruct long tracks in cases where (a) the muon has an associated MuonTT track and (b) the muon does not have an associated MuonTT track. On average, C_{bias} is about 99%. The second correction is for the inefficiency of the matching procedure ε^{match}. This is obtained by switching the roles of the MuonTT track and the long track in the tag-and-probe procedure described above. The average value of ε^{match} is greater than 99%. The tracking efficiency is then

$$\epsilon_{trk} = \frac{\epsilon_{trk}^{TP} \cdot C^{bias}}{\epsilon^{match}}. \tag{4.6}$$

The tracking efficiencies as functions of probe muons and anti-muons are shown in Figure 4.18 for the sub-samples of the data where the magnet polarity is down. The

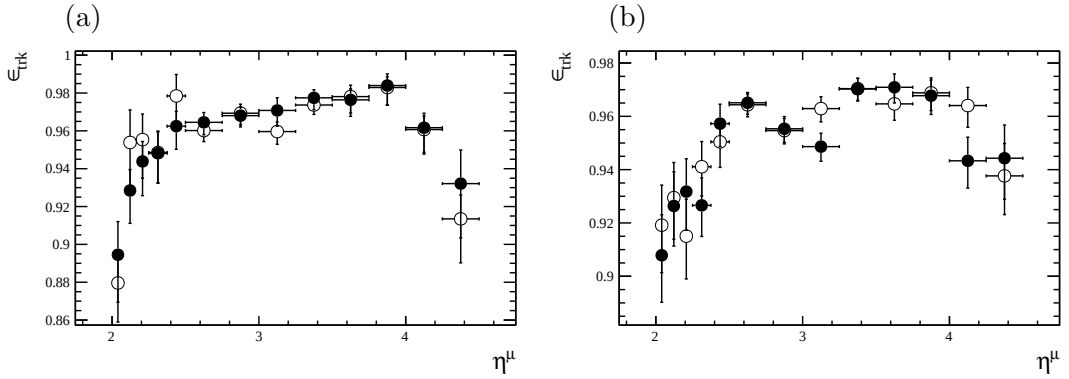

Figure 4.18: Muon tracking efficiencies as functions of η in (a) SAMPLE-I and (b) SAMPLE-II with the LHCb magnet in the down configuration. Filled markers represent muons and open markers represent anti-muons.

efficiency varies between 89.5% and 98.5% with uncertainties between 0.4% and 1.9%. These vales are given in Table 4.7. The first component of the uncertainty ($\delta\epsilon_{trk}^{TP}$) is due to the size of the tag-and-probe sample. The other uncertainties are due to the efficiency of the track matching procedure ($\delta\epsilon_{trk}^{TM}$) and the inherent bias of the MuonTT track method $\delta\epsilon_{trk}^{Bias1}$ and $\delta\epsilon_{trk}^{Bias2}$. The uncertainty $\delta\epsilon_{trk}^{Bias2}$ is correlated between muon η bins. The others are uncorrelated in this regard.

Total efficiency

The efficiency to reconstruct an event is the product of the tracking and identification efficiencies for each muon combined with the efficiency for at least one of the muons

η	ϵ_{trk}	$\delta\epsilon_{trk}^{TP}$	$\delta\epsilon_{trk}^{TM}$	$\delta\epsilon_{trk}^{Bias1}$	$\delta\epsilon_{trk}^{Bias2}$	$\delta\epsilon_{trk}$
2.000-2.080	0.895	0.011	0.007	0.003	0.010	0.017
2.080-2.165	0.939	0.010	0.007	0.002	0.001	0.012
2.165-2.250	0.948	0.010	0.006	0.002	0.001	0.011
2.250-2.375	0.955	0.008	0.006	0.001	0.001	0.010
2.375-2.500	0.970	0.006	0.005	0.001	0.001	0.008
2.500-2.750	0.961	0.004	0.002	0.001	0.001	0.004
2.750-3.000	0.970	0.004	0.002	0.001	0.001	0.004
3.000-3.250	0.964	0.004	0.002	0.001	0.002	0.005
3.250-3.500	0.975	0.003	0.002	0.001	0.001	0.004
3.500-3.750	0.975	0.004	0.003	0.001	0.001	0.005
3.750-4.000	0.985	0.004	0.003	0.002	0.001	0.006
4.000-4.250	0.960	0.006	0.003	0.002	0.002	0.007
4.250-4.500	0.919	0.013	0.006	0.002	0.003	0.015

Table 4.7: Single muon tracking efficiencies and their total uncertainties as a function of pseudorapidity. The corresponding efficiencies for SAMPLE-II can be found in Appendix B.

to fire the trigger. It is determined on an event-by-event basis as a function of muon pseudorapidity.

$$\epsilon = \epsilon_{trk}^{\mu^+} \cdot \epsilon_{trk}^{\mu^-} \cdot \epsilon_{id}^{\mu^+} \cdot \epsilon_{id}^{\mu^-} \cdot \left(\epsilon_{trg}^{\mu^+} + \epsilon_{trg}^{\mu^-} - \epsilon_{trg}^{\mu^+} \cdot \epsilon_{trg}^{\mu^-}\right) \tag{4.7}$$

Equation 4.7 shows how the efficiency ϵ is factorised. ϵ_{trk}, ϵ_{id} and ϵ_{trg} denote tracking, identification and trigger efficiencies respectively. The validity of the factorised form in Equation 4.7 is tested using MC2011 simulation, where the true distributions of variables in $Z \to \mu^+\mu^-$ events are compared to the reconstructed distributions after the efficiency correction. Agreement is achieved at the level of 0.4%. This uncertainty is largely due to the available statistics, and since these uncertainties are also included in the data-driven determinations of the efficiency, this number is not included as an additional systematic uncertainty.

Effects that correlate the inefficiency of the two muons arising from Z boson decay can bias the tag-and-probe efficiency toward higher values. Examples of such effects are the existence of inefficient regions in the detector that are back-to-back in ϕ, or a dependence of the efficiency on detector occupancy. The MC closure test explained above suggests that such effects bias the result below the level of 5 per mille, but this is only true if these effects are accurately modelled by the simulation. The simulation models the inefficient regions back-to-back in ϕ, but it does not model the detector occupancy well.

To estimate the size of the bias, an iterative tag-and-probe technique is employed. In the first iteration the tag-and-probe method is used to measure the efficiency as a function

of η and occupancy. In the second iteration, events in the tag-and-probe sample are reweighted by the efficiency as a function of occupancy from the first iteration. This yields a new set of efficiencies as a function of η. The reweighting recovers the events where neither leg of the Z decay is reconstructed, which contribute to the true efficiency. The corrections to the original efficiencies are $\sim$0.02% and are considered negligible for this analysis.

4.4.3 Global event cut efficiency

In order to prevent large events from dominating the processing time, global event cuts (GEC) are applied in the trigger to reject events with large particle multiplicities. The main effect comes from the requirement that, for the L0Muon trigger, events with more than 600 hits in the scintillating pad detector (SPD) are rejected. The efficiency of the GEC is evaluated from data using two independent methods. The first determines the efficiency by superimposing the event multiplicities of randomly triggered, single PV (primary interaction vertex), events on those of single PV events containing a Z boson. The second fits the SPD distribution directly. These methods are explained in more detail below. The efficiency calculated with both methods agree and $(94.0 \pm 0.2)\%$ is the value used in the analysis of Sample-I data. A value of $(93.0 \pm 0.3)\%$ is measured for Sample-II data.

The evaluation of the efficiency is facilitated with the use of a Z candidate sample, which is identical to the sample described in Section 4.1 except for the trigger definition. The triggers used in this sample have the SPD hit threshold set to 900 (see Section 3.2.10). The shapes of the SPD distributions for both sets of Z candidate samples are identical up to 600 hits, as can be seen in Figure 4.19. This fact is used to help determine the efficiency.

Determination of GEC efficiency by superimposing pileup events

The first method simulates higher pileup (thus higher multiplicity) events by adding the multiplicities of randomly triggered events with one PV to the multiplicities of Z events with one PV. The PV multiplicity distribution of Z candidates in data is shown in Figure 4.20. The method relies on the SPD multiplicities in data, both single PV Z candidate events and single PV randomly triggered events, being unaffected by the 900 SPD hit threshold. The relevant distributions are shown in Figures 4.21, 4.22. One can see that the assumption that there are no events with more than 900 SPD hits is a good one. This is discussed further in Section 4.5

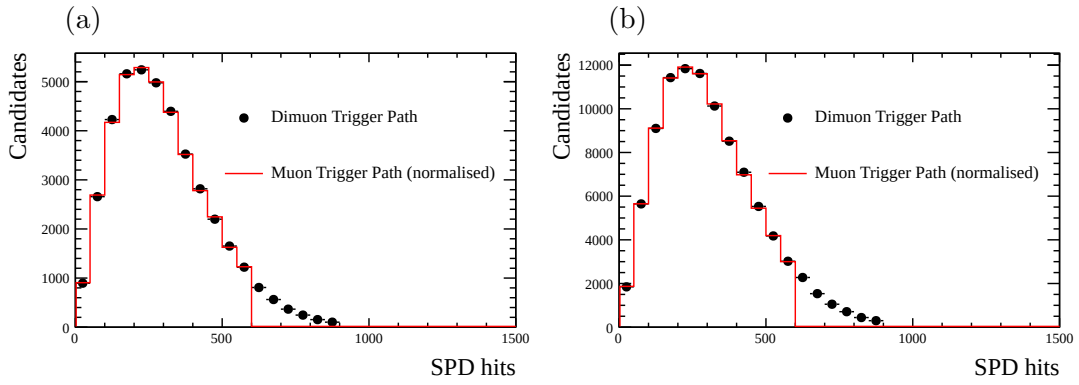

Figure 4.19: The SPD hit multiplicity for events containing a Z candidate in (a) SAMPLE-I and (b) SAMPLE-II. The black points correspond to candidates that satisfy the dimuon triggers. The red histogram shows the shape of candidate events satisfying single muon triggers.

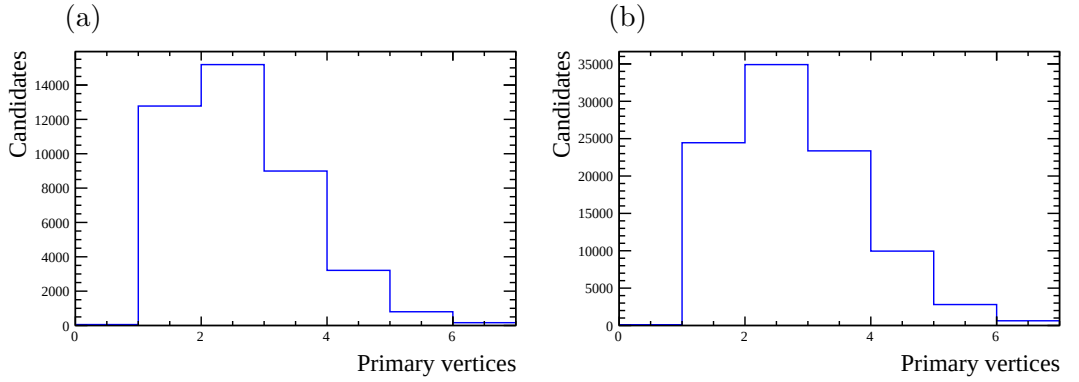

Figure 4.20: The primary vertex multiplicity in data for (a) SAMPLE-I and (b) SAMPLE-II. Each event considered satisfies the dimuon triggers and contains a Z candidate.

Naively adding the multiplicities can result in an over-counting. There are three main causes of this.

- The same cell could be counted by the randomly triggered event and the Z candidate event. This results in an over-counting because a real event with two charged particles in the vicinity of the same cell would still be counted as one SPD hit.
- There is noise in the the SPD sub-detector. Noise exists in both the randomly triggered event and the Z candidate event, and would be double counted unless accounted for.
- There may be hits from previous bunch crossings (spillover). If the events selected to construct the multiplicity distribution happen to have left-over hits from the previous crossing, then the multiplicities may be artificially large.

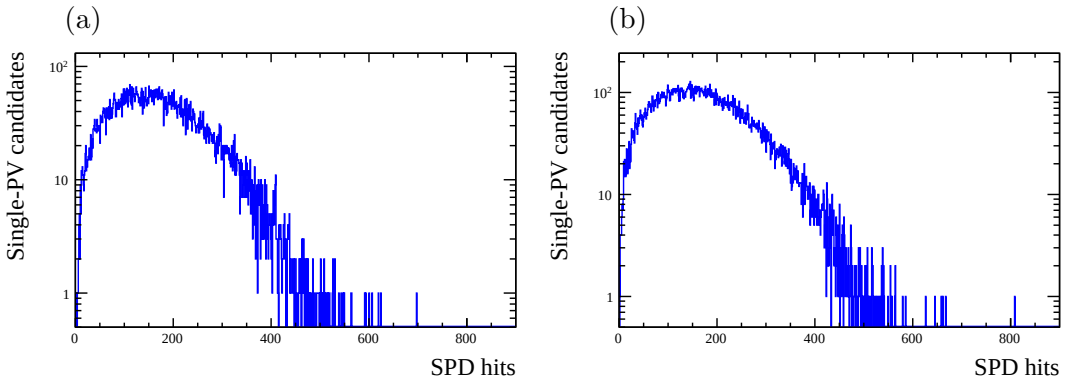

Figure 4.21: SPD multiplicities for Z events with one primary vertex that satisfy the dimuon triggers in (a) SAMPLE-I and (b) SAMPLE-II.

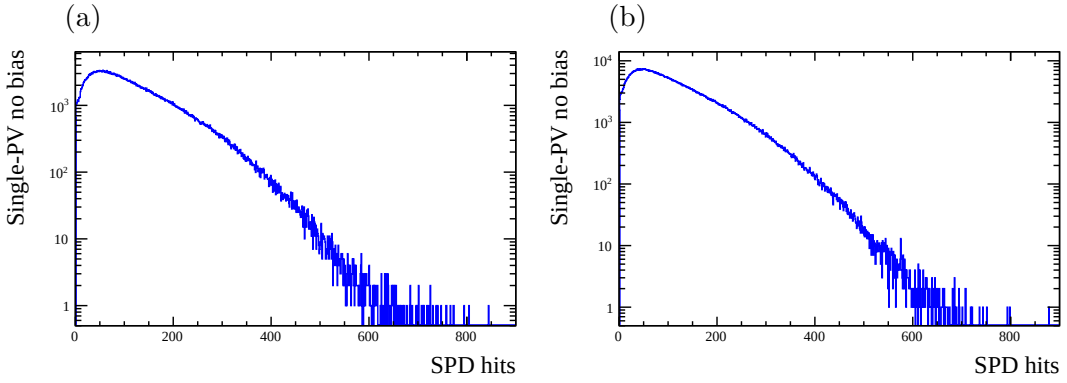

Figure 4.22: SPD multiplicities of randomly triggered events with one primary vertex in (a) SAMPLE-I and (b) SAMPLE-II.

To see how these issues are resolved, consider Equation 4.8.

$$Z(\text{2PV}) = Z(\text{1PV}) \oplus \text{NoBias(1 PV)}_{\text{noise/spillover}} \tag{4.8}$$

This equation represents the addition of the multiplicities of a single PV Z candidate event and a single PV, randomly triggered (no bias) event. The terms of the equation are to be understood as two dimensional grid maps. Each grid map has the same spatial resolution as the SPD, as shown in Figure 3.13(a). Cells in these grids have values of 0 or 1, depending on whether or not a charged particle has activated the pad corresponding to that cell. The sense of the addition indicated by $\oplus$ is that cell(i,j) of the grid on the left-hand-side of Equation 4.8 is considered activated if cell(i,j) is activated in at least one of the two grids on the right-hand-side of the equation. The first grid on the right-hand-side is populated by randomly selecting an SPD multiplicity from the distribution of SPD multiplicities in 1 PV Z events (see Figure 4.21) and distributing

this multiplicity according to the probability density in Figure 4.23. The second grid on the right-hand-side is populated in a similar fashion, randomly selecting a multiplicity from the distribution in Figure 4.22 and distributing according to the probability density shown in Figure 4.24. The subscript on the NoBias term is to indicate that 6% of the hits sampled from the distribution in Figure 4.22 are subtracted to account for noise and spillover. This 6% is motivated by comparing the average multiplicities of single PV randomly triggered events (117) and noise events (7). Noise events are randomly triggered events with no primary vertices that do not fire a physics trigger. Finally, the constructed SPD multiplicity is obtained by summing over occupied cells in the composite grid (the left-hand-side of Equation 4.8).

The result obtained from the method described above is an estimate for the SPD multiplicity of an event containing a Z with two PVs. The method may be extended to account for events with n PVs by iterating. This is represented by Equation 4.9.

$$Z(n\ \mathrm{PV}) = Z(n-1\ \mathrm{PV}) \oplus \mathrm{NoBias}(1\ \mathrm{PV})_{\mathrm{noise/spillover}} \tag{4.9}$$

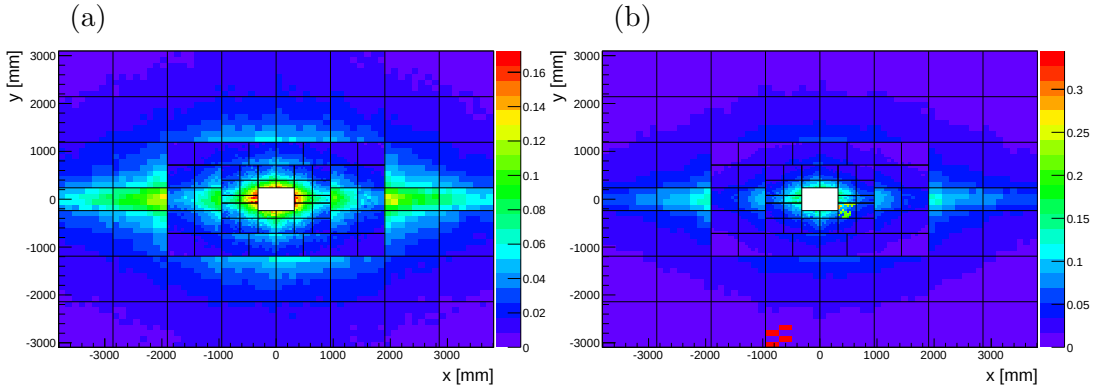

Figure 4.23: Occupancies in the SPD detector for Z boson events with one primary vertex in (a) Sample-I and (b) Sample-II.

The suitability of the method can be seen in Figure 4.25. Here the SPD hit distribution of the constructed sample is compared to Z candidate events that satisfy the dimuon triggers. The χ^2/ndf of the constructed sample with respect to the data is 0.91.

Since the constructed, higher multiplicity, events have no upper limit to the SPD multiplicity, it is a sample on which the efficiency can be determined. When the SPD multiplicity cut at 600 hits is applied, it is found to have an efficiency of $(94.0 \pm 0.1)\%$ for Sample-I, and $(93.0 \pm 0.1)\%$ for Sample-II.

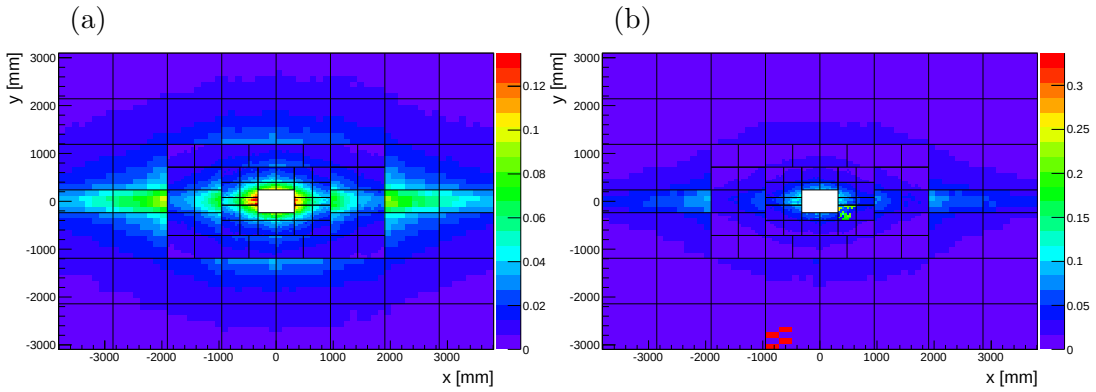

Figure 4.24: Occupancies in the SPD detector for randomly triggered events with one primary vertex in (a) SAMPLE-I and (b) SAMPLE-II.

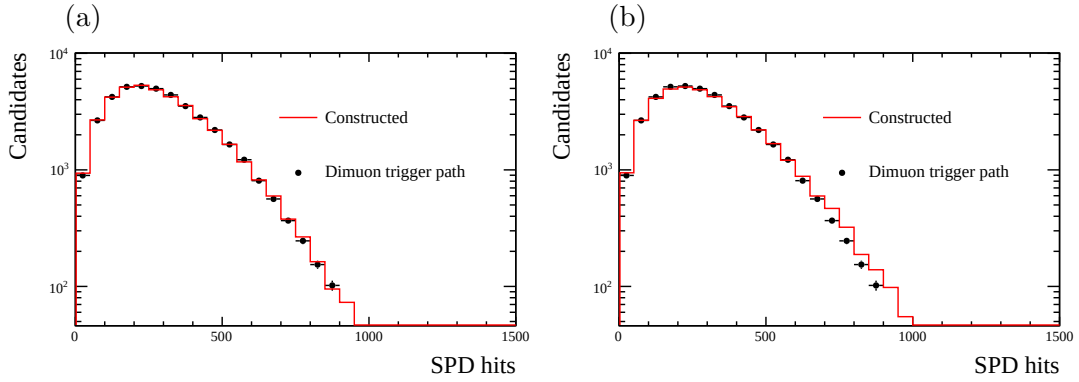

Figure 4.25: Constructed SPD hit multiplicity distributions compared to candidates passing the dimuon trigger path, where data corresponding to SAMPLE-I has been used. The good agreement in (a) indicates that the constructed sample may be used to calculate the GEC. Noise has not been subtracted in (b).

Determination of the GEC efficiency from a fit to the SPD distribution

The second method to determine the GEC efficiency fits a function to the SPD multiplicity distribution of Z candidate events that satisfy the dimuon triggers (Figure 4.26). Various shapes were tested and the best fit to the data is obtained with a Γ distribution. The χ^2/ndf of the fit shown is 1.6. The efficiency is determined to be $(94.1 \pm 0.5)\,\%$ for SAMPLE-I, and $(93.0 \pm 0.3)\%$ for SAMPLE-II.

Dependence of GEC efficiency

Both methods described above give consistent measurements of the GEC efficiency. The first method is used in the cross-section determination as it has better precision, while the second acts as a cross-check.

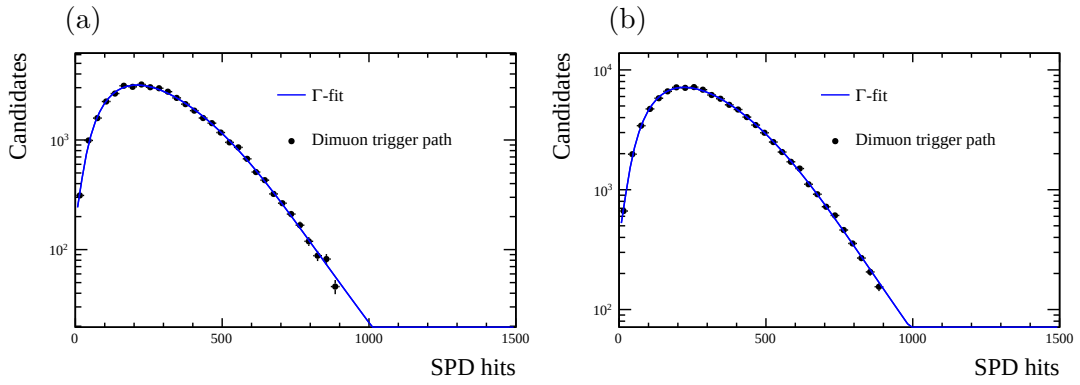

Figure 4.26: SPD multiplicity distributions for candidate events firing the dimuon trigger path in (a) SAMPLE-I and (b) SAMPLE-II. The data are fitted with a Γ distribution.

It is also important to establish the dependence of the efficiency on the variables under study. This is investigated using the Z candidates that satisfy the dimuon triggers and checking the fraction of these events that survive the 600 SPD hit cut. This gives a good estimate of the shape of the GEC efficiency.

In the case of the p_T and ϕ^* distributions, there is little evidence of variation. A linear dependence is observed as a function of boson rapidity, as shown in Figure 4.27. The same behaviour is observed for the efficiency as a function of muon pseudorapidity. This is explained as follows. The soft tracks from the underlying event are mainly produced close to the beam line. If the Z boson and accompanying jet are produced centrally in rapidity, their resulting charged tracks will not overlap with those from the underlying event. This gives rise to high SPD multiplicities and low GEC efficiencies. Conversely, if the Z boson and accompanying jet are quite boosted, the charged tracks are close to the soft tracks from the underlying event. This increases the chance of two tracks lighting up the same SPD cell, thus producing low SPD multiplicities and high GEC efficiencies.

4.4.4 Luminosity

The absolute luminosity scale was measured at specific periods during the data taking, using both van der Meer scans and beam-gas imaging methods [62, 98]. Both methods give similar results and are combined to give the final luminosity estimate with an uncertainty of 1.7% in SAMPLE-I and 1.2% in SAMPLE-II. The corresponding integrated luminosities are 975 ± 17 and 1978 ± 23 pb^{-1}.

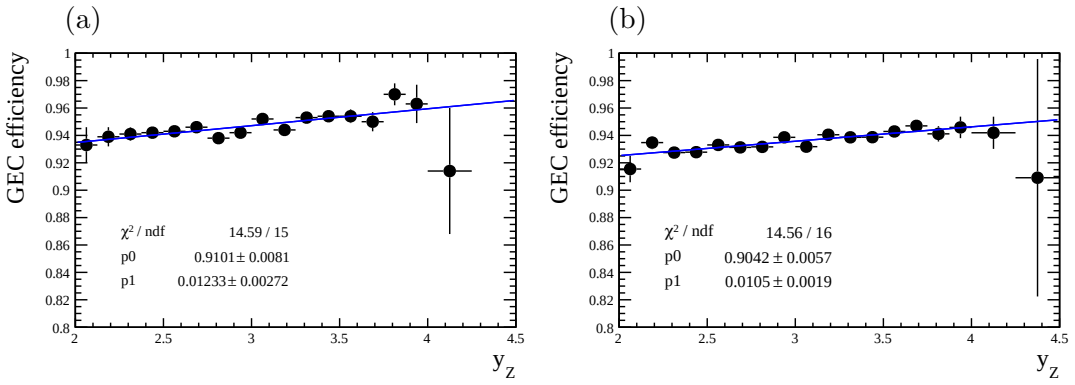

Figure 4.27: GEC efficiencies as a function of Z boson rapidity in (a) SAMPLE-I and (b) SAMPLE-II.

4.4.5 Final-state radiation

The measured cross-sections are corrected to Born level in quantum electrodynamics (QED) in order to provide a consistent comparison with NLO and NNLO QCD predictions, which do not include the effects of final-state radiation (FSR). The corrections are defined by lepton momenta, at the truth level, before and after QED FSR. Corrections have been calculated with both HERWIG++ [48] and PYTHIA8 [47]. The final FSR correction is taken as the mean of the HERWIG++ and PYTHIA8 values, which is about 2.1%. Figure 4.28 shows the FSR correction as a function of Z boson p_T. As a function of rapidity, the dependence is flat.

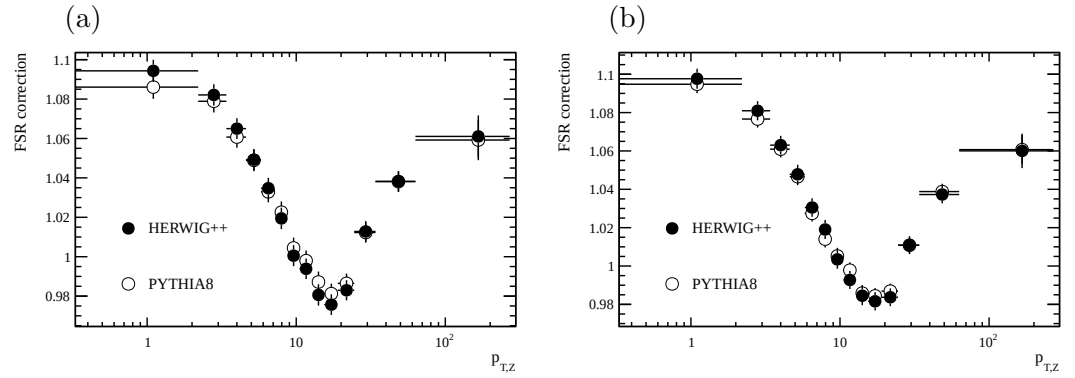

Figure 4.28: Correction factors for QED final state radiation as a function of Z boson p_T for (a) SAMPLE-I and (b) SAMPLE-II.

4.4.6 Calibrated simulation and unfolding

In this analysis, cross-sections are measured differentially in Z boson y, p_T, ϕ^* and muon η. The choice of bin size must take into account the desired statistical precision, the rate of change of the underlying physical distribution, as well as the experimental resolution. If the binning is too fine, due to the finite resolution of the variable in question, the bin that is assigned to a variable may be different to the bin that nature intended. This problem can be solved, in part, by increasing the bin width. Unfortunately, information about the shape of the distribution is then lost. The solution is to use detector simulation to determine the extent to which reconstructed variables deviate from their true values and, in turn, use this information to correct data. For this to work, the resolution in simulation must reflect the resolution in data.

Consider a vector of measurements ν_i and the corresponding true values μ_j. These are related by a matrix R, known as the response of the detector, such that

$$\nu_i = R_i{}^j \mu_j. \tag{4.10}$$

The ideal situation, with true and measured values falling in the same bin, is represented mathematically by a diagonal response matrix. The response matrix will be populated with off-diagonal entries if the variable is poorly resolved, if the bin width is too fine, or both.

For data, the response matrix R is unknown. Detector simulation allows simultaneous knowledge of the reconstructed- and truth-level values of some variable. As a consequence, for simulation, R is known. To unfold data, R may be determined on simulation, inverted, and applied to data to obtain the true distribution. The procedure is called unfolding.

For the unfolding procedure to work, the simulation must model detector response well. In Figure 4.29 the Z mass peak observed in data is compared to simulation (uncalibrated). A discrepancy in the modeling of the resolution and scale for high p_T muons is evident. There are many reasons for such a discrepancy, including a mismodelling of the magnetic field map of the LHCb dipole spectrometer magnet, or translational and rotational misalignment of the tracking stations.

The momentum in simulation can be calibrated to data with the parameterisation,

$$p_i = s\left(p_i{}^{\mathrm{FSR}} + r(p_i{}^{\mathrm{REC}} - p_i{}^{\mathrm{FSR}})\right) \tag{4.11}$$

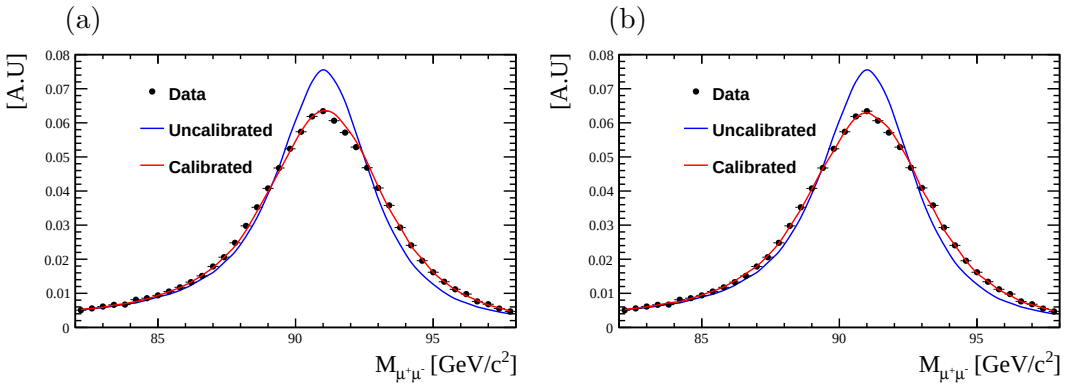

Figure 4.29: The Z boson mass peak from data (black points) compared to uncalibrated (blue curve) and calibrated (red curve) simulation for (a) SAMPLE-I and (b) SAMPLE-II.

where p_i is the calibrated x, y, or z-component of momentum, ${p_i}^{\mathrm{FSR}}$ is the post-FSR generator-level momentum component, and ${p_i}^{\mathrm{REC}}$ is the reconstructed-level momentum component. The parameter s governs the scale of the calibration, while the parameter r controls the resolution. The Z mass peak from data is fit with simulation according to Equation 4.11 to determine values for s and r. These values depend on the ϕ_{μ^+} so fits in bins of ϕ_{μ^+} are performed (they also depend on ϕ_{μ^-} but the choice doesn't effect the result). The values for s and r obtained with different magnet polarity are shown in Figures 4.30 and 4.31. Using these values, the simulation is calibrated prior to building the response matrix.

To build the response matrix, a 2D histogram is filled with fully reconstructed events from a simulated sample that has been calibrated as described above.[2] The rows and columns of this histogram represent the calibrated values of the variable, and the true values of the variable after QED final-state radiation. The histogram is filled such that (a) the sum of the entries in the first (second, third, etc) row is the total number of events whose calibrated value is in the first (second, third, etc) bin, and (b) the sum of the entries in the first (second, third, etc) column is the total number of true events in the first (second, third, etc) bin. The response matrix is obtained by dividing the first (second, third, etc) column by the total number of true events in the first (second, third, etc) bin. In this way Equation 4.10 is satisfied.

There are a number of different methods that unfold for detector resolution effects. The first method is to invert the response matrix R that is described above. This method has the advantage of being unbiased (in the sense of estimators). The disadvantages are that the matrix R must be invertible and that the covariance matrix is often troublesome [99].

[2]For an event to be fully reconstructed, two long-tracks must be reconstructed, both long-tracks must be identified as muons, and both muons must fire the trigger.

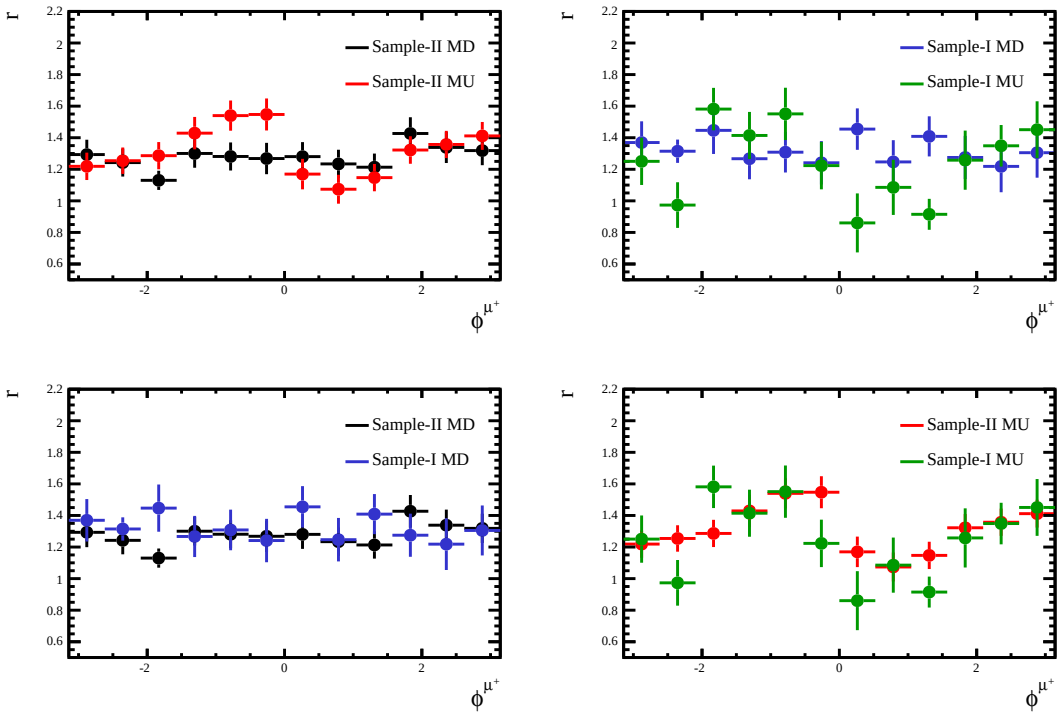

Figure 4.30: Momentum resolution correction factors (factor r in Equation 4.11) for different magnet polarities in SAMPLE-I and SAMPLE-II.

The second is called the bin-by-bin method. Correction factors C_i are evaluated and applied to the data, where these are defined using the same notation as in Equation 4.10.

$$C_i = \frac{\mu_i}{\nu_i}. \tag{4.12}$$

This method gives biased unfolded estimates [99], where the bias is induced by the model used in the simulation (PYTHIA8 in this case). The third is the singular value decomposition (SVD) method, which is a regularisation method that treats the singularities that may prevent the response matrix from being invertible [100]. The fourth method is based on Bayes' theorem and iteratively determines the unfolded estimate based on the best possible information at hand. This last method is used in this analysis. The other methods are used for cross-checks and uncertainty evaluation.

The iterative Bayesian approach implemented in ROOUNFOLD [101] is used to determine an unfolding matrix for the data, where 4 iterations of the algorithm are used. The unfolding techniques of bin-by-bin corrections, SVD (with regularisation parameter k=7), and simple inversion have also been tested and provide similar results to the Bayesian method.

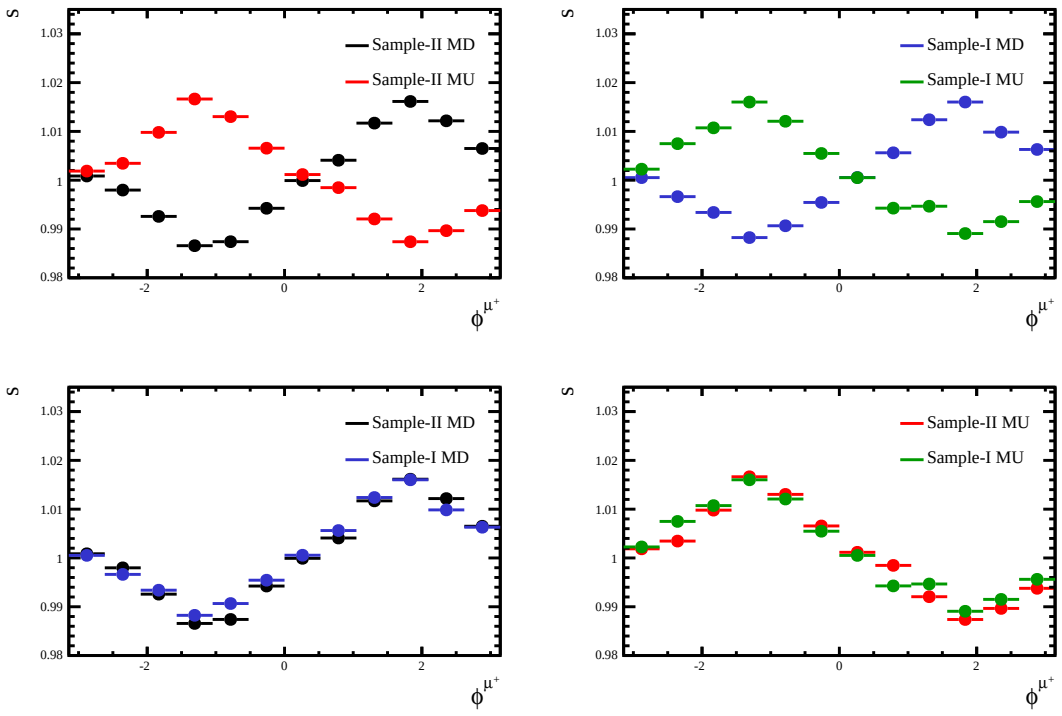

Figure 4.31: Momentum scale correction factors (factor s in Equation 4.11) for different magnet polarities in SAMPLE-I and SAMPLE-II.

The simulation uses the PYTHIA8 event generator. The dependence of the result on the model used has been checked by reweighting the PYTHIA8 p_T distribution at truth level using p_T distributions from other generators. All methods except bin-by-bin corrections are found to be model independent.

4.5 Systematic uncertainties

Various sources of systematic uncertainty are considered. Their effect on the total cross-section measurement is discussed below.[3] The measured differential cross-sections as a function of $p_{T,Z}$ and ϕ^*_Z have additional systematic uncertainties due to unfolding.

4.5.1 Muon reconstruction efficiencies

The systematic uncertainty on cross-sections measurements associated with the trigger, identification and tracking efficiencies is determined as follows. First, the cross-sections are re-evaluated with the values of the individual efficiencies increased or decreased by one standard deviation. Second, the difference between these values and the nominal cross-section is divided by the uncertainty on the efficiency to give a matrix of numerical derivatives, **G**. Each element of this matrix is defined as

$$G_{ij} = \frac{\sigma_i - {\sigma_i}^j}{\delta\epsilon^j} \tag{4.13}$$

where i indexes the cross-section, j indexes the efficiency, σ_i represents the nominal cross-section, ${\sigma_i}^j$ represents the cross-section with efficiency j varied, and $\delta\epsilon^j$ is the uncertainty on the efficiency j. More details on this are given in Appendix C. For cross-section measurements in Z boson rapidity, **G** is an 18 x 13 matrix. The full covariance matrix of the differential cross-section measurements $\mathbf{V}_\sigma$ is evaluated as

$$\mathbf{V}_\sigma = \mathbf{G}\mathbf{V}_\epsilon\mathbf{G}^\mathbf{T}, \tag{4.14}$$

for each source of uncertainty separately. The matrix $\mathbf{V}_\epsilon$ is a 13 x 13 diagonal matrix and the elements are the squares of the uncertainties on the efficiencies. Depending on whether the efficiencies are varied up or down gives different results for $\mathbf{V}_\sigma$, so the average is taken.

The covariance matrices ($\mathbf{V}_\sigma$) for each source are added and the diagonal elements of the result determine the total systematic uncertainty due to reconstruction efficiencies (the usual definition of a covariance matrix), which vary between 0.5 and 2.0% on the differential cross-section measurements, depending on the particular bin.

[3] Many of the systematic uncertainties detailed here have a statistical component but are quoted as part of the systematic uncertainty. The statistical uncertainty on the final measurement is only due to the number of observed Z candidates. In the case of unfolded measurements, the statistical uncertainty is provided by the covariance matrix returned by RooUnfold.

4.5.2 Magnet polarity

As a cross-check the full analysis has been performed separately using data with magnet polarity up and magnet polarity down. The polarity dependent cross-sections are given in Table 4.8. The differences are within the statistical uncertainties. In addition,

[pb]	MU	MD	All
SAMPLE-I	75.4 ± 0.5	76.4 ± 0.4	76.0 ± 0.3
SAMPLE-II	95.1 ± 0.4	94.9 ± 0.4	95.0 ± 0.3

Table 4.8: Total cross-section calculated using magnet up (MU) and magnet down (MD) data sub-samples. Statistical uncertainties are indicated.

there is no discrepancy seen in the differential distributions (see Appendix D). Thus, no additional systematic is applied.

4.5.3 Unfolding and calibration

A systematic uncertainty due to the particular unfolding method chosen in the analysis is considered. As a first step, the total cross-sections are recalculated with the various unfolding methods. Results are in Table 4.9. The largest deviation of the total cross-section with respect to the method used in this analysis (Bayesian) suggests a 0.3% systematic uncertainty. However, this uncertainty is driven by the bin-by-bin correction method, which is known to be biased by the p_T distribution of the generator, in this case PYTHIA8 [99]. For the differential distributions, the systematic uncertainty is taken as the difference between the cross-sections as calculated using the Bayesian [102] and matrix inversion [99] unfolded estimates. As a function of p_T, this uncertainty varies between 0.1–3.0% while as a function of ϕ^*, the variation is 0.1–4.0%, except for the last bin where the uncertainty is 24%. This is not of concern because the measurement in the last bin in ϕ^* is limited statistically (17%) and only accounts for 0.05% of the total cross-section.

An uncertainty is also assigned due to the calibration of the momentum in simulation. The values of r and s determined in Section 4.4.6 are changed up and down by their uncertainty. This changes the calibrated momentum used to train the unfolding procedure and in turn induces a spread in the Bayesian unfolded estimates. This spread sets the uncertainty due to calibration. As a function of p_T it varies between 0.2–1.6% while as a function of ϕ^* it is less than 0.1%.

	Cross-section [pb]	
Unfolding method	SAMPLE-I	SAMPLE-II
None	75.9 ± 0.3	95.1 ± 0.3
Bayesian	76.0 ± 0.3	95.0 ± 0.3
Bin-by-bin	76.2 ± 0.3	95.1 ± 0.3
SVD	75.9 ± 0.6	94.9 ± 0.4
Inversion	76.0 ± 0.2	95.0 ± 0.2

Table 4.9: Total cross-section calculated using the p_T distribution and different unfolding methods. Statistical uncertainties are indicated.

4.5.4 FSR correction

The uncertainty on the FSR correction is the quadratic sum of the statistical uncertainty from HERWIG++ and half the difference between the total corrections determined using HERWIG++ and PYTHIA8. Half of the difference is taken because the FSR correction is an average of the HERWIG++ and PYTHIA8 corrections. As a function of boson rapidity, the uncertainty on the correction varies between 0.3–3.0%. As a function of boson transverse momentum, the uncertainty varies between 0.3–0.7% and as a function of boson ϕ^*, the uncertainty varies between 0.3–4.0%.

4.5.5 Purity

The statistical uncertainty on the determination of the sample purity leads to a 0.2% uncertainty on the total cross-section. This uncertainty is mainly due to the uncertainties on the data-driven methods for determining heavy flavour and hadron misidentification backgrounds.

As explained in Section 4.3.1, the heavy flavour background is determined using different samples (HF-ISO and HF-VTX), different muon transverse momentum thresholds (10–20 GeV/c) and different fitting regimes (either above 40 GeV/c^2 or between 40 and 60 GeV/c^2). By lowering the p_T cut in steps of 1 GeV/c^2 the statistics in the low mass region are increased allowing better fits. Lowering the transverse momentum threshold is not expected to allow Z boson decays (see Table A.2) into the sample.

The average of the background estimates at different p_T thresholds (see Appendix A) is taken for each combination of HF sample and fitting regime. The results of this are presented in Table 4.10. Conservative uncertainties are set by taking the largest deviation between the estimates at different p_T thresholds and their average. For SAMPLE-I, the background estimate 227 ± 32 is most precise and is taken for the analysis. For SAMPLE-II, 490 ± 72 is taken.

	Sample-I		Sample-II	
Fitting regime	HF-ISO	HF-VTX	HF-ISO	HF-VTX
Above 40 GeV/c^2	226 ± 64	233 ± 49	572 ± 140	568 ± 157
Between 40–60 GeV/c^2	227 ± 32	215 ± 41	467 ± 58	490 ± 72

Table 4.10: Average heavy flavour backgrounds calculated with the different HF samples and fitting regimes. The uncertainty is the largest difference between the average value shown in this table and the background estimates at different transverse momentum thresholds.

The systematic uncertainty for hadron misidentification is defined as the difference between the default estimate (see Section 4.3.2) and the estimate obtained using the same-sign muon-pair sample. For Sample-I, this difference is 32 events so the hadron misidentification background is 116 ± 45. For Sample-II, the background is 262 ± 110.

In this analysis the purity is assumed not to vary with η^{μ}, y_Z, ϕ^*_Z and $p_{T,Z}$. To assign an uncertainty due to this assumption, the cross-section measurements are repeated but this time using a bin dependent purity. The total cross-section does not change. Differential cross-sections change by up to 0.1–5.0%, except for the highest ϕ^*, which changes by 24%. The per bin percentage difference is assigned as the per bin systematic uncertainty.

4.5.6 GEC efficiency

The uncertainty on the overall GEC efficiency (distinct from the binned ones discussed below) is the quadratic sum of three parts. The first part is the uncertainty due to the size of the sample used in evaluating it, which is 0.1%. The second part is due to how well the constructed SPD hit multiplicity distribution matches the data. To evaluate this, an efficiency ϵ_{900} is calculated using:

- the constructed sample of Section 4.4.3, but in this case, the constructed sample is required to have no events above 900 SPD hits;
- the Z candidate sample where events satisfy dimuon triggers.

The efficiency ϵ_{900} is calculated for both samples as the number of events below 600 SPD hits divided by the total number of events. The difference in ϵ_{900} calculated with the two samples is considered a systematic uncertainty and contributes 0.16%. Finally the difference of 0.1%, between the two methods described in Section 4.4.3, is taken as the third component. The total systematic uncertainty is thus 0.2%.

Since there is some indication that the GEC efficiency varies across the variables of interest (see Figure 4.27), the GEC is applied on a per bin basis. The total uncertainty is then the sum in quadrature of the uncertainty on the total GEC efficiency described above plus the statistical uncertainty of the efficiencies measured in each bin. The statistical component is considered uncorrelated between bins and varies between 0.3–4.0%.

4.5.7 Proton beam energy

The measurements are specified at centre-of-mass energies of $\sqrt{s} = 7$ TeV or $\sqrt{s} = 8$ TeV. The beam energy, and consequently the centre-of-mass energy, is known to 0.65% [64]. This uncertainty is fully correlated between different centre-of-mass energies, as explained in Section 3.1.3. The sensitivity of the cross-section to the centre-of-mass energy is evaluated using DYNNLO [42] with the MSTW08 [25] PDF set at centre-of-mass energies between 1–20 TeV. The result is shown in Figure 4.32 where a cubic spline is used to interpolate between predictions. At $\sqrt{s} = 7$ TeV ($\sqrt{s} = 8$ TeV) a 0.65% variation of the beam energy corresponds to a 1.25% (1.15%) variation in the cross-section.

4.5.8 Summary

For the total cross-section measurement, the systematic uncertainties are combined by taking the uncertainties associated with the GEC, the luminosity, the beam energy, as well as the purity and muon reconstruction efficiencies, to be correlated between measurement bins. Most of the muon reconstruction efficiencies are partially correlated between rapidity bins. The other contributions are treated as uncorrelated. The contributions to the uncertainty on the total cross-section are listed in Table 4.11, as well as the correlation between Z boson rapidity bins.

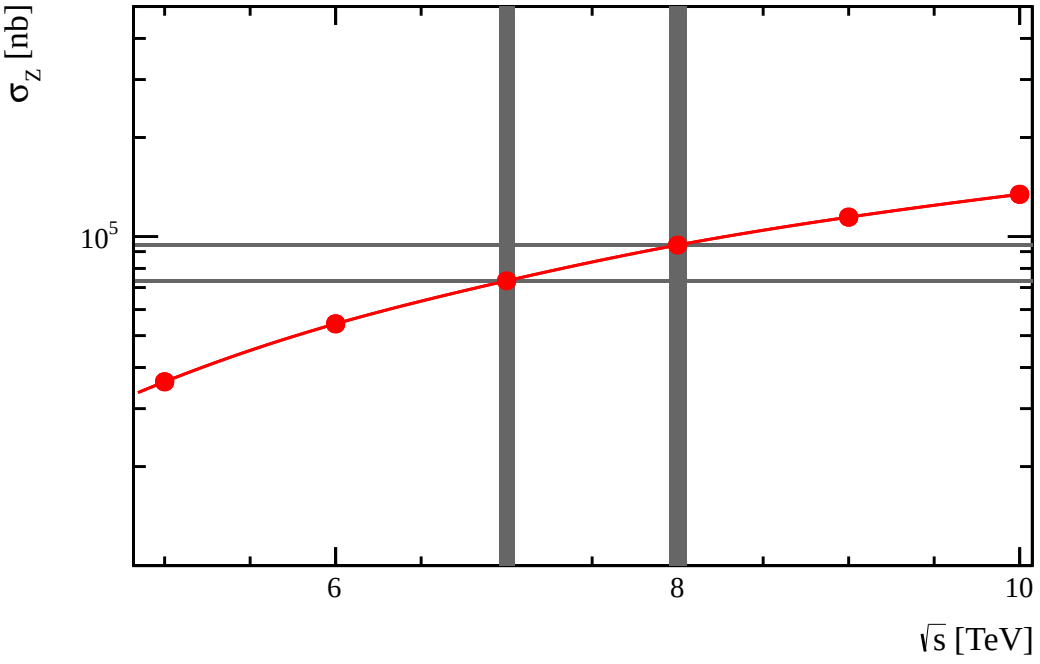

Figure 4.32: The curve is the DYNNLO prediction of the Z boson cross-section as a function of centre-of-mass energy. The vertical grey bands indicate the uncertainty on the centre-of-mass energy and the horizontal grey bands indicate the resulting uncertainty on the cross-section.

Source	Uncertainty (%)		Correlation between y_Z bins
	Sample-I	Sample-II	
Statistical	0.39	0.27	Uncorrelated
Muon Trigger Eff. (TP)	0.07	0.05	Partially Correlated
Muon Identification Eff. (TP)	0.11	0.07	Partially Correlated
Muon Identification Eff. (Sys.)	0.20	0.20	Correlated
Muon Tracking Eff. (TP)	0.34	0.29	Partially Correlated
Muon Tracking Eff. (TM)	0.22	0.13	Partially Correlated
Muon Tracking Eff. (Bias1)	0.08	0.10	Partially Correlated
Muon Tracking Eff. (Bias2)	0.33	0.35	Correlated
FSR correction	0.11	0.13	Uncorrelated
Purity	0.20	0.20	Correlated
Purity (Binned)	0.09	0.06	Uncorrelated
GEC Eff.	0.23	0.32	Correlated
GEC Eff. (Binned)	0.12	0.09	Uncorrelated
Systematic	0.68	0.67	Partially Correlated
Beam Energy	1.25	1.15	Correlated
Luminosity	1.72	1.16	Correlated
Total	2.27	1.78	

Table 4.11: Contributions to the uncertainty on the total Z cross-section. If ρ_{ij} denotes the correlation between measurements in distinct y bins i and j due to a particular source, then correlated means that $\rho_{ij}=1\ \forall\ i$ and j, uncorrelated means that $\rho_{ij}=0\ \forall\ i$ and j, while partially correlated means that $0 < |\rho_{ij}| < 1\ \forall\ i$ and j.

4.6 Results

4.6.1 Differential cross-sections

As explained in Section 4.4, the fundamental measurements of the analysis are differential cross-sections as functions of η^{μ}, y_Z, ϕ^*_Z and $p_{T,Z}$.

Rapidity

The y_Z distribution is shown in Figure 4.33 for Sample-I, together with predictions from Fewz [41, 103]. The orange and yellow bands indicate the measurements, while the predictions from Fewz, configured with six different PDF sets, are indicated by the open markers. Excellent agreement is observed between measurement and prediction, and any small difference is accounted for by the different overall normalisations of the distributions. The differential cross-section measurements are given in Table 4.12 for Sample-I. The quoted uncertainties, in order, are due to the sample size, systematic effects, the beam energy and the luminosity. The last column is the FSR correction. The corresponding results for Sample-II are displayed in Figure 4.34 and given in

y_Z	σ_Z [pb]	f_{FSR}
2.000 – 2.125	0.969 ± 0.039 ± 0.032 ± 0.012 ± 0.017	1.050±0.020
2.125 – 2.250	2.840 ± 0.063 ± 0.050 ± 0.036 ± 0.049	1.032±0.008
2.250 – 2.375	4.428 ± 0.077 ± 0.078 ± 0.055 ± 0.076	1.027±0.006
2.375 – 2.500	5.823 ± 0.088 ± 0.060 ± 0.073 ± 0.100	1.026±0.004
2.500 – 2.625	6.877 ± 0.095 ± 0.068 ± 0.086 ± 0.118	1.025±0.004
2.625 – 2.750	7.669 ± 0.100 ± 0.069 ± 0.096 ± 0.132	1.026±0.004
2.750 – 2.875	8.306 ± 0.104 ± 0.070 ± 0.104 ± 0.143	1.026±0.003
2.875 – 3.000	8.241 ± 0.103 ± 0.066 ± 0.103 ± 0.142	1.025±0.003
3.000 – 3.125	7.783 ± 0.099 ± 0.059 ± 0.097 ± 0.134	1.026±0.003
3.125 – 3.250	7.094 ± 0.096 ± 0.058 ± 0.089 ± 0.122	1.028±0.004
3.250 – 3.375	5.894 ± 0.087 ± 0.049 ± 0.074 ± 0.101	1.026±0.004
3.375 – 3.500	4.160 ± 0.073 ± 0.041 ± 0.052 ± 0.072	1.027±0.005
3.500 – 3.625	2.896 ± 0.061 ± 0.030 ± 0.036 ± 0.050	1.026±0.005
3.625 – 3.750	1.741 ± 0.047 ± 0.023 ± 0.022 ± 0.030	1.021±0.007
3.750 – 3.875	0.825 ± 0.032 ± 0.014 ± 0.010 ± 0.014	1.025±0.010
3.875 – 4.000	0.321 ± 0.020 ± 0.008 ± 0.004 ± 0.006	1.011±0.015
4.000 – 4.250	0.115 ± 0.013 ± 0.006 ± 0.001 ± 0.002	1.018±0.033
4.250 – 4.500	–	–

Table 4.12: Inclusive differential cross-sections for Z boson production as functions of y_Z in Sample-I. Uncertainties are due to the sample size, systematic effects, the beam energy and the luminosity. No candidates are observed in the 4.25–4.50 bin.

y_Z	σ_Z [pb]	f_{FSR}
2.000 – 2.125	1.223 ± 0.033 ± 0.055 ± 0.014 ± 0.014	1.047±0.040
2.125 – 2.250	3.263 ± 0.051 ± 0.060 ± 0.038 ± 0.038	1.031±0.012
2.250 – 2.375	4.983 ± 0.062 ± 0.064 ± 0.057 ± 0.058	1.028±0.007
2.375 – 2.500	6.719 ± 0.070 ± 0.072 ± 0.077 ± 0.078	1.025±0.006
2.500 – 2.625	8.051 ± 0.076 ± 0.074 ± 0.093 ± 0.094	1.026±0.005
2.625 – 2.750	8.967 ± 0.079 ± 0.074 ± 0.103 ± 0.105	1.026±0.003
2.750 – 2.875	9.561 ± 0.081 ± 0.076 ± 0.110 ± 0.112	1.026±0.004
2.875 – 3.000	9.822 ± 0.082 ± 0.071 ± 0.113 ± 0.115	1.025±0.003
3.000 – 3.125	9.721 ± 0.081 ± 0.074 ± 0.112 ± 0.114	1.028±0.004
3.125 – 3.250	9.030 ± 0.078 ± 0.071 ± 0.104 ± 0.105	1.026±0.003
3.250 – 3.375	7.748 ± 0.072 ± 0.074 ± 0.089 ± 0.090	1.026±0.007
3.375 – 3.500	6.059 ± 0.063 ± 0.051 ± 0.070 ± 0.071	1.025±0.004
3.500 – 3.625	4.385 ± 0.054 ± 0.041 ± 0.050 ± 0.051	1.026±0.006
3.625 – 3.750	2.724 ± 0.042 ± 0.027 ± 0.031 ± 0.032	1.023±0.005
3.750 – 3.875	1.584 ± 0.032 ± 0.020 ± 0.018 ± 0.019	1.018±0.008
3.875 – 4.000	0.749 ± 0.022 ± 0.012 ± 0.009 ± 0.009	1.021±0.010
4.000 – 4.250	0.383 ± 0.016 ± 0.008 ± 0.004 ± 0.004	1.018±0.014
4.250 – 4.500	0.011 ± 0.003 ± 0.001 ± 0.000 ± 0.000	1.018±0.076

Table 4.13: Inclusive differential cross-sections for Z boson production as functions of y_Z for Sample-II. Uncertainties are due to the sample size, systematic effects, the beam energy and the luminosity.

Table 4.13. The relationship between the measurements and predictions in Sample-II is qualitatively the same as for Sample-I.

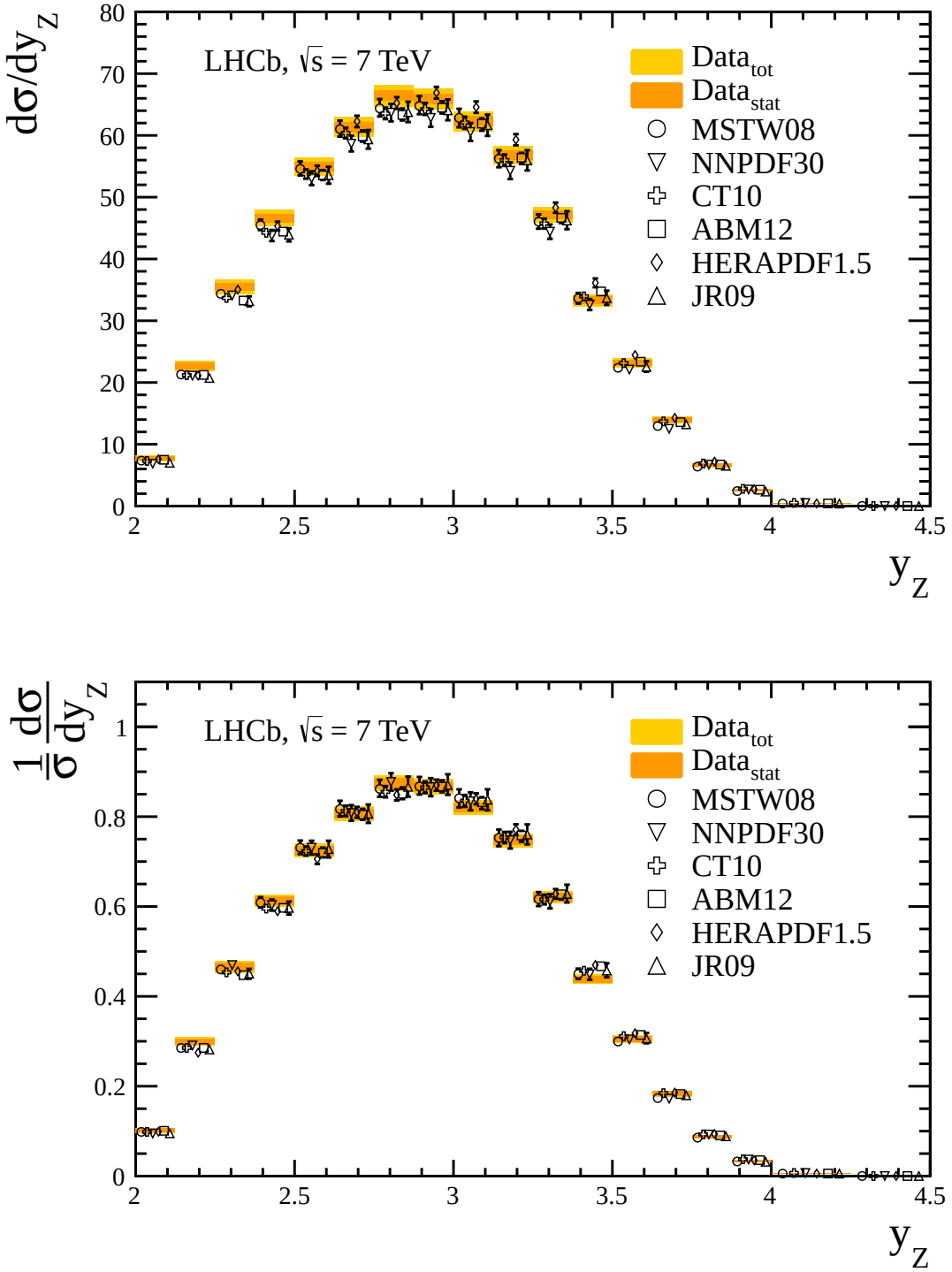

Figure 4.33: Differential cross-sections (top) and normalised differential cross-sections (bottom) as functions of y_Z for Sample-I compared with the prediction of Fewz, configured with various PDF sets. Different predictions are displaced horizontally for visibility. The shaded (yellow) bands indicate the statistical and total uncertainties on the measurements, which are symmetric about the central value.

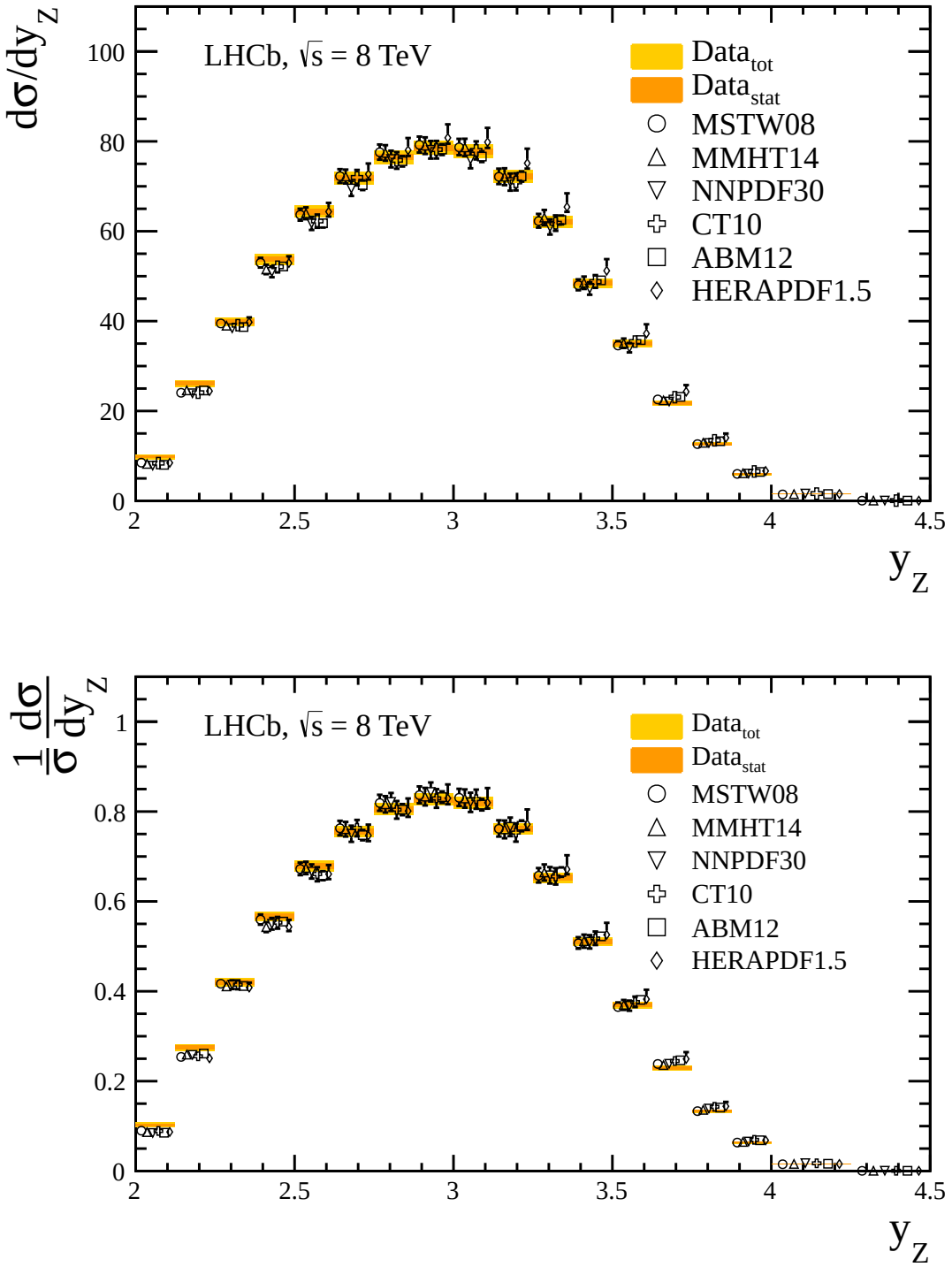

Figure 4.34: Differential cross-sections (top) and normalised differential cross-sections (bottom) as functions of y_Z for Sample-II compared with the prediction of Fewz, configured with various PDF sets. Different predictions are displaced horizontally for visibility. The shaded (yellow) bands indicate the statistical and total uncertainties on the measurements, which are symmetric about the central value.

Transverse momentum

In Figure 4.35, the differential cross-section measurements as functions of $p_{T,Z}$ are compared to the predictions from RESBOS [44–46] and POWHEG [104], where events are interfaced with a parton shower that is simulated using HERWIG [56, 57]. The distributions are well described. The differential cross-section measurements are given in Table 4.14 for SAMPLE-I. As before, the quoted uncertainties are due to the sample size, systematic effects, the beam energy and the luminosity. The last column is the FSR correction. The corresponding results for SAMPLE-II are displayed in Figure 4.36 and

$p_{T,Z}[GeV/c]$	σ_Z [pb]	f_{FSR}
0.0 – 2.2	6.454 ± 0.105 ± 0.129 ± 0.081 ± 0.111	1.090±0.006
2.2 – 3.4	6.520 ± 0.106 ± 0.150 ± 0.081 ± 0.112	1.080±0.004
3.4 – 4.6	6.209 ± 0.102 ± 0.221 ± 0.078 ± 0.107	1.063±0.004
4.6 – 5.8	5.868 ± 0.099 ± 0.208 ± 0.073 ± 0.101	1.049±0.004
5.8 – 7.2	5.749 ± 0.098 ± 0.154 ± 0.072 ± 0.099	1.034±0.004
7.2 – 8.7	5.607 ± 0.098 ± 0.083 ± 0.070 ± 0.096	1.021±0.004
8.7 – 10.5	5.637 ± 0.098 ± 0.054 ± 0.070 ± 0.097	1.002±0.004
10.5 – 12.8	5.524 ± 0.096 ± 0.081 ± 0.069 ± 0.095	0.996±0.004
12.8 – 15.4	5.158 ± 0.092 ± 0.067 ± 0.064 ± 0.089	0.984±0.005
15.4 – 19.0	4.963 ± 0.087 ± 0.053 ± 0.062 ± 0.085	0.978±0.005
19.0 – 24.5	5.517 ± 0.088 ± 0.055 ± 0.069 ± 0.095	0.985±0.004
24.5 – 34.0	5.465 ± 0.085 ± 0.067 ± 0.068 ± 0.094	1.013±0.004
34.0 – 63.0	5.789 ± 0.085 ± 0.076 ± 0.072 ± 0.100	1.038±0.004
63.0 – 270.0	1.516 ± 0.043 ± 0.044 ± 0.019 ± 0.026	1.060±0.007

Table 4.14: Inclusive differential cross-sections for Z boson production as functions of $p_{T,Z}$ in SAMPLE-I. Uncertainties are due to the sample size, systematic effects, the beam energy and the luminosity.

given in Table 4.15.

Comparisons of these measurements with MC@NLO + HERWIRI and MC@NLO + HERWIG are shown in Figure 4.37 for SAMPLE-I and Figure 4.38 for SAMPLE-II. Here HERWIG is configured with the RMS of the intrinsic k_T (see Section 2.4.4) distribution set to 0 GeV/c in one instance and 2.2 GeV/c in another. The predictions straddle the measurement at low $p_{T,Z}$. The high $p_{T,Z}$ tails are underestimated.

$p_{T,Z}[GeV/c]$	σ_Z [pb]	f_{FSR}
0.0 – 2.2	7.903 ± 0.082 ± 0.130 ± 0.091 ± 0.092	1.096±0.005
2.2 – 3.4	7.705 ± 0.080 ± 0.108 ± 0.089 ± 0.090	1.079±0.006
3.4 – 4.6	7.609 ± 0.078 ± 0.080 ± 0.088 ± 0.089	1.062±0.004
4.6 – 5.8	7.073 ± 0.075 ± 0.078 ± 0.081 ± 0.083	1.047±0.004
5.8 – 7.2	7.379 ± 0.078 ± 0.069 ± 0.085 ± 0.086	1.029±0.004
7.2 – 8.7	6.813 ± 0.076 ± 0.074 ± 0.078 ± 0.080	1.017±0.006
8.7 – 10.5	6.751 ± 0.075 ± 0.064 ± 0.078 ± 0.079	1.004±0.004
10.5 – 12.8	7.204 ± 0.078 ± 0.073 ± 0.083 ± 0.084	0.995±0.006
12.8 – 15.4	6.270 ± 0.073 ± 0.053 ± 0.072 ± 0.073	0.985±0.004
15.4 – 19.0	6.534 ± 0.072 ± 0.064 ± 0.075 ± 0.076	0.983±0.004
19.0 – 24.5	6.953 ± 0.071 ± 0.066 ± 0.080 ± 0.081	0.985±0.004
24.5 – 34.0	6.999 ± 0.069 ± 0.062 ± 0.080 ± 0.082	1.011±0.003
34.0 – 63.0	7.602 ± 0.070 ± 0.072 ± 0.087 ± 0.089	1.038±0.003
63.0 – 270.0	2.176 ± 0.037 ± 0.025 ± 0.025 ± 0.025	1.060±0.006

Table 4.15: Inclusive differential cross-sections for Z boson production as functions of $p_{T,Z}$ in SAMPLE-II. Uncertainties are due to the sample size, systematic effects, the beam energy and the luminosity.

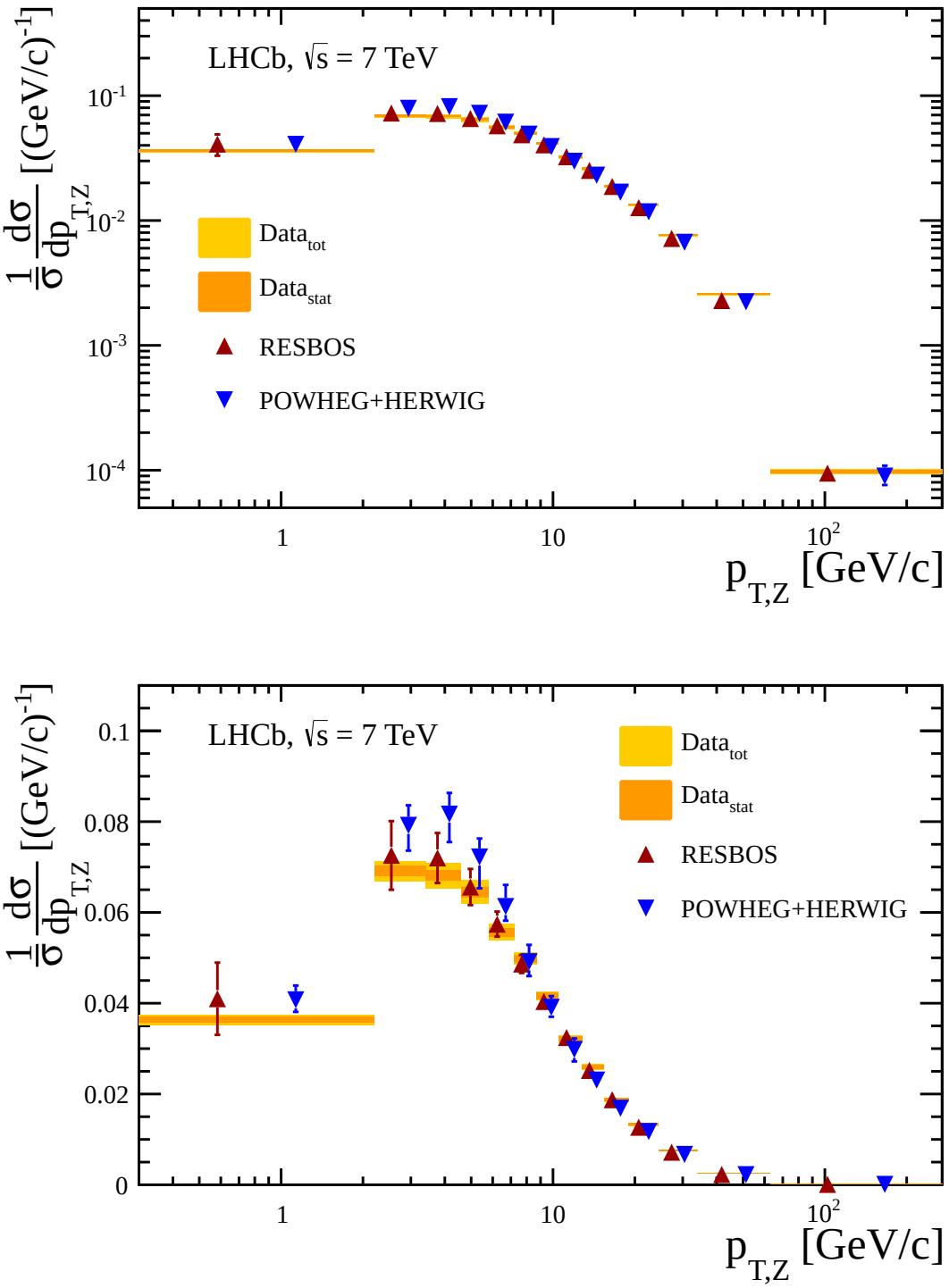

Figure 4.35: Normalised differential cross-sections as functions of $p_{T,Z}$ in SAMPLE-I on logarithmic (top) and linear (bottom) scales. The shaded (yellow) bands indicate the statistical and total uncertainties on the measurements, which are symmetric about the central value. The measurements are compared to the predictions of RESBOS and POWHEG + HERWIG.

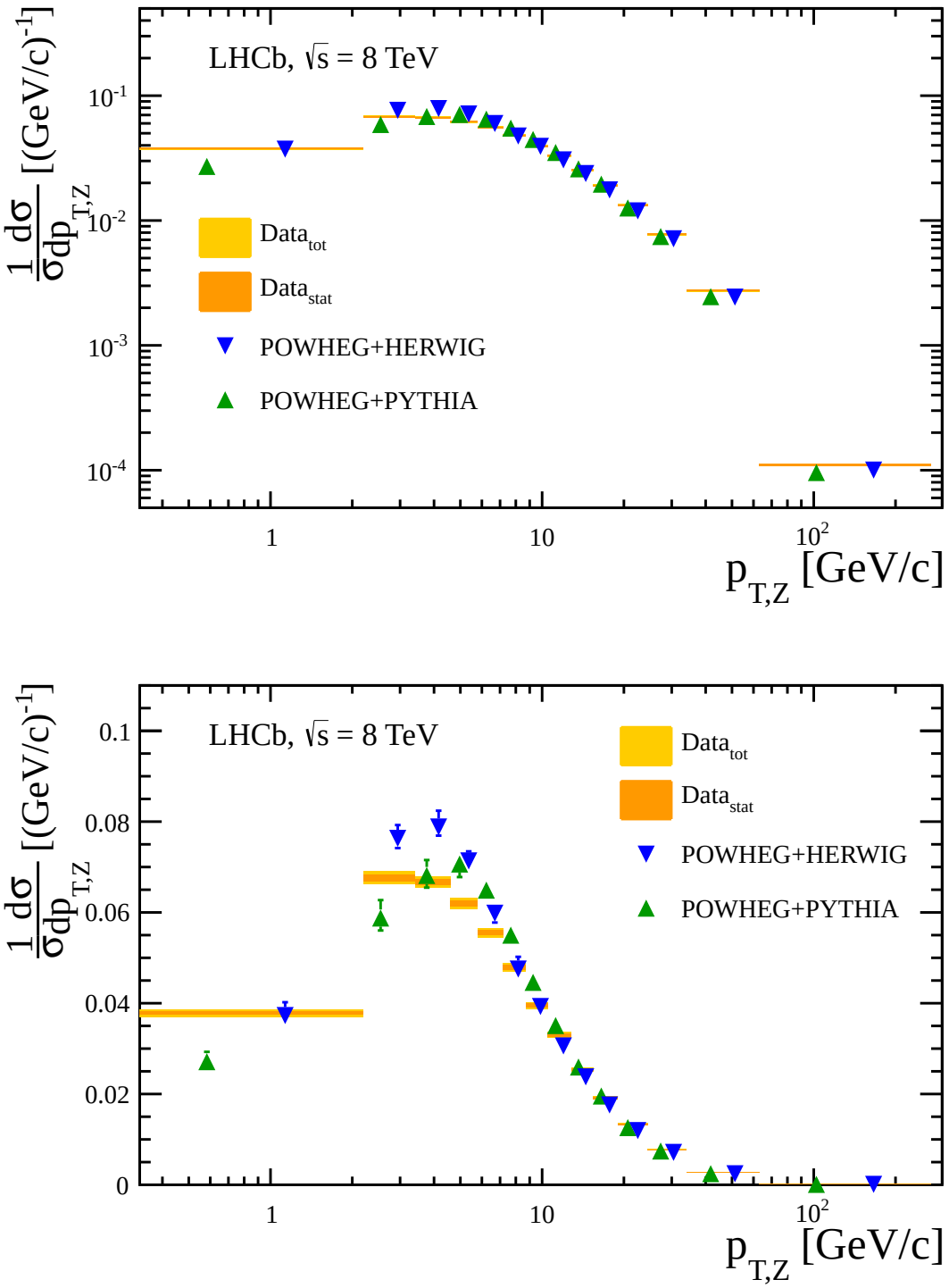

Figure 4.36: Normalised differential cross-sections as functions of $p_{T,Z}$ in SAMPLE-II on logarithmic (top) and linear (bottom) scales. The shaded (yellow) bands indicate the statistical and total uncertainties on the measurements, which are symmetric about the central value. The measurements are compared to the predictions of POWHEG + PYTHIA and POWHEG + HERWIG.

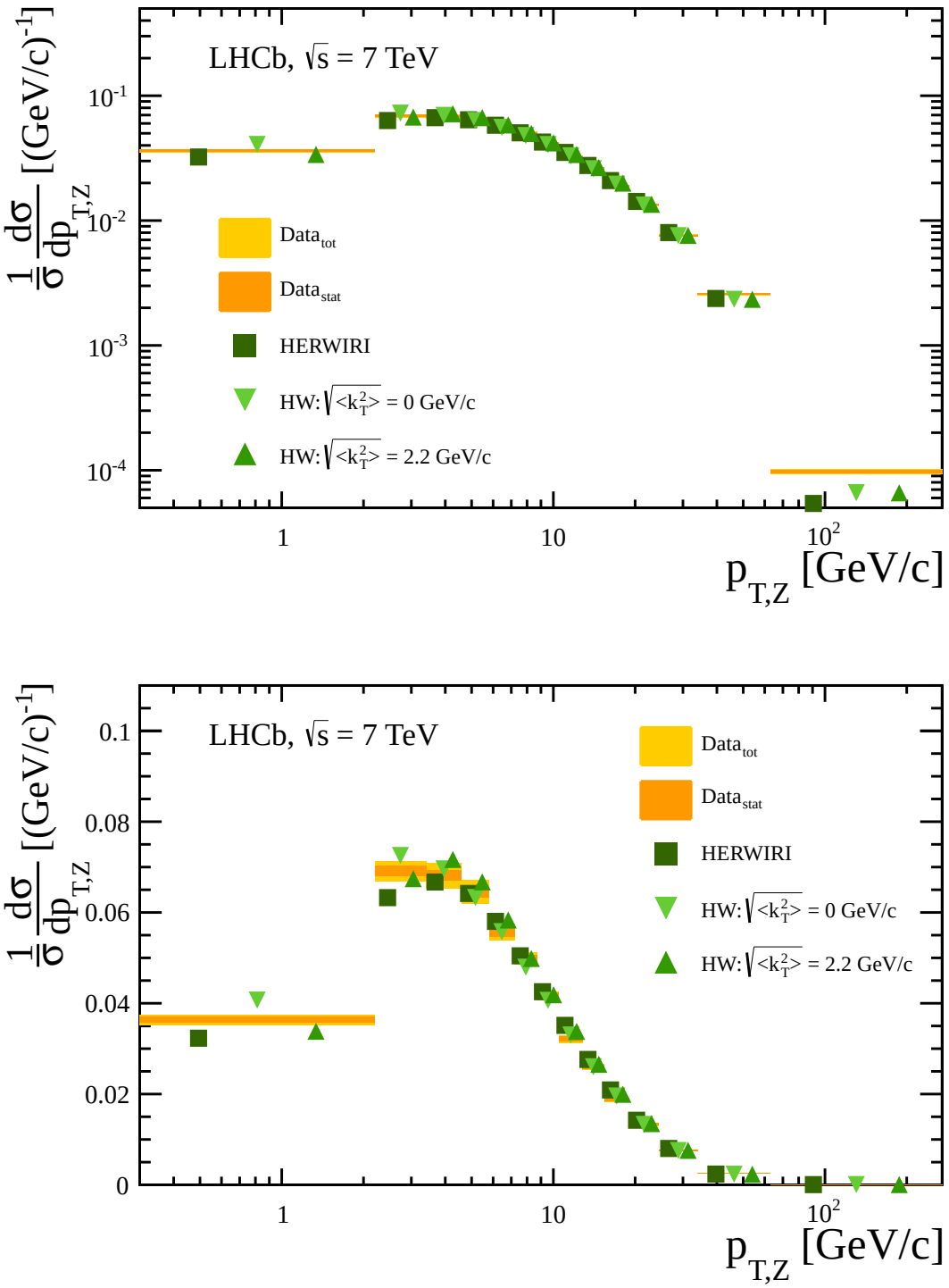

Figure 4.37: Normalised differential cross-sections as functions of $p_{T,Z}$ in SAMPLE-I on logarithmic (top) and linear (bottom) scales. The shaded (yellow) bands indicate the statistical and total uncertainties on the measurements, which are symmetric about the central value. The measurements are compared to MC@NLO + HERWIG (HW) and MC@NLO + HERWIRI (HERWIRI). HERWIG is configured with two choices of the RMS of the intrinsic k_T distribution, 0 and 2.2 GeV/c.

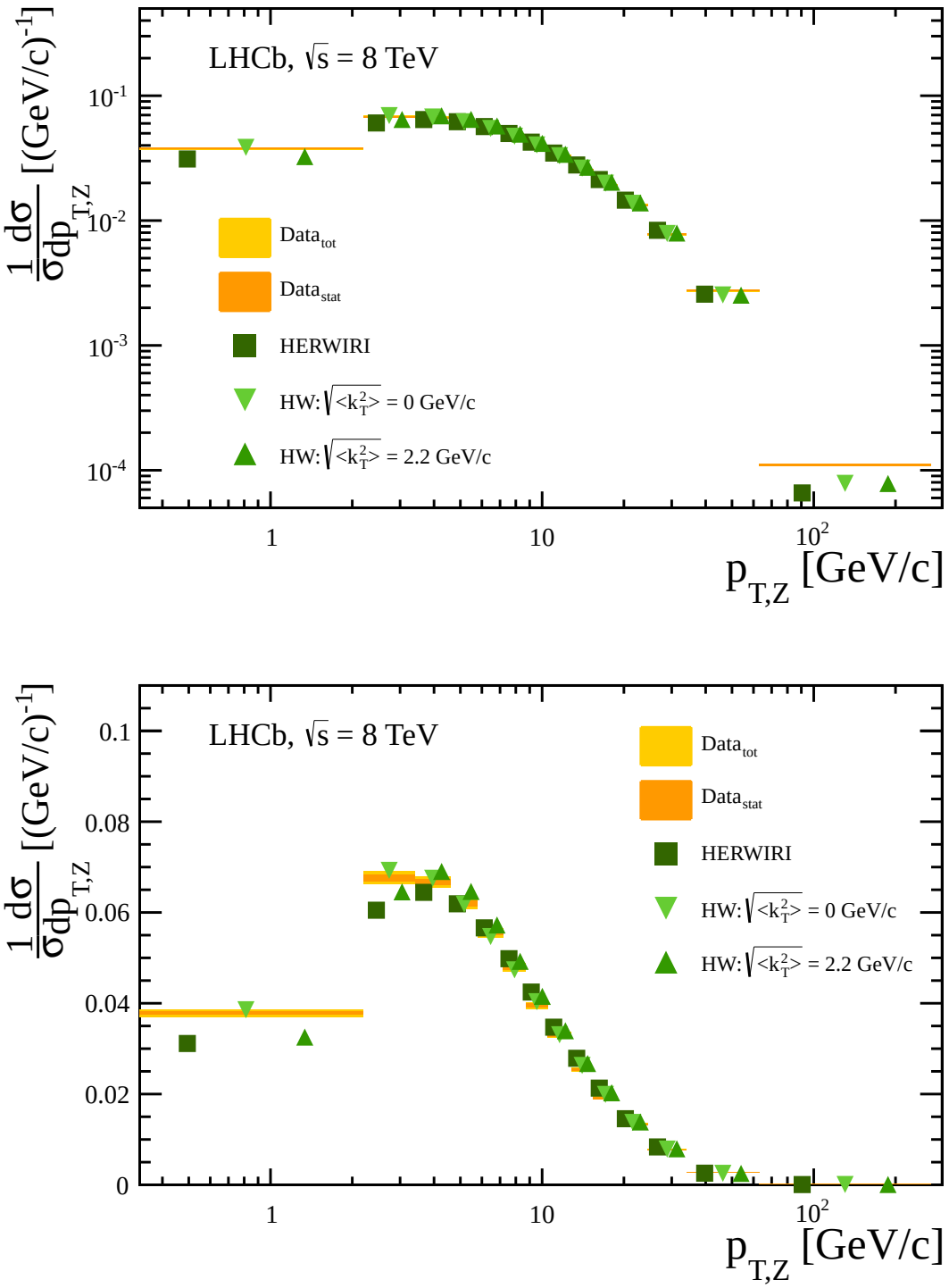

Figure 4.38: Normalised differential cross-section as functions of $p_{T,Z}$ in SAMPLE-II on logarithmic (top) and linear (bottom) scales. The shaded (yellow) bands indicate the statistical and total uncertainties on the measurements, which are symmetric about the central value. The measurements are compared to MC@NLO + HERWIG (HW) and MC@NLO + HERWIRI (HERWIRI). HERWIG is configured with two choices of the RMS of the intrinsic k_T distribution, 0 and 2.2 GeV/c.

ϕ^*

In Figure 4.39, differential measurements as functions of ϕ^*_Z are compared to the predictions from RESBOS [44–46] and POWHEG [104], where events are interfaced with a parton shower that is simulated using HERWIG [56, 57]. The differential cross-section measurements are given in Table 4.14 for SAMPLE-I. The quoted uncertainties are due to the sample size, systematic effects, the beam energy and the luminosity. The last column is the FSR correction. The corresponding results for SAMPLE-II are displayed

ϕ^*_Z	σ_Z [pb]	f_{FSR}
0.00 – 0.01	8.549 ± 0.099 ± 0.088 ± 0.107 ± 0.147	1.034±0.004
0.01 – 0.02	7.805 ± 0.096 ± 0.106 ± 0.098 ± 0.134	1.035±0.003
0.02 – 0.03	7.051 ± 0.091 ± 0.083 ± 0.088 ± 0.121	1.034±0.004
0.03 – 0.05	11.362 ± 0.114 ± 0.108 ± 0.142 ± 0.195	1.029±0.003
0.05 – 0.07	8.124 ± 0.097 ± 0.120 ± 0.102 ± 0.140	1.026±0.003
0.07 – 0.10	8.436 ± 0.097 ± 0.074 ± 0.105 ± 0.145	1.021±0.003
0.10 – 0.15	8.611 ± 0.098 ± 0.131 ± 0.108 ± 0.148	1.020±0.003
0.15 – 0.20	4.819 ± 0.073 ± 0.092 ± 0.060 ± 0.083	1.018±0.004
0.20 – 0.30	5.206 ± 0.076 ± 0.058 ± 0.065 ± 0.090	1.019±0.004
0.30 – 0.40	2.541 ± 0.054 ± 0.051 ± 0.032 ± 0.044	1.022±0.006
0.40 – 0.60	2.018 ± 0.048 ± 0.060 ± 0.025 ± 0.035	1.024±0.007
0.60 – 0.80	0.755 ± 0.029 ± 0.035 ± 0.009 ± 0.013	1.029±0.011
0.80 – 1.20	0.457 ± 0.023 ± 0.018 ± 0.006 ± 0.008	1.025±0.014
1.20 – 2.00	0.166 ± 0.014 ± 0.011 ± 0.002 ± 0.003	1.030±0.023
2.00 – 4.00	0.045 ± 0.008 ± 0.017 ± 0.001 ± 0.001	1.031±0.041

Table 4.16: Inclusive differential cross-sections for Z boson production as a function of ϕ^*_Z at $\sqrt{s} = 7$ TeV. Uncertainties are due to the sample size, systematic effects, the beam energy and the luminosity.

in Figure 4.40 and given in Table 4.17.

Comparisons of measurements to MC@NLO + HERWIRI and MC@NLO + HERWIG are shown in Figure 4.41 and Figure 4.42. Here HERWIG is configured with the RMS of the intrinsic k_T (see Section 2.4.4) distribution set to 0 GeV/c in one instance and 2.2 GeV/c in another. The predictions straddle the measurement at low ϕ^*_Z. The high ϕ^*_Z tails are underestimated.

ϕ^*_Z	σ_Z [pb]	f_{FSR}
0.00 – 0.01	10.442 ± 0.077 ± 0.118 ± 0.120 ± 0.122	1.037±0.003
0.01 – 0.02	9.704 ± 0.076 ± 0.116 ± 0.112 ± 0.113	1.035±0.003
0.02 – 0.03	8.510 ± 0.071 ± 0.130 ± 0.098 ± 0.099	1.032±0.003
0.03 – 0.05	13.749 ± 0.089 ± 0.151 ± 0.158 ± 0.161	1.029±0.002
0.05 – 0.07	10.085 ± 0.076 ± 0.119 ± 0.116 ± 0.118	1.025±0.004
0.07 – 0.10	10.662 ± 0.077 ± 0.159 ± 0.123 ± 0.125	1.021±0.003
0.10 – 0.15	10.575 ± 0.077 ± 0.133 ± 0.122 ± 0.123	1.020±0.003
0.15 – 0.20	6.322 ± 0.059 ± 0.074 ± 0.073 ± 0.074	1.018±0.003
0.20 – 0.30	6.681 ± 0.061 ± 0.085 ± 0.077 ± 0.078	1.019±0.004
0.30 – 0.40	3.213 ± 0.042 ± 0.064 ± 0.037 ± 0.038	1.021±0.006
0.40 – 0.60	2.837 ± 0.040 ± 0.055 ± 0.033 ± 0.033	1.025±0.007
0.60 – 0.80	1.030 ± 0.024 ± 0.027 ± 0.012 ± 0.012	1.026±0.011
0.80 – 1.20	0.670 ± 0.020 ± 0.030 ± 0.008 ± 0.008	1.027±0.011
1.20 – 2.00	0.263 ± 0.013 ± 0.022 ± 0.003 ± 0.003	1.028±0.021
2.00 – 4.00	0.094 ± 0.008 ± 0.023 ± 0.001 ± 0.001	1.035±0.040

Table 4.17: Inclusive differential cross-sections for Z boson production in Sample-II as functions of ϕ^*_Z. Uncertainties are due to the sample size, systematic effects, the beam energy and the luminosity.

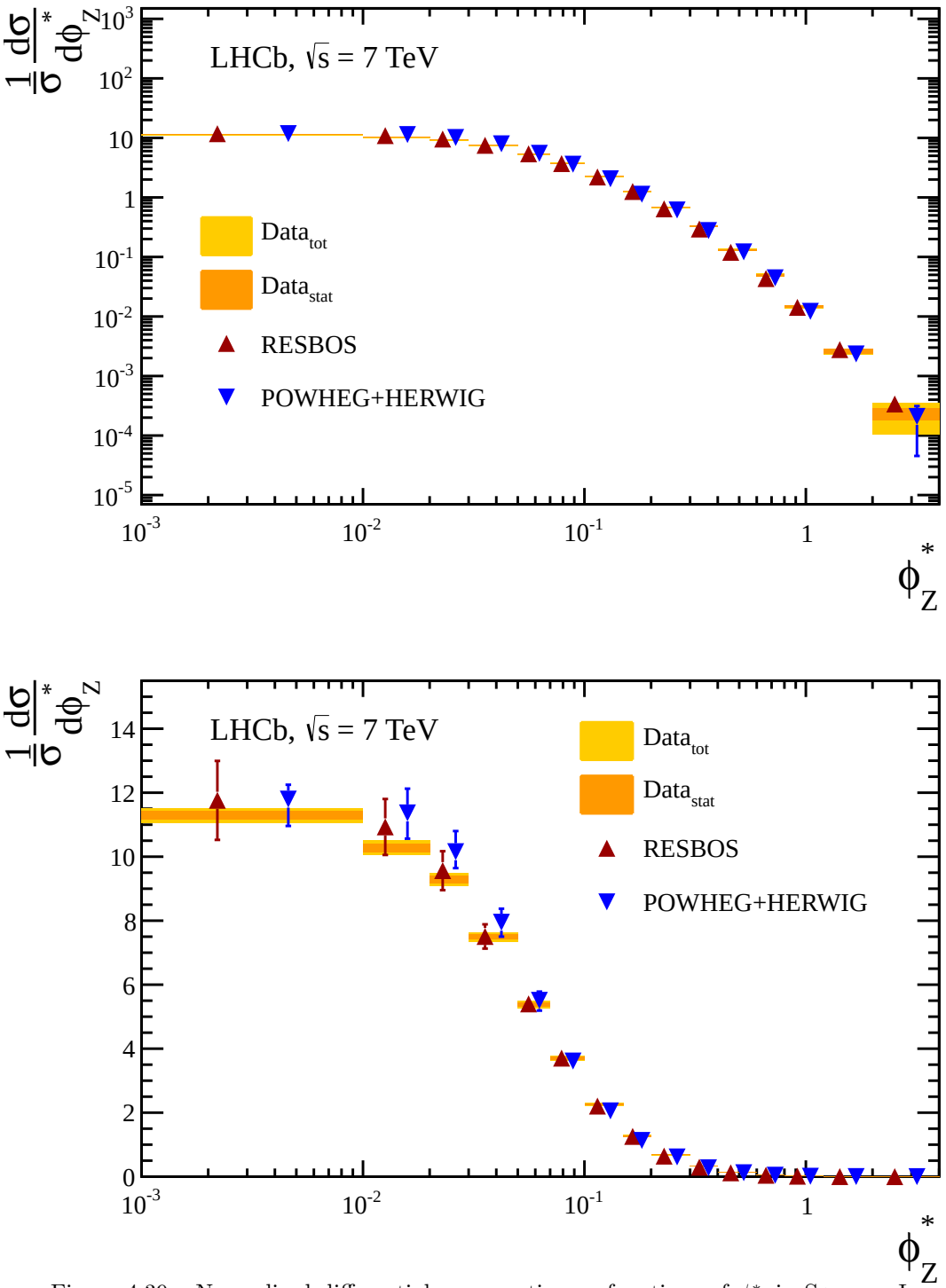

Figure 4.39: Normalised differential cross-section as functions of ϕ_Z^* in SAMPLE-I on logarithmic (top) and linear (bottom) scales. The shaded (yellow) bands indicate the statistical and total uncertainties on the measurements, which are symmetric about the central value. The measurements are compared to the predictions of RESBOS and POWHEG + HERWIG.

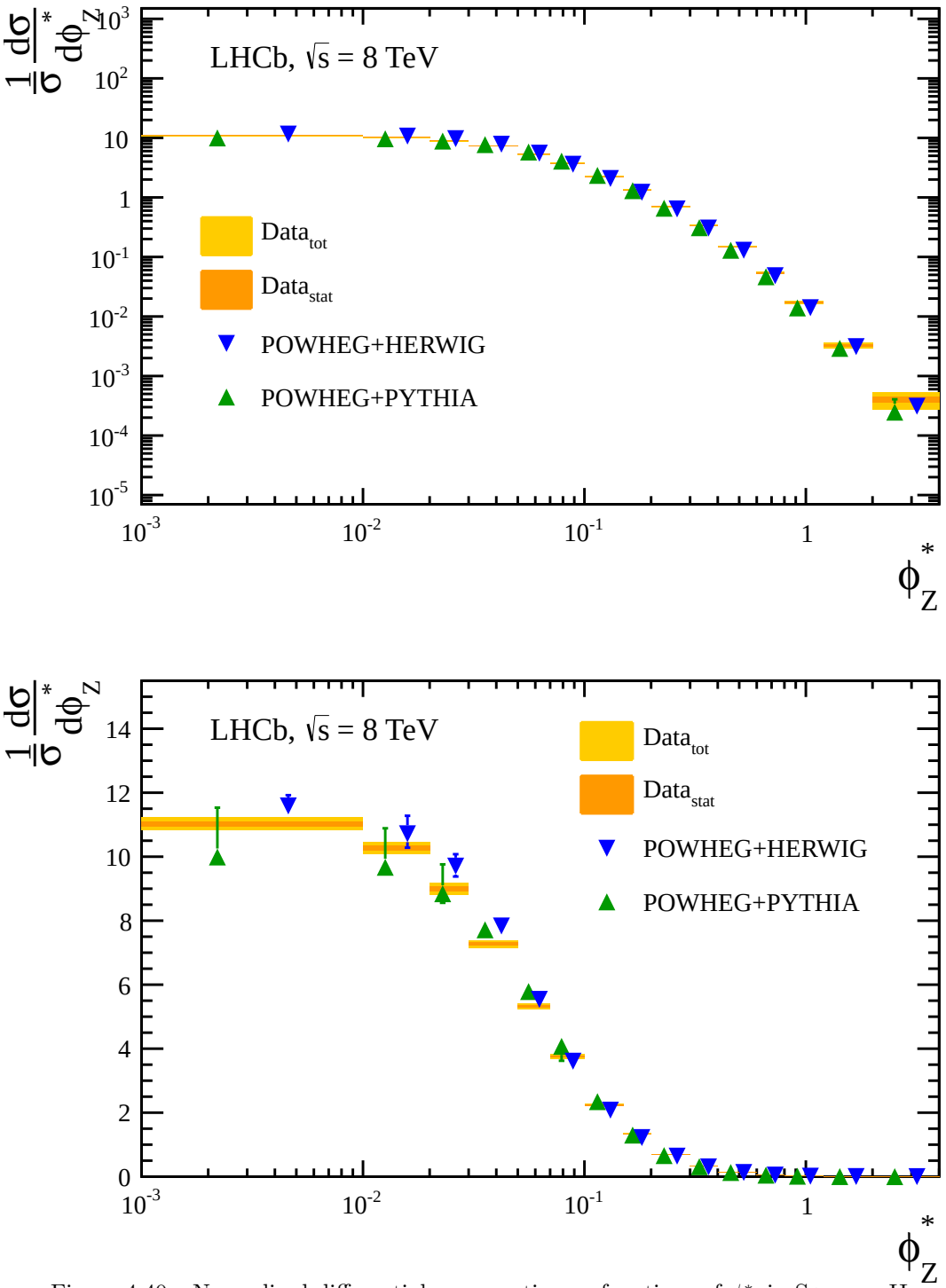

Figure 4.40: Normalised differential cross-section as functions of ϕ^*_Z in SAMPLE-II on logarithmic (top) and linear (bottom) scales. The shaded (yellow) bands indicate the statistical and total uncertainties on the measurements, which are symmetric about the central value. The measurements are compared to the predictions of POWHEG + PYTHIA and POWHEG + HERWIG.

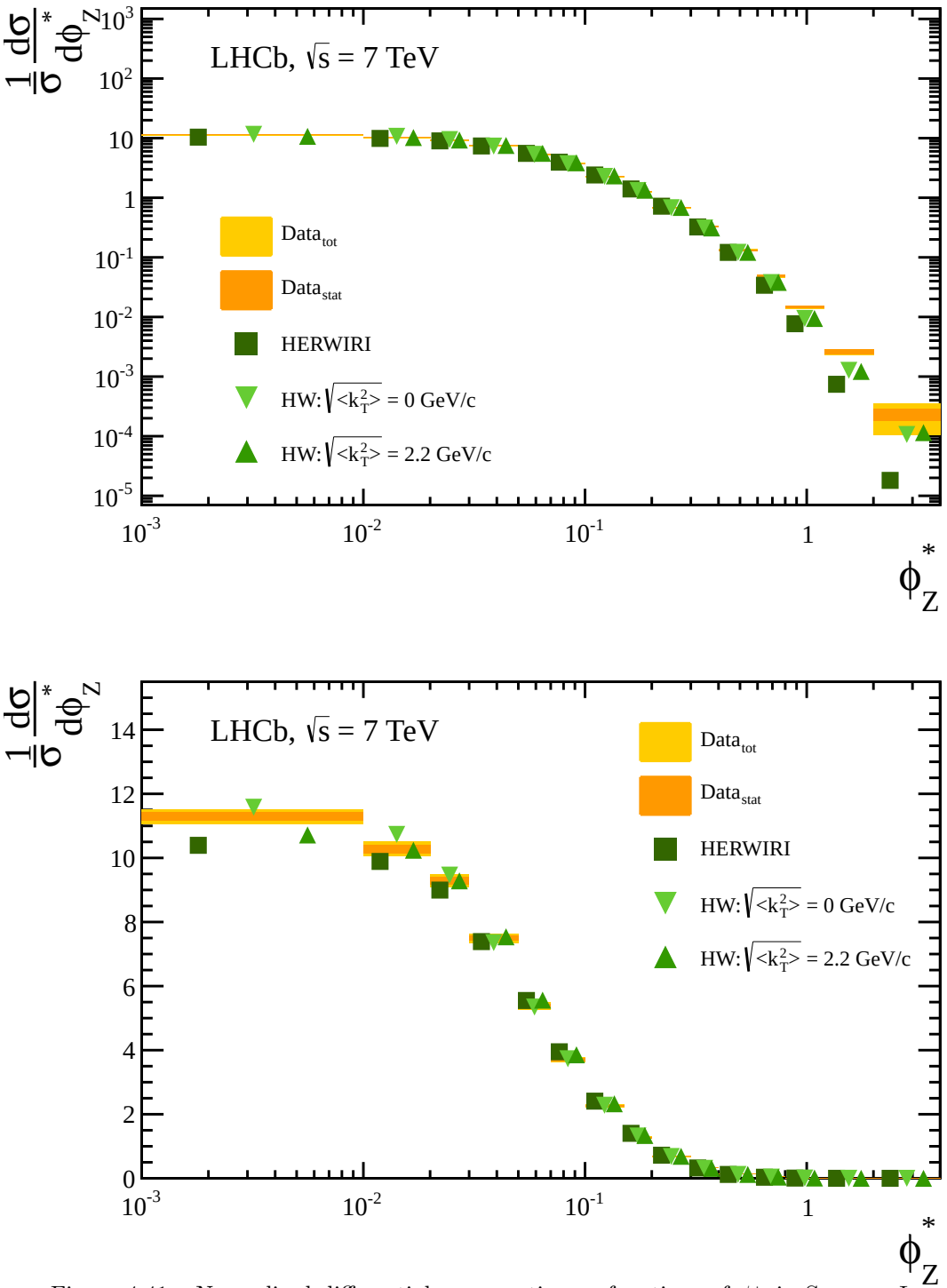

Figure 4.41: Normalised differential cross-section as functions of ϕ_Z^* in SAMPLE-I on logarithmic (top) and linear (bottom) scales. The shaded (yellow) bands indicate the statistical and total uncertainties on the measurements, which are symmetric about the central value. The measurements are compared to MC@NLO + HERWIG (HW) and MC@NLO + HERWIRI (HERWIRI). HERWIG is configured with two choices of the RMS of the intrinsic k_T distribution, 0 and 2.2 GeV/c.

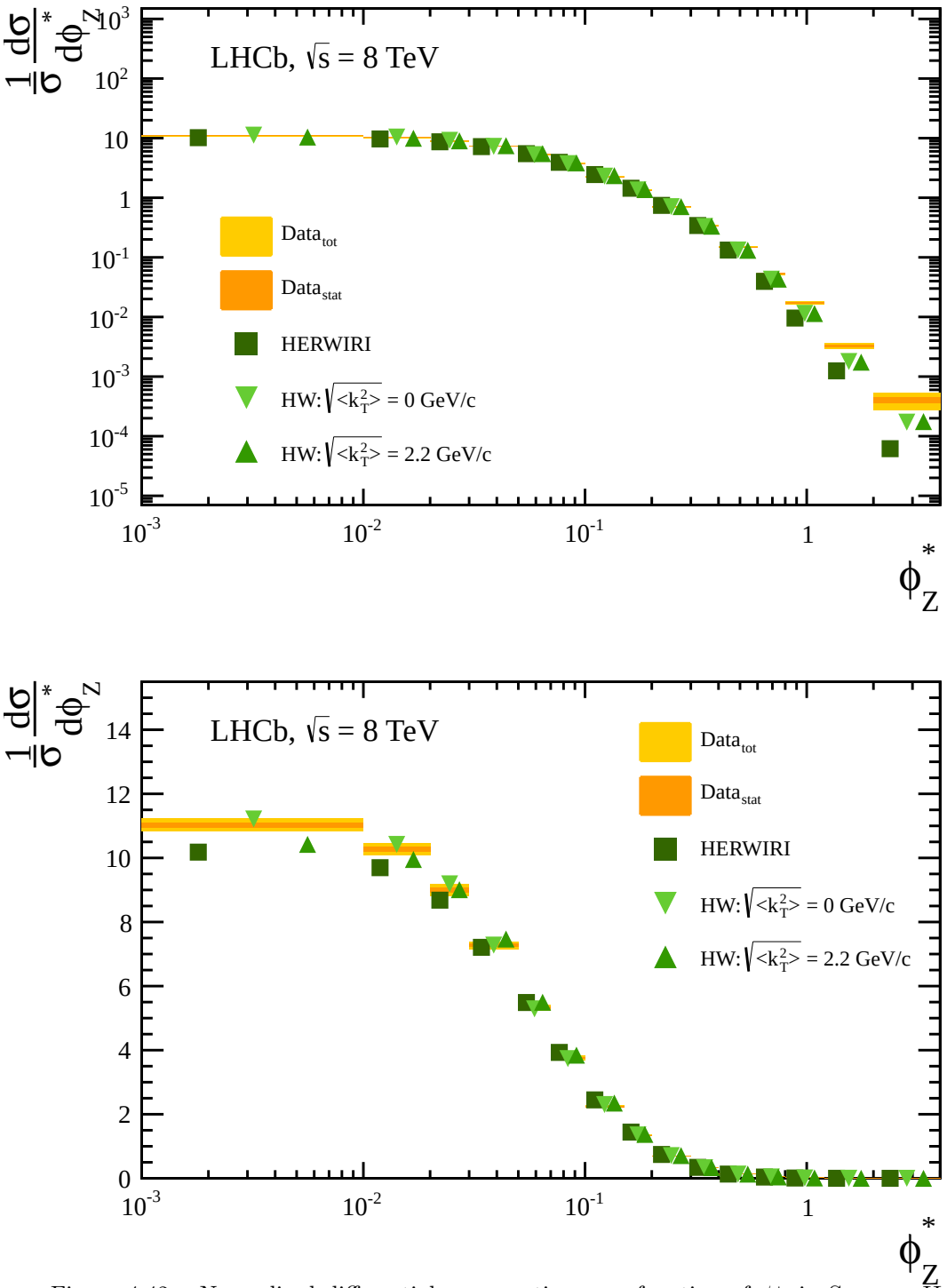

Figure 4.42: Normalised differential cross-section as a function of ϕ_Z^* in Sample-II on logarithmic (top) and linear (bottom) scales. The shaded (yellow) bands indicate the statistical and total uncertainties on the measurements, which are symmetric about the central value. The measurements are compared to MC@NLO + Herwig (HW) and MC@NLO + Herwiri (HERWIRI). Herwig is configured with two choices of the RMS of the intrinsic k_T distribution, 0 and 2.2 GeV/c.

Muon pseudorapidity

The measurements of the Z boson cross-sections as functions of η^{μ} are shown in Figure 4.43. The plot shows that there is a preference for the Z to decay to forward muons and central anti-muons. The differential cross-section measurements are given in Table 4.18 for SAMPLE-I. The quoted uncertainties are due to the sample size, systematic effects, the beam energy and the luminosity. The last column is the FSR correction.

η^{μ}	$\sigma_Z(\eta^{\mu^-})$ [pb]	$f_{\mathrm{FSR}}(\eta^{\mu^-})$
2.00 – 2.25	50.747 ± 0.525 ± 0.628 ± 0.634 ± 0.872	1.029±0.004
2.25 – 2.50	49.236 ± 0.505 ± 0.506 ± 0.615 ± 0.847	1.025±0.003
2.50 – 2.75	45.096 ± 0.483 ± 0.405 ± 0.564 ± 0.775	1.024±0.004
2.75 – 3.00	40.651 ± 0.457 ± 0.392 ± 0.508 ± 0.699	1.024±0.004
3.00 – 3.25	33.748 ± 0.417 ± 0.310 ± 0.422 ± 0.580	1.023±0.003
3.25 – 3.50	28.578 ± 0.380 ± 0.272 ± 0.357 ± 0.491	1.026±0.005
3.50 – 4.00	18.961 ± 0.219 ± 0.155 ± 0.237 ± 0.326	1.029±0.003
4.00 – 4.50	8.971 ± 0.156 ± 0.108 ± 0.112 ± 0.154	1.039±0.004

η^{μ}	$\sigma_Z(\eta^{\mu^+})$ [pb]	$f_{\mathrm{FSR}}(\eta^{\mu^+})$
2.00 – 2.25	47.718 ± 0.510 ± 0.749 ± 0.596 ± 0.820	1.029±0.005
2.25 – 2.50	46.445 ± 0.490 ± 0.566 ± 0.581 ± 0.799	1.025±0.003
2.50 – 2.75	44.459 ± 0.480 ± 0.476 ± 0.556 ± 0.764	1.024±0.003
2.75 – 3.00	39.707 ± 0.451 ± 0.405 ± 0.496 ± 0.683	1.024±0.003
3.00 – 3.25	35.621 ± 0.429 ± 0.427 ± 0.445 ± 0.612	1.024±0.004
3.25 – 3.50	29.553 ± 0.387 ± 0.319 ± 0.369 ± 0.508	1.025±0.005
3.50 – 4.00	20.320 ± 0.227 ± 0.216 ± 0.254 ± 0.349	1.027±0.005
4.00 – 4.50	9.889 ± 0.164 ± 0.170 ± 0.124 ± 0.170	1.038±0.005

Table 4.18: Inclusive differential cross-sections for Z boson production as functions of muon η in SAMPLE-I. Uncertainties are due to the sample size, systematic effects, the beam energy and the luminosity.

The corresponding results for SAMPLE-II are displayed in Figure 4.44 and given in Table 4.19.

η^{μ}	$\sigma_Z(\eta^{\mu^-})$ [pb]	$f_{\mathrm{FSR}}(\eta^{\mu^-})$
2.00 – 2.25	61.108 ± 0.432 ± 0.718 ± 0.703 ± 0.714	1.029±0.004
2.25 – 2.50	57.539 ± 0.404 ± 0.516 ± 0.662 ± 0.672	1.025±0.003
2.50 – 2.75	53.542 ± 0.382 ± 0.455 ± 0.616 ± 0.625	1.024±0.004
2.75 – 3.00	49.479 ± 0.367 ± 0.417 ± 0.569 ± 0.578	1.024±0.003
3.00 – 3.25	43.710 ± 0.343 ± 0.366 ± 0.503 ± 0.510	1.023±0.004
3.25 – 3.50	36.089 ± 0.308 ± 0.315 ± 0.415 ± 0.421	1.025±0.005
3.50 – 4.00	25.886 ± 0.186 ± 0.200 ± 0.298 ± 0.302	1.027±0.003
4.00 – 4.50	13.344 ± 0.138 ± 0.136 ± 0.153 ± 0.156	1.037±0.004

η^{μ}	$\sigma_Z(\eta^{\mu^+})$ [pb]	$f_{\mathrm{FSR}}(\eta^{\mu^+})$
2.00 – 2.25	56.277 ± 0.415 ± 0.706 ± 0.647 ± 0.657	1.029±0.006
2.25 – 2.50	54.725 ± 0.395 ± 0.501 ± 0.629 ± 0.639	1.025±0.003
2.50 – 2.75	52.359 ± 0.378 ± 0.409 ± 0.602 ± 0.611	1.025±0.003
2.75 – 3.00	49.736 ± 0.368 ± 0.419 ± 0.572 ± 0.581	1.024±0.003
3.00 – 3.25	44.050 ± 0.346 ± 0.387 ± 0.507 ± 0.514	1.023±0.004
3.25 – 3.50	37.968 ± 0.317 ± 0.325 ± 0.437 ± 0.443	1.025±0.004
3.50 – 4.00	27.702 ± 0.192 ± 0.223 ± 0.319 ± 0.323	1.027±0.004
4.00 – 4.50	14.705 ± 0.144 ± 0.148 ± 0.169 ± 0.172	1.035±0.005

Table 4.19: Inclusive differential cross-sections for Z boson production as functions of muon η in SAMPLE-II. Uncertainties are due to the sample size, systematic effects, the beam energy and the luminosity.

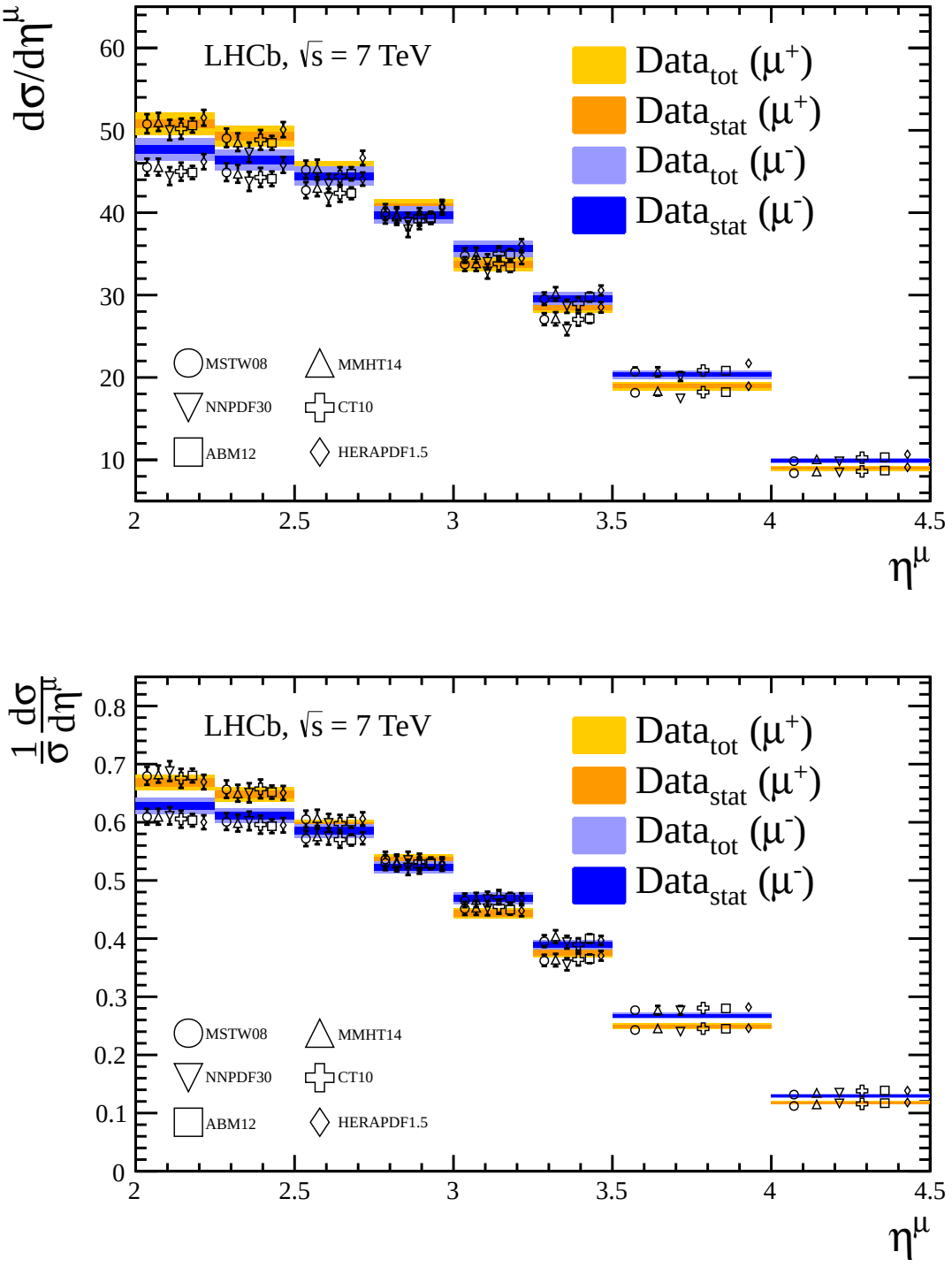

Figure 4.43: Differential (top) and normalised differential (bottom) Z cross-sections in bins of muon pseudorapidity for SAMPLE-I. Measurements, represented as bands corresponding to the (orange (blue) for $\mu^+(\mu^-)$) statistical and (yellow (light blue) for $\mu^+(\mu^-)$) total uncertainty, are compared to NNLO predictions with different parameterisations of the PDFs.

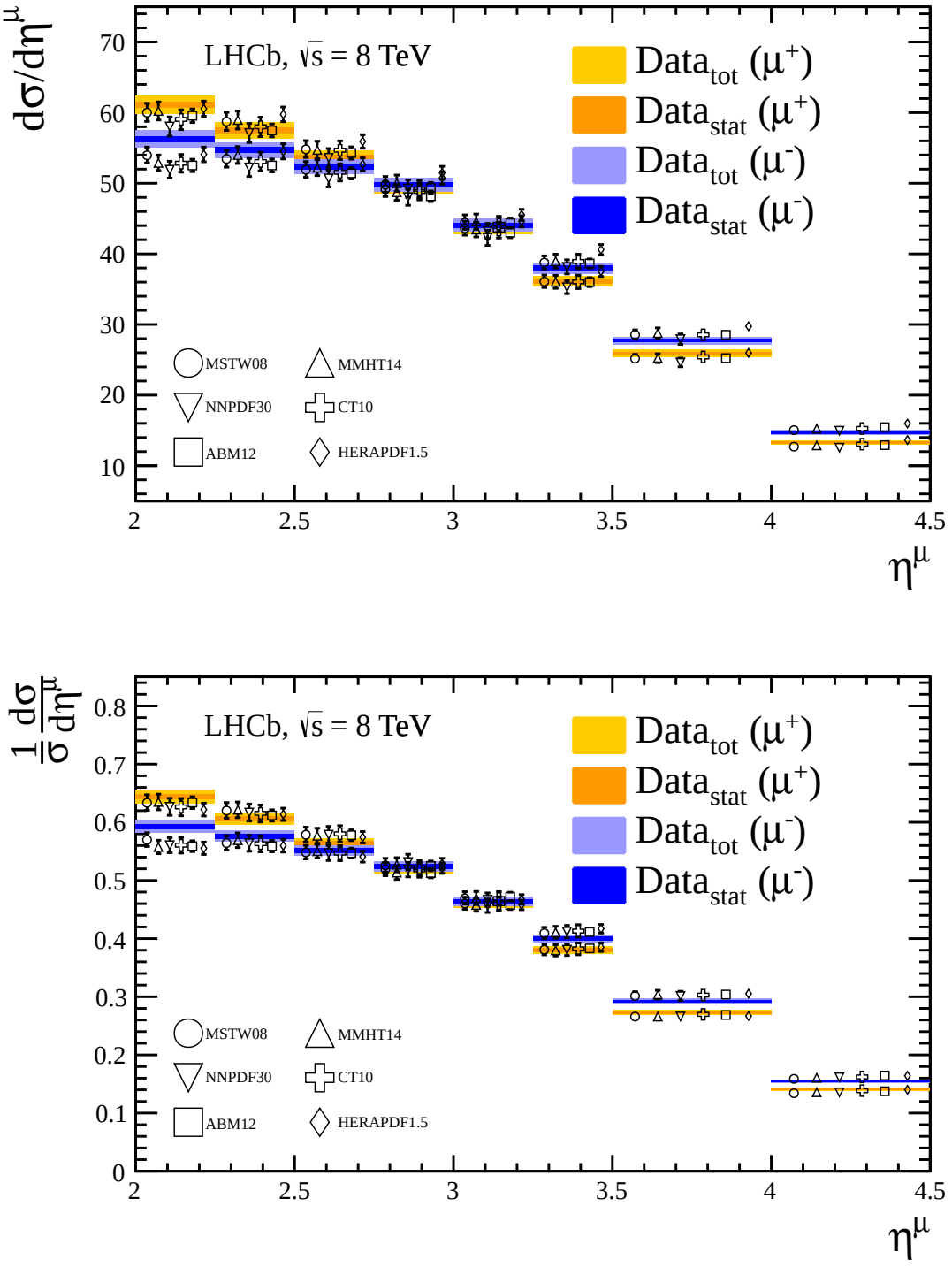

Figure 4.44: Differential (top) and normalised differential (bottom) Z cross-sections in bins of muon pseudorapidity for Sample-II. Measurements, represented as bands corresponding to the (orange (blue) for $\mu^+(\mu^-)$) statistical and (yellow (light blue) for $\mu^+(\mu^-)$) total uncertainty, are compared to NNLO predictions with different parameterisations of the PDFs.

4.6.2 Total cross-section

The total cross-section is obtained by summing the contributions of the y_Z bins. The total inclusive cross-section for $Z \to \mu^+\mu^-$ production at $\sqrt{s} = 7$ TeV for muons with $p_T > 20$ GeV/c in the pseudorapidity region $2.0 < \eta < 4.5$ and the invariant mass range $60 < M_{\mu^+\mu^-} < 120$ GeV/c^2 is measured to be

$$\sigma^{7\ \mathrm{TeV}}_{Z\to\mu^+\mu^-} = 76.0 \pm 0.3 \pm 0.5 \pm 1.0 \pm 1.3 \ \ \mathrm{pb} \tag{4.15}$$

where the quoted uncertainties are due to the sample size, systematic effects, the beam energy and the luminosity. The uncertainties are calculated by taking the correlation between the measurements into account. These are calculated using the methods explained in Section 5.3, and are given in Appendix E. Summing the ϕ^* and p_T distributions give the same central value for the cross-section with slightly larger uncertainties.

This measurement agrees with the NNLO prediction of FEWZ. The agreement can be seen in Figure 4.45, where the total cross-section measurement is compared to the predictions of FEWZ configured with various PDF sets. It is noted that the HERAPDF1.5

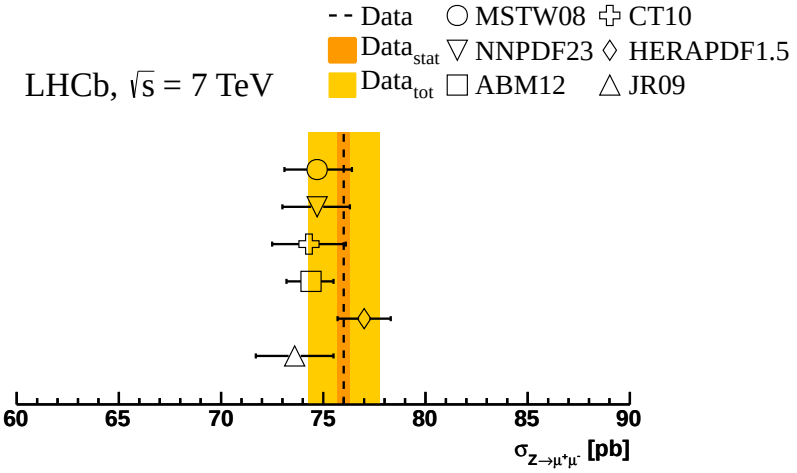

Figure 4.45: Measurement of the Z boson production cross-section times branching ratio to muons at $\sqrt{s} = 7$ TeV. The data are compared to predictions of NNLO perturbative QCD, as implemented by the FEWZ generator, using various PDF sets.

set leads to a prediction that is slightly higher than that measured, while other PDF sets are systematically lower than the measurement. The cross-section at $\sqrt{s} = 8$ TeV is measured as

$$\sigma^{8\ \mathrm{TeV}}_{Z\to\mu^+\mu^-} = 95.0 \pm 0.3 \pm 0.7 \pm 1.1 \pm 1.1 \ \ \mathrm{pb}. \tag{4.16}$$

The correlation coefficients are given in Appendix E. Comparisons with FEWZ and various PDF sets are shown in Figure 4.46 and good agreement is again observed. The central value of the HERAPDF1.5 prediction is again slightly higher than the measurement. As explained in Section 2.3.3, the MMHT14 PDF set is an update of the MSTW08 PDF set. MMHT14 gives only a slightly higher cross-section than MSTW08, so one can conclude that the updates have little impact on Z boson production.

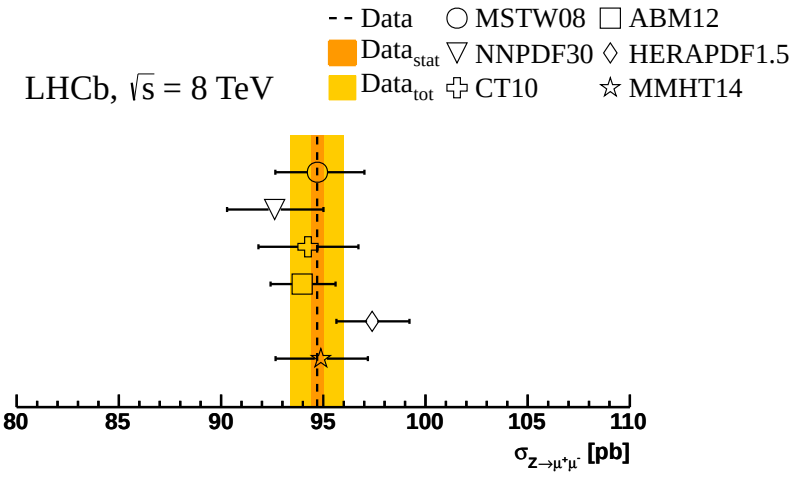

Figure 4.46: Measurement of the Z boson production cross-section times branching ratio to muons at $\sqrt{s} = 8$ TeV. The data are compared to predictions of NNLO perturbative QCD, as implemented by the FEWZ generator, using various PDF sets.

The Z boson cross-section has also been measured by the ATLAS [105] and CMS [106], [107] collaborations in their respective fiducial volumes. The results are summarised in Table 4.20. The relative precision of the measurements is expressed in terms of the fiducial cross-sections $\sigma_Z^{\text{fid.}}$ and their total uncertainties $\delta\sigma_Z^{\text{fid.}}$. The integrated luminosities ($\mathcal{L}$)

	$\sqrt{s} = 7$ TeV		$\sqrt{s} = 8$ TeV	
Collaboration	$\mathcal{L}$ [pb^{-1}]	$\frac{\delta\sigma_Z^{\text{fid.}}}{\sigma_Z^{\text{fid.}}}$ x 100 [%]	$\mathcal{L}$ [pb^{-1}]	$\frac{\delta\sigma_Z^{\text{fid.}}}{\sigma_Z^{\text{fid.}}}$ x 100 [%]
ATLAS	36	3.5	–	–
CMS	36	4.0	18	4.2
LHCb	1000	2.3	2000	1.8

Table 4.20: Relative precision on Z boson cross-section measurements from different LHC experiments. The ATLAS and CMS results do not include uncertainties due to proton beam energy.

and centre-of-mass energies of the samples are also indicated. The LHCb result has smaller uncertainties due to more precise luminosity determinations and the negligible effect of pileup.

4.6.3 Lepton universality

LHCb has also measured the Z boson cross-section at $\sqrt{s}$= 7 TeV in the electon [108] and tau lepton [109] channels. Consequently, a measurement of lepton universality in the forward region can be made. A summary of the Z boson cross-section measurements at $\sqrt{s}$= 7 TeV is provided in Figure 4.47. The ratio $R_{e\mu}$ is defined as the ratio of the Z

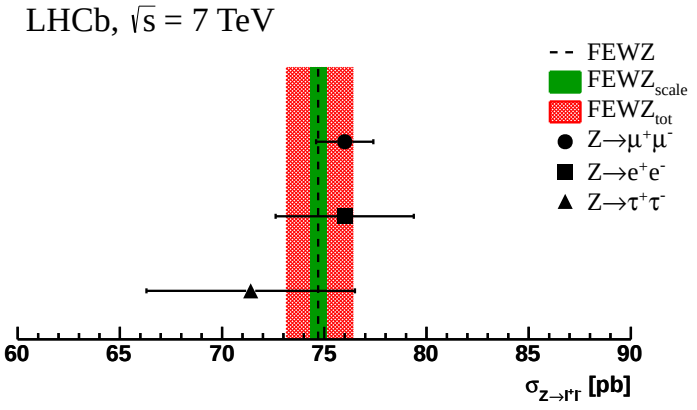

Figure 4.47: Measurements of the Z boson production cross-section times branching ratio to three charged lepton species at $\sqrt{s}$ = 7 TeV. Beam energy uncertainties are not displayed. The data are compared to predictions of NNLO perturbative QCD, as implemented by the FEWZ generator.

production cross-sections in the electron and muon channels. The ratio $R_{\tau\mu}$ is defined as the ratio of the Z production cross-sections in the tau-lepton and muon channels.

$$R_{e\mu} = \frac{\sigma_{Z\to e^+e^-}}{\sigma_{Z\to\mu^+\mu^-}} \tag{4.17}$$

$$R_{\tau\mu} = \frac{\sigma_{Z\to\tau^+\tau^-}}{\sigma_{Z\to\mu^+\mu^-}} \tag{4.18}$$

For this calculation the luminosity uncertainty is assumed fully correlated and cancels in the ratio. All other uncertainties are assumed uncorrelated. The values are found to be $R_{e\mu} = 1.00 \pm 0.03$ and $R_{\tau\mu} = 0.94 \pm 0.06$ consistent with a universal coupling of the Z boson to charged leptons. This is to be compared with similar measurements from the SLC and LEP ep-colliders [4], where these quantities are determined with a precision of 0.3%.

4.6.4 Extraction of intrinsic k_T

As explained in Section 2.4.4, the RMS of the intrinsic k_T distribution is a parameter used in shower MC programmes. It accounts for any transverse momentum given to initial-state partons other than that generated by initial-state radiation [110]. The width of the p_T distribution of generated Z bosons is sensitive to this parameter. The default value used in HERWIG++ 2.7.0 is 2.2 GeV/c.

The measured Z boson p_T distributions (see Tables 4.14 and 4.15) may be used to extract this parameter, as in Ref. [110]. Using HERWIG++ 2.7.0, a scan in steps of 0.1 GeV/c from 1.5 to 2.9 GeV/c is performed. The predicted p_T distributions are superimposed on measured cross-sections from SAMPLE-I in Figure 4.48. The χ^2/ndf between the

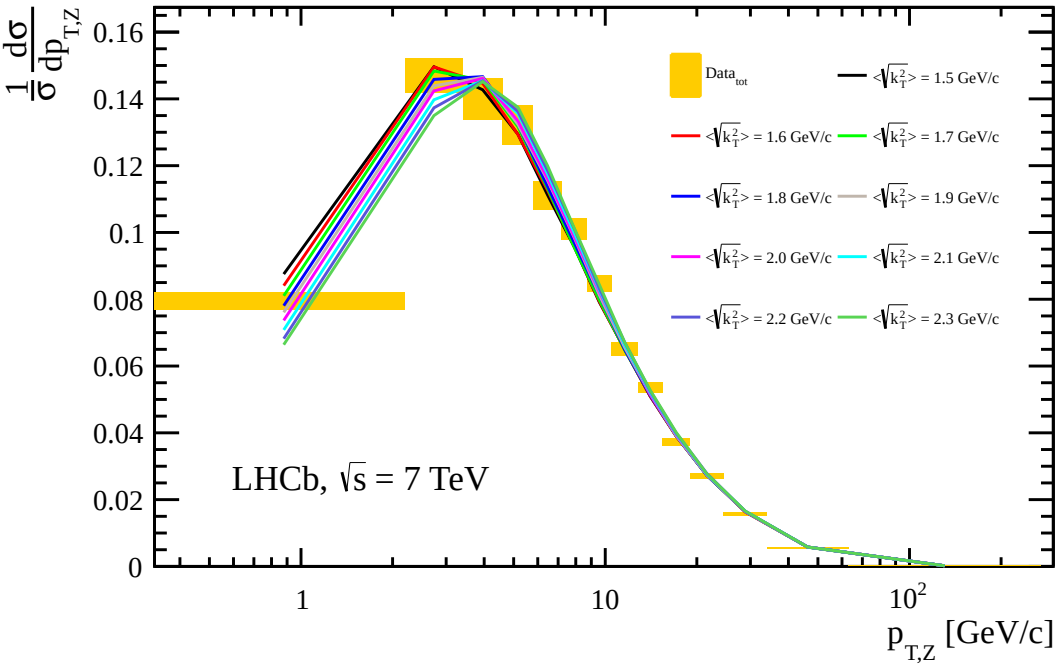

Figure 4.48: The Z boson p_T distribution measured from SAMPLE-I compared to HERWIG++. The best agreement is achieved with $< \sqrt{k_T^2} > = 1.9$ GeV/c, which is slightly less than the default value in HERWIG++ of 2.2 GeV/c.

these distributions and the data are shown in Table 4.21. The data show a preference for a value of 1.9 GeV/c. The same procedure applied to SAMPLE-II data indicates a preferred value of 1.8 GeV/c (see Figure 4.49). These values are consistent with the values obtained from the CDF collaboration's data [110, 111].

$< \sqrt{k_T^2} >$ [GeV/c]	1.5	1.6	1.7	1.8	1.9	2.0	2.1	2.2	2.3
χ^2/ndf (SAMPLE-I)	1.54	1.37	1.26	1.24	1.23	1.37	1.57	1.78	1.99
χ^2/ndf (SAMPLE-II)	1.72	1.53	1.48	1.44	1.70	1.84	2.12	2.35	2.73

Table 4.21: χ^2 compatibility between HERWIG++ and data for different choices of the RMS of the intrinsic k_T distribution.

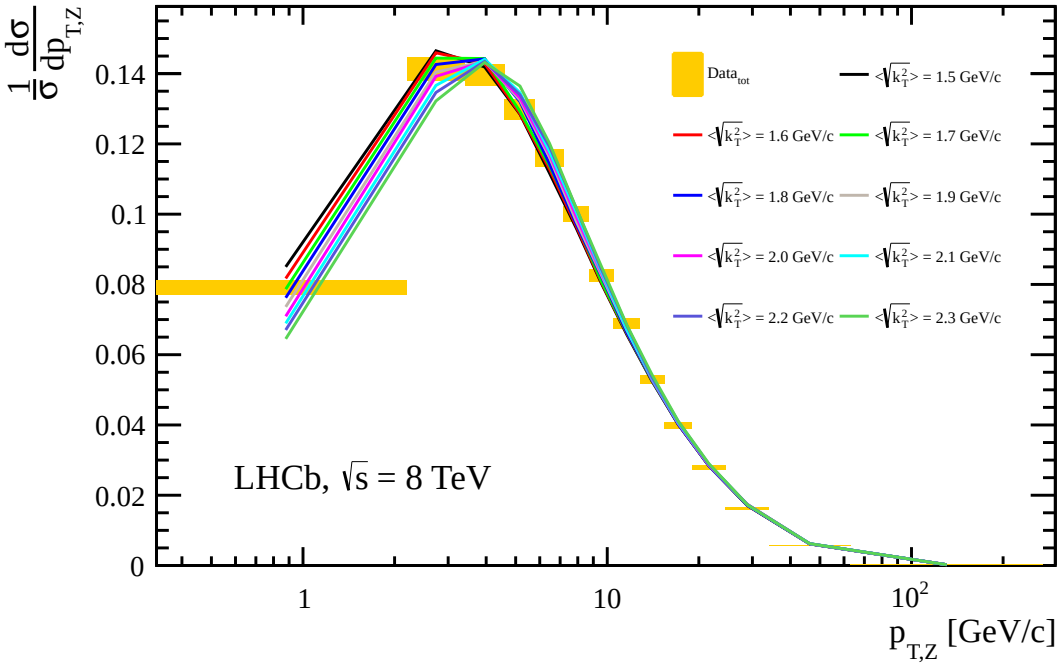

Figure 4.49: The Z boson p_T distribution measured from SAMPLE-II compared to HERWIG++. The best agreement is achieved with $< \sqrt{k_T^2} > = 1.8$ GeV/c, which is slightly less than the default value in HERWIG++ of 2.2 GeV/c.

Chapter 5

A precise test of the Standard Model

Both measurements in the previous chapter have a precision of approximately 2%, where the majority of the uncertainty is due to the luminosity and the proton beam energy. Of course, the luminosity and its uncertainty are not specific to the current analysis. The same value is used for any production cross-section measurement, provided the data samples used to make the measurement are the same. The size of the uncertainty due to the proton beam energy depends on the rate of change of the cross-section in the vicinity of the nominal centre-of-mass energy.

It is interesting to consider what happens when cross-sections are combined, for instance a Z boson cross-section measurement and a W boson cross-section measurement from the same data set. How do uncertainties propagate onto their sum, difference, product and quotient? The answer depends on the degree of correlation between the measurements. The correlations between electroweak boson cross-section measurements, and the correlations between electroweak boson cross-section predictions, are usually positive. This means that the relative precision on a sum, difference or product is larger than the relative precision on the cross-sections individually, while the relative precision on a quotient is smaller. This chapter describes the measurement of W to Z boson production cross-section ratios.

As can be seen from Figures 4.45 and 4.46, the SM predictions of the Z boson cross-sections also have a precision of about 2%. Similar uncertainties apply to the predicted W boson cross-sections. The uncertainties on these predictions are due to the PDFs, the factorisation and renormalisation scales, the numerical integration errors and α_s. The initial-state quark energy is larger for Z production than W production due to its

higher mass, otherwise the PDF uncertainties are largely correlated. The scale and α_s uncertainties are also highly correlated [83]. Since uncertainties are correlated between cross-section predictions, predicted cross-section ratios are relatively much more precise. The high precision, at both the experimental and theoretical level, make measurements of cross-section ratios a stringent test of the SM (at the level of about 1%).

Ratios of cross-sections and ratios-of-ratios of cross-sections at different centre-of-mass energies may also be measured, and are important for two reasons. First, they can be used to calibrate the ratio between the luminosities of each data set [112]. Consider the ratio of Z boson cross-sections at two different centre-of-mass energies as an example. The PDF uncertainties on the cross-section predictions are highly correlated (although the contribution from the quark sea is greater at larger beam energies) and cancel in the ratio. As a consequence, the SM prediction of this ratio is largely independent of the PDF set, varying by only a few parts per mille [112]. If the measurement differs from these predictions, where these are still within the dominant luminosity uncertainty, and if it is assumed that SM physics is the only physics at play, then the measurement can be used to calibrate the ratio of the luminosities. Second, the measurements can be used to search for Beyond Standard Model (BSM) contributions to the measured cross-sections [112]. It is important to point out that for a BSM particle (or BSM energy) to be detected with this method, it must decay to muons in the same kinematic region, and the production must have a sufficiently different dependence on centre-of-mass energy. BSM production that grows with centre-of-mass energy at the same rate as SM production cannot be excluded with this method because the measured (BSM+SM) and predicted (SM) ratios have the same values. This is shown explicitly in Appendix F.

5.1 W boson cross-section

About 11% of W bosons decay to muons and neutrinos. Neutrinos have negligibly small interaction cross-sections with typical particle-detector materials (see Chapter 3). Their presence is often inferred from a large imbalance between the known initial transverse energy, which is zero, and the visible transverse energy, $\vec{E}_T^{vis}$, of all final-state particles. The energy that accounts for this imbalance is called the missing transverse energy $\vec{E}_T^{miss}$, defined by

$$0 = \vec{E}_T^{miss} + \sum_i (\vec{E}_T^{vis})_i, \tag{5.1}$$

where i indexes the final-state particles.

Experiments with cylindrical geometry are well equipped to reconstruct the energies of all final-state particles. For these experiments, $\vec{E}_T^{miss}$ is an important variable [113, 114]. Since LHCb is a forward arm spectrometer, much of the initial centre-of-mass energy is not reconstructed inside the detector and $\vec{E}_T^{miss}$ cannot be accurately measured. This means that at LHCb, only the muon momentum is known; neither the mass nor p_T of the W boson is reconstructed. For this reason, W boson cross-sections are defined for muons with $p_T > 20$ GeV/c and $2 < \eta < 4.5$. This is the fiducial volume for the W boson measurements, which differs from that of the Z boson in that the muon kinematic requirements only apply to one lepton instead of two, and there is no W boson invariant mass requirement, since it is not reconstructed. Although the fiducial volumes differ, ratios of the fiducial cross-sections are still well-defined, and because they are similar, there is partial cancellation of common systematic uncertainties when one takes this ratio (see Section 5.3).

In this thesis, use is made of the $\sqrt{s} = 7$ TeV W boson cross-section measurements published in Ref. [115]. Preliminary measurements (soon to be published) of W boson cross-sections at $\sqrt{s} = 8$ TeV are also used. In order to measure the W boson cross-sections, samples of high-p_T muons are selected (SAMPLE-I and SAMPLE-II as before). The selection criteria are summarised in Table 5.1. Similar to the requirements of muons for the Z boson selection, muons for the W boson selection must satisfy the kinematic criteria $2.0 < \eta < 4.5$ and $20 < p_T < 70$ GeV/c. The muon tracks must also be of good quality with $Prob(\chi^2) > 1\%$ and $\frac{\sigma_p}{p} < 10\%$. The additional criteria that are not

$$
\begin{gathered}
2.0 < \eta < 4.5 \\
20 < p_T < 70 \text{ GeV/c} \\
Prob(\chi^2) > 1\% \\
\tfrac{\sigma_p}{p} < 10\% \\
p_T^{\text{cone}} < 2 \text{ GeV/c} \\
E_T^{\text{cone}} < 2 \text{ GeV} \\
p_T^{extra} < 2 \text{ GeV/c} \\
IP < 40\ \mu m \\
(E_{ECAL} + E_{HCAL})/pc < 4\%
\end{gathered}
$$

Table 5.1: Summary of muon selection requirements.

required of muons from decays of Z bosons are to reduce backgrounds.

Muons from decays of W bosons are generally isolated. To establish the degree of isolation, a cone with radius $R = \sqrt{\Delta\eta + \Delta\phi} < 0.5$ is constructed about the direction of the muon track. Neglecting the candidate muon's momentum, requiring that there is a small amount of transverse energy ($E_T^{\text{cone}} < 2$ GeV) and momentum ($p_T^{\text{cone}} < 2GeV/c$) in the cone cuts out generic QCD events. The variable p_T^{extra} denotes the p_T of other muons in

the event. Requiring that the transverse momentum of all other muons in the event is less than 2 GeV/c reduces the $Z \to \mu^+\mu^-$ contamination. The requirement on the impact parameter (IP), defined in Section 3.2, removes events whose muons are not consistent with originating at the primary vertex. These could be due to electroweak boson decays to τ-leptons, which in turn decay to muons, or semi-leptonic decays of heavy flavour hadrons. Genuine muons are expected to leave low energy deposits in the electromagnetic and hadronic calorimeters. The upper limit on the variable $(E_{ECAL} + E_{HCAL})/pc$ reduces punch-through of energetic pions and kaons to the muon stations.

The efficiency of these requirements is evaluated using a sample of Z bosons from data, where one muon plays the role of a neutrino. This sample is called the Pseudo-W sample. Selection efficiencies are evaluated by applying the requirements to the designated muon of the Pseudo-W sample. With the available statistics, the efficiency is the same for positively and negatively charged muons [116].

Evaluating the selection efficiency in this way biases the efficiency because the p_T distribution of muons from Z bosons is harder than the p_T distribution of muons from W bosons. The bias is corrected using differences observed on simulated W and Z boson samples. The correction has the effect of reducing the efficiency that is evaluated using the Pseudo-W sample. Simulation is also used to correct for the fact that the Pseudo-W sample requires two muons in the acceptance [116].

The muon p_T distributions of these samples are then fitted with templates representing both signal and background using the method of extended maximum likelihood. The fit for SAMPLE-I is shown in Figure 5.1. The cross-sections are then measured as a function of η using Equation 5.2.

$$\sigma_{W^\pm \to \mu^\pm \nu}(i) = \frac{1}{\mathcal{L}} \cdot \frac{N^{W^\pm}}{\varepsilon_{GEC}} \cdot \frac{\rho^{W^\pm}(i) \cdot f^{W^\pm}_{FSR}(i)}{\mathcal{A}^{W^\pm}(i) \cdot \varepsilon^{W}(i) \cdot \varepsilon^{W^\pm}_{SEL}(i)} \tag{5.2}$$

The number of W boson candidates in each η bin is given by $N^{W^\pm}$, and the purities evaluated from the template fit are denoted $\rho^{W^\pm}$. The luminosity is given by $\mathcal{L}$ and the GEC efficiency by ε_{GEC}. The W boson reconstruction efficiency ε^W is given by the product of a trigger efficiency, an identification efficiency and a tracking efficiency.

$$\epsilon^W(\eta^\mu) = \epsilon_{trg}(\eta^\mu) \cdot \epsilon_{id}(\eta^\mu) \cdot \epsilon_{trk}(\eta^\mu) \tag{5.3}$$

The acceptance correction, $\mathcal{A}^{W^\pm}$, corrects for the 70 GeV/c upper limit on the muon p_T. The efficiency of the selection criteria (E_T^{cone}, p_T^{cone}, p_T^{extra}, IP, and $(E_{ECAL}+E_{HCAL})/pc$) is denoted by $\epsilon^{W^\pm}_{SEL}$. The components that are common with the Z boson cross-sections

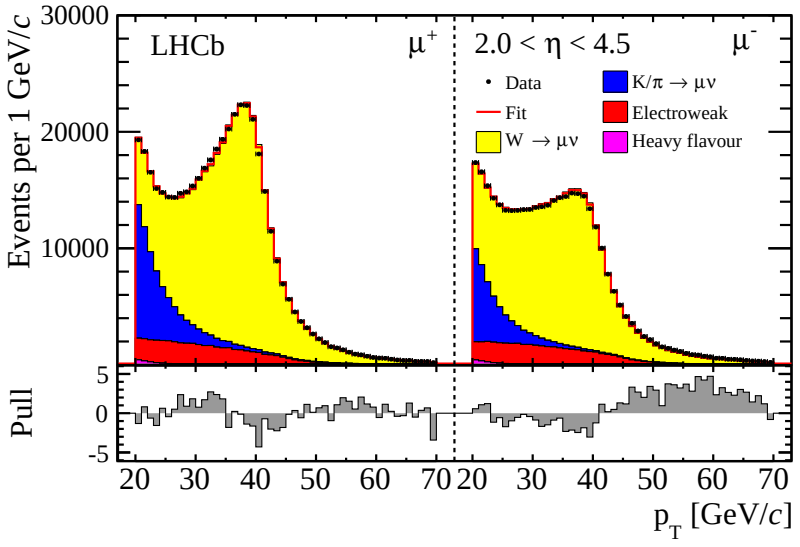

Figure 5.1: Transverse momentum distribution of the (left panel) positive and (right panel) negative muon candidates in SAMPLE-I. The data are compared to fitted contributions described in the legend. The fit residuals normalised to the data uncertainty are shown at the bottom of each distribution. Taken from Ref. [116].

defined in Equation 4.4 are the luminosity, the GEC efficiency and the individual muon reconstruction efficiencies.

The W^+ boson cross-sections measured at $\sqrt{s} = 7$ TeV used in this analysis is

$$\sigma_{W^+ \to \mu^+ \nu_\mu} = (878.0 \pm 2.1 \pm 6.7 \pm 9.3 \pm 15.0) \text{ pb}, \tag{5.4}$$

where the uncertainties are due to the sample size, systematic effects, the beam energy and the luminosity determination. The W^- boson cross-section is

$$\sigma_{W^- \to \mu^- \bar{\nu}_\mu} = (689.5 \pm 2.0 \pm 5.3 \pm 6.3 \pm 11.8) \text{ pb}. \tag{5.5}$$

These measurements are in good agreement with the predictions of NNLO perturbative QCD, as shown in Figure 5.2. The Z boson cross-section from Equation 4.15 is also plotted for completeness. The differential W boson cross-sections are given in Table 5.2.

At $\sqrt{s} = 8$ TeV, the W^+ boson cross-section is

$$\sigma_{W^+ \to \mu^+ \nu_\mu} = (1093.6 \pm 2.1 \pm 7.2 \pm 10.9 \pm 12.7) \text{ pb}, \tag{5.6}$$

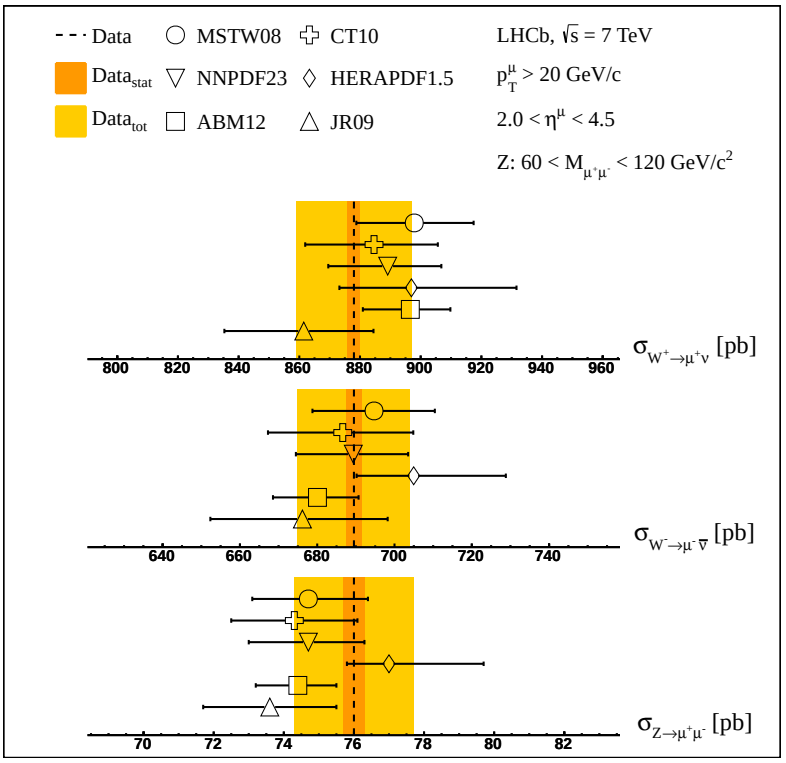

Figure 5.2: SAMPLE-I measurements ($\sqrt{s} = 7$ TeV) of electroweak boson production cross-sections compared to NNLO perturbative QCD, as implemented by the FEWZ generator using various PDF sets. The shaded (yellow) bands indicate the statistical and total uncertainties on the measurements, which are symmetric about the central value. The uncertainties on the theoretical predictions are due to the PDFs. Scale and α_s uncertainties are similar and about one third of the size.

and the W^- boson cross-section is

$$\sigma_{W^-\to\mu^-\bar{\nu}_\mu} = (818.4 \pm 1.9 \pm 5.0 \pm 7.0 \pm 9.5) \text{ pb}. \tag{5.7}$$

These measurements are also in good agreement with the predictions of NNLO perturbative QCD, as shown in Figure 5.3. The Z boson cross-section from Equation 4.16 is also plotted for completeness. The differential W boson cross-sections are given in Table 5.3.

The systematic uncertainties on the W boson cross-sections are summarised in Table 5.4. These uncertainties are discussed in Section 5.3, when considering how uncertainties on cross-sections propagate onto ratios.

η^μ	σ_{W^+} [pb]	$f_{\mathrm{FSR}}^{W^+}$
2.00 – 2.25	$192.2 \pm 1.2 \pm 3.5 \pm 2.0 \pm 3.3$	1.016 ± 0.004
2.25 – 2.50	$178.8 \pm 0.9 \pm 3.1 \pm 1.9 \pm 3.1$	1.018 ± 0.004
2.50 – 2.75	$154.3 \pm 0.8 \pm 2.1 \pm 1.6 \pm 2.6$	1.025 ± 0.005
2.75 – 3.00	$122.8 \pm 0.7 \pm 1.6 \pm 1.3 \pm 2.1$	1.015 ± 0.004
3.00 – 3.25	$94.3 \pm 0.6 \pm 1.3 \pm 1.0 \pm 1.6$	1.021 ± 0.005
3.25 – 3.50	$61.6 \pm 0.5 \pm 0.9 \pm 0.7 \pm 1.1$	1.015 ± 0.005
3.50 – 4.00	$60.0 \pm 0.5 \pm 0.7 \pm 0.6 \pm 1.0$	1.024 ± 0.005
4.00 – 4.50	$14.3 \pm 0.4 \pm 0.4 \pm 0.2 \pm 0.2$	1.021 ± 0.005

η^μ	σ_{W^-} [pb]	$f_{\mathrm{FSR}}^{W^-}$
2.00 – 2.25	$111.1 \pm 0.9 \pm 2.1 \pm 1.0 \pm 1.9$	1.019 ± 0.003
2.25 – 2.50	$104.9 \pm 0.7 \pm 1.9 \pm 1.0 \pm 1.8$	1.015 ± 0.003
2.50 – 2.75	$96.1 \pm 0.7 \pm 1.3 \pm 0.9 \pm 1.6$	1.010 ± 0.003
2.75 – 3.00	$88.4 \pm 0.7 \pm 1.5 \pm 0.8 \pm 1.5$	1.007 ± 0.002
3.00 – 3.25	$80.6 \pm 0.6 \pm 1.4 \pm 0.7 \pm 1.4$	1.009 ± 0.003
3.25 – 3.50	$68.6 \pm 0.6 \pm 1.5 \pm 0.6 \pm 1.2$	1.017 ± 0.005
3.50 – 4.00	$95.9 \pm 0.7 \pm 1.2 \pm 0.9 \pm 1.6$	1.012 ± 0.005
4.00 – 4.50	$43.8 \pm 0.8 \pm 1.2 \pm 0.4 \pm 0.7$	1.000 ± 0.000

Table 5.2: Inclusive differential cross-sections for W^+ (left) and W^- (right) boson production as functions of muon η, measured with SAMPLE-I data. Uncertainties are due to the sample size, systematic effects, the beam energy and the luminosity. These results are taken from Ref. [115].

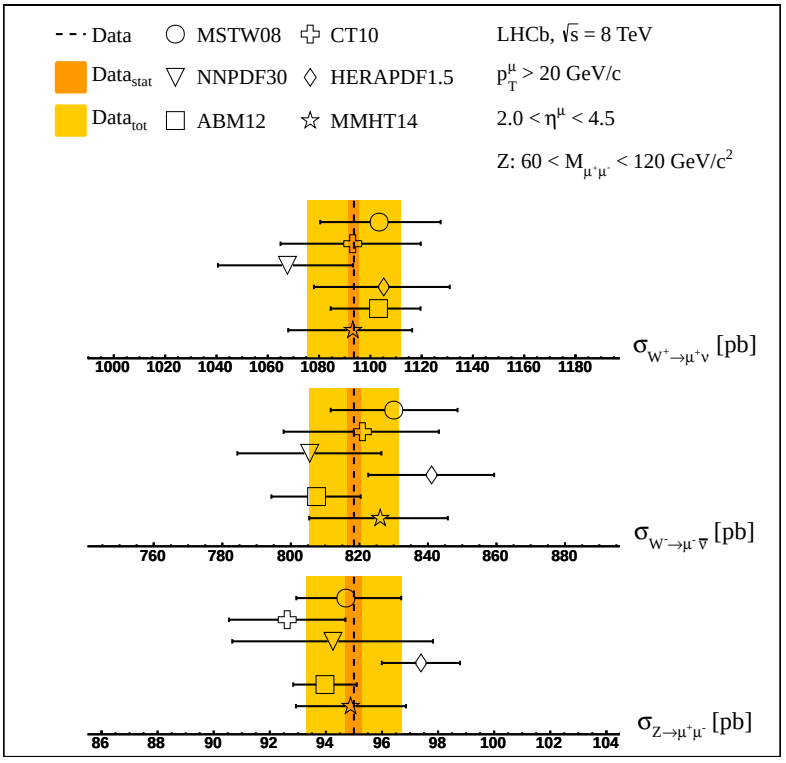

Figure 5.3: SAMPLE-II measurements ($\sqrt{s} = 8$ TeV) of electroweak boson production cross-sections compared to NNLO perturbative QCD, as implemented by the FEWZ generator using various PDF sets. The shaded (yellow) bands indicate the statistical and total uncertainties on the measurements, which are symmetric about the central value. The uncertainties on the theoretical predictions are due to the PDFs. Scale and α_s uncertainties are similar and about one third of the size.

η^μ	σ_{W^+} [pb]	$f_{\mathrm{FSR}}^{W^+}$
2.00 – 2.25	$236.5 \pm 1.2 \pm 3.2 \pm 2.4 \pm 2.7$	1.019 ± 0.005
2.25 – 2.50	$208.4 \pm 0.9 \pm 2.2 \pm 2.1 \pm 2.4$	1.016 ± 0.003
2.50 – 2.75	$182.0 \pm 0.8 \pm 1.8 \pm 1.8 \pm 2.1$	1.016 ± 0.003
2.75 – 3.00	$153.3 \pm 0.7 \pm 1.6 \pm 1.5 \pm 1.8$	1.015 ± 0.003
3.00 – 3.25	$119.5 \pm 0.6 \pm 1.3 \pm 1.2 \pm 1.4$	1.015 ± 0.003
3.25 – 3.50	$84.4 \pm 0.5 \pm 1.0 \pm 0.8 \pm 1.0$	1.015 ± 0.005
3.50 – 4.00	$86.4 \pm 0.5 \pm 1.2 \pm 0.9 \pm 1.0$	1.018 ± 0.005
4.00 – 4.50	$23.0 \pm 0.4 \pm 0.7 \pm 0.2 \pm 0.3$	1.021 ± 0.009

η^μ	σ_{W^-} [pb]	$f_{\mathrm{FSR}}^{W^-}$
2.00 – 2.25	$134.0 \pm 0.9 \pm 1.8 \pm 1.2 \pm 1.6$	1.017 ± 0.003
2.25 – 2.50	$119.8 \pm 0.7 \pm 1.4 \pm 1.0 \pm 1.4$	1.016 ± 0.003
2.50 – 2.75	$110.6 \pm 0.6 \pm 1.2 \pm 1.0 \pm 1.3$	1.015 ± 0.003
2.75 – 3.00	$102.4 \pm 0.6 \pm 1.2 \pm 0.9 \pm 1.2$	1.016 ± 0.003
3.00 – 3.25	$92.5 \pm 0.6 \pm 1.1 \pm 0.8 \pm 1.1$	1.016 ± 0.003
3.25 – 3.50	$79.9 \pm 0.5 \pm 0.9 \pm 0.7 \pm 0.9$	1.018 ± 0.003
3.50 – 4.00	$119.3 \pm 0.6 \pm 1.5 \pm 1.0 \pm 1.4$	1.020 ± 0.003
4.00 – 4.50	$60.0 \pm 0.7 \pm 1.6 \pm 0.5 \pm 0.7$	1.024 ± 0.005

Table 5.3: Inclusive differential cross-sections for W^+ (left) and W^- (right) boson production as functions of muon η, measured with SAMPLE-II data. Uncertainties are due to the sample size, systematic effects, the beam energy and the luminosity. These results are preliminary.

Source	Uncertainty (%)			
	Sample-I		Sample-II	
	W^+	W^-	W^+	W^-
Statistical	0.24	0.28	0.19	0.23
Muon Eff.				
Trigger (TP)	0.23	0.21	0.14	0.13
Identification (TP)	0.06	0.06	0.04	0.04
Identification (Sys.)	0.10	0.10	0.10	0.10
Tracking (TP)	0.22	0.18	0.17	0.14
Tracking (TM)	0.14	0.11	0.07	0.06
Tracking (Bias1)	0.05	0.04	0.06	0.05
Tracking (Bias2)	0.17	0.16	0.18	0.18
Acceptance/FSR	0.18	0.12	0.16	0.14
Purity	0.30	0.40	0.28	0.21
Selection	0.33	0.32	0.24	0.24
GEC Eff.	0.23	0.23	0.32	0.32
GEC Eff. (ΔWZ)	0.27	0.27	0.20	0.20
GEC Eff. (ΔW^+W^-)	0.13	0.15	0.07	0.10
Systematic	0.73	0.74	0.64	0.60
Beam energy	1.06	0.91	1.00	0.86
Luminosity	1.71	1.71	1.16	1.16
Total	2.15	2.09	1.67	1.58

Table 5.4: Contributions to the relative uncertainty on the W boson cross-section.

5.2 Definition of observables

The cross-section ratios are defined for muons with $p_T > 20$ GeV/c, $2.0 < \eta < 4.5$ and, in the case of the Z boson cross-section, a dimuon invariant mass between 60 and 120 GeV/c^2. The ratio of W boson to Z boson production is defined as

$$R_{WZ} = \frac{\sigma_{W^+\to\mu^+\nu_\mu} + \sigma_{W^-\to\mu^-\bar{\nu}_\mu}}{\sigma_{Z\to\mu^+\mu^-}}. \tag{5.8}$$

The separate ratios of W^+ and W^- to Z boson production cross-sections are defined as

$$R_{W^\pm Z} = \frac{\sigma_{W^\pm\to\mu^\pm\nu_\mu}}{\sigma_{Z\to\mu^+\mu^-}}, \tag{5.9}$$

while the W boson cross-section ratio is defined as

$$R_W = \frac{\sigma_{W^+\to\mu^+\nu_\mu}}{\sigma_{W^-\to\mu^-\bar{\nu}_\mu}}. \tag{5.10}$$

The cross-sections above are all obtained by summing differential cross-section measurements. The W boson cross-sections are obtained by summing differential cross-sections as functions of muon η, while the Z boson cross-section is obtained by summing differential cross-sections as functions of boson y.[1] For example, Equation 5.8 written in terms of the differential measurements is

$$R_{WZ} = \frac{\sum_{i=1}^{8} W_i^+ + \sum_{i=j}^{8} W_j^-}{\sum_{k=1}^{18} Z_k}. \tag{5.11}$$

It is important to keep this in mind, especially when the propagation of uncertainties is discussed in Section 5.3. Since the ratios defined above are measured using cross-sections from identical data sets, the uncertainty due to luminosity drops out.

The ratios of cross-sections at different centre-of-mass energies (either 7 or 8 TeV) are

$$R_{W^+}^{8/7} = \frac{\sigma_{W^+\to\mu^+\nu_\mu}^{8\text{ TeV}}}{\sigma_{W^+\to\mu^+\nu_\mu}^{7\text{ TeV}}}, \tag{5.12}$$

$$R_{W^-}^{8/7} = \frac{\sigma_{W^-\to\mu^-\bar{\nu}_\mu}^{8\text{ TeV}}}{\sigma_{W^-\to\mu^-\bar{\nu}_\mu}^{7\text{ TeV}}}, \tag{5.13}$$

[1] There are two main reasons for measuring cross-sections differentially. First, muon reconstruction efficiencies depend on η, so binning the measurements reduces the systematic uncertainty. Second, the shapes of measurements may be compared with predictions, which very often have different shapes.

$$R_Z^{8/7} = \frac{\sigma^{8\text{ TeV}}_{Z\to\mu^+\mu^-}}{\sigma^{7\text{ TeV}}_{Z\to\mu^+\mu^-}}. \tag{5.14}$$

Unlike ratios of cross-sections measured on the same data set, the uncertainty due to luminosity does not fully cancel and it is still the dominant uncertainty for these measurements. The theoretical predictions for these ratios have uncertainties that are small in comparison to the uncertainties on the predicted cross-sections. This is mainly due to the cancellation of the PDF uncertainty, which is significant since the cross-sections are for the same type of boson. This interplay between experimental and theoretical uncertainty makes measurements of these quantities ideal for calibrating the ratio of luminosities from distinct data sets, as explained in the introduction to this chapter and Ref. [112].

Ratios-of-ratios of cross-sections at different centre-of-mass energies are defined as

$$R^{8/7}_{R_W} = \frac{R^{8\text{ TeV}}_W}{R^{7\text{ TeV}}_W}, \tag{5.15}$$

$$R^{8/7}_{R_{W^\pm Z}} = \frac{R^{8\text{ TeV}}_{W^\pm Z}}{R^{7\text{ TeV}}_{W^\pm Z}}, \tag{5.16}$$

$$R^{8/7}_{R_{WZ}} = \frac{R^{8\text{ TeV}}_{WZ}}{R^{7\text{ TeV}}_{WZ}}. \tag{5.17}$$

The uncertainty due to luminosity drops out in these ratios. Measurements of these quantities constitute precision tests of the SM, and may be used in searches for BSM physics, as explained in the introduction to this chapter.

5.3 Systematic uncertainties

The ratios defined in Equations 5.8 - 5.17 are calculated from the total cross-sections in Equations 4.15 - 4.16 and 5.4 - 5.7. In order to correctly assign uncertainties on the derived quantities, the correlations between the cross-section measurements must be taken into account.

The cross-section measurements depend on the determination of various different components, efficiencies, correction factors, etc, all of which are given in Equations 4.4 and 5.2. If these components are common to any two cross-section measurements, the effect of an under- or over-estimate of this component may be to either under-estimate both

cross-sections, over-estimate both cross-sections or under-estimate one cross-section and over-estimate the other. This is the basic notion of correlation. Two measurements are positively correlated when they increase or decrease together, and negatively correlated when one decreases and the other increases. Ratios of the cross-section measurements are better determined if there is a positive correlation (see Appendix C).

In the following sections, the components of the W and Z cross-sections measurements are discussed. Particular attention is given to the correlations (if any) that these components induce on the cross-section measurements, which in turn dictate how uncertainties are propagated onto cross-section ratios. Only the uncertainties on SAMPLE-I measurements are discussed. Similar arguments apply to the propagation of uncertainties onto SAMPLE-II measurements. A summary of all relevant systematic uncertainties is given in Table 5.5.

5.3.1 Muon reconstruction efficiencies

The measurement of an electroweak boson cross-section relies on the measurement of the efficiency to reconstruct high-p_T muons. These measurements are described in Section 4.4.2, where the efficiencies are measured as functions of muon η. Since the same efficiencies are used in the W and Z cross-section measurements, these measurements are correlated to some degree. Seven different uncertainties were described in Section 4.4.2: three uncertainties related to the sizes of the tag-and-probe samples; one uncertainty due to backgrounds in the tag-and-probe sample used to measure the identification efficiency; one uncertainty due to the inefficiency of the track matching procedure; and two uncertainties due to the use of the MuonTT track method to determine the tracking efficiency. Most of these sources of uncertainty are uncorrelated between muon η bins. The uncertainties due to backgrounds in the sample used to measure the muon identification efficiency, and one of the uncertainties due to the MuonTT track method for measuring the tracking efficiency, are correlated between η bins.

Once the covariance matrix in known, the correlation matrix may be determined (see Appendix C). These correlation coefficients are used in standard error propagation formulae (see Appendix G) to propagate uncertainties due to muon reconstruction efficiencies onto the cross-section ratios. The resulting uncertainties are given in Table 5.5. These should be compared to those on the Z boson cross-section measurement in Table 4.11, and the relative uncertainties on the efficiencies given in Tables 4.5, 4.6, and 4.7. The W boson cross-sections are measured as functions of η just like the efficiencies, therefore the relative uncertainties on the W boson cross-sections are identical to the relative uncertainties

on the efficiencies. From this comparison, it is clear that relative uncertainties due to reconstruction efficiencies are smaller on ratios of cross-sections than on cross-sections.

Source	Uncertainty (%)							
	Sample-I				Sample-II			
	R_{WZ}	R_{W^+Z}	R_{W^-Z}	R_W	R_{WZ}	R_{W^+Z}	R_{W^-Z}	R_W
Statistical	0.45	0.48	0.50	0.38	0.31	0.33	0.36	0.30
Muon Eff.								
Trigger (TP)	0.15	0.16	0.13	0.07	0.09	0.10	0.09	0.04
Identification (TP)	0.06	0.06	0.05	0.03	0.04	0.04	0.04	0.01
Identification (Sys.)	0.10	0.10	0.10	0.00	0.10	0.10	0.10	0.00
Tracking (TP)	0.14	0.14	0.16	0.07	0.13	0.13	0.15	0.05
Tracking (TM)	0.07	0.09	0.11	0.04	0.06	0.06	0.07	0.02
Tracking (Bias1)	0.04	0.04	0.04	0.02	0.05	0.05	0.05	0.02
Tracking (Bias2)	0.16	0.16	0.17	0.01	0.17	0.16	0.17	0.01
Acceptance/FSR	0.16	0.21	0.17	0.21	0.17	0.21	0.19	0.21
Purity (Z)	0.20	0.20	0.20	0.00	0.20	0.20	0.20	0.00
Purity (W)	0.18	0.30	0.40	0.60	0.22	0.28	0.21	0.25
Selection	0.31	0.33	0.32	0.18	0.23	0.24	0.24	0.10
GEC Eff.	0.00	0.00	0.00	0.00	0.00	0.00	0.00	0.00
GEC Eff. (ΔWZ)	0.27	0.27	0.27	0.00	0.20	0.20	0.20	0.00
GEC Eff. (ΔW^+W^-)	0.10	0.13	0.15	0.20	0.06	0.07	0.10	0.13
Systematic	0.60	0.68	0.72	0.70	0.54	0.58	0.55	0.37
Beam energy	0.26	0.19	0.34	0.15	0.21	0.15	0.29	0.14
Total	0.79	0.85	0.94	0.81	0.66	0.68	0.72	0.50

Table 5.5: Contributions to the relative uncertainty on the electroweak boson cross-section ratios.

In order to get a feel for these uncertainties, consider those of Sample-I. The precision of the trigger efficiency, labelled Trigger (TP) in Table 5.5, leads to an uncertainty on $W^+(W^-)$ cross-sections of 0.23(0.21)% and 0.07% on the Z boson cross-section (see Tables 4.11 and 5.4). The uncertainty on the Z boson cross-section is relatively smaller because the trigger efficiency is higher, having two chances to fire the muon trigger. In the ratios involving W and Z bosons, the precision is about 0.15%. This is smaller than the relative uncertainties on the W boson cross-sections, as there is cancellation of the uncertainty that is correlated between W and Z boson cross-sections.

The uncertainties on the ratios arising from the tag-and-probe sample used to measure the muon identification efficiencies, labelled Identification (TP), are related to the uncertainties on the W and Z cross-sections in a similar way to what was described above for the trigger efficiency. The obvious difference is the size of the uncertainties, which are smaller due to the fact that muon identification efficiencies are higher. The component of the uncertainty that is correlated between bins, labelled Identification (Sys.), is 0.1% for

ratios involving the Z boson cross-section, and cancels completely for R_W. This may be understood by first noticing that the uncertainties on the W and Z boson cross-sections are 0.1 and 0.2%, respectively. Since the uncertainties are fully correlated, taking the ratio of two cross-sections amounts to cancelling the uncertainty from one muon, which is 0.1%. For the ratio of W boson cross-sections the uncertainty is cancelled completely, while for ratios involving W and Z boson cross-sections, 0.1% remains.

The first three components of uncertainty arising from the determination of muon tracking efficiencies, labelled Tracking (TP), Tracking (TM) and Tracking (Bias1), are all uncorrelated between muon η bins. The uncertainties on the ratios arising from these are related to the uncertainties on the W and Z cross-sections in a similar way to what was described above for the trigger efficiency. The final uncertainty, labelled Tracking (Bias2), is correlated between muon η bins. The correlated uncertainty varies between 0.1 and 1.1% of the efficiency, depending on the bin. For this reason, the related uncertainty on the ratios is not simply the difference of the uncertainties on the W and Z boson cross-sections, as was the case with the uncertainty labelled Identification (Sys.).

5.3.2 Final-state radiation and kinematic acceptance

The QED final-state radiation factors are evaluated as functions of η^{μ}, ϕ^{*}_{Z}, y_Z and $p_{T,Z}$. As explained in Section 4.4.5, the uncertainties are composed of two parts. One is purely statistical, reflecting the size of the generated samples used to determine the correction. Since the FSR correction is taken as the average of the corrections determined with Herwig++ or Pythia8 separately, the second uncertainty is taken as half of the difference between the two estimates. The values of the FSR corrections and their uncertainties are given in Tables 4.12 - 4.19 and 5.2 - 5.3. The uncertainties on the W boson cross-sections due to kinematic acceptance (accounting for the upper limit on muon p_T of 70 GeV/c) are combined with the final-state radiation uncertainties; for the purposes of error propagation, the uncertainties are treated similarly.

The relative uncertainty on the Z boson cross-section is 0.11%, while on $W^{+}(W^{-})$ cross-sections it is 0.18(0.12)% (see Tables 4.11 and 5.4). These give rise to the uncertainties on the ratios, shown in Table 5.5, upon application of standard propagation of uncorrelated uncertainties.

5.3.3 Purity

All ratios involving the Z boson cross-section have a 0.2% uncertainty that arises from the purity of the Z boson sample, which was discussed in Section 4.3. Similarly, the W^+ and W^- cross-sections have uncertainties due to purity (see Table 5.4) of 0.30% and 0.40%. These uncertainties propagate directly onto R_{W^+Z} and R_{W^-Z}. For the R_{WZ} and R_W ratios, correlations between these uncertainties are important and result in 0.18% and 0.60% uncertainties, respectively. To understand why the relative uncertainty is smaller for R_{WZ}, and larger for R_W, consider two aspects to the fitting procedure of Section 5.1. The first is that the entire sample of W muons, including both positively and negatively charged muons, is fit with two signal templates (one for each charge). The second is that the ratio of positive- and negative-muon hadron misidentification background is fixed. As a result, if the fit chooses to increase the W^- signal in one bin, then this is compensated by a decrease of the W^+ signal in the same bin, and the purities are anti-correlated. This anti-correlation leads to a large uncertainty on the ratio of W boson cross-sections, as in R_W, and a reduced uncertainty on their sum, as in R_{WZ}. See Appendix C for more details on the effects of correlated uncertainties.

5.3.4 Selection

The selection criteria (E_T^{cone}, p_T^{cone}, p_T^{extra}, IP, and $(E_{ECAL} + E_{HCAL})/pc$) for W boson candidate samples are detailed in Table 5.1. The uncertainties due to the efficiencies of these requirements are composed of two parts. The first is due to size of the Pseudo-W sample. The second is due to the statistical precision on the correction that is applied to account for the different p_T distributions of muons from W and Z bosons, and the fact that the Pseudo-W sample requires two muons inside the LHCb acceptance. These uncertainties are fully correlated between measurements in identical η bins, i.e., there is full correlation between the W^+ and W^- cross-sections measured in the same bin, but no correlation between measurements in different bins.

The total selection uncertainties on the W^+ and W^- cross-sections are 0.33% and 0.32% respectively (see Table 5.4). These uncertainties transfer directly onto R_{W^+Z} and R_{W^-Z}. A similar uncertainty of 0.31% appears on R_{WZ}. The correlated uncertainty mentioned above cancels in the measurement of R_W, but the cancellation is not complete. The residual uncertainty (0.20%) is due to the fact that the selection uncertainty is uncorrelated between measurements in different bins.

5.3.5 Luminosity

Each cross-section measurement contains the luminosity in the denominator, so ratios of cross-sections are independent of the luminosity.

5.3.6 GEC efficiency for electroweak bosons

The connection between the GEC efficiency and SPD hits has already been discussed in Section 4.4.3. SPD hits are correlated with the charged particle multiplicity of the event, and since production of W and Z are similar in terms of the hard scale at which they are produced, it is expected that the differences between the GEC efficiencies for these processes are very small.

This assumption is investigated in three ways. Firstly, charged particle multiplicities in the LHCb acceptance are studied using the PYTHIA and HERWIG MC generators with both LO and NLO matrix elements and a variety of PDF sets. The multiplicity distributions are shown in Figure 5.4. One concludes that the charged particle multiplicities of events containing different electroweak bosons are very similar. These studies also indicate that W^- (W^+) events have slightly higher (lower) multiplicities than Z events. In addition, particle multiplicities at generator-level are much lower than detector occupancies in data. This is because the parameters of the parton shower have not been tuned [110] to replicate the particle multiplicities in data.

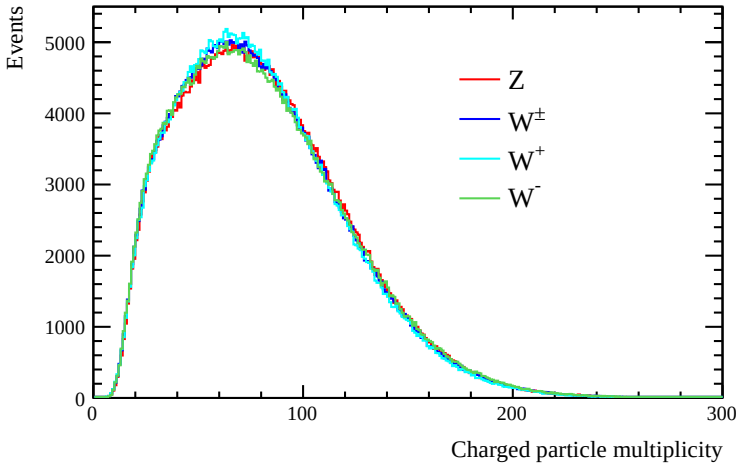

Figure 5.4: Charged particle multiplicities in events generated by HERWIG++.

Secondly, fully simulated MC (Pythia6 and Pythia8) is used to understand how charged particle multiplicities translate into detector occupancies (SPD hits, see Section 3.2.8). One expects detector occupancies to be slightly less than generated charged particle multiplicities due to the spatial resolution of the detector. Similar to the generator-level tests, the detector occupancies of events containing different electroweak bosons are very similar. The W events have a slightly larger occupancy than Z events, where a difference of $(0.32 \pm 0.03 \pm 0.07)\%$ in the equivalent GEC efficiency is observed. The first uncertainty here is statistical and the second reflects the difference between Pythia6 and Pythia8. The average detector occupancy in simulation is a factor of 0.7 smaller than the average detector occupancy in data, so an equivalent efficiency must be determined. The equivalent efficiency gives the same efficiency on simulated Z boson events as the 600 SPD hit threshold does on Z boson events in data. This is achieved with an SPD hit threshold of 428 in simulation.

Thirdly, differences between the W and Z boson GEC efficiency are studied in data using a background subtracted W sample. As can be seen from Figure 5.1, the W boson sample is purest at high muon p_T. A pure sample of W bosons is obtained by requiring the muon p_T to be larger than 35 GeV/c. The resulting selection is $\sim$88% signal, and as can be seen from Figure 5.1, the residual background is largely due to Z bosons with one muon in the acceptance. Using the known SPD multiplicity distribution of Z boson events in data and simulation, the shape of the SPD multiplicity distribution of W boson events can be obtained, which can give an estimate of the W boson GEC efficiency. The SPD multiplicity distributions of W boson events are fitted up to 600 SPD hits, similar to what is done in Section 4.4.3. The function is extrapolated beyond 600 hits and the efficiency is determined. Statistical and fit uncertainties on the W^+ and W^- GEC efficiencies are determined to be 0.13% and 0.15%. The corresponding precision on the efficiency determined from Z candidates is 0.27%, and this is the degree to which one may say that the efficiencies for W and Z bosons are the same. As with the first two checks, this data-driven method also suggests higher detector occupancies for events containing W bosons.

From the studies above, the difference between the efficiency for W and Z events is clearly small. Consequently, the difference between the W and Z boson GEC efficiencies is accounted for with additional systematic uncertainties instead of introducing a correction to the central value. Since the SPD multiplicity is not well-modelled by the simulation, the data-driven studies are used to set these additional uncertainties. The nominal GEC efficiency is given by $\varepsilon^{Z}_{GEC} = (94.00 \pm 0.20)\%$, as quoted in Section 4.4.3. The uncertainties that are added to this are mentioned in the preceding paragraph. The results are $\varepsilon^{W^+}_{GEC} = (94.00 \pm 0.20 \pm 0.13 \pm 0.27)\%$ and $\varepsilon^{W^-}_{GEC} = (94.00 \pm 0.20 \pm 0.15 \pm 0.27)\%$.

The first uncertainty is fully correlated between all electroweak boson cross-sections, the second is fully uncorrelated between W^+ and W^- cross-sections and the third is fully correlated between W^+ and W^- cross-sections.

In the cross-section ratios, the first uncertainty, labelled GEC Eff. in Table 5.5, cancels as it is fully correlated between all electroweak boson cross-section measurements. The second uncertainty, labelled GEC Eff. (ΔW^+W^-) in Table 5.5, is uncorrelated between W^+ and W^- cross-sections, and is not applicable to Z cross-sections. Consequently, the uncertainty translates directly onto the $R_{W^\pm Z}$ ratios, is relatively smaller on the R_{WZ} ratio, and is relatively larger on the R_W ratio. The third uncertainty is labelled as GEC Eff. (ΔWZ) in Table 5.5. It is fully correlated between W boson cross-section measurements and, as such, passes directly to the ratios involving the Z boson, and cancels in the R_W ratio.

5.3.7 Proton beam energy

Measurements in this thesis are specified at centre-of-mass energies of $\sqrt{s} = 7$ TeV or $\sqrt{s} = 8$ TeV. The beam energy, and consequently the centre-of-mass energy, is known to 0.65% [64]. This uncertainty is fully correlated between different centre-of-mass energies, as explained in Section 3.1.3. The sensitivity of the cross-section to the centre-of-mass energy is studied using DYNNLO [42] with the MSTW08 [25] PDF set. A cubic spline is used to interpolate between predictions at integer centre-of-mass energies between 1–20 TeV as in Figure 5.5. At $\sqrt{s} = 7$ TeV ($\sqrt{s} = 8$ TeV) a 0.65% variation of the beam energy corresponds to a 1.06% (1.00%) variation in the W^+ cross-section, a 0.91% (0.86%) variation in the W^- cross-section, and as mentioned in Section 4.5.7, a 1.25% (1.15%) variation in the Z cross-section, which is shown in Figure 4.32. Since these uncertainties are fully correlated between measurements, uncertainties cancel in the ratios. The residual uncertainty is the difference of the relative uncertainties. For example, the uncertainty on the ratio R_{W^+Z} at $\sqrt{s} = 7$ TeV is 0.19%, which is the difference between 1.25% for the Z boson cross-section and 1.06% for the W^+ boson cross-section.

5.3.8 Ratios at different centre-of-mass energy

The following assumptions are made when evaluating cross-section ratios at different centre-of-mass energies. The uncertainties due to statistically independent samples are uncorrelated. These include uncertainties due to: the number of candidates in each

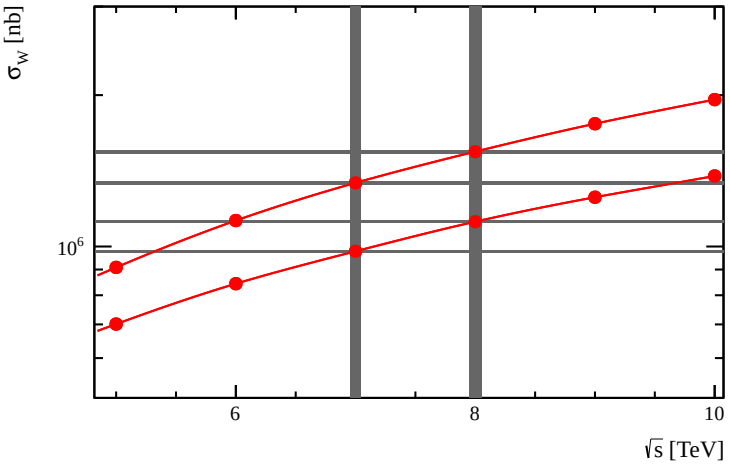

Figure 5.5: The DYNNLO prediction of the W^+ (upper curve) and W^- (lower curve) boson cross-section as a function of centre-of-mass energy. The vertical grey bands indicate the uncertainty on the centre-of-mass energy and the horizontal grey bands indicate the resulting uncertainty on the cross-section.

measurement bin; the uncertainties on the muon reconstruction efficiencies that are uncorrelated between η bins; the uncertainty that arises when correcting for having two muons inside the acceptance when measuring the selection efficiencies of W bosons; and the W boson purity estimation. The uncertainties reflecting common methods are correlated. These include: the Z candidate sample purity estimation; the components of the muon reconstruction efficiencies that are correlated between muon η bins; the uncertainty that arises when measuring selection efficiencies for W bosons; and all aspects of the GEC efficiency determination. The uncertainty due to FSR is taken to be correlated in identical measurement bins and uncorrelated between different measurement bins. The beam energy uncertainty is correlated, as explained in Section 3.1.3.

The uncertainties entering the luminosity estimates are given in Ref. [62]. For many of these uncertainties, the degree of correlation between the luminosity measurements at different centre-of-mass energies cannot be known exactly. Instead, each source of uncertainty is assigned a correlation coefficient of 0, 1, [0,0.5], [0.5,1] or [0,1], where the latter three represent intervals of ignorance. Correlation coefficients are sampled from both uniform and arcsin distributions across these intervals. With this prescription, the total correlation is estimated to be 0.55 ± 0.06 [117]. For the purposes of the analysis presented here, a correlation coefficient of 0.55 is used.

A summary of the uncertainties on ratios of quantities at different centre-of-mass energies is given in Table 5.6.

Source	Uncertainty (%)						
	$R_{W^+}^{8/7}$	$R_{W^-}^{8/7}$	$R_Z^{8/7}$	$R_{R_{WZ}}^{8/7}$	$R_{R_{W+Z}}^{8/7}$	$R_{R_{W-Z}}^{8/7}$	$R_{R_W}^{8/7}$
Statistical	0.30	0.37	0.49	0.55	0.58	0.62	0.48
Muon Eff.							
Trigger (TP)	0.27	0.25	0.09	0.17	0.19	0.16	0.08
Identification (TP)	0.07	0.07	0.13	0.07	0.07	0.06	0.03
Identification (Sys.)	0.00	0.00	0.00	0.00	0.00	0.00	0.00
Tracking (TP)	0.28	0.23	0.45	0.20	0.19	0.22	0.08
Tracking (TM)	0.16	0.13	0.25	0.11	0.11	0.13	0.04
Tracking (Bias1)	0.08	0.07	0.13	0.06	0.06	0.07	0.02
Tracking (Bias2)	0.02	0.01	0.02	0.03	0.03	0.03	0.00
Acceptance/FSR	0.05	0.06	0.04	0.06	0.07	0.07	0.08
Purity (Z)	–	–	0.00	0.00	0.00	0.00	–
Purity (W)	0.41	0.45	–	0.29	0.41	0.45	0.65
Selection	0.17	0.17	–	0.16	0.17	0.17	0.04
GEC Eff.	0.09	0.09	0.09	0.00	0.00	0.00	0.00
GEC Eff. (ΔWZ)	0.07	0.07	–	0.07	0.07	0.07	0.00
GEC Eff. (ΔW^+W^-)	0.06	0.05	–	0.04	0.06	0.05	0.07
Systematic	0.64	0.63	0.56	0.46	0.55	0.59	0.67
Beam energy	0.06	0.05	0.10	0.05	0.04	0.05	0.00
Luminosity	1.45	1.45	1.45	0.00	0.00	0.00	0.00
Total	1.61	1.62	1.63	0.72	0.80	0.86	0.82

Table 5.6: Contributions to the relative uncertainty on the electroweak boson cross-section ratios at different centre-of-mass energies.

5.4 Results

5.4.1 Sample-I error ellipses

Another way to visualise the cross-section measurements of Chapter 4 and Section 5.1 is with error ellipses. In Figure 5.6, the values of the measured W and Z boson cross-sections from Sample-I are indicated by black crosses. The purple and yellow ellipses represent two dimensional uncertainty intervals about the measurements. Similarly, open markers and ellipses, representing PDF uncertainty intervals, denote the predictions of NNLO perturbative QCD.

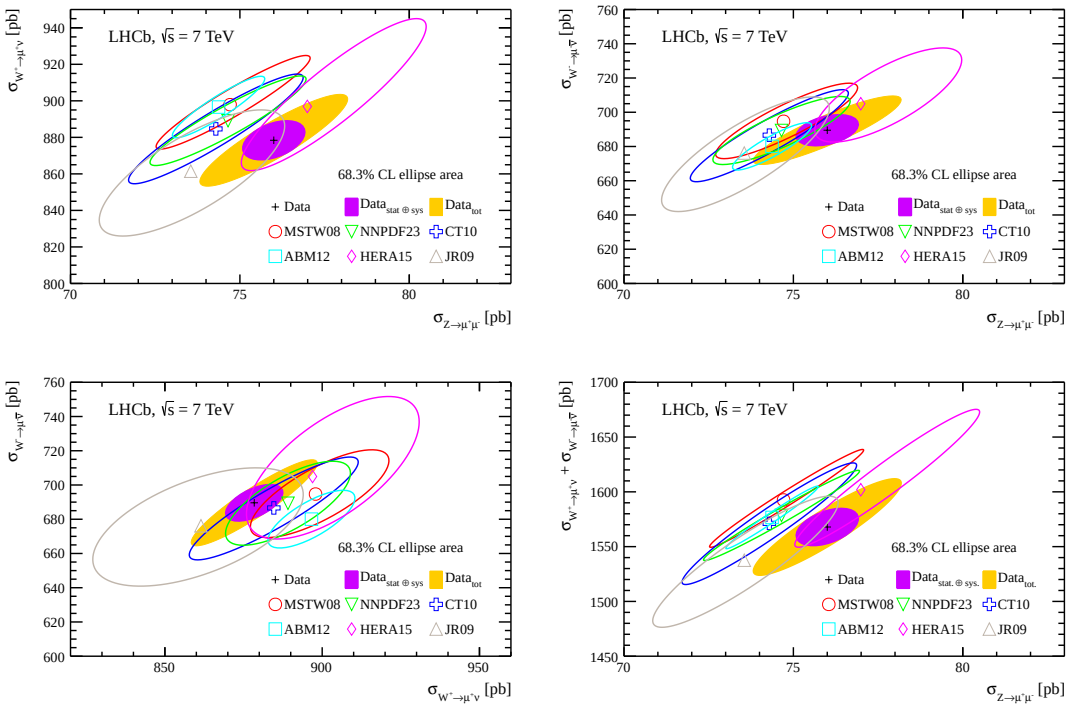

Figure 5.6: Two dimensional plots of electroweak boson cross-sections compared to NNLO predictions for various parameterisations of the PDFs. The outer, shaded (yellow) ellipse corresponds to the total uncertainty on the measurements. The inner, shaded (purple) ellipse excludes the beam energy and luminosity uncertainties. The uncertainty on the theoretical predictions corresponds to the PDF uncertainty only. All ellipses correspond to uncertainties at 68.3% confidence level.

To define these ellipses, first consider the covariance matrix, A, of two cross-section measurements, σ_1 and σ_2.[2] The eigenvectors, $\mathbf{v}_{1,2}$, and eigenvalues, $\lambda_{1,2}$, of this matrix

[2]The covariance matrix may be constructed using the uncertainties on the cross-sections and the correlation between the cross-sections, which is given in Appendix E.

are defined by

$$A\mathbf{v}_1 = \lambda_1\mathbf{v}_1 \qquad\qquad A\mathbf{v}_2 = \lambda_2\mathbf{v}_2. \tag{5.18}$$

The equation of each ellipse is then given by

$$\left(\frac{\sigma_1}{\lambda_1}\right)^2 + \left(\frac{\sigma_2}{\lambda_2}\right)^2 = s. \tag{5.19}$$

The lengths of the axes of the ellipse are $2\sqrt{s\lambda_1}$ and $2\sqrt{s\lambda_2}$.

The value of s is chosen to represent a certain confidence interval. Here, the 68.3% confidence level is used. Since the left-hand side of Equation 5.19 is a sum of squares of two independent, and normally distributed random variables, it is distributed as a χ^2 distribution with two degrees of freedom [99]. The value of s is determined by setting the integral of the χ^2 distribution with two degrees of freedom ($\chi^2_{k=2}$) to the desired confidence level, in this case 68.3%. One has

$$\int_0^s dx\ \chi^2_{k=2} = 0.683, \tag{5.20}$$

and the corresponding value of s is 2.2977.

The orientation of the ellipses with respect to the co-ordinate axes indicate the degree of correlation between the cross-sections. The angle, α, is defined as the angle that the eigenvector with the largest eigenvalue makes with the x-axis. Suppose $\lambda_1 > \lambda_2$, the relevant eigenvector is $\mathbf{v}_1$, and it has components v_1^x and v_1^y. Then,

$$\alpha = \tan^{-1}\frac{v_1^y}{v_1^x}. \tag{5.21}$$

The inclinations of the yellow error ellipses indicate a high degree of correlation between measurements, suggesting that that the relative uncertainties on ratios of these quantities will be very much reduced.

Superimposed on the measurements in Figure 5.6, are the NNLO FEWZ predictions, configured with different choices of PDF set. Error ellipses for these theoretical predictions are computed in the same way as explained above. Again, the inclinations of the error ellipses indicate a high degree of correlation between these predictions, suggesting that ratios of these quantities will be better determined. While these observations demonstrate the advantages of cross-section ratios, it is also clear from these two-dimensional plots that cross-section measurements, when considered as pairs, are

sensitive to the choice of PDF set, even when luminosity and beam energy uncertainties are considered. This is not apparent from cross-section measurements considered individually, as in Figure 5.2.

5.4.2 Sample-II error ellipses

The error ellipses corresponding to the cross-section measurements on Sample-II are shown in Figure 5.7.

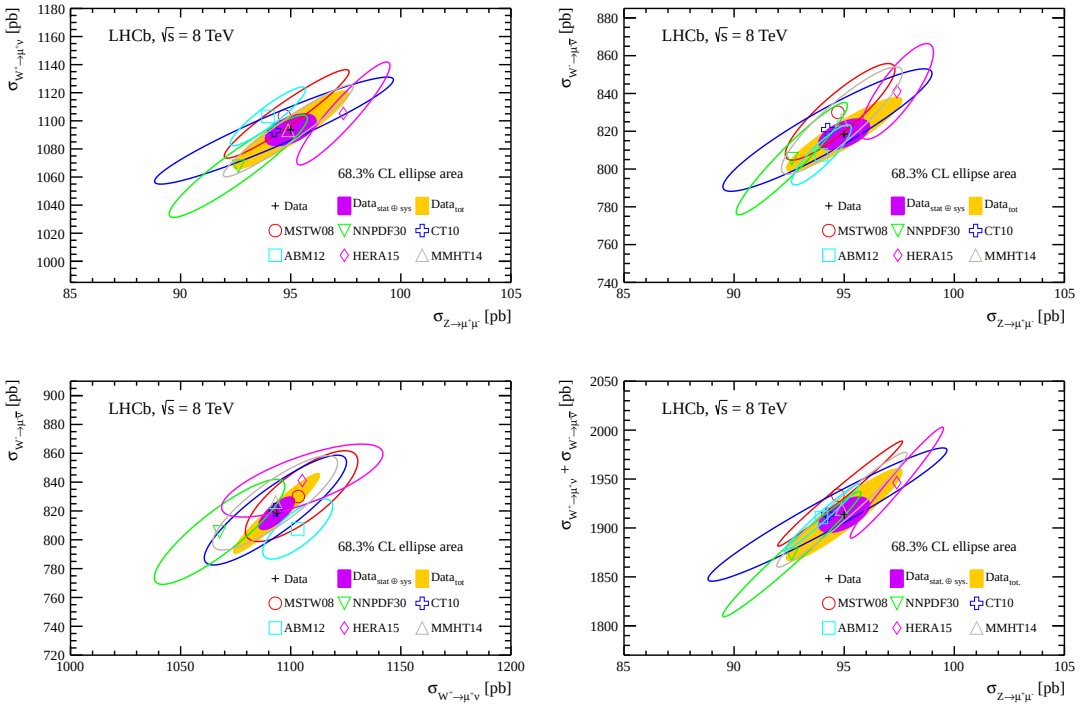

Figure 5.7: Two dimensional plots of electroweak boson cross-sections compared to NNLO predictions for various parameterisations of the PDFs. The outer, shaded (yellow) ellipse corresponds to the total uncertainty on the measurements. The inner, shaded (purple) ellipse excludes the beam energy and luminosity uncertainties. The uncertainty on the theoretical predictions corresponds to the PDF uncertainty only. All ellipses correspond to uncertainties at 68.3% confidence level.

5.4.3 Sample-I W/Z ratio

The W to Z boson cross-section ratio at $\sqrt{s} = 7$ TeV is measured as

$$R_{WZ} = 20.63 \pm 0.09 \pm 0.12 \pm 0.05,$$

where the first uncertainty is statistical, the second is systematic and the third is due to the beam energy. The total precision is 0.8%, while the statistical precision is 0.5%. The largest systematic uncertainty is due to the uncertainties arising from the W boson sample selection, which is 0.3% as in Table 5.5. The charged W to Z boson cross-section ratios are measured as

$$R_{W^+Z} = 11.56 \pm 0.06 \pm 0.08 \pm 0.02,$$
$$R_{W^-Z} = \ 9.07 \pm 0.05 \pm 0.07 \pm 0.03,$$

while the W boson cross-section ratio is measured as

$$R_W = 1.274 \pm 0.005 \pm 0.009 \pm 0.002.$$

These are 0.9%, 0.9% and 0.8% measurements respectively. The largest systematic uncertainties on the R_{W^+Z} and R_{W^-Z} ratios are due to the W^+ boson selection (0.3%) and the W^- boson purity estimation (0.4%), respectively. The largest uncertainty on the measurement of R_W is due to the template shapes and normalisations used to extract the W boson signal from the W event sample, which is 0.6% (this source only contributes 0.2% to R_{WZ} due to the anti-correlation between W^+ and W^-; see Section 5.3.3 and Table 5.5).

The ratio measurements, as well as their predictions, are displayed in Figure 5.8. For the ratios involving the Z boson cross-sections, the general trend is that the predicted ratios are larger than the measured ratios. The behaviour of the different PDF sets with respect to the measurements is worthy of comment. The central values from HERAPDF1.5 [21] and JR09 [39] sit on top of the measurements in all cases. Both of these PDF sets use data that largely come from ep collisions at HERA, and do not use the $\nu N \to \mu^+\mu^- X$ dimuon data (see Table 2.2). Those from CT10, MSTW08 and NNPDF23 lie slightly above the measurements. ABM12 differs more significantly for R_{WZ} and R_{W^+Z}, though the R_{W^-Z} prediction sits on the data. For the ratio of W boson cross-sections, R_W, all predictions align very well with the measurement except for ABM12, which is about 2σ above.

The ratios R_{W^+Z} and R_{W^-Z} are also measured differentially as a function of muon η. These measurements are displayed in Figure 5.9. Good agreement between measured and predicted values is observed. It is noted that the measured R_{W^-Z} ratio is a more constant function of η^μ than predicted.

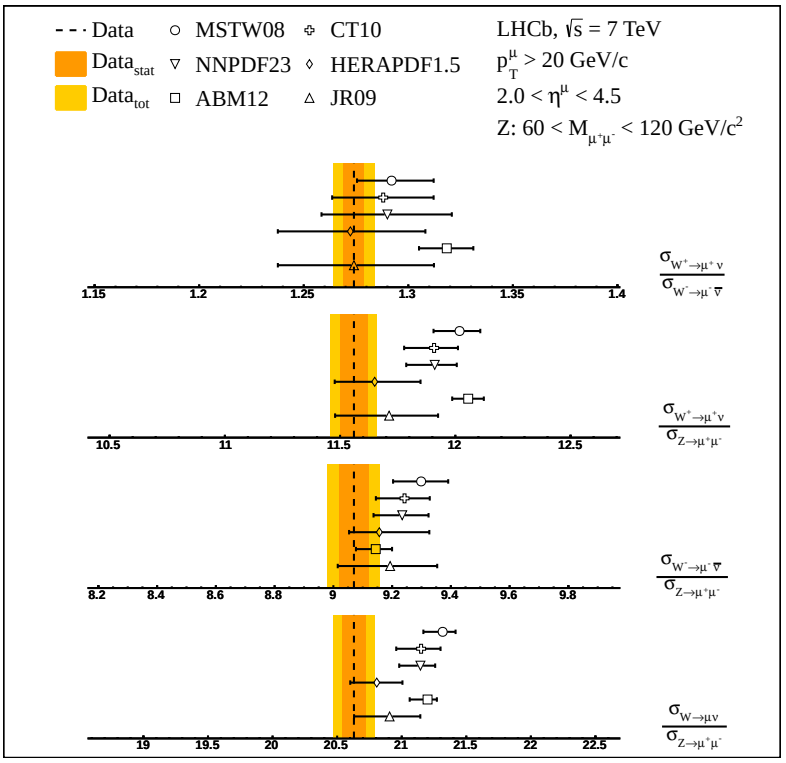

Figure 5.8: SAMPLE-I measurements ($\sqrt{s} = 7$ TeV) of electroweak boson cross-section ratios R_{W^+Z}, R_{W^-Z}, R_{WZ}, R_W compared to NNLO perturbative QCD, as implemented by the FEWZ generator using various PDF sets. The shaded (yellow) bands indicate the statistical and total uncertainties on the measurements, which are symmetric about the central value. The uncertainties on the theoretical predictions are due to the PDFs, scale and α_s uncertainties.

Discussion

The cross-sections in Figure 5.2 show excellent agreement with predictions. The cross-section ratios in Figure 5.8 also show agreement, but with the increased relative precision in the ratios, there is more sensitivity to the choice of PDF set. It is important to stress that the precision of the SM prediction is represented by the spread of the NNLO predictions, which arises due to the many PDFs. With this in mind, the measurements are still in agreement with the SM.

In the forward region of LHCb, the W^+/W^- ratio is an approximate measure of the u/d quark ratio at high-x [118]. As is clear from Figure 5.8, measurement and prediction agree very well. The W/Z ratio, by the same approximation, is insensitive to u- and d-quark PDF uncertainties [83, 105, 118]. While the measurement of this ratio is in agreement with the predictions, this agreement is not as good as observed for the W^+/W^- ratio. The best agreement here is achieved with the HERAPDF1.5 and JR09 PDF sets. As evident from Table 2.2, these PDF sets do not use the $\nu N \to \mu^+\mu^- X$

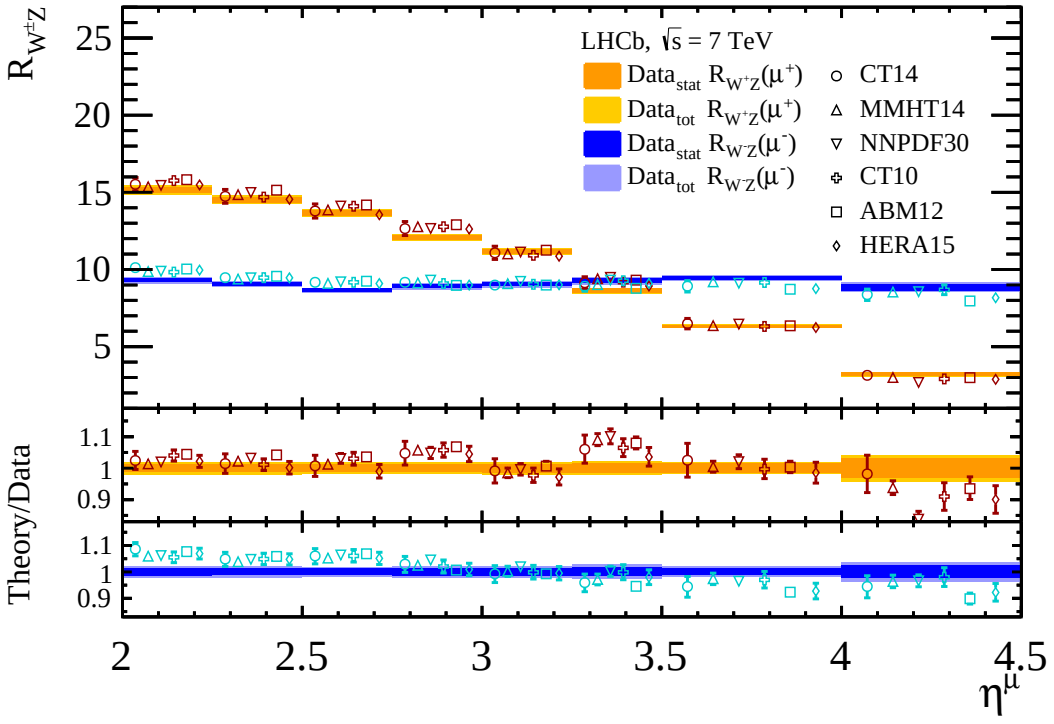

Figure 5.9: Differential W^+ (W^-) to Z cross-section ratio in bins of μ^+ (μ^-) pseudorapidity, as measured on Sample-I. Measurements, represented as bands corresponding to the statistical (orange (blue) for R_{W^+Z} (R_{W^-Z})) and total (yellow (light blue) for R_{W^+Z} (R_{W^-Z})) uncertainty, are compared to NNLO predictions with different parameterisations of the PDFs.

dimuon data in their fit. This data is obtained by colliding a neutrino with a fixed target of Fe. A Feynman diagram representing the process is shown in Figure 5.10. These data are very interesting because they have also been used to motivate the suppression of the s-quark sea with respect to the u- and d-quark sea in PDF fits [25]. This is at odds with the ATLAS observation that suggests that the quark sea has no preference for any of the light quark flavours [40]. Furthermore, it has been shown that the s-quark PDF at low-x is particularly sensitive to nuclear modification factors, which are required to extract the proton PDFs from the nuclear PDFs obtained from the νN dimuon data [119].

Since production of Z bosons is more sensitive to the strange content of the proton than W bosons [120], it could be possible to attribute differences between measurements and predictions of the W/Z ratios to the s-quark parameterisation in PDFs. It is clear that the W/Z measurements presented above are an interesting prospect for further study and analysis.

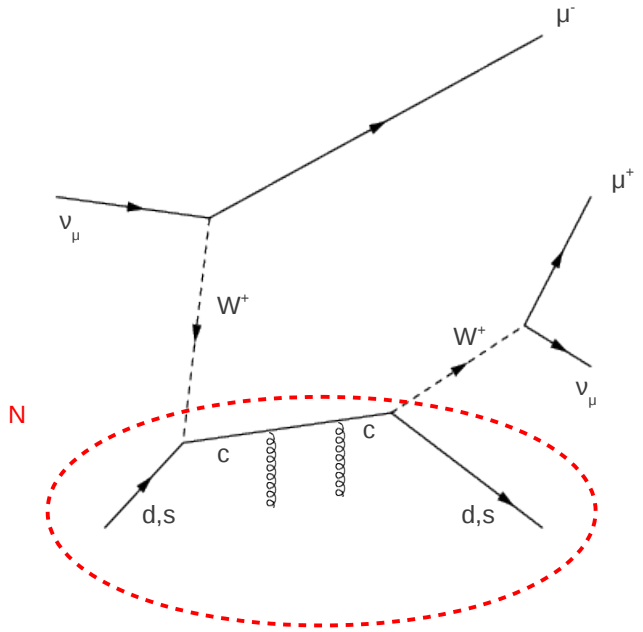

Figure 5.10: Feynman diagram representing neutrino-nucleon dimuon production ($\nu N \rightarrow \mu^+\mu^- X$). In this example, the down-type (d, s) content of the nucleon is probed. The red ellipse represents the nucleon N, which is typically Fe.

5.4.4 Sample-II W/Z ratio

The W to Z boson cross-section ratio at $\sqrt{s} = 8$ TeV is measured as

$$R_{WZ} = 20.13 \pm 0.06 \pm 0.11 \pm 0.04.$$

As before, the first uncertainty is statistical, the second is systematic and the third is due to the beam energy. The total precision is 0.7%, while the statistical precision is 0.3%. The largest systematic uncertainty is due to the determination of the W boson sample selection efficiency, which is 0.2%. The charged W to Z boson cross-section ratios are measured as

$$\begin{aligned} R_{W^+Z} &= 11.51 \pm 0.04 \pm 0.07 \pm 0.02, \\ R_{W^-Z} &= \ \ 8.62 \pm 0.03 \pm 0.05 \pm 0.02, \end{aligned}$$

while the W boson cross-section ratio is measured as

$$R_W = 1.336 \pm 0.004 \pm 0.005 \pm 0.002.$$

These are 0.7%, 0.7% and 0.5% measurements respectively. The largest systematic uncertainty on the R_{W^+Z} ratio is due to the purity of the W boson sample (0.3%),

while the largest systematic uncertainty on the R_{W^-Z} ratio is due to the selection (0.2%). As with SAMPLE-I, the largest uncertainty on the measurement of R_W is due to the template shapes and normalisations used to extract the W boson signal from the W event sample, which is 0.3%. The breakdown of the uncertainties on the cross-section ratios is given in Table 5.5.

The ratio measurements, as well as their predictions, are displayed in Figure 5.11. The

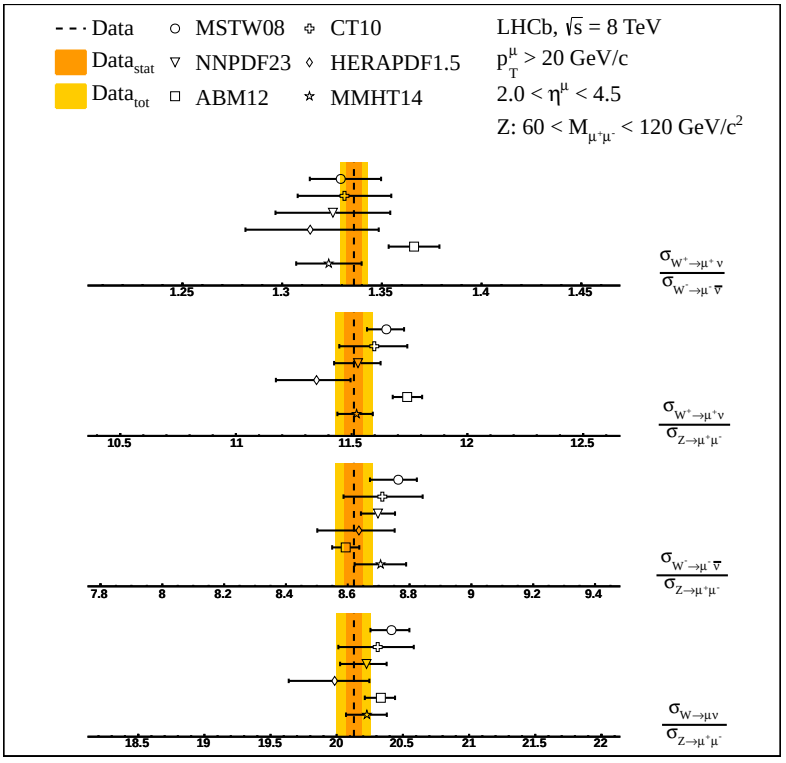

Figure 5.11: SAMPLE-II measurements ($\sqrt{s} = 8$ TeV) of electroweak boson cross-section ratios R_{W^+Z}, R_{W^-Z}, R_{WZ}, R_W compared to NNLO perturbative QCD, as implemented by the FEWZ generator using various PDF sets. The shaded (yellow) bands indicate the statistical and total uncertainties on the measurements, which are symmetric about the central value. The uncertainties on the theoretical predictions are due to the PDFs, scale and α_s uncertainties.

agreement between measurement and prediction is excellent.

The ratios R_{W^+Z} and R_{W^-Z} are also measured differentially as a function of muon η. These measurements are displayed in Figure 5.12. Good agreement between measured and predicted values is observed, and as with SAMPLE-I, it is noted that the measured R_{W^-Z} ratio is a more constant function of η^μ than predicted.

Electroweak boson cross-section ratios have also been measured by the ATLAS [105] and CMS [106], [107] collaborations in their respective fiducial volumes. The results are summarised in Table 5.7. The relative precision of the measurements is expressed in

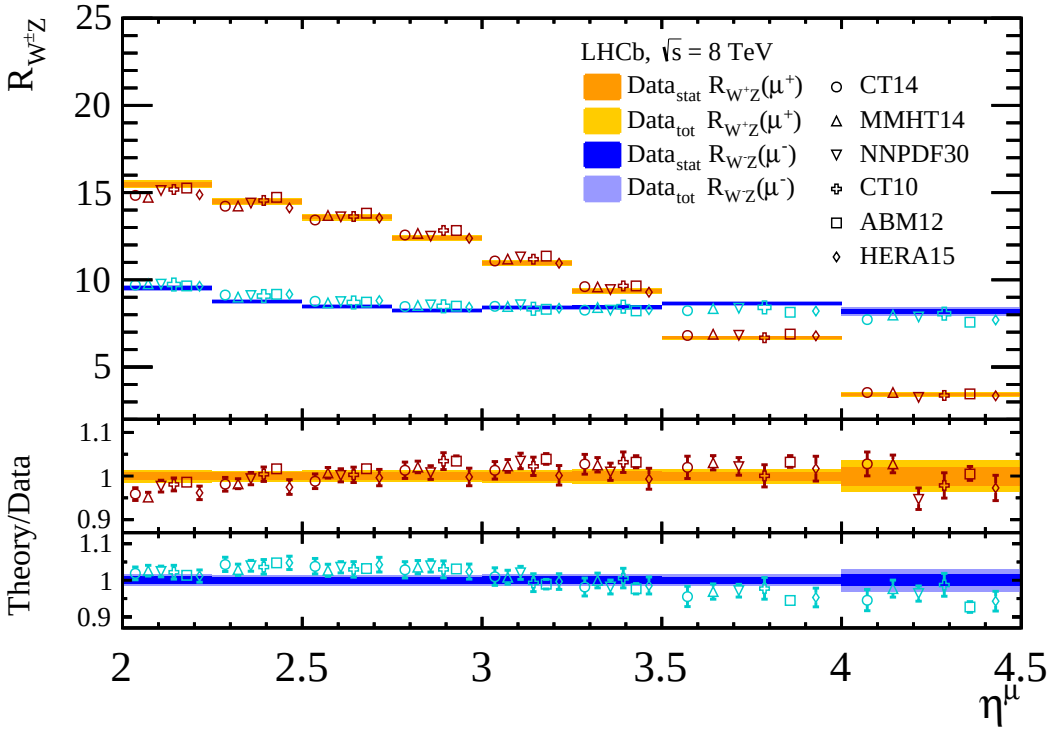

Figure 5.12: Differential W^+ (W^-) to Z cross-section ratio in bins of μ^+ (μ^-) pseudorapidity, as measured on SAMPLE-II. Measurements, represented as bands corresponding to the statistical (orange (blue) for R_{W^+Z} (R_{W^-Z})) and total (yellow (light blue) for R_{W^+Z} (R_{W^-Z})) uncertainty, are compared to NNLO predictions with different parameterisations of the PDFs.

terms of the ratios of fiducial cross-sections $R_{WZ}^{\text{fid.}}$ and their total uncertainties $\delta R_{WZ}^{\text{fid.}}$. The integrated luminosities ($\mathcal{L}$) and centre-of-mass energies of the samples are also indicated.

	$\sqrt{s} = 7$ TeV		$\sqrt{s} = 8$ TeV	
Collaboration	$\mathcal{L}$ [pb^{-1}]	$\frac{\delta R_{WZ}^{\text{fid.}}}{R_{WZ}^{\text{fid.}}}$ x 100 [%]	$\mathcal{L}$ [pb^{-1}]	$\frac{\delta R_{WZ}^{\text{fid.}}}{R_{WZ}^{\text{fid.}}}$ x 100 [%]
ATLAS	36	1.3	–	–
CMS	36	2.1	18	3.0
LHCb	1000	0.8	2000	0.7

Table 5.7: Relative precision on electroweak boson cross-section ratio measurements from different LHC experiments. The ATLAS and CMS results do not include uncertainties due to proton beam energy.

5.4.5 Ratios at different centre-of-mass energy

As explained in Ref. [112], the large degree of correlation between cross-sections (and cross-section ratios) at different centre-of-mass energies, both theoretically and experimentally, makes them an interesting set of observables. From the theoretical side, the PDF uncertainty cancellation is particularly large if similar cross-sections are analysed; the PDFs are probed at the exact same Q^2, which is set by the boson mass. However, at higher beam energies the proportion of quark pairs from the sea is increased and the required x value to produce a boson in the rapidity range is reduced.

The cross-section ratios at different centre-of-mass energies are measured as

$$R_{W^+}^{8/7} = \frac{\sigma_{W^+}^{8\text{ TeV}}}{\sigma_{W^+}^{7\text{ TeV}}} = 1.245 \pm 0.004 \pm 0.008 \pm 0.001 \pm 0.018,$$
$$R_{W^-}^{8/7} = \frac{\sigma_{W^-}^{8\text{ TeV}}}{\sigma_{W^-}^{7\text{ TeV}}} = 1.187 \pm 0.004 \pm 0.007 \pm 0.001 \pm 0.017,$$
$$R_{Z}^{8/7} = \frac{\sigma_{Z}^{8\text{ TeV}}}{\sigma_{Z}^{7\text{ TeV}}} = 1.250 \pm 0.006 \pm 0.007 \pm 0.001 \pm 0.018.$$

The first uncertainty is statistical, the second is systematic, the third is due to the beam energy and the fourth is due to the luminosity. The treatment of uncertainty is explained in Section 5.3.8 and the breakdown is given in Table 5.6. The precision is about 1.6% in all cases, where this is dominated by the uncertainty due to the luminosity determination (1.45%). It is estimated that about 50% of the uncertainty due to luminosity in Sample-I and Sample-II is correlated, as mentioned in Section 5.3.8. These measurements are shown in Figure 5.13, along with their predictions.

The measurements and predictions are in agreement. Compared to Figures 5.2, 5.3, 5.8 and 5.11, the degree to which the predictions line up is striking. The fact that there is very little spread in their central value indicates that the uncertainty due to the PDF is very much reduced, which is also reflected in the calculated uncertainties on the individual PDF predictions. The theoretical uncertainties shown here are due to PDF, scale, α_s and numerical integration. These are similar in size.

According to Ref. [112], these measurements may be used in two ways. The first takes advantage of the fact that the PDF predictions give the same value at the per mille level. Assuming that the SM is correct, the differences between the predictions and the measured ratio can be used to measure a miscalibration of the ratio of luminosities in Sample-I and Sample-II, also at the per mille level. The second infers the existence of BSM physics due to discrepancies in the scaling of the predicted and measured

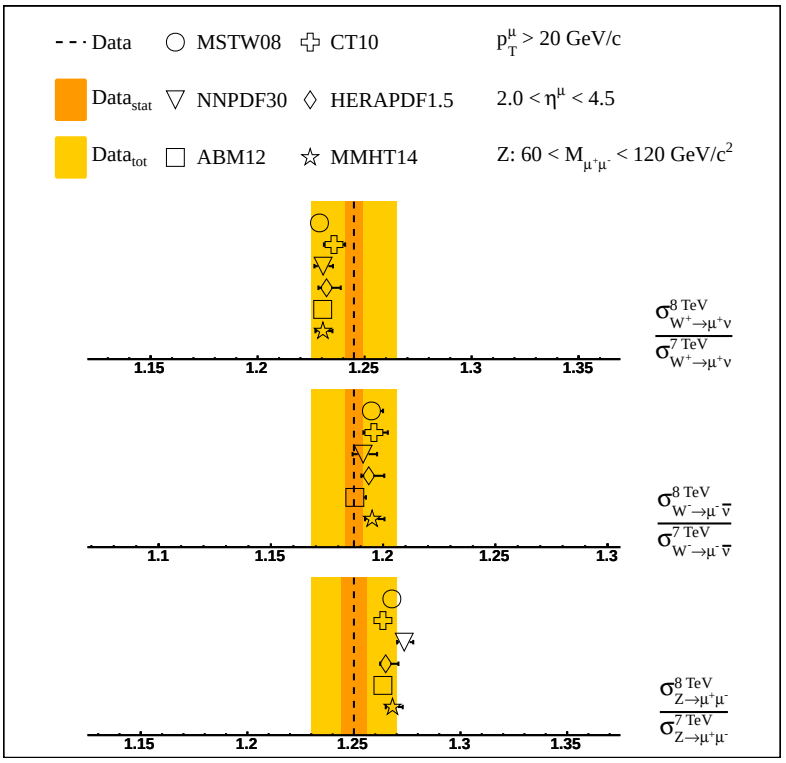

Figure 5.13: Ratios of electroweak boson production cross-sections measured in Sample-I and Sample-II compared to NNLO perturbative QCD, as implemented by the Fewz generator using various PDF sets. The shaded (yellow) bands indicate the statistical and total uncertainties on the measurements, which are symmetric about the central value. The uncertainties on the theoretical predictions are due to PDFs, scale, α_s and numerical integration, all of which are similar in size.

cross-sections with centre-of-mass energy. In particular, this can occur if a BSM signal evolves differently with centre-of-mass energy to electroweak boson production (see Appendix F).

To be confident that the data suggest a miscalibration in the ratio of luminosities, the central values of all three measurements should be either consistently higher or lower than the corresponding sets of theoretical predictions. As can be seen from Figure 5.13, this is not the case. As a consequence, no correction is measured. In addition, since the measurements and predictions are in agreement, there is no evidence of BSM physics.

More precise measurements are obtained through ratios-of-ratios of cross-sections. In this case, the luminosity uncertainty cancels, and there is more sensitivity to a BSM

signal. The ratios-of-ratios of cross-sections at different centre-of-mass energies are measured as

$$R^{8/7}_{R_W} = \frac{R^{8\text{ TeV}}_{W}}{R^{7\text{ TeV}}_{W}} = 1.049 \pm 0.005 \pm 0.007,$$
$$R^{8/7}_{R_{W^+Z}} = \frac{R^{8\text{ TeV}}_{W^+Z}}{R^{7\text{ TeV}}_{W^+Z}} = 0.996 \pm 0.006 \pm 0.005,$$
$$R^{8/7}_{R_{W^-Z}} = \frac{R^{8\text{ TeV}}_{W^-Z}}{R^{7\text{ TeV}}_{W^-Z}} = 0.950 \pm 0.006 \pm 0.006,$$
$$R^{8/7}_{R_{WZ}} = \frac{R^{8\text{ TeV}}_{WZ}}{R^{7\text{ TeV}}_{WZ}} = 0.976 \pm 0.005 \pm 0.004,$$

where the first uncertainty is statistical, the second is systematic and the third is due to the beam energy. The precision of these ratios could be greatly improved with a larger data set since the statistical uncertainty is one of the dominating uncertainties, ranging between 0.5–0.6%. The largest source of systematic uncertainty on these ratios is due to the evaluation of the purity of the W boson sample, which ranges between 0.3–0.7%. The breakdown of all relevant uncertainties is given in Table 5.6.

These ratio measurements are shown in Figure 5.14, along with their predictions. As in Figure 5.13, the scatter of the predictions is small suggesting the uncertainty due to PDFs is small. Since they are of similar magnitude, the scale, α_s and numerical integration uncertainties are included. The ratios $R^{8/7}_{R_{W^-Z}}$ and $R^{8/7}_{R_{WZ}}$ agree theoretically and experimentally, but there is some discrepancy in the $R^{8/7}_{R_W}$ and $R^{8/7}_{R_{W^+Z}}$ ratios. However, at the current level of precision, the discrepancies are not large enough to claim deviation from the SM.

It is not immediately obvious why the theoretical values for the ratios $R^{8/7}_{R_W}$, $R^{8/7}_{R_{W^+Z}}$, $R^{8/7}_{R_{W^-Z}}$ and $R^{8/7}_{R_{WZ}}$, should have values slightly above and below unity. The answer lies in the rates at which the W and Z boson cross-sections increase with centre-of-mass energy. The cross-section rises approximately logarithmically as evident in Figures 4.32 and 5.5. The partonic cross-section (see Section 2.3) goes as the inverse square of the centre-of-mass energy for all three bosons [121]. Thus, it is the PDFs that account for the logarithmic growth of the hadronic cross-section. The rate of increase in the Z boson cross-section is greatest, followed closely by that of the W^+ cross-section. The W^- cross-section grows less rapidly.

The ratios $R^{8/7}_{R_{W^+Z}}$, $R^{8/7}_{R_{W^-Z}}$ are also measured differentially as a function of muon η. These measurements are displayed in Figure 5.15. Only uncertainties due to PDFs are included on the predictions. Good agreement between measurement and prediction is observed, especially for the $R^{8/7}_{R_{W^-Z}}$ ratio. The measurement of the $R^{8/7}_{R_{W^+Z}}$ ratio is larger

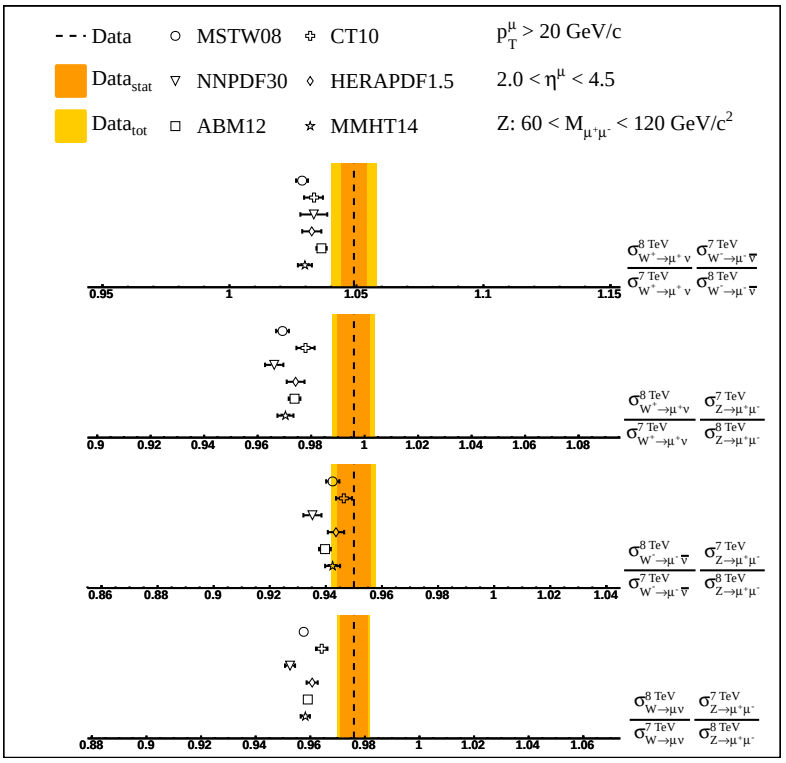

Figure 5.14: Ratios-of-ratios of electroweak boson production cross-sections measured in SAMPLE-I and SAMPLE-II compared to NNLO perturbative QCD, as implemented by the FEWZ generator using various PDF sets. The shaded (yellow) bands indicate the statistical and total uncertainties on the measurements, which are symmetric about the central value. The uncertainties on the theoretical predictions are due to PDFs, scale, α_s and numerical integration, all of which are similar in size.

than the predicted values in the range $2 < \eta^\mu < 3$. The individual cross-sections are large in this region (see Figures 4.43 - 4.44 and Tables 5.2 - 5.3), and have the greatest weight in the integrated ratio shown in Figure 5.14.

The $R^{8/7}_{R_{W+Z}}$ ratio increases as a function of η^μ, while the $R^{8/7}_{R_{W+Z}}$ ratio decreases as a function of η^μ. The PDF uncertainties are largest for the $R^{8/7}_{R_{W+Z}}$ ratio at high pseudorapidity, suggesting that these measurements can improve the determination of the PDFs in this region.

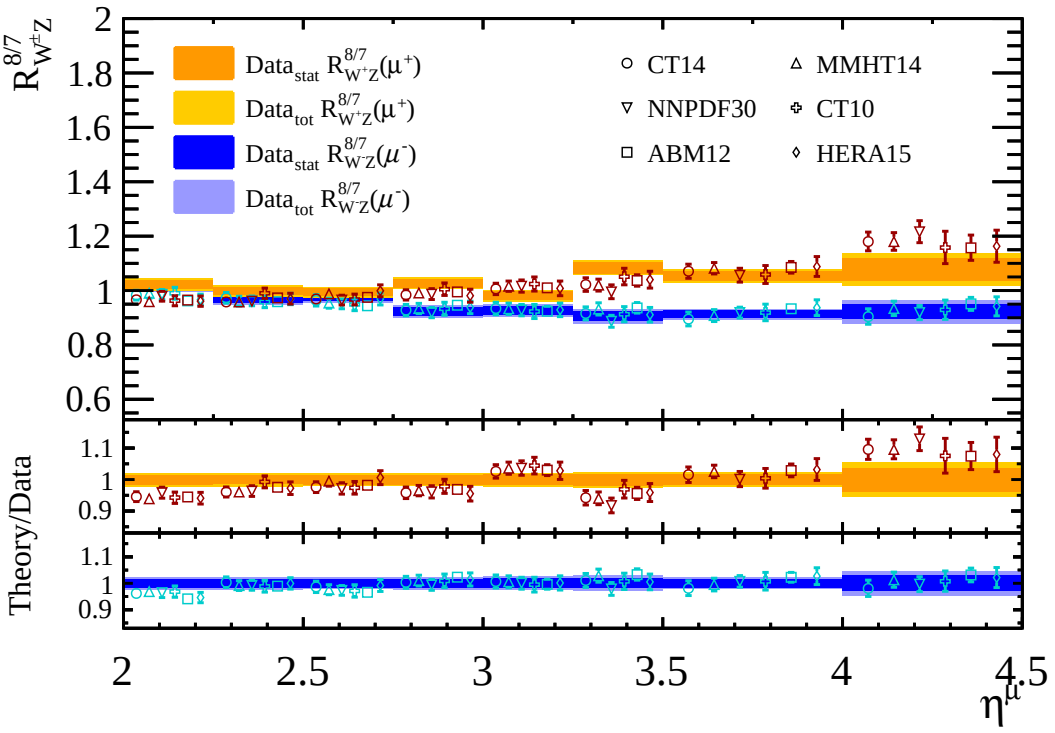

Figure 5.15: Cross-section ratios-of-ratios at different centre-of-mass energies as a function of muon η. Measurements, represented as bands corresponding to the statistical (orange (blue) for η^+ (η^-)) and total (yellow (light blue) for η^+ (η^-)) uncertainty, are compared to NNLO predictions with different parameterisations of the PDFs.

Chapter 6

Conclusions

This thesis describes a number of measurements involving electroweak boson cross-sections that were performed using data collected by the LHCb detector during Run-I of LHC operation. The measurements were undertaken with two primary objectives in mind; the first, measure the Z boson cross-section at different centre-of-mass energies; the second, use these cross-sections, in conjunction with W boson cross-sections, to make precision tests of the Standard Model. A synopsis of the measurements is provided in the following paragraphs, where comments are given on the agreement of measurements with predictions, the precision achieved, and thoughts for future development of similar analyses.

The first objective is addressed in Chapter 4, where measurements of Z boson production cross-sections at centre-of-mass energies of 7 and 8 TeV are presented with relative precision of about 2%. Most of the uncertainty is due to the determination of the integrated luminosity and proton beam energy. This precision is at a similar level to the theoretical precision of the NNLO QCD predictions. Despite the potential sensitivity to new physics, the measurements are in excellent agreement with these predictions and the SM in general. Although it is not the first time the Z boson cross-section has been measured, the overall precision is almost halved with respect to previous measurements, which have 3.5–4.2% relative precision.

The second objective is addressed in Chapter 5, where measurements of electroweak boson cross-section ratios at centre-of-mass energies of either 7 or 8 TeV are presented, with relative precision varying between 0.5–0.9%. The dominant uncertainties on these ratio measurements are due to the sizes of the samples of Z bosons (0.3–0.5%) and the determinations of W boson sample purities (0.2–0.6%). As with the cross-section measurements mentioned above, the ratio measurements are in agreement with the SM

and NNLO QCD predictions, with some PDF sets favoured over others. Previous measurements of similar quantities, at 1.3–3.0% relative precision, are improved by more than a factor of two. In addition, measurements of the charged W to Z boson ratio, differential in muon η, are performed for the first time at the LHC. Good agreement with predictions is observed, although the negatively charged ratio is flatter in η than predicted.

Chapter 5 also includes measurements of cross-section ratios at different centre-of-mass energies, which are determined with a relative precision of about 1.6%. The dominant uncertainty is due to the luminosity, which contributes 1.45%. These measurements are the first of their kind to be performed at the LHC, and are performed for two specific reasons. The first is to investigate contributions to the cross-section due to sources other then the SM. No evidence of this is observed. The second is to use the measurements to calibrate the ratio of luminosities on two different data sets. No evidence of a need for such a calibration is observed either.

The ratios-of-ratios of cross-sections at different centre-of-mass energies constitute the final set of measurements. These are presented in Chapter 5, and the relative precision achieved varies between 0.7–0.9%. The dominant uncertainties are again due to the sizes of the samples of Z bosons (0.5–0.6%) and the determinations of the W boson sample purities (0.3–0.7%). A sensitivity to individual PDF sets is displayed by some of these ratio measurements. These measurements are also the first of their kind to be performed at the LHC.

Measurements of the quantities mentioned above using Run-II data at centre-of-mass energies of 13 and 14 TeV will test the SM at the highest energies and have increased sensitivity to BSM effects. It is not sufficient to repeat the analysis presented here with Run-II data alone. Comparisons must be made between Run-I and Run-II data. Taking the ratio of Z boson cross-sections as the example to demonstrate the permutations, each of $R_Z^{14/13}$, $R_Z^{14/8}$, $R_Z^{14/7}$, $R_Z^{13/8}$ and $R_Z^{13/7}$ have the potential to reveal new physics. The larger samples sizes will reduce the statistical uncertainties, which dominate the precision at which the electroweak boson cross-section ratios are measured here.

This thesis has presented the measurements of cross-sections, cross-sections ratios, ratios of cross-sections at different centre-of-mass energies, and ratios-of-ratios of cross-sections at different centre-of-mass energies. Measurements from the latter two categories are presented for the first time. The precision on all measurements is the best obtained at the LHC to date. In general, the measurements agree with SM predictions, and the high level of experimental precision provides a sensitive test of the SM, as well as giving results that can be used to improve the PDFs.

Appendix A

Heavy flavour systematics

p_T [GeV/c]	Cand-Mod	HF-VTX	HF-ISO	HF-VTX-ISO
10	72445	908	977	277
11	72078	858	912	264
12	71586	795	834	248
13	70985	710	748	228
14	70308	643	650	208
15	69569	572	555	177
16	68718	491	470	151
17	67774	411	381	122
18	66707	336	311	99
19	65539	282	263	91
20	64248	227	196	66

Table A.1: Shown are the number of events in a modified Sample-I candidate sample (Cand-Mod), where the mass cut is loosened to $M_{\mu^+\mu^-} > 40$ GeV/c^2, and the p_T cut on the muons is relaxed to various different thresholds. The number of events in the corresponding heavy flavour enriched samples (HF-VTX, HF-ISO and HF-VTX-ISO) are also shown. The column HF-VTX-ISO shows the overlap between the HF-VTX and HF-ISO samples.

p_T [GeV/c]	MC-MOD	MC-VTX	MC-ISO	MC-VTX-ISO
10	161902	21	8	0
11	161638	21	8	0
12	161216	21	8	0
13	160638	21	8	0
14	159780	20	8	0
15	158669	20	8	0
16	157235	20	8	0
17	155576	19	7	0
18	153570	19	7	0
19	151237	17	7	0
20	148603	17	6	0

Table A.2: Shown are the number of events in the $\sqrt{s} = 7$ TeV MC simulated sample (MC-MOD), where the p_T cut on the muons is relaxed to various different thresholds. The number of events in the heavy flavour enriched samples (MC-VTX, MC-ISO and MC-VTX-ISO) are also shown. The column MC-VTX-ISO shows the overlap between the MC-VTX and MC-ISO samples. The mass window remains $60 < M_{\mu^+\mu^-} < 120$ GeV/c^2.

p_T [GeV/c]	$\int_{60}^{120} e^x$	ϵ_{vtx}	Bkg.
10	77.9	0.28	274
11	78.3	0.29	269
12	78.8	0.30	263
13	78.5	0.31	255
14	78.0	0.32	243
15	78.0	0.32	244
16	69.2	0.32	215
17	67.1	0.32	209
18	67.8	0.32	214
19	66.1	0.35	191
20	62.1	0.34	184

Table A.3: Numbers relating to the heavy flavour background estimate for Sample-I when all events in the HF-VTX sample with masses above 40 GeV/c^2 are considered in the fit. The first column indicates the p_T threshold on the muons. The second column shows the integral of the fitted exponential function in the mass region of the measurement. The third column is the efficiency of the HF-VTX cut on heavy flavour events. The final column is the estimated background.

p_T [GeV/c]	$\int_{60}^{120} e^x$	ϵ_{iso}	Bkg.
10	83.6	0.31	273
11	83.8	0.31	271
12	84.3	0.31	269
13	78.1	0.32	242
14	76.7	0.33	236
15	72.4	0.31	233
16	66.3	0.31	213
17	63.6	0.30	212
18	59.3	0.30	201
19	55.1	0.33	169
20	47.5	0.29	162

Table A.4: Numbers relating to the heavy flavour background estimate for SAMPLE-I when all events in the HF-ISO sample with masses above 40 GeV/c^2 are considered in the fit. The first column indicates the p_T threshold on the muons. The second column shows the integral of the fitted exponential function in the mass region of the measurement. The third column is the efficiency of the HF-ISO cut on heavy flavour events. The final column is the estimated background.

p_T [GeV/c]	$\int_{60}^{120} e^x$	ϵ_{vtx}	Bkg.
10	56.9	0.28	200
11	57.5	0.29	198
12	59.5	0.30	198
13	61.7	0.31	201
14	63.2	0.32	197
15	66.5	0.32	208
16	71.0	0.32	221
17	82.0	0.32	256
18	80.1	0.32	253
19	90.9	0.35	263
20	112.4	0.34	334

Table A.5: Numbers relating to the heavy flavour background estimate for SAMPLE-I when all events in the HF-VTX sample with masses between 40 and 60 GeV/c^2 are considered in the fit. The first column indicates the p_T threshold on the muons. The second column shows the integral of the fitted exponential function in the mass region of the measurement. The third column is the efficiency of the HF-VTX cut on heavy flavour events. The final column is the estimated background.

p_T [GeV/c]	$\int_{60}^{120} e^x$	ϵ_{iso}	Bkg.
10	59.7	0.31	195
11	63.2	0.31	204
12	68.3	0.31	218
13	74.9	0.32	232
14	80.4	0.33	247
15	76.1	0.31	244
16	77.1	0.31	248
17	93.3	0.30	311
18	111.7	0.30	378
19	171.3	0.33	525
20	296.0	0.29	1011

Table A.6: Numbers relating to the heavy flavour background estimate for SAMPLE-I when all events in the HF-ISO sample with masses between 40 and 60 GeV/c^2 are considered in the fit. The first column indicates the p_T threshold on the muons. The second column shows the integral of the fitted exponential function in the mass region of the measurement. The third column is the efficiency of the HF-ISO cut on heavy flavour events. The final column is the estimated background.

Appendix B

Reconstruction efficiencies

η	ϵ_{trg}	$\delta\epsilon_{trg}$
2.000-2.080	0.731	0.005
2.080-2.165	0.773	0.005
2.165-2.250	0.782	0.005
2.250-2.375	0.791	0.004
2.375-2.500	0.798	0.004
2.500-2.750	0.796	0.003
2.750-3.000	0.779	0.003
3.000-3.250	0.785	0.003
3.250-3.500	0.799	0.003
3.500-3.750	0.795	0.004
3.750-4.000	0.790	0.004
4.000-4.250	0.808	0.005
4.250-4.500	0.799	0.006

Table B.1: Single muon trigger efficiencies and their uncertainties as a function of pseudorapidity. These numbers correspond to SAMPLE-II.

η	ϵ_{ID}	$\delta\epsilon_{ID}^{TP}$	$\delta\epsilon_{ID}^{sys.}$	$\delta\epsilon_{ID}$
2.000-2.080	0.970	0.002	0.001	0.003
2.080-2.165	0.987	0.002	0.001	0.002
2.165-2.250	0.988	0.002	0.001	0.002
2.250-2.375	0.989	0.001	0.001	0.002
2.375-2.500	0.989	0.002	0.001	0.002
2.500-2.750	0.990	0.001	0.001	0.002
2.750-3.000	0.988	0.001	0.001	0.002
3.000-3.250	0.986	0.001	0.001	0.002
3.250-3.500	0.988	0.001	0.001	0.002
3.500-3.750	0.972	0.002	0.001	0.002
3.750-4.000	0.984	0.002	0.001	0.002
4.000-4.250	0.990	0.002	0.001	0.002
4.250-4.500	0.913	0.005	0.001	0.005

Table B.2: Single muon identification efficiencies and their uncertainties as a function of pseudorapidity. These numbers correspond to SAMPLE-II.

η	ϵ_{trk}	$\delta\epsilon_{trk}^{TP}$	$\delta\epsilon_{trk}^{TM}$	$\delta\epsilon_{trk}^{Bias1}$	$\delta\epsilon_{trk}^{Bias2}$	$\delta\epsilon_{trk}$
2.000-2.080	0.818	0.014	0.004	0.004	0.009	0.015
2.080-2.165	0.872	0.010	0.004	0.003	0.001	0.012
2.165-2.250	0.865	0.010	0.003	0.003	0.001	0.011
2.250-2.375	0.870	0.008	0.003	0.002	0.001	0.009
2.375-2.500	0.932	0.006	0.002	0.002	0.001	0.006
2.500-2.750	0.937	0.003	0.001	0.001	0.001	0.004
2.750-3.000	0.940	0.003	0.001	0.001	0.001	0.004
3.000-3.250	0.946	0.003	0.001	0.001	0.002	0.004
3.250-3.500	0.967	0.003	0.001	0.001	0.001	0.003
3.500-3.750	0.968	0.004	0.002	0.001	0.001	0.004
3.750-4.000	0.963	0.004	0.002	0.002	0.001	0.005
4.000-4.250	0.942	0.005	0.002	0.002	0.002	0.006
4.250-4.500	0.921	0.009	0.003	0.003	0.002	0.010

Table B.3: Single muon tracking efficiencies and their uncertainties as a function of pseudorapidity. These numbers correspond to SAMPLE-II.

Appendix C

Analysis of uncertainty

In this appendix, the formalism used to derive correlation coefficients is given. A number of concepts are defined before defining the correlation. Much of the notation and discussion is taken from Ref. [122].

C.1 Variance

The spread of data is measured using a function called the variance. Suppose there is some function f of one variable x. The variance of f, $V(f)$, is given by

$$V(f) = \frac{1}{N}\sum_i (f(x_i) - \bar{f})^2. \tag{C.1}$$

The variance is essentially the average squared deviation from the mean. The square-root of the variance gives the standard deviation δ_f, which is the uncertainty on f. If g is another function of x, one may define the covariance of f and g

$$\mathrm{cov}(f(x), g(x)) = \frac{1}{N}\sum_i (f(x_i) - \bar{f})(g(x_i) - \bar{g}). \tag{C.2}$$

If $g = f$, one obtains the formula for the variance of f, given in Equation C.1.

C.2 Expectation value

Given a probability density $P(x)$ of some variable x, the expected value of a function of x is given by

$$< f > = \int dx\ f(x)\ P(x), \tag{C.3}$$

which is also known as the expectation value of f. The variance of f and the expectation value of f are related by the formula

$$V(f) = < f^2 > - < f >^2 . \tag{C.4}$$

C.3 Ratios of correlated quantites

Consider a function $f(x, y)$ of two variables x and y. The function f may be expanded in a Taylor series about some point x_0, y_0.

$$f(x, y) \approx f(x_0, y_0) + (x - x_0)\frac{df}{dx}\bigg|_{x=x_0} + (y - y_0)\frac{df}{dy}\bigg|_{y=y_0} \tag{C.5}$$

Using the expression in Equation C.5, it can be shown that

$$V(f) = \Big(\frac{df}{dx}\Big)^2 V(x) + \Big(\frac{df}{dy}\Big)^2 V(y) + 2\Big(\frac{df}{dx}\Big)\Big(\frac{df}{dy}\Big)(< xy > - < x >< y >). \tag{C.6}$$

The $< xy > - < x >< y >$ part is the covariance between x and y. The correlation coefficient ρ is defined by

$$< xy > - < x >< y > = \rho \sqrt{V(x)V(y)} = \rho\, \sigma_x \sigma_y. \tag{C.7}$$

If $f = x/y$, the derivative with respect to y in the third term of Equation C.6 is negative. If x and y are correlated ($0 < \rho \leq 1$) then the uncertainty on f will be less than if they are uncorrelated ($\rho = 0$). If x and y are anti-correlated ($-1 \leq \rho < 0$) then the uncertainty on f will be greater than if they are uncorrelated ($\rho = 0$).

C.4 Covariance and correlation matrices

The analysis above may be extended to m functions $f_1, f_2, ..., f_m$ in n variables $x_1, x_2, ..., x_n$. In this thesis, the f_k are differential cross-sections and the x_i are measurements that they depend on, such as muon reconstruction efficiencies. The result for the covariance between these functions is

$$< f_k f_l > - < f_k >< f_l > = \sum_i^n \sum_j^n \Big(\frac{\partial f_k}{\partial x_i}\Big)\Big(\frac{\partial f_l}{\partial x_j}\Big)(< x_i x_j > - < x_i >< x_j >). \tag{C.8}$$

This equation can be written in matrix notation as

$$\mathbf{V_f} = \mathbf{G}\mathbf{V_x}\mathbf{G^T}, \tag{C.9}$$

where $\mathbf{V_f}$ is the covariance between the f_k and $\mathbf{V_x}$ is the covariance between the x_i. The elements of the matrix $\mathbf{G}$ are identified with the partial derivatives, $G_{ki} = \frac{\partial f_k}{\partial x_i}$.

Elements of the matrix $\mathbf{V_f}$ are related to elements of the correlation matrix $\mathbf{C}$ (the correlation coefficients) by

$$\mathrm{C}_{ij} = \frac{(\mathrm{V}_f)_{ij}}{\sqrt{(\mathrm{V}_f)_{ii}(\mathrm{V}_f)_{jj}}}. \tag{C.10}$$

C.5 Evaluation of covariance matrices for measured quantities in this thesis

In this section, details are given on how the covariance matrix is evaluated for each source of uncertainty relevant to this thesis. For each source, the covariance matrix, $\mathbf{V_f}$, is determined by calculating a matrix $\mathbf{G}$ and a matrix $\mathbf{V_x}$.

C.5.1 Muon reconstruction efficiencies

As the first example, consider muon reconstruction efficiencies. There are three different types of efficiency, trigger, tracking and identification; there are thirteen muon η bins; and uncertainties are either correlated or uncorrelated between these bins.

In the case of uncorrelated uncertainties between η bins, the matrix $\mathbf{V_x}$ in Equation C.9 is diagonal, the entries being the squares of the uncertainties on the efficiencies.

$$\mathbf{V_x} = \begin{bmatrix} \delta^2_{\epsilon_1} & \cdots & 0 \\ \vdots & \ddots & \vdots \\ 0 & \cdots & \delta^2_{\epsilon_{13}} \end{bmatrix} \tag{C.11}$$

In the case of correlated uncertainties between η bins, the matrix $\mathbf{V_x}$ is not diagonal.

$$\mathbf{V_x} = \begin{bmatrix} \delta^2_{\epsilon_1} & \delta_{\epsilon_1}\delta_{\epsilon_2} & \cdots & \delta_{\epsilon_1}\delta_{\epsilon_{13}} \\ \delta_{\epsilon_2}\delta_{\epsilon_1} & \delta^2_{\epsilon_2} & \cdots & \delta_{\epsilon_2}\delta_{\epsilon_{13}} \\ \vdots & \vdots & \ddots & \vdots \\ \delta_{\epsilon_{13}}\delta_{\epsilon_1} & \delta_{\epsilon_{13}}\delta_{\epsilon_2} & \cdots & \delta^2_{\epsilon_{13}} \end{bmatrix} \tag{C.12}$$

The method for evaluating the partial derivatives, G_{ki}, is identical, whether the uncertainties between η bins are correlated or not. The k indexes cross-section measurements and the i indexes efficiencies. The numerator of the G_{ki} is the difference between the differential cross-section measured in bin k and a hypothetical measurement of this cross-section when a component of the muon reconstruction efficiency is changed by its uncertainty. The denominator is the estimated uncertainty on the efficiency. This has been expressed mathematically in Equation 4.13.

Since there are 34 cross-section measurements (18 measurements in Z boson rapidity and 16 measurements in W boson muon η) and 13 muon reconstruction efficiencies, the matrix **G** has dimension 34 x 13.

C.5.2 Selection

The uncertainties on the W^+ and W^- cross-sections due to selection requirements (E_T^{cone}, p_T^{cone}, p_T^{extra}, IP, and $(E_{ECAL} + E_{HCAL})/pc$) are fully correlated between measurements in the same muon η bin. The correlation matrix between W^+ and W^- measurements is thus block diagonal, the block being given by Equation C.13.

$$\mathbf{B_{SEL}} = \begin{bmatrix} 1 & 1 \\ 1 & 1 \end{bmatrix} \tag{C.13}$$

The correlation matrix can then be written neatly as in Equation C.14.

$$\mathbf{C_{SEL}} = \begin{bmatrix} \mathbf{B_{SEL}} & \cdots & 0 \\ \vdots & \ddots & \vdots \\ 0 & \cdots & \mathbf{B_{SEL}} \end{bmatrix} \tag{C.14}$$

C.5.3 Luminosity (fully correlated uncertainty)

In the case of luminosity, and indeed for any source giving rise to fully correlated uncertainties, the correlation matrix can be written down immediately. It is a 34 x 34 matrix and the value of each element is unity.

The covariance matrix is calculated by multiplying each element by the corresponding uncertainties. This can be implemented easily using matrix multiplication. First define a vector of uncertainties as

$$\mathbf{v} = [\delta_{W_1^+}, \delta_{W_1^-}, ..., \delta_{W_8^+}, \delta_{W_8^-}, \delta_{Z_1}, ..., \delta_{Z_{18}}], \tag{C.15}$$

where the ordering of the uncertainties is a convention adopted for this analysis. Then define the matrices $\mathbf{D}$ and $\mathbf{R}$, which are determined by $\mathbf{v}$.

$$\mathbf{D} = \begin{bmatrix} \delta_{W_1^+} & 0 & 0 & 0 & 0 & 0 & 0 & 0 \\ 0 & \delta_{W_1^-} & 0 & 0 & 0 & 0 & 0 & 0 \\ 0 & 0 & \ddots & 0 & 0 & 0 & 0 & 0 \\ 0 & 0 & 0 & \delta_{W_8^+} & 0 & 0 & 0 & 0 \\ 0 & 0 & 0 & 0 & \delta_{W_8^-} & 0 & 0 & 0 \\ 0 & 0 & 0 & 0 & 0 & \delta_{Z_1} & 0 & 0 \\ 0 & 0 & 0 & 0 & 0 & 0 & \ddots & 0 \\ 0 & 0 & 0 & 0 & 0 & 0 & 0 & \delta_{Z_{18}} \end{bmatrix} \tag{C.16}$$

$$\mathbf{R} = \begin{bmatrix} \delta_{W_1^+} & \delta_{W_1^-} & \cdots & \delta_{W_8^+} & \delta_{W_8^-} & \delta_{Z_1} & \cdots & \delta_{Z_{18}} \\ \delta_{W_1^+} & \delta_{W_1^-} & \cdots & \delta_{W_8^+} & \delta_{W_8^-} & \delta_{Z_1} & \cdots & \delta_{Z_{18}} \\ \vdots & \vdots & \vdots & \vdots & \vdots & \vdots & \vdots & \vdots \\ \delta_{W_1^+} & \delta_{W_1^-} & \cdots & \delta_{W_8^+} & \delta_{W_8^-} & \delta_{Z_1} & \cdots & \delta_{Z_{18}} \end{bmatrix} \tag{C.17}$$

With these definitions, the covariance matrix between measurements with correlated uncertainties is given by $\mathbf{V_f} = \mathbf{DR}$.

Appendix D

Magnet polarity

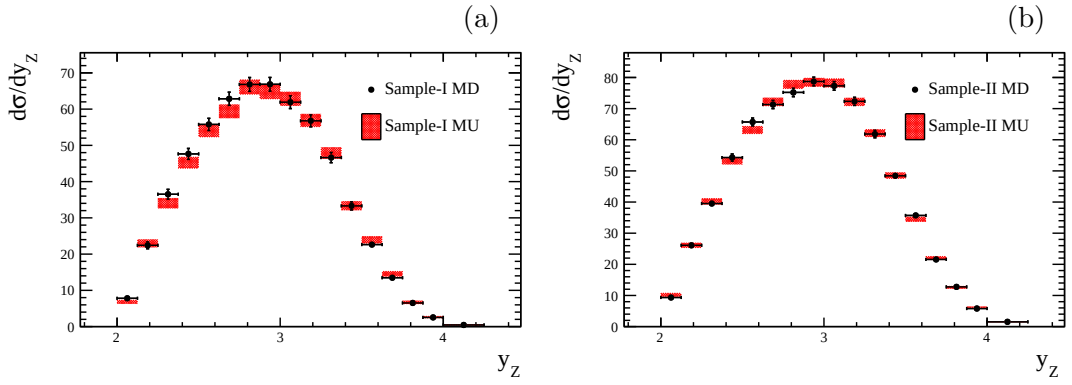

Figure D.1: Differerntial cross-sections as functions of Z boson rapidity for different magnet polarities in SAMPLE-I in (a) and SAMPLE-II in (b). No discrepancy is observed between the different magnet polarities so no systematic uncertainty is considered.

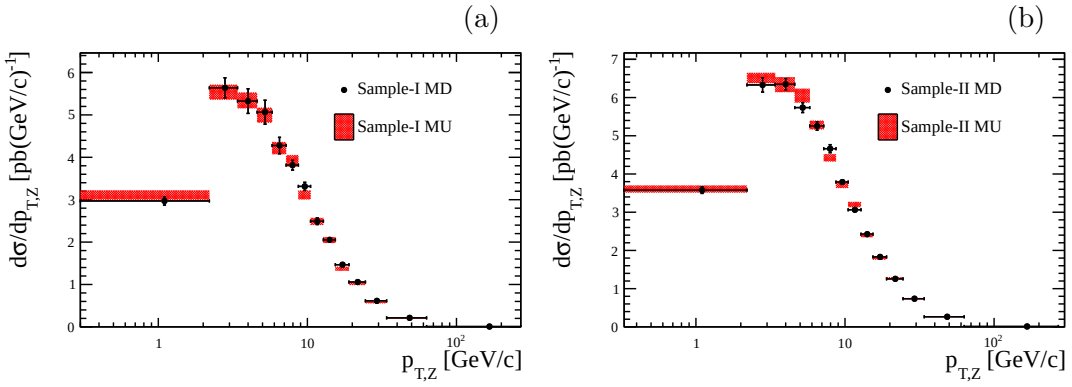

Figure D.2: Differerntial cross-sections as functions of Z boson p_T for different magnet polarities in SAMPLE-I in (a) and SAMPLE-II in (b). No discrepancy is observed between the different magnet polarities so no systematic uncertainty is considered.

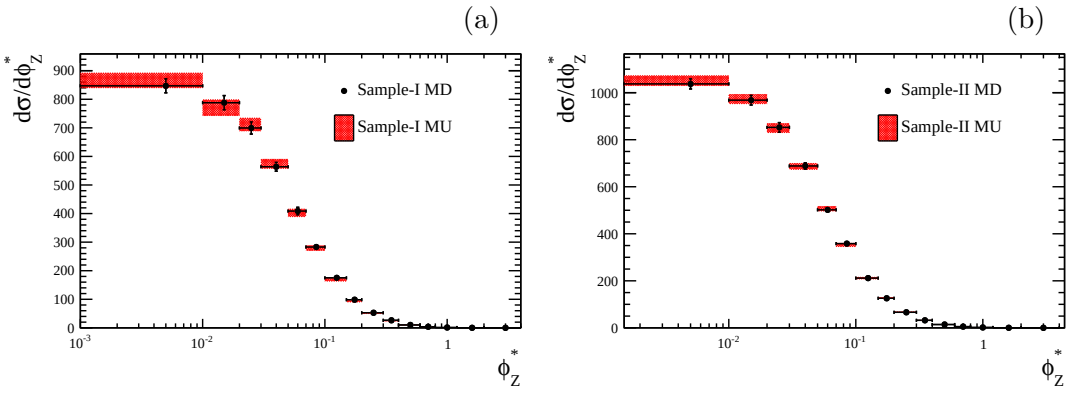

Figure D.3: Differerntial cross-sections as functions of Z boson ϕ^* for different magnet polarities in SAMPLE-I in (a) and SAMPLE-II in (b). No discrepancy is observed between the different magnet polarities so no systematic uncertainty is considered.

Appendix E

Correlation coefficients

E.1 Correlation coefficients for the integrated cross-sections

Uncertainty	$\rho_{W^+W^-}$	ρ_{W^+Z}	ρ_{W^-Z}	ρ_{WZ}
stat $\oplus$ syst	0.496	0.431	0.384	0.472
stat $\oplus$ syst $\oplus$ beam $\oplus$ lumi	0.928	0.925	0.908	0.934

Table E.1: Correlation coefficients between the integrated W^+, W^- and Z cross-sections measured with SAMPLE-I.

Uncertainty	$\rho_{W^+W^-}$	ρ_{W^+Z}	ρ_{W^-Z}	ρ_{WZ}
stat $\oplus$ syst	0.748	0.538	0.535	0.573
stat $\oplus$ syst $\oplus$ beam $\oplus$ lumi	0.956	0.922	0.914	0.929

Table E.2: Correlation coefficients between the integrated W^+, W^- and Z cross-sections measured with SAMPLE-II.

E.2 Correlation coefficients for the differential measurements

y_Z	2–2.125	2.125–2.25	2.25–2.375	2.375–2.5	2.5–2.625	2.625–2.75	2.75–2.875	2.875–3	3–3.125	3.125–3.25	3.25–3.375	3.375–3.5	3.5–3.625	3.625–3.75	3.75–3.875	3.875–4	4–4.25	4.25–4.5
2–2.125	1																	
2.125–2.25	0.18	1																
2.25–2.375	0.14	0.19	1															
2.375–2.5	0.14	0.19	0.18	1														
2.5–2.625	0.13	0.18	0.16	0.19	1													
2.625–2.75	0.12	0.16	0.15	0.18	0.18	1												
2.75–2.875	0.11	0.15	0.14	0.17	0.17	0.18	1											
2.875–3	0.10	0.13	0.13	0.16	0.16	0.17	0.17	1										
3–3.125	0.09	0.12	0.12	0.14	0.15	0.15	0.16	0.16	1									
3.125–3.25	0.08	0.1	0.10	0.12	0.13	0.14	0.14	0.14	0.14	1								
3.25–3.375	0.06	0.08	0.08	0.11	0.11	0.12	0.12	0.13	0.13	0.13	1							
3.375–3.5	0.05	0.06	0.06	0.08	0.09	0.09	0.10	0.10	0.11	0.11	0.11	1						
3.5–3.625	0.04	0.05	0.05	0.06	0.07	0.08	0.08	0.09	0.09	0.10	0.10	0.10	1					
3.625–3.75	0.03	0.04	0.03	0.04	0.05	0.06	0.06	0.07	0.07	0.08	0.09	0.08	0.08	1				
3.75–3.875	0.02	0.03	0.02	0.03	0.03	0.04	0.04	0.05	0.05	0.06	0.06	0.06	0.06	0.06	1			
3.875–4	0.02	0.02	0.02	0.02	0.02	0.02	0.02	0.03	0.03	0.04	0.04	0.04	0.04	0.04	0.03	1		
4–4.25	0.01	0.01	0.01	0.01	0.01	0.01	0.01	0.02	0.02	0.02	0.03	0.03	0.03	0.03	0.02	0.02	1	
4.25–4.5	–	–	–	–	–	–	–	–	–	–	–	–	–	–	–	–	–	–

Table E.3: Correlation coefficients between differential cross-section measurements as a function of y_Z in SAMPLE-I. The beam energy and luminosity uncertainties, which are fully correlated between cross-section measurements, are excluded.

y_Z	2–2.125	2.125–2.25	2.25–2.375	2.375–2.5	2.5–2.625	2.625–2.75	2.75–2.875	2.875–3	3–3.125	3.125–3.25	3.25–3.375	3.375–3.5	3.5–3.625	3.625–3.75	3.75–3.875	3.875–4	4–4.25	4.25–4.5
2–2.125	1																	
2.125–2.25	0.19	1																
2.25–2.375	0.17	0.27	1															
2.375–2.5	0.16	0.26	0.28	1														
2.5–2.625	0.16	0.25	0.28	0.29	1													
2.625–2.75	0.15	0.24	0.27	0.29	0.30	1												
2.75–2.875	0.14	0.23	0.26	0.28	0.29	0.30	1											
2.875–3	0.14	0.21	0.25	0.27	0.29	0.30	0.30	1										
3–3.125	0.13	0.20	0.23	0.25	0.27	0.28	0.29	0.29	1									
3.125–3.25	0.11	0.17	0.20	0.23	0.25	0.26	0.27	0.28	0.27	1								
3.25–3.375	0.09	0.14	0.16	0.18	0.20	0.22	0.22	0.23	0.23	0.23	1							
3.375–3.5	0.08	0.12	0.15	0.17	0.19	0.20	0.21	0.22	0.22	0.22	0.20	1						
3.5–3.625	0.07	0.10	0.12	0.14	0.16	0.17	0.18	0.19	0.19	0.20	0.18	0.19	1					
3.625–3.75	0.06	0.08	0.10	0.11	0.13	0.14	0.15	0.16	0.16	0.17	0.16	0.16	0.15	1				
3.75–3.875	0.05	0.07	0.08	0.09	0.10	0.11	0.11	0.12	0.13	0.13	0.12	0.13	0.12	0.11	1			
3.875–4	0.03	0.05	0.06	0.06	0.07	0.08	0.08	0.09	0.09	0.10	0.09	0.10	0.09	0.08	0.07	1		
4–4.25	0.03	0.04	0.04	0.05	0.05	0.06	0.06	0.06	0.07	0.07	0.07	0.08	0.07	0.07	0.06	0.05	1	
4.25–4.5	0.01	0.01	0.01	0.01	0.01	0.01	0.01	0.01	0.01	0.01	0.01	0.02	0.02	0.01	0.01	0.01	0.01	1

Table E.4: Correlation coefficients between differential cross-section measurements as a function of y_Z in Sample-II. The beam energy and luminosity uncertainties, which are fully correlated between cross-section measurements, are excluded.

$p_{T,Z}$ [GeV/c]	0.0–2.2	2.2–3.4	3.4–4.6	4.6–5.8	5.8–7.2	7.2–8.7	8.7–10.5	10.5–12.8	12.8–15.4	15.4–19	19–24.5	24.5–34	34–63	63–270
0.0–2.2	1													
2.2–3.4	-0.01	1												
3.4–4.6	0.00	0.03	1											
4.6–5.8	0.04	0.00	0.02	1										
5.8–7.2	0.05	0.05	0.00	0.03	1									
7.2–8.7	0.07	0.07	0.05	0.00	0.03	1								
8.7–10.5	0.08	0.08	0.06	0.06	0.02	0.02	1							
10.5–12.8	0.07	0.06	0.05	0.05	0.07	0.04	0.00	1						
12.8–15.4	0.07	0.07	0.05	0.05	0.06	0.09	0.07	-0.01	1					
15.4–19	0.08	0.08	0.05	0.06	0.07	0.10	0.12	0.08	-0.01	1				
19–24.5	0.08	0.08	0.06	0.06	0.07	0.10	0.12	0.10	0.10	0.02	1			
24.5–34	0.08	0.07	0.05	0.06	0.07	0.10	0.11	0.09	0.10	0.11	0.05	1		
34–63	0.07	0.06	0.05	0.05	0.06	0.08	0.09	0.08	0.08	0.09	0.10	0.06	1	
63–270	0.20	0.20	0.15	0.15	0.19	0.26	0.30	0.26	0.27	0.30	0.32	0.31	0.30	1

Table E.5: Correlation coefficients between differential cross-section measurements as a function of $p_{T,Z}$ in Sample-I. The beam energy and luminosity uncertainties, which are fully correlated between cross-section measurements, are excluded.

$p_{T,Z}$ [GeV/c]	0.0–2.2	2.2–3.4	3.4–4.6	4.6–5.8	5.8–7.2	7.2–8.7	8.7–10.5	10.5–12.8	12.8–15.4	15.4–19	19–24.5	24.5–34	34–63	63–270
0.0–2.2	1													
2.2–3.4	0.06	1												
3.4–4.6	0.08	0.16	1											
4.6–5.8	0.13	0.09	0.20	1										
5.8–7.2	0.15	0.16	0.12	0.19	1									
7.2–8.7	0.14	0.16	0.18	0.11	0.17	1								
8.7–10.5	0.14	0.16	0.20	0.19	0.14	0.15	1							
10.5–12.8	0.14	0.16	0.19	0.19	0.21	0.14	0.12	1						
12.8–15.4	0.15	0.17	0.20	0.19	0.22	0.20	0.17	0.11	1					
15.4–19	0.14	0.16	0.20	0.19	0.21	0.19	0.21	0.18	0.11	1				
19–24.5	0.15	0.17	0.21	0.20	0.22	0.20	0.21	0.21	0.21	0.13	1			
24.5–34	0.16	0.18	0.22	0.21	0.23	0.21	0.22	0.22	0.23	0.22	0.17	1		
34–63	0.16	0.18	0.22	0.21	0.23	0.21	0.22	0.22	0.23	0.22	0.23	0.21	1	
63–270	0.11	0.12	0.15	0.14	0.16	0.15	0.15	0.15	0.16	0.15	0.16	0.17	0.15	1

Table E.6: Correlation coefficients between differential cross-section measurements as a function of $p_{T,Z}$ in SAMPLE-II. The beam energy and luminosity uncertainties, which are fully correlated between cross-section measurements, are excluded.

ϕ_Z^*	0.00–0.01	0.01–0.02	0.02–0.03	0.03–0.05	0.05–0.07	0.07–0.10	0.10–0.15	0.15–0.20	0.20–0.30	0.30–0.40	0.40–0.60	0.60–0.80	0.80–1.20	1.20–2.00	2.00–4.00
0.00–0.01	1														
0.01–0.02	0.14	1													
0.02–0.03	0.16	0.12	1												
0.03–0.05	0.20	0.17	0.17	1											
0.05–0.07	0.15	0.12	0.13	0.16	1										
0.07–0.10	0.19	0.16	0.17	0.21	0.15	1									
0.10–0.15	0.14	0.12	0.13	0.16	0.12	0.15	1								
0.15–0.20	0.11	0.10	0.10	0.13	0.10	0.12	0.09	1							
0.20–0.30	0.15	0.13	0.13	0.17	0.13	0.16	0.13	0.10	1						
0.30–0.40	0.10	0.08	0.09	0.11	0.08	0.10	0.08	0.06	0.08	1					
0.40–0.60	0.07	0.06	0.07	0.08	0.06	0.08	0.06	0.05	0.07	0.04	1				
0.60–0.80	0.05	0.04	0.04	0.05	0.04	0.05	0.04	0.03	0.04	0.03	0.02	1			
0.80–1.20	0.05	0.04	0.04	0.05	0.04	0.05	0.04	0.03	0.04	0.03	0.02	0.01	1		
1.20–2.00	0.02	0.02	0.02	0.03	0.02	0.03	0.02	0.02	0.02	0.01	0.01	0.01	0.00	1	
2.00–4.00	0.005	0.004	0.005	0.006	0.004	0.005	0.004	0.004	0.004	0.002	0.002	0.002	0.002	0.001	1

Table E.7: Correlation coefficients between differential cross-section measurements as a function of ϕ_Z^* in Sample-I. The beam energy and luminosity uncertainties, which are fully correlated between cross-section measurements, are excluded.

ϕ_Z^*	0.00–0.01	0.01–0.02	0.02–0.03	0.03–0.05	0.05–0.07	0.07–0.10	0.10–0.15	0.15–0.20	0.20–0.30	0.30–0.40	0.40–0.60	0.60–0.80	0.80–1.20	1.20–2.00	2.00–4.00
0.00–0.01	1														
0.01–0.02	0.50	1													
0.02–0.03	0.42	0.39	1												
0.03–0.05	0.57	0.55	0.44	1											
0.05–0.07	0.52	0.50	0.41	0.55	1										
0.07–0.10	0.44	0.42	0.34	0.47	0.42	1									
0.10–0.15	0.50	0.48	0.40	0.54	0.49	0.41	1								
0.15–0.20	0.49	0.47	0.38	0.52	0.48	0.40	0.46	1							
0.20–0.30	0.47	0.45	0.37	0.50	0.45	0.39	0.44	0.43	1						
0.30–0.40	0.31	0.30	0.24	0.33	0.30	0.26	0.29	0.29	0.27	1					
0.40–0.60	0.31	0.29	0.24	0.33	0.30	0.25	0.29	0.28	0.27	0.18	1				
0.60–0.80	0.21	0.20	0.16	0.23	0.20	0.17	0.20	0.19	0.19	0.12	0.12	1			
0.80–1.20	0.13	0.13	0.10	0.14	0.13	0.11	0.13	0.12	0.12	0.08	0.08	0.05	1		
1.20–2.00	0.07	0.07	0.06	0.08	0.07	0.06	0.07	0.07	0.06	0.04	0.04	0.03	0.02	1	
2.00–4.00	0.02	0.02	0.02	0.02	0.02	0.02	0.02	0.02	0.02	0.01	0.01	0.01	0.01	0.00	1

Table E.8: Correlation coefficients between differential cross-section measurements as a function of ϕ_Z^* in Sample-II. The beam energy and luminosity uncertainties, which are fully correlated between cross-section measurements, are excluded.

η^{μ}	2–2.25		2.25–2.5		2.5–2.75		2.75–3		3–3.25		3.25–3.5		3.5–4		4–4.5		
2–2.25	1																W^+
	0.46	1															W^-
2.25–2.5	-0.15	0.34	1														W^+
	0.30	-0.24	0.09	1													W^-
2.5–2.75	-0.03	0.23	0.27	-0.13	1												W^+
	0.24	-0.14	-0.21	0.35	0.41	1											W^-
2.75–3	0.20	-0.07	-0.10	0.25	-0.00	0.21	1										W^+
	-0.19	0.39	0.46	-0.37	0.27	-0.24	0.28	1									W^-
3–3.25	-0.03	0.24	0.28	-0.16	0.20	-0.08	-0.01	0.29	1								W^+
	0.31	-0.23	-0.32	0.46	-0.13	0.35	0.25	-0.37	0.27	1							W^-
3.25–3.5	-0.12	0.29	0.36	-0.27	0.22	-0.17	-0.07	0.40	0.24	-0.27	1						W^+
	0.33	-0.32	-0.41	0.52	-0.19	0.40	0.28	-0.47	-0.21	0.53	-0.07	1					W^-
3.5–4	0.02	0.15	0.18	-0.05	0.15	-0.01	0.04	0.17	0.14	-0.04	0.15	-0.08	1				W^+
	0.21	-0.09	-0.14	0.30	-0.02	0.25	0.19	-0.17	-0.04	0.30	-0.12	0.33	0.45	1			W^-
4–4.5	-0.01	0.13	0.17	-0.08	0.14	-0.05	-0.01	0.15	0.11	-0.07	0.11	-0.12	0.09	0.02	1		W^+
	0.08	0.01	-0.01	0.09	0.03	0.08	0.07	-0.02	0.02	0.10	-0.02	0.09	0.03	0.10	0.11	1	W^-
	W^+	W^-	W^+	W^-	W^+	W^-	W^+	W^-	W^+	W^-	W^+	W^-	W^+	W^-	W^+	W^-	

Table E.9: Correlation coefficients between differential cross-section measurements as a function of W boson muon η in Sample-I. The beam energy and luminosity uncertainties, which are fully correlated between cross-section measurements, are excluded.

η^{μ}	2–2.25		2.25–2.5		2.5–2.75		2.75–3		3–3.25		3.25–3.5		3.5–4		4–4.5		
2–2.25	1																W^+
	0.67	1															W^-
2.25–2.5	0.20	0.10	1														W^+
	0.07	0.21	0.54	1													W^-
2.5–2.75	0.13	0.24	0.12	0.23	1												W^+
	0.05	0.18	0.03	0.22	0.64	1											W^-
2.75–3	0.06	0.22	0.03	0.28	0.26	0.27	1										W^+
	0.04	0.21	0.00	0.25	0.25	0.31	0.70	1									W^-
3–3.25	0.07	0.22	0.03	0.28	0.25	0.26	0.33	0.30	1								W^+
	0.06	0.22	0.03	0.28	0.26	0.27	0.32	0.32	0.68	1							W^-
3.25–3.5	0.03	0.23	-0.01	0.28	0.28	0.27	0.35	0.33	0.34	0.32	1						W^+
	0.07	0.23	0.04	0.23	0.30	0.29	0.28	0.32	0.27	0.28	0.63	1					W^-
3.5–4	-0.00	0.26	-0.06	0.33	0.31	0.32	0.41	0.39	0.40	0.38	0.45	0.36	1				W^+
	0.14	-0.06	0.20	-0.04	-0.13	-0.04	-0.08	-0.11	-0.07	-0.07	-0.17	-0.19	-0.04	1			W^-
4–4.5	-0.07	0.14	-0.14	0.24	0.14	0.23	0.32	0.29	0.32	0.26	0.35	0.22	0.45	-0.15	1		W^+
	0.12	-0.09	0.17	-0.11	-0.18	-0.14	-0.17	-0.19	-0.15	-0.18	-0.23	-0.24	-0.31	0.48	0.05	1	W^-
	W^+	W^-	W^+	W^-	W^+	W^-	W^+	W^-	W^+	W^-	W^+	W^-	W^+	W^-	W^+	W^-	

Table E.10: Correlation coefficients between differential cross-section measurements as a function of W boson muon η in Sample-II. The beam energy and luminosity uncertainties, which are fully correlated between cross-section measurements, are excluded.

		y_Z																	
		2–2.125	2.125–2.25	2.25–2.375	2.375–2.5	2.5–2.625	2.625–2.75	2.75–2.875	2.875–3	3–3.125	3.125–3.25	3.25–3.375	3.375–3.5	3.5–3.625	3.625–3.75	3.75–3.875	3.875–4	4–4.25	4.25–4.5	
η^μ	2–2.25	0.24	0.25	0.19	0.19	0.17	0.16	0.15	0.13	0.12	0.10	0.08	0.06	0.05	0.04	0.03	0.02	0.01	–	W^+
		0.22	0.23	0.17	0.17	0.16	0.15	0.13	0.12	0.11	0.09	0.07	0.05	0.04	0.04	0.03	0.02	0.01	–	W^-
	2.25–2.5	0.03	0.11	0.13	0.14	0.12	0.11	0.10	0.10	0.09	0.07	0.06	0.04	0.03	0.02	0.01	0.01	0.01	–	W^+
		0.03	0.10	0.12	0.13	0.11	0.10	0.10	0.09	0.08	0.07	0.06	0.04	0.03	0.02	0.01	0.01	0.00	–	W^-
	2.5–2.75	0.03	0.04	0.06	0.10	0.10	0.10	0.09	0.09	0.08	0.07	0.07	0.05	0.04	0.03	0.02	0.01	0.01	–	W^+
		0.03	0.03	0.06	0.10	0.09	0.09	0.08	0.08	0.08	0.07	0.06	0.05	0.04	0.02	0.02	0.01	0.01	–	W^-
	2.75–3	0.03	0.04	0.04	0.07	0.09	0.10	0.09	0.09	0.09	0.08	0.07	0.06	0.05	0.04	0.02	0.01	0.01	–	W^+
		0.02	0.03	0.03	0.05	0.07	0.07	0.07	0.07	0.06	0.06	0.05	0.04	0.04	0.03	0.01	0.01	0.01	–	W^-
	3–3.25	0.04	0.04	0.04	0.06	0.08	0.10	0.10	0.10	0.09	0.09	0.08	0.07	0.06	0.05	0.03	0.01	0.01	–	W^+
		0.03	0.04	0.03	0.05	0.06	0.08	0.08	0.08	0.08	0.07	0.07	0.06	0.05	0.04	0.02	0.01	0.01	–	W^-
	3.25–3.5	0.02	0.03	0.03	0.04	0.04	0.05	0.06	0.06	0.06	0.06	0.05	0.05	0.04	0.03	0.02	0.01	0.01	–	W^+
		0.02	0.02	0.02	0.03	0.03	0.04	0.05	0.05	0.05	0.04	0.04	0.03	0.03	0.02	0.02	0.01	0.00	–	W^-
	3.5–4	0.03	0.03	0.03	0.04	0.04	0.05	0.06	0.08	0.09	0.08	0.08	0.07	0.07	0.05	0.04	0.03	0.02	–	W^+
		0.03	0.03	0.03	0.04	0.04	0.05	0.06	0.08	0.09	0.09	0.08	0.07	0.07	0.05	0.04	0.03	0.02	–	W^-
	4–4.5	0.02	0.02	0.02	0.02	0.02	0.02	0.02	0.02	0.03	0.04	0.05	0.05	0.06	0.06	0.04	0.03	0.03	–	W^+
		0.02	0.02	0.02	0.03	0.03	0.03	0.03	0.03	0.04	0.05	0.07	0.07	0.07	0.07	0.05	0.04	0.03	–	W^-

Table E.11: Correlation coefficients between differential cross-section measurements as a function of y_Z and W boson muon η in Sample-I. The LHC beam energy and luminosity uncertainties, which are fully correlated between cross-section measurements, are excluded.

		y_Z																	
		2–2.125	2.125–2.25	2.25–2.375	2.375–2.5	2.5–2.625	2.625–2.75	2.75–2.875	2.875–3	3–3.125	3.125–3.25	3.25–3.375	3.375–3.5	3.5–3.625	3.625–3.75	3.75–3.875	3.875–4	4–4.25	4.25–4.5	
η^μ	2–2.25	0.23	0.30	0.28	0.27	0.26	0.25	0.24	0.23	0.21	0.18	0.15	0.13	0.11	0.10	0.07	0.05	0.04	0.01	W^+
		0.21	0.28	0.26	0.25	0.24	0.24	0.22	0.21	0.20	0.17	0.14	0.12	0.11	0.09	0.07	0.05	0.04	0.01	W^-
	2.25–2.5	0.05	0.15	0.21	0.20	0.20	0.20	0.20	0.19	0.18	0.16	0.14	0.12	0.10	0.08	0.06	0.04	0.03	0.01	W^+
		0.04	0.14	0.19	0.18	0.18	0.18	0.18	0.17	0.16	0.15	0.12	0.11	0.09	0.07	0.05	0.04	0.03	0.00	W^-
	2.5–2.75	0.04	0.07	0.12	0.15	0.16	0.17	0.17	0.17	0.16	0.15	0.13	0.13	0.11	0.08	0.06	0.05	0.03	0.01	W^+
		0.04	0.07	0.11	0.14	0.15	0.15	0.15	0.15	0.15	0.14	0.12	0.12	0.10	0.08	0.06	0.04	0.03	0.01	W^-
	2.75–3	0.05	0.08	0.10	0.13	0.16	0.17	0.17	0.17	0.16	0.16	0.14	0.13	0.12	0.09	0.07	0.05	0.03	0.01	W^+
		0.05	0.07	0.09	0.12	0.14	0.15	0.15	0.16	0.15	0.14	0.12	0.12	0.11	0.08	0.06	0.04	0.03	0.01	W^-
	3–3.25	0.06	0.08	0.10	0.11	0.14	0.16	0.17	0.17	0.16	0.16	0.14	0.14	0.12	0.10	0.07	0.05	0.03	0.01	W^+
		0.05	0.08	0.09	0.10	0.13	0.15	0.15	0.16	0.15	0.15	0.13	0.13	0.11	0.09	0.07	0.05	0.03	0.01	W^-
	3.25–3.5	0.04	0.06	0.07	0.09	0.10	0.11	0.12	0.13	0.13	0.12	0.11	0.11	0.09	0.08	0.06	0.04	0.03	0.00	W^+
		0.04	0.06	0.08	0.09	0.10	0.12	0.13	0.13	0.13	0.13	0.11	0.11	0.10	0.08	0.06	0.04	0.03	0.00	W^-
	3.5–4	0.04	0.06	0.07	0.08	0.09	0.10	0.11	0.12	0.12	0.12	0.11	0.11	0.10	0.09	0.07	0.05	0.04	0.00	W^+
		0.04	0.06	0.08	0.09	0.10	0.11	0.12	0.13	0.14	0.14	0.12	0.12	0.11	0.10	0.08	0.06	0.04	0.01	W^-
	4–4.5	0.02	0.03	0.04	0.04	0.04	0.04	0.05	0.05	0.06	0.06	0.06	0.07	0.06	0.06	0.05	0.04	0.04	0.01	W^+
		0.03	0.04	0.04	0.05	0.05	0.06	0.06	0.06	0.07	0.07	0.07	0.08	0.08	0.07	0.06	0.05	0.04	0.01	W^-

Table E.12: Correlation coefficients between differential cross-section measurements as a function of y_Z and W boson muon η in Sample-II. The LHC beam energy and luminosity uncertainties, which are fully correlated between cross-section measurements, are excluded.

		Z							
η^{μ^+}	2.00–2.25	2.25–2.50	2.50–2.75	2.75–3.00	3.00–3.25	3.25–3.50	3.50–4.00	4.00–4.50	
	2.00–2.25	1							
	2.25–2.50	0.20	1						
	2.50–2.75	0.20	0.17	1					
Z	2.75–3.00	0.19	0.16	0.15	1				
	3.00–3.25	0.20	0.16	0.15	0.15	1			
	3.25–3.50	0.17	0.14	0.13	0.12	0.13	1		
	3.50–4.00	0.21	0.17	0.16	0.15	0.15	0.13	1	
	4.00–4.50	0.17	0.14	0.13	0.12	0.12	0.10	0.11	1

		Z							
η^{μ^-}	2.00–2.25	2.25–2.50	2.50–2.75	2.75–3.00	3.00–3.25	3.25–3.50	3.50–4.00	4.00–4.50	
	2.00–2.25	1							
	2.25–2.50	0.20	1						
	2.50–2.75	0.19	0.17	1					
Z	2.75–3.00	0.19	0.17	0.15	1				
	3.00–3.25	0.19	0.16	0.15	0.15	1			
	3.25–3.50	0.18	0.15	0.13	0.13	0.13	1		
	3.50–4.00	0.20	0.18	0.16	0.15	0.14	0.13	1	
	4.00–4.50	0.17	0.15	0.13	0.13	0.12	0.10	0.11	1

Table E.13: Correlation coefficients between the differential Z cross-sections in bins of (top) η^{μ^+} and (bottom) η^{μ^-} in Sample-I. The LHC beam energy and luminosity uncertainties, which are fully correlated between cross-section measurements, are excluded.

		Z							
	η^{μ^+}	2.00–2.25	2.25–2.50	2.50–2.75	2.75–3.00	3.00–3.25	3.25–3.50	3.50–4.00	4.00–4.50
W	2.00–2.25	0.39	0.11	0.12	0.12	0.12	0.11	0.13	0.10
	2.25–2.50	0.08	0.28	0.07	0.07	0.07	0.07	0.08	0.06
	2.50–2.75	0.07	0.07	0.20	0.07	0.07	0.06	0.07	0.05
	2.75–3.00	0.08	0.07	0.07	0.19	0.07	0.06	0.07	0.05
	3.00–3.25	0.09	0.07	0.07	0.07	0.20	0.06	0.07	0.06
	3.25–3.50	0.05	0.05	0.05	0.05	0.05	0.12	0.05	0.03
	3.50–4.00	0.07	0.06	0.06	0.06	0.06	0.05	0.16	0.04
	4.00–4.50	0.03	0.03	0.03	0.03	0.03	0.02	0.03	0.11

		Z							
	η^{μ^-}	2.00–2.25	2.25–2.50	2.50–2.75	2.75–3.00	3.00–3.25	3.25–3.50	3.50–4.00	4.00–4.50
W	2.00–2.25	0.35	0.10	0.11	0.11	0.11	0.10	0.12	0.10
	2.25–2.50	0.08	0.27	0.07	0.07	0.07	0.06	0.08	0.06
	2.50–2.75	0.07	0.06	0.19	0.07	0.06	0.06	0.07	0.05
	2.75–3.00	0.06	0.05	0.05	0.15	0.05	0.05	0.05	0.04
	3.00–3.25	0.07	0.06	0.06	0.06	0.16	0.05	0.06	0.05
	3.25–3.50	0.04	0.04	0.04	0.04	0.03	0.09	0.07	0.03
	3.50–4.00	0.07	0.06	0.06	0.06	0.06	0.05	0.16	0.04
	4.00–4.50	0.05	0.04	0.04	0.04	0.04	0.03	0.03	0.13

Table E.14: Correlation coefficients between the differential W and Z cross-sections in bins of (top) η^{μ^+} and (bottom) η^{μ^-} in SAMPLE-I. The LHC beam energy and luminosity uncertainties, which are fully correlated between cross-section measurements, are excluded.

		Z							
η^{μ^+}	2.00–2.25	2.25–2.50	2.50–2.75	2.75–3.00	3.00–3.25	3.25–3.50	3.50–4.00	4.00–4.50	
	2.00–2.25	1							
	2.25–2.50	0.31	1						
	2.50–2.75	0.30	0.27	1					
Z	2.75–3.00	0.31	0.28	0.26	1				
	3.00–3.25	0.32	0.28	0.26	0.27	1			
	3.25–3.50	0.27	0.25	0.23	0.23	0.23	1		
	3.50–4.00	0.33	0.30	0.28	0.28	0.28	0.25	1	
	4.00–4.50	0.28	0.25	0.23	0.24	0.23	0.20	0.23	1

		Z							
η^{μ^-}	2.00–2.25	2.25–2.50	2.50–2.75	2.75–3.00	3.00–3.25	3.25–3.50	3.50–4.00	4.00–4.50	
	2.00–2.25	1							
	2.25–2.50	0.29	1						
	2.50–2.75	0.30	0.29	1					
Z	2.75–3.00	0.30	0.28	0.28	1				
	3.00–3.25	0.30	0.27	0.27	0.27	1			
	3.25–3.50	0.27	0.25	0.25	0.24	0.24	1		
	3.50–4.00	0.31	0.29	0.29	0.28	0.28	0.25	1	
	4.00–4.50	0.28	0.25	0.25	0.24	0.24	0.21	0.24	1

Table E.15: Correlation coefficients between the differential Z cross-sections in bins of (top) η^{μ^+} and (bottom) η^{μ^-} in Sample-II. The LHC beam energy and luminosity uncertainties, which are fully correlated between cross-section measurements, are excluded.

		Z							
	η^{μ^+}	2.00–2.25	2.25–2.50	2.50–2.75	2.75–3.00	3.00–3.25	3.25–3.50	3.50–4.00	4.00–4.50
W	2.00–2.25	0.48	0.19	0.19	0.20	0.20	0.18	0.22	0.18
	2.25–2.50	0.15	0.38	0.16	0.16	0.16	0.14	0.17	0.14
	2.50–2.75	0.14	0.14	0.26	0.14	0.14	0.13	0.16	0.12
	2.75–3.00	0.14	0.14	0.14	0.26	0.15	0.13	0.16	0.12
	3.00–3.25	0.15	0.14	0.14	0.15	0.25	0.13	0.15	0.12
	3.25–3.50	0.11	0.11	0.11	0.11	0.11	0.17	0.12	0.09
	3.50–4.00	0.10	0.10	0.11	0.11	0.11	0.10	0.18	0.08
	4.00–4.50	0.06	0.06	0.06	0.06	0.06	0.05	0.06	0.11

		Z							
	η^{μ^-}	2.00–2.25	2.25–2.50	2.50–2.75	2.75–3.00	3.00–3.25	3.25–3.50	3.50–4.00	4.00–4.50
W	2.00–2.25	0.43	0.18	0.19	0.19	0.19	0.18	0.21	0.18
	2.25–2.50	0.13	0.35	0.15	0.15	0.14	0.14	0.16	0.13
	2.50–2.75	0.12	0.13	0.25	0.13	0.13	0.12	0.14	0.12
	2.75–3.00	0.12	0.13	0.14	0.24	0.13	0.12	0.14	0.12
	3.00–3.25	0.13	0.13	0.14	0.14	0.23	0.13	0.15	0.12
	3.25–3.50	0.11	0.11	0.12	0.12	0.12	0.18	0.12	0.10
	3.50–4.00	0.11	0.12	0.12	0.12	0.12	0.11	0.20	0.10
	4.00–4.50	0.07	0.06	0.07	0.07	0.07	0.06	0.07	0.13

Table E.16: Correlation coefficients between the differential W and Z cross-sections in bins of (top) η^{μ^+} and (bottom) η^{μ^-} in Sample-II. The LHC beam energy and luminosity uncertainties, which are fully correlated between cross-section measurements, are excluded.

Appendix F

BSM through $\sqrt{s}$ evolution

The measurement of electroweak boson cross-sections and cross-section ratios at different centre-of-mass energies presents an opportunity to search for Beyond Standard Model (BSM) physics. An explanation is given in this appendix. The discussion closely follows Ref. [112].

Consider a cross-section for electroweak boson production, σ_X, where $X = W^+, W^-, Z$.[1] Suppose that σ_X obtains contributions from Standard Model (SM) and BSM processes, as represented by Equation F.1.

$$\sigma_X = \sigma_X^{SM} + \sigma_X^{BSM} \tag{F.1}$$

Suppose also that this cross-section is evaluated at two centre-of-mass energies E_1 and E_2. The ratio of cross-sections at different centre-of-mass energies can be written as

$$\begin{aligned}
R^X_{E_1/E_2} &= \frac{\sigma_X(E_1)}{\sigma_X(E_2)} \\
&= \frac{\sigma_X^{SM}(E_1) + \sigma_X^{BSM}(E_1)}{\sigma_X^{SM}(E_2) + \sigma_X^{BSM}(E_2)} \\
&= \frac{\sigma_X^{SM}(E_1)}{\sigma_X^{SM}(E_2)} \left[\frac{\sigma_X^{SM}(E_2) + \frac{\sigma_X^{BSM}(E_1)\sigma_X^{SM}(E_2)}{\sigma_X^{SM}(E_1)}}{\sigma_X^{SM}(E_2) + \sigma_X^{BSM}(E_2)} \right] \\
&= \frac{\sigma_X^{SM}(E_1)}{\sigma_X^{SM}(E_2)} \left[\frac{\left(1 + \frac{\sigma_X^{BSM}(E_1)}{\sigma_X^{SM}(E_1)}\right)\sigma_X^{SM}(E_2)}{\sigma_X^{SM}(E_2) + \sigma_X^{BSM}(E_2)} \right] \\
&= \frac{\sigma_X^{SM}(E_1)}{\sigma_X^{SM}(E_2)} \left[\frac{1 + \frac{\sigma_X^{BSM}(E_1)}{\sigma_X^{SM}(E_1)}}{1 + \frac{\sigma_X^{BSM}(E_2)}{\sigma_X^{SM}(E_2)}} \right]
\end{aligned} \tag{F.2}$$

[1] The argument applies to any cross-section or ratio of cross-sections.

where the steps amount to the rearrangement of the SM and BSM contributions. If the BSM contribution to the cross-section is small, then one can perform a Taylor expansion on the denominator inside the square brackets of Equation F.2 to obtain

$$\left(1+\frac{\sigma_X^{BSM}(E_2)}{\sigma_X^{SM}(E_2)}\right)^{-1} \sim 1-\frac{\sigma_X^{BSM}(E_2)}{\sigma_X^{SM}(E_2)}. \tag{F.3}$$

Neglecting terms that are second order in BSM cross-sections gives

$$R^X_{E_1/E_2} \approx \frac{\sigma_X^{SM}(E_1)}{\sigma_X^{SM}(E_2)}\left[1+\frac{\sigma_X^{BSM}(E_1)}{\sigma_X^{SM}(E_1)}-\frac{\sigma_X^{BSM}(E_2)}{\sigma_X^{SM}(E_2)}\right]. \tag{F.4}$$

The value of the square bracket in Equation F.4 is unity in the SM. The measured value of the square bracket is not necessarily unity and this is how the presence of BSM physics may be detected. For BSM physics to be detected in this way, it must scale with centre-of-mass energy at a different rate to the SM prediction, otherwise the bracket in Equation F.4 would still be unity. The condition can be expressed as

$$\frac{\sigma_X^{BSM}(E_2)}{\sigma_X^{BSM}(E_1)} \neq \frac{\sigma_X^{SM}(E_2)}{\sigma_X^{SM}(E_1)}. \tag{F.5}$$

Appendix G

Uncertainty propagation

In this appendix, formulae for the propagation of uncertainties onto the ratios R_{WZ}, R_{W^+Z} and R_{W^-Z} are given. Each ratio is expressed in terms of the differential cross-sections measured as functions of Z boson y and W boson muon η. Formulae for the partial derivatives that enter the standard error propagation formula are also provided. At the end of each section, the uncertainty (represented by δ) on the cross-section ratios due to a particular source is expressed in terms of the partial derivatives, the uncertainties on differential measurements, and the correlation between measurements ρ.

G.1 R_{WZ}

$$R_{WZ} = \frac{\sum_{i=1}^{8} W_i^+ + \sum_{j=1}^{8} W_j^-}{\sum_{k=1}^{18} Z_k} \tag{G.1}$$

$$\frac{\partial R_{WZ}}{\partial W_i^+} = \frac{1}{\sum_{k=1}^{18} Z_k} \tag{G.2}$$

$$\frac{\partial R_{WZ}}{\partial W_j^-} = \frac{1}{\sum_{k=1}^{18} Z_k} \tag{G.3}$$

$$\frac{\partial R_{WZ}}{\partial Z_k} = -\frac{\sum_{i=1}^{8} W_i^+ + \sum_{j=1}^{8} W_j^-}{\left(\sum_{k=1}^{18} Z_k\right)^2} \tag{G.4}$$

$$\begin{aligned}
\delta^2_{R_{WZ}} = &\sum_{i=1}^{8}\sum_{j=1}^{8}\left(\frac{\partial R_{WZ}}{\partial W_i^+}\right)\left(\frac{\partial R_{WZ}}{\partial W_j^+}\right)\delta_{W_i^+}\delta_{W_j^+}\rho_{W_i^+W_j^+} \\
&+\sum_{i=1}^{8}\sum_{j=1}^{8}\left(\frac{\partial R_{WZ}}{\partial W_i^-}\right)\left(\frac{\partial R_{WZ}}{\partial W_j^-}\right)\delta_{W_i^-}\delta_{W_j^-}\rho_{W_i^-W_j^-} \\
&+2\sum_{i=1}^{8}\sum_{j=1}^{8}\left(\frac{\partial R_{WZ}}{\partial W_i^+}\right)\left(\frac{\partial R_{WZ}}{\partial W_j^-}\right)\delta_{W_i^+}\delta_{W_j^-}\rho_{W_i^+W_j^-} \\
&+2\sum_{i=1}^{8}\sum_{k=1}^{18}\left(\frac{\partial R_{WZ}}{\partial W_i^+}\right)\left(\frac{\partial R_{WZ}}{\partial Z_k}\right)\delta_{W_i^+}\delta_{Z_k}\rho_{W_i^+Z_k} \\
&+2\sum_{j=1}^{8}\sum_{k=1}^{18}\left(\frac{\partial R_{WZ}}{\partial W_j^-}\right)\left(\frac{\partial R_{WZ}}{\partial Z_k}\right)\delta_{W_j^-}\delta_{Z_k}\rho_{W_j^-Z_k} \\
&+\sum_{k=1}^{18}\sum_{l=1}^{18}\left(\frac{\partial R_{WZ}}{\partial Z_k}\right)\left(\frac{\partial R_{WZ}}{\partial Z_l}\right)\delta_{Z_k}\delta_{Z_l}\rho_{Z_kZ_l}
\end{aligned} \tag{G.5}$$

G.2 R_{W^+Z}

$$R_{W^+Z} = \frac{\sum_{i=1}^{8} W_i^+}{\sum_{k=1}^{18} Z_k} \tag{G.6}$$

$$\frac{\partial R_{W^+Z}}{\partial Z_k} = -\frac{\sum_{i=1}^{8} W_i^+}{\left(\sum_{k=1}^{18} Z_k\right)^2} \tag{G.7}$$

$$\frac{\partial R_{W^+Z}}{\partial W_i^+} = \frac{\partial R_{WZ}}{\partial W_i^+} \tag{G.8}$$

$$\begin{aligned}\delta^2_{R_{W^+Z}} = &\sum_{i=1}^{8}\sum_{j=1}^{8}\left(\frac{\partial R_{W^+Z}}{\partial W_i^+}\right)\left(\frac{\partial R_{W^+Z}}{\partial W_j^+}\right)\delta_{W_i^+}\delta_{W_j^+}\rho_{W_i^+W_j^+}\\ &+2\sum_{i=1}^{8}\sum_{k=1}^{18}\left(\frac{\partial R_{W^+Z}}{\partial W_i^+}\right)\left(\frac{\partial R_{W^+Z}}{\partial Z_k}\right)\delta_{W_i^+}\delta_{Z_k}\rho_{W_i^+Z_k}\\ &+\sum_{k=1}^{18}\sum_{l=1}^{18}\left(\frac{\partial R_{W^+Z}}{\partial Z_k}\right)\left(\frac{\partial R_{W^+Z}}{\partial Z_l}\right)\delta_{Z_k}\delta_{Z_l}\rho_{Z_kZ_l}\end{aligned} \tag{G.9}$$

G.3 R_{W^-Z}

$$R_{W^-Z} = \frac{\sum_{j=1}^{8} W_j^-}{\sum_{k=1}^{18} Z_k} \tag{G.10}$$

$$\frac{\partial R_{W^-Z}}{\partial Z_k} = -\frac{\sum_{j=1}^{8} W_j^-}{\left(\sum_{k=1}^{18} Z_k\right)^2} \tag{G.11}$$

$$\frac{\partial R_{W^-Z}}{\partial W_j^-} = \frac{\partial R_{WZ}}{\partial W_j^-} \tag{G.12}$$

$$\begin{aligned}\delta^2_{R_{W^-Z}} = &\sum_{i=1}^{8}\sum_{j=1}^{8}\left(\frac{\partial R_{W^-Z}}{\partial W_i^-}\right)\left(\frac{\partial R_{W^-Z}}{\partial W_j^-}\right)\delta_{W_i^-}\delta_{W_j^-}\rho_{W_i^-W_j^-}\\ &+2\sum_{j=1}^{8}\sum_{k=1}^{18}\left(\frac{\partial R_{W^-Z}}{\partial W_j^-}\right)\left(\frac{\partial R_{W^-Z}}{\partial Z_k}\right)\delta_{W_j^-}\delta_{Z_k}\rho_{W_j^-Z_k}\\ &+\sum_{k=1}^{18}\sum_{l=1}^{18}\left(\frac{\partial R_{W^-Z}}{\partial Z_k}\right)\left(\frac{\partial R_{W^-Z}}{\partial Z_l}\right)\delta_{Z_k}\delta_{Z_l}\rho_{Z_kZ_l}\end{aligned} \tag{G.13}$$

Bibliography

[1] LHCb collaboration, A. A. Alves Jr. *et al.*, *The LHCb detector at the LHC*, JINST **3** (2008) S08005.

[2] LHCb collaboration, L. Evans and P. Bryant, *LHC Machine*, JINST **3** (2008) S08001.

[3] Particle Data Group, K. Nakamura *et al.*, *Review of particle physics*, J. Phys. **G37** (2010) 075021.

[4] The ALEPH Collaboration, The DELPHI Collaboration, The L3 Collaboration, The OPAL Collaboration, The SLD Collaboration, The LEP Electroweak Working Group, The SLD Electroweak and Heavy Flavour Groups, J. Bagger *et al.*, *Precision electroweak measurements on the Z resonance*, Physics Reports **427** (2006) 257, `arXiv:hep-ex/0509008`.

[5] D. Tong, *Lectures on quantum field theory*, `http://www.damtp.cam.ac.uk/user/tong/qft.html`.

[6] H. Goldstein, *Classical Mechanics*, Poole and Safko, 2002.

[7] M. E. Peskin and D. V. Schroeder, *An introduction to quantum field theory*, Westview Press, 1995.

[8] W. Pauli, *The connection between spin and statistics*, Phys. Rev. **58** (1940) 716.

[9] H. Georgi, *Lie algebras in particle physics*, Westview press, 1999.

[10] A. Kronfeld and C. Quigg, *Resource Letter QCD-1: Quantum Chromodynamics*, Am. J. Phys. **78** (2010) 1081, `arXiv:1002.5032`.

[11] A. Pich, *The Standard Model of electroweak interactions*, `arXiv:0705.4264`.

[12] P. Aurenche, *The Standard Model of particle physics*, `arXiv:hep-ph/9712342`.

[13] W. Hollik, *Quantum field theory and the Standard Model*, `arXiv:1012.3883`.

[14] J. Goldstone, *Field theories with superconductor solutions*, Nuov. Cim. **19** (1961) 154.

[15] R. Taylor, J. Friedman, and H. Kendell, *Deep inelastic scattering: the early years*, Rev. Mod. Phys. **63** (1991) 573.

[16] J. D. Bjorken and E. A. Paschos, *Inelastic electron-proton and γ-proton scattering and the structure of the nucleon*, Phys. Rev. **185** (1975) .

[17] A. Benvenuti *et al.*, *A high statistics measurement of the proton structure functions $F(2)(x, Q^2)$ and R from deep inelastic muon scattering at high Q^2*, Phys. Lett. B **223** (1989) 485.

[18] M. Arneodo *et al.*, *Measurement of the proton and the deuteron structure functions, F_p^2 and F_d^2*, Phys. Lett. B **364** (1995) 107.

[19] CCFR collaboration, A. O. Bazarko *et al.*, *Determination of the strange quark content of the nucleon from a next-to-leading-order QCD analysis of neutrino charm production*, Z. Phys. C **65** (1995) 189, `arXiv:hep-ex/9406007`.

[20] NuTeV collaboration, M. Goncharov, P. Spentzouris *et al.*, *Precise measurement of dimuon production cross-sections in muon neutrino Fe and muon antineutrino Fe deep inelastic scattering at the Tevatron*, Phys. Rev. D **64** (2001) 112006, `arXiv:hep-ex/0102049`.

[21] H1 and ZEUS collaborations, F. D. Aaron *et al.*, *Combined measurement and QCD analysis of the inclusive $e^{\pm}p$ scattering cross sections at HERA*, JHEP **01** (2010) 109, `arXiv:0911.0884`.

[22] J. Poucher *et al.*, *High-energy single-arm inelastic e-p and e-d scattering at 6 and 10°*, Phys. Rev. Lett. **32** (1974) 118.

[23] J. C. Collins, D. E. Soper, and G. Sterman, *Factorization of hard processes in QCD*, `arXiv:hep-ph/0409313`.

[24] S. Farry, *Electroweak physics at LHCb*, `https://cds.cern.ch/record/1957187`.

[25] A. D. Martin, W. J. Stirling, R. S. Thorne, and G. Watt, *Parton distributions for the LHC*, Eur. Phys. J. **C63** (2009) 189, `arXiv:0901.0002`.

[26] G. Altarelli and G. Parisi, *Asymptotic freedom in parton language*, Nucl. Phys. **B126** (1977) 298.

[27] Y. L. Dokshitzer, *Calculation of the structure functions for deep inelastic scattering and e^+e^- annihilation by perturbation theory in Quantum Chromodynamics.*, Sov. Phys. JETP **46** (1977) 641.

[28] L. Lipatov, *The parton model and perturbation theory*, Yad. Fiz **20** (1974) 181.

[29] V. Gribov and L. Lipatov, *e^+e^- pair annihilation and deep inelastic ep scattering in perturbation theory*, Sov. J. Nucl. Phys. **15** (1972) 675.

[30] L. Lipatov, *Reggeization of the vector meson and the vacuum singularity in non-abelian gauge*, Sov. Jour. Nucl. Phys. **23** (1976) 338.

[31] Kuraev, E.A. and Lipatov, L.N. and Fadin, V.S., *Multiregge processes in the Yang-Mills theory*, Sov. Jour. JETP **45** (1977) 199.

[32] I. Balitsky and L. Lipatov, *The Pomeranchuk singularity in quantum chromodynamics*, Sov. Jour. Nucl. Phys. **28** (1978) 822.

[33] L. Harland-Lang, A. Martin, P. Motylinski, and R. Thorne, *Parton distributions in the LHC era: MMHT 2014 PDFs*, Eur. Phys. C. **75** (2015) 204, arXiv:1412.3989.

[34] H.-L. Lai *et al.*, *New parton distributions for collider physics*, Phys. Rev. **D82** (2010) 074024, arXiv:1007.2241.

[35] S. Dulat *et al.*, *The CT14 Global Analysis of Quantum Chromodynamics*, arXiv:1506.07443.

[36] R. D. Ball *et al.*, *A first unbiased global NLO determination of parton distributions and their uncertainties*, Nucl. Phys. **B838** (2010) 136, arXiv:1002.4407.

[37] NNPDF Collaboration, R. D. Ball *et al.*, *Parton distributions for the LHC run II*, arXiv:1410.8849.

[38] S. Alekhin, J. Blümlein, and S. Moch, *The ABM parton distributions tuned to LHC data*, Phys. Rev. D (2014) , arXiv:1310.3059.

[39] P. Jimenez-Delgado and E. Reya, *Dynamical NNLO parton distributions*, Phys. Rev. **D79** (2009) 074023, arXiv:0810.4274.

[40] ATLAS collaboration, G. Aad *et al.*, *Determination of the strange quark density of the proton from ATLAS measurements of the $W \to l\nu$ and $Z \to ll$ cross sections*, Phys. Rev. Lett. **109** (2012) 012001, arXiv:1203.4051.

[41] Y. Li and F. Petriello, *Combining QCD and electroweak corrections to dilepton production in FEWZ*, Phys. Rev. D **86** (2012) 094034, arXiv:1208.5967.

[42] S. Catani *et al.*, *Vector boson production at hadron colliders: a fully exclusive QCD calculation at NNLO*, Phys. Rev. Lett. **103** (2009) 082001, arXiv:0903.2120.

[43] J. C. Collins, D. E. Soper, and G. F. Sterman, *Transverse momentum distribution in Drell-Yan pair and W and Z boson production*, Nucl. Phys. B **250** (1984) 199.

[44] G. A. Ladinsky and C.-P. Yuan, *The nonperturbative regime in QCD resummation for gauge boson production at hadron colliders*, Phys. Rev. **D50** (1994) 4239, arXiv:hep-ph/9311341.

[45] C. Blazs and C.-P. Yuan, *Soft gluon effects on lepton pairs at hadron colliders*, Phys. Rev. **D56** (1997) 5558, arXiv:hep-ph/9704258.

[46] F. Landry, R. Brock, P. Nadolsky, and C.-P. Yuan, *Tevatron Run-1 Z Boson Data and Collins-Soper-Sterman Resummation Formalism*, Phys. Rev. **D67** (2003) 073016, arXiv:hep-ph/0212159.

[47] T. Sjöstrand, S. Mrenna, and P. Skands, *A brief introduction to PYTHIA 8.1* , Comput. Phys. Comm. **178** (2008) 852, arXiv:1011.3540.

[48] M. Bahr *et al.*, *Herwig++ physics and manual*, Eur. Phys. J. **C58** (2008) 639, arXiv:0803.0883.

[49] G. Andersson, G. Gustafson, G. Ingelman, and T. Sjostrand, *Parton fragmentation and string dynamics*, Phys. Rept. **97** (1983) 31.

[50] G. Fox and S. Wolfram, *A model for parton showers in QCD*, Nucl. Phys. B **168** (1980) 285.

[51] S. Frixione, P. Nason, and C. Oleari, *Matching NLO QCD computations with parton shower simulations: the POWHEG method*, JHEP **11** (2007) 070, arXiv:0709.2092.

[52] S. Alioli, P. Nason, C. Oleari, and E. Re, *A general framework for implementing NLO calculations in shower Monte Carlo programs: the POWHEG BOX*, JHEP **06** (2010) 043, arXiv:1002.2581.

[53] S. Frixione and B. Webber, *Matching NLO QCD computations and parton shower simulations*, JHEP **06** (2002) 029, arXiv:hep-ph/0204244.

[54] S. Frixione, F. Stoeckli, P. Torrielli, and B. Webber, *NLO QCD corrections in Herwig++ with MC@NLO*, JHEP **01** (2011) 053, arXiv:1010.0568.

[55] T. Sjöstrand, S. Mrenna, and P. Skands, *PYTHIA 6.4 physics and manual*, JHEP **05** (2006) 026, arXiv:hep-ph/0603175.

[56] G. Corcella *et al.*, *HERWIG 6: An event generator for hadron emission reactions with interfering gluons (including supersymmetric processes)*, JHEP **01** (2001) 0101, arXiv:hep-ph/0011363.

[57] G. Corcella *et al.*, *HERWIG 6.5 release note*, arXiv:hep-ph/0210213.

[58] S. Joseph *et al.*, *HERWIRI1.0: MC realization of IR-improved DGLAP-CS parton showers*, Phys. Lett. **B685** (2010) 283, arXiv:0906.0788.

[59] S. Joseph *et al.*, *New approach to parton shower MC's for precision QCD theory: HERWIRI1.0(31)*, Phys. Rev. **D81** (2010) 076008, arXiv:1001.1434.

[60] S. Majhi *et al.*, *Phenomenology of the interplay between IR-improved DGLAP-CS theory and NLO ME matched parton shower MC precision*, Phys. Lett. **B719** (2013) 367, arXiv:1208.4750.

[61] K. Hamilton, P. Nason, E. Re, and G. Zanderighi, *NNLOPS simulation of Higgs boson production*, JHEP **10** (2013) 222, arXiv:1309.0017.

[62] LHCb collaboration, R. Aaij *et al.*, *Precision luminosity measurements at LHCb*, JINST **12** (2014) P12005, arXiv:1410.0149.

[63] J. Wenninger. Private communication.

[64] J. Wenninger, *Energy calibration of the LHC beams at 4 TeV*, Tech. Rep. CERN-ATS-2013-040, CERN, 2013.

[65] W. Herr and B. Muratori, *The concept of luminosity*, https://cds.cern.ch/record/941318/?ln=sv, 2006.

[66] M. Furman, *The Møller luminosity factor*, http://mafurman.lbl.gov/LBNL-53553.pdf, 2003.

[67] S. van der Meer, *Calibration of the effective beam height in the ISR*, ISR-PO/68-31, 1968.

[68] M. Ferro-Luzzi, *Proposal for an absolute luminosity determination in colliding beam experiments using vertex detection of beam-gas interactions*, Nucl. Instrum. Meth. **A553** (2005) 388.

[69] LHCb collaboration, *LHCb VELO (VErtex LOcator): Technical Design Report*, CERN-LHCC-2001-011. LHCB-TDR-005.

[70] *LHCb silicon tracker material for puclications*, http://lhcb.physik.uzh.ch/ST/public/material/.

[71] LHCb collaboration, *LHCb inner tracker: Technical Design Report*, CERN-LHCC-2002-029. LHCB-TDR-008.

[72] LHCb collaboration, *LHCb magnet: Technical Design Report*, CERN-LHCC-2000-007. LHCB-TDR-001.

[73] LHCb collaboration, *LHCb outer tracker: Technical Design Report*, CERN-LHCC-2001-024. LHCB-TDR-006.

[74] LHCb Collaboration, J. V. Tilberg, *Track simulation and reconstruction in LHCb*, CERN-THESIS-2005-040.

[75] M. Kucharczyk, P. Morawski, and M. Witek, *Primary vertex reconstruction at LHCb*, `https://cds.cern.ch/record/1756296?ln=en`, 2014.

[76] LHCb collaboration, *LHCb RICH: Technical Design Report*, CERN-LHCC-2000-037. LHCB-TDR-003.

[77] LHCb collaboration, *LHCb calorimeters: Technical Design Report*, CERN-LHCC-2000-036. LHCB-TDR-002.

[78] E. Picatoste Olloqui, *LHCb preshower (PS) and scintillating pad detector (SPD): commissioning, calibration, and monitoring*, J. Phys. Conf. Ser. **160** (2009) 012046.

[79] LHCb collaboration, R. Aaij *et al.*, *Performance of the LHCb muon system*, JINST **8** (2013) P02022, `arXiv:1211.1346`.

[80] LHCb collaboration, *LHCb muon system: Technical Design Report*, CERN-LHCC-2001-010. LHCB-TDR-004.

[81] LHCb collaboration, *LHCb trigger system: Technical Design Report*, CERN-LHCC-2003-031. LHCB-TDR-010.

[82] LHCb collaboration, R. Aaij *et al.*, *The LHCb trigger and its performance in 2011*, JINST **8** (2013) P04022, `arXiv:1211.3055`.

[83] S. Malik and G. Watt, *Ratios of W and Z cross sections at large boson p_T as a constraint on PDFs and background to new physics*, JHEP **02** (2014) 025, `arXiv:1304.2424`.

[84] M. Vesterinen and T. Wyatt, *A novel technique for studying the Z boson transverse momentum distribution at hadron colliders*, Nucl. Instrum. Meth. **A602** (2009) 432, `arXiv:0807.4956`.

[85] W. Herr *et al.*, *How do we have to operate the LHCb spectrometer magnet?*, Tech. Rep. LHC Project Note 419, CERN, 2009.

[86] W. Herr and Y. Papaphilippou, *Alternative running scenarios for the LHCb experiment.*, Tech. Rep. LHC Project Report 1009, CERN, 2007.

[87] R. Alemany-Fernandez *et al.*, *Study and operational implementation of a tilted crossing angle in LHCb*, Tech. Rep. TUPFI011, CERN, 2013.

[88] LHCb Collaboration, J. Anderson, *Testing the electroweak sector and determining the absolute luminosity scale using dimuon final states*, CERN-THESIS-2009-020.

[89] ATLAS collaboration, G. Aad *et al.*, *Measurement of the $Z \to \tau\tau$ cross section with the ATLAS detector*, Phys. Rev. D **84** (2011) 112006, arXiv:1108.2016.

[90] CMS collaboration, S. Chatrchyan *et al.*, *Measurement of the inclusive Z cross section via decays to tau pairs in pp collisions at $\sqrt{s}$=7 TeV*, JHEP **117** (2011) 08, arXiv:1104.1617.

[91] M. Cacciari *et al.*, *Top-pair production at hadron colliders with next-to-next-to-leading logarithmic soft-gluon resummation*, arXiv:1111.5869.

[92] ATLAS collaboration, G. Aad *et al.*, *Measurement of the cross section for top-quark pair production in pp collisions at $\sqrt{s}$ = 7 TeV with the ATLAS detector using final states with two high-pt leptons*, JHEP **05** (2012) 059, arXiv:1202.4892.

[93] CMS collaboration, S. Chatrchyan *et al.*, *Measurement of the t t-bar production cross section in the dilepton channel in pp collisions at $\sqrt{s}$ = 7 TeV*, JHEP **11** (2012) 067, arXiv:1208.2671.

[94] J. M. Campbell, R. Ellis, and C. Williams, *Vector boson pair production at the LHC*, JHEP **1107:018** (2011) , arXiv:1105.0020.

[95] ATLAS collaboration, G. Aad *et al.*, *Measurement of the WW cross section in $\sqrt{s}$ = 7 TeV pp collisions with the ATLAS detector and limits on anomalous gauge couplings*, Phys. Lett. B **712** (2012) 289, arXiv:1203.6232.

[96] CMS collaboration, S. Chatrchyan *et al.*, *Measurement of the W^+W^- cross section in pp collisions at $\sqrt{s}$ = 7 TeV and limits on anomalous $WW\gamma$ and WWZ couplings*, The European Physical Journal C **73** (2013) 1434, arXiv:1306.1126.

[97] LHCb Collaboration, S. Farry and N. Chiapolini, *A measurement of high-pT muon reconstruction efficiencies in 2011 and 2012 data*, LHCb-INT-2014-030.

[98] LHCb collaboration, R. Aaij *et al.*, *Absolute luminosity measurements with the LHCb detector at the LHC*, JINST **7** (2012) P01010, arXiv:1110.2866.

[99] G. Cowan, *Statistical data analysis*, Oxford Science Publications, 1998.

[100] A. Höcker and V. Kartvelishvili, *SVD approach to data unfolding*, Nucl. Instrum. Meth. A **372** (1996) 469, arXiv:hep-ph/9509307v2.

[101] T. Adye, *Unfolding algorithms and tests using RooUnfold*, in proceedings of the PHYSTAT 2011 workshop on statistical issues related to discovery claims in search experiments and unfolding, CERN, Geneva, Switzerland, January 2011, edited by H. B. Prosper and L. Lyons arXiv:1105.1160.

[102] G. D'Agostini, *A multidimensional unfolding method based on Bayes' theorem*, Nucl. Instrum. Meth. A **362** (1995) 487.

[103] R. Gavin, Y. Li, F. Petriello, and S. Quackenbush, *FEWZ 2.0: A code for hadronic Z production at next-to-next-to-leading order*, Comput. Phys. Commun. **182** (2011) 2388, arXiv:1011.3540.

[104] P. Nason, *A new method for combining NLO QCD with shower Monte Carlo algorithms*, JHEP **11** (2004) 040, arXiv:hep-ph/0409146.

[105] ATLAS collaboration, G. Aad *et al.*, *Measurement of the inclusive $W^{\pm}$ and Z/γ^{*} cross sections in the e and μ decay channels in pp collisions $\sqrt{s}$ = 7 TeV with the ATLAS detector*, Phys. Rev. D **85** (2012) 072004, arXiv:1109.5141.

[106] CMS collaboration, S. Chatrchyan *et al.*, *Measurement of the inclusive W and Z cross sections in pp collisions at $\sqrt{s}$ = 7 TeV with the CMS experiment*, JHEP **10** (2011) 132, arXiv:1107.4789.

[107] CMS collaboration, S. Chatrchyan *et al.*, *Measurement of inclusive W and Z cross sections in pp collisions at $\sqrt{s}$ = 8 TeV* , Phys. Rev. Lett. **112** (2014) 191802, arXiv:1402.0923.

[108] LHCb collaboration, R. Aaij *et al.*, *Measurement of the cross-section for $Z \to e^{+}e^{-}$ production in pp collisions at $\sqrt{s}$ = 7 TeV*, JHEP **02** (2013) 106, arXiv:1212.4620.

[109] LHCb Collaboration, R. Aaij *et al.*, *A study of the Z production cross-section in pp collisions at $\sqrt{s}$ = 7 TeV using tau final states*, JHEP **01** (2013) 111, arXiv:1210.6289.

[110] A. Buckley *et al.*, *General-purpose event generators for LHC physics*, arXiv:1101.2599.

[111] CDF collaboration, T. Affolder *et al.*, *The transverse momentum and total cross section of E^+ E^- pairs in the Z-boson region from P anti-P collisions at $s^{1/2}$ = 1.8-Tev*, Phys. Rev. Lett. **84** (2000) 845, arXiv:hep-ex/0001021.

[112] M. L. Mangano and J. Rojo, *Cross section ratios between different CM energies at the LHC: opportunities for precision measurements and BSM sensitivity*, JHEP **1208** (2012) 010, arXiv:1206.3557.

[113] ATLAS collaboration, G. Aad *et al.*, *Performance of missing transverse momentum reconstruction in proton-proton collisions at 7 TeV with ATLAS*, Eur. Phys. J. **C72** (2012) 1844, arXiv:1108.5602.

[114] CMS collaboration, S. Chatrchyan *et al.*, *Missing transverse energy performance of the CMS detector*, JINST **6** (2011) 09001, arXiv:1106.5048.

[115] LHCb Collaboration, R. Aaij *et al.*, *Measurement of the forward Z boson production cross-section in pp collisions at $\sqrt{s}$ = 7 TeV*, JHEP **08** (2015) 039, arXiv:1505.07024.

[116] LHCb Collaboration, R. Aaij *et al.*, *Measurement of the forward W boson cross-section in pp collisions at $\sqrt{s} = 7$ TeV*, JHEP **12** (2014) 079, arXiv:1408.4354.

[117] C. Barschel and R. Matev. Private communication.

[118] A. D. Martin, W. J. Stirling, R. S. Thorne, and G. Watt, *Parton distributions and QCD at LHCb*, arXiv:0808.1847v.

[119] K. Kovařík *et al.*, *A survey of heavy quark theory for PDF analyses*, Proceedings of the Ringsberg workshop (2011) arXiv:1201.1946.

[120] A. D. Martin, W. J. Stirling, R. S. Thorne, and G. Watt, *Parton distributions and the LHC: W and Z production*, Eur. Phys. J. **C14** (2000) 133, arXiv:hep-ph/9907231.

[121] R. Ellis, W. Stirling, and B. Webber, *QCD and Collider Physics*, Cambridge University Press, 1996.

[122] R. J. Barlow, *Statistics: A guide to the use of statistical methods in the physical sciences*, Wiley, 1989.